**POLITECNICO DI MILANO**

Facoltà di Ingegneria Industriale e dell'Informazione

Dipartimento di Energia

Dipartimento di Chimica, Materiali e Ingegneria Chimica

"Giulio Natta"


# AN EFFICIENT COMPUTATIONAL FRAMEWORK FOR THE ADVANCED MODELING AND DESIGN OF INDUSTRIAL CATALYTIC REACTORS

Relatori: Prof. Alberto CUOCI

Prof. Matteo MAESTRI

Correlatore: Dr. Tiziano MAFFEI

Tesi di Laurea in Ingegneria Chimica di:

Giancarlo GENTILE 781545

Filippo MANELLI 782418

Anno Accademico 2012-2013

# Abstract

The present Thesis proposes an extensive and comprehensive optimization of the catalyticFOAM solver, a CFD code for the modeling of multi-dimensional systems with homogeneous and heterogeneous reactions. The final aim of the work is the improvement and the validation of the code and its application to cases of industrial interest.

The catalyticFOAM solver was developed in a couple of previous Theses [1,2] in order to investigate catalytic systems on the basis of the so-called “first principle approach”. In particular, two different versions of the code were implemented, but both of them were tested only with simple geometries, without exploring all their capabilities. As a consequence, before applying the codes for the simulation of industrial cases, usually characterized by huge dimensions and complex boundary conditions, several critical points had to be investigated and corrected during this work. Moreover, in order to exploit the possibility to use multi-processor machines, several parts of the codes were completely rewritten or optimized.

The first solver, named catalyticFOAM-0.9, is a CFD code able to simulate catalytic reactive systems in arbitrarily complex multi-dimensional geometries with a detailed microkinetic description of the surface reactivity. Nevertheless, the modeling of the solid catalyst was neglected. Two main open issues were found and fixed during this Thesis: i) the coupling strategy between the species and energy transport equations; ii)the order in which the transport equations are solved in the context of the operator-splitting algorithm, on which the catalyticFOAM solver is based. The first aspect is a critical step in the development of a reliable and accurate CFD code, because of the strong non-linearities of the system that may cause instability during the numerical solution. The effectiveness of the mathematical coupling here introduced has been tested in different cases with several reactive systems: hydrogen combustion, reverse water gas shift and steam reforming.The second issue has been addressed to identify an efficient numerical methodology that allows to solve accurately the equations following the operator splitting technique. In particular the influence of the position of the stiff term, which corresponds to the reactive (or chemical) term, has been investigated in order to find the best solution that guarantees stability of the algorithm. In agreement with several literature articles, in order to have high level of accuracy, it was demonstrated that the stiff term has always to terminate the splitting process due to its stabilizing effect on the solution.

The second solver, named catalyticFOAM-multiRegion, introduces a detailed description of the solid catalyst. It allows for the dynamic solution of reacting flows over solid catalysts through the development of a multi-region structure. In this way is possible to investigate complex systems with an arbitrary number of different domains. The most critical issue in this code was a weak mathematical description of the interface coupling between the different regions. A new coupling strategy, based on a physical arguments, was identified during this work. In particular a segregated approach for the coupling of the neighboring regions at the interface was implemented, involving the solution in sequence on each domain and the achievement of convergence on the boundary conditions through an iterative loop, named PIMPLE loop. The capability of the new solver was tested by performing several simulations of increasing complexity. In particular, the results in steady-state conditions were compared with available analytical solutions and experimental data.

Another important novelty introduced in this work is the parallelization of the multi-region solver. This issue is of utmost importance to reduce the computational simulation times and allow the modeling of industrial cases with very large and complex meshes.

Eventually, once the improved versions of the two codes had been developed, several numerical simulations of a packed bed catalytic reactor for the ethylene oxidation have been carried out during an internship period at the CFD Department of the BASF production plant of Ludwigshafen (Germany). Three different beds (spheres, cylinders and rings) of different lengths have been analyzed. They have been set up using a computational tool based on the DEM (Discrete Element Method) methodology; Different tests have been performed in a wide range of operative conditions in order to analyze the effect of the geometry of the catalytic bed on the reactants conversion. Moreover, using the multi-region approach, the presence of diffusive limitations inside the catalyst, reducing the performances of the whole process, has been highlighted.

In conclusion, the capabilities of the two codes to successfully describe inter and intra-phase phenomena in both the solid and the fluid phase have been demonstrated in the present Thesis. The possibility to model cases of industrial interest highlights the potential of the codes, representing an important breakthrough with respect to the literature.

# Sommario

Il presente lavoro di tesi ha come obiettivo l'ottimizzazione estesa del solver catalyticFOAM in modo da rendere possibile la sua applicazione alla simulazione di casi di rilevanza industriale.

In precedenti tesi sono stati sviluppati due differenti strumenti di modellazione fluidodinamica capaci di modellare sistemi catalitici attraverso un approccio "first principle". Questi due codici erano stati testati solamente su casi caratterizzati da sistemi reattivi e geometrie semplici. I risultati, tuttavia, presentavano diverse criticità che necessitavano di essere risolte in modo da garantire elevata stabilità del solutore e accuratezza dei risultati. Tale prerequisito è fondamentale nell'ottica di una sua successiva applicazione a casi di grandi dimensioni tipici della scala industriale.

Il primo risolutore, chiamato catalyticFOAM, simula sistemi reattivi attraverso un efficiente accoppiamento tra fluidodinamica computazionale e microcinetica. Le reazioni eterogenee interessano solo la superficie esterna del catalizzatore trascurando in prima approssimazione la modellazione dettagliata della fase solida. Le problematiche presenti riguardavano il corretto accoppiamento tra bilancio materiale e di energia e lo sviluppo di un'efficiente strategia di applicazione della tecnica dell'operator splitting. La prima questione è di fondamentale importanza per lo sviluppo di un codice CFD, in quanto, le forti non-linearità del sistema causano notevoli instabilità nella risoluzione. L'efficacia dell'accoppiamento introdotto è stato testato su diversi sistemi reattivi, quali combustione di idrogeno, reverse water gas shift e steam reforming.

Come detto, il secondo aspetto riguarda la tecnica dell'operator splitting che consente di separare il termine di trasporto da quello reattivo nelle equazioni costitutive di bilancio materiale e energetico in modo da ottenere un'accurata risoluzione del problema tramite una notevole diminuzione dei tempi di calcolo. E' stato riscontrato che tale soluzione è fortemente influenzata dalla posizione del termine stiff, ovvero del termine reattivo. In accordo con la letteratura scientifica si è dimostrato che la migliore strategia risolutiva prevede di risolvere il termine stiff a valle delle altre equazioni a causa del suo effetto stabilizzante sulla soluzione.

Il secondo risolutore, chiamato catalyticFOAM multiRegion, estende la modellazione catalitica anche alla fase solida. In questo modo si rende possibile una più completa analisi di sistemi costituiti da più regioni. La criticità di questo strumento era dettata da una non corretta

descrizione matematica dell'interfaccia tra domini differenti. Di conseguenza l'obiettivo principale è stato quello di sviluppare una nuova strategia di risoluzione che permettesse di descrivere in maniera più fisica il sistema. A fronte di queste esigenze è stato implementato un approccio segregato di accoppiamento tra regioni adiacenti. Questo prevede la soluzione separata di ogni dominio in modo da raggiungere condizioni di convergenza all'interfaccia attraverso un ciclo iterativo denominato PIMPLE loop. Le capacità di questo nuovo strumento sono state testate su casi di progressiva complessità andando a comparare i risultati ottenutati con le simulazioni CFD e dati reperibili in letteratura.

Un' altra importante novità introdotta in questo lavoro è stata la completa parallelizzazione del codice. Tale aspetto è di vitale importanza allo scopo di ridurre notevolmente i tempi di calcolo e quindi di permettere la simulazione di casi industriali di notevole complessità.

Infine, una volta sviluppata l'architettura generale dei solutori si è resa possibile la loro applicazione alla modellazione del reattore a letto impaccato adibito alla produzione di ossido di etilene. Queste tematiche sono state argomento di studio durante un periodo di internship presso il dipartimento di fluidodinamica della società BASF a Ludwigshafen (Germania). In particolar modo è stata studiata l'influenza della geometria del letto sulle prestazioni del reattore catalitico stesso. La struttura di questi letti è stata generata attraverso l'ausilio di software basati sulla metodologia DEM (discrete element method). Questi modelli sono in grado di comporre geometrie random attraverso bilanci di forze applicate sulle unità fondamentali costituenti il sistema complessivo.

A questo punto sono stati eseguiti differenti test in un ampio intervallo di condizioni operative con entrambi i solutori sviluppati. Questo ha permesso di identificare l'influenza di eventuali limitazioni diffusive sulla reattività del sistema.

La capacità di questi strumenti di descrivere efficacemente i fenomeni inter e intra fasici sia nella regione fluida che in quella solida evidenziano la grande flessibilità di questi due solutori e l'innovazione che questi introducono rispetto alla letteratura esistente.

# Table of contents

# 1 Introduction

## 1.1 Motivation

Catalysis and catalytic processes are central to many aspects of Chemical Engineering. Whether it's securing plentiful energy supplies, protecting the environment or helping to improve industry's financial bottom-line, catalysis has a key role to play.

The most well-defined areas of industrial catalysis are petroleum, pharmaceutical, and environmental catalysis. Petroleum catalysis employs catalysts to manufacture petrochemicals derived from crude oil. Pharmaceutical catalysis uses catalysts in the manufacture of molecules that have a targeted and very specific function in the body. Environmental catalysis uses catalysts to remove toxic or waste products from manufacturing effluent [2, 3].

The simultaneous developments in catalysis and reaction engineering in 1930s and 1940s acted as a driving force for the onset of rational design of catalytic reactors. These rigorous design efforts, firmly based on sound mathematical principles, in turn triggered the development of several profitable catalytic processes. Several authors have studied the engineering aspects of diffusional mass transport and reaction rate interaction. In particular, Thiele [4, 5] explained the fractional reductions in catalyst particle activity due to intraparticle mass transfer limitations and the concept of the effectiveness factor reflecting the extent of utilization of the catalyst pellet was proposed. The diffusional disguise of the activity of a catalyst pellet is now routinely gauged by a dimensional parameter known as the Thiele modulus. Based on this concept, rigorous mathematical models developed in the 1950s and the 1960s showed the importance of intra- and inter-particle diffusion for a variety of complex situations. With the advent of computers, solutions of complex mathematical models became relatively easy and sophisticated heterogeneous reactor models were proposed and solved. In parallel, research in catalysis grew rapidly with an aim for identifying and preparing highly active, selective and stable catalysts. With advancements in new instrumentation and analytical technique, it is possible to study catalysis at the atomic level, determine the structure and compositions of the catalyst and precisely carry out quantitative estimation of the interaction of the reactant and product at the surface of the catalyst. This

information is highly useful in determining the effect of the surface chemistry on the overall performance of the catalyst.

Nowadays rigorous implementation of optimal policies for maximizing conversion and integration of control strategies has also been given importance. Performance enhancement employing CFD enabled flow modeling has received serious attention of industry as well as academia. The availability of super-fast computing facilities has prompted the coupling between such detailed fluid dynamic and kinetic descriptions.

## 1.2 General overview

One of the main difficulties encountered in the numerical modeling of a catalytic system with complex kinetics and geometry is without any doubts the great gap of different time and length scales involved, since the dominant reaction pathway is the result of the interplay between micro-, meso-and macro-scale phenomena (Figure 1).

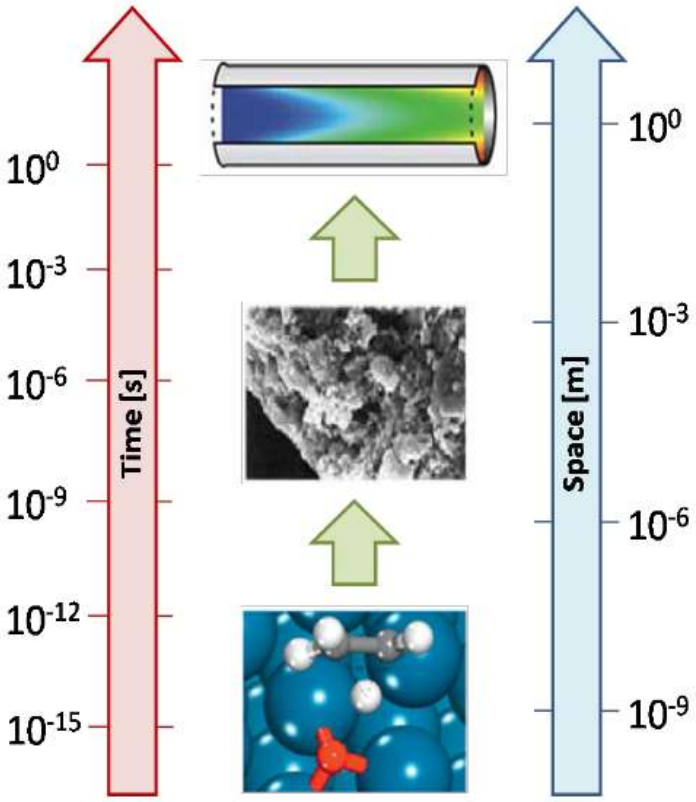


Figure 1: Time and length scales involved in heterogeneous catalytic processes

The microscopic scale is associated with making and breaking of chemical bonds between atoms and molecules. At the mesoscale the interplay between all the elementary steps involved in the catalytic process determines the main reaction pathway. At the macroscopic scale transport of mass, energy and momentum determines local composition, temperature and pressure.

This means that the dominant reaction mechanism is a multi-scale property of the system [6]. The description of different phenomena is achieved by employing a "first principles" approach, i.e. at each scale the fundamental governing equations are used.

- At the molecular scale the behavior of the system is described through detailed kinetic models, whose parameters are computed via first-principles electronic-structure calculations.
- At the meso-scale statistical methods give a rigorous representation of mechanisms taking place at the catalytic surface. Anyway the most common approach used in literature is the mean field approximation [7]. This approach assumes a perfect and rapid mixing of reactants, products and intermediates on the surface.
- At the macro-scale methods based on continuum approximation are employed, e.g. resolution of Navier-Stokes equations with Computational Fluid Dynamics (CFD) methodologies [8].

Such a fundamental approach implies the development of efficient methodologies to connect the fundamental aspects across all the scales involved and link them in one multi-scale simulation.

Unluckily, the resulting numerical problem places highly computational demands:

- The dimensions of the system are proportional to the number of species involved in the reacting process. Therefore, the more detailed the kinetic scheme is, the higher the required time is.
- The discretization of the geometric domain is required to solve the problem. The number of cells in which the volume is divided is proportional to the accuracy and to the dimensions of the problem.
- The problem is very stiff because of the difference among the characteristic times of the scales.
- The presence of a reacting term implies a strong non-linearity of the governing equations.

Furthermore, an accurate description of the problem should include a characterization of the catalytic phase and the modeling of intra-solid phenomena constituting the true nature of the diffusion-reaction mechanism. This acquires particular importance, especially when dealing with systems where the heat and mass transfer limitations play a major role in determining the conditions holding on the catalytic surface. In these cases, neglecting the catalyst morphology can have a critical impact on the description of the system.

## 1.3 Aims of this work

In previous works ([9] and [1]) two CFD solvers (catalyticFOAM and catalyticFOAM multiRegion) have been built up in the OpenFOAM® framework, an open source CFD framework.

The first one is able to investigate catalytic systems with a first-principles approach, i.e. employing the governing equations to describe each scale, coupling computational fluid dynamics methodologies with a detailed microkinetic description of surface reactivity. Nevertheless, the catalytic phase was not modeled into detail. This aspect has been accounted for in the second work where a multi-region solver has been developed, which allows the solver to investigate systems with an arbitrary number of different domains with their own properties, whose geometry can be of arbitrary complexity. A detail modeling of the both regions (fluid and solid) has been provided through the resolution of the fundamentals equations describing the physics of the system in each phase.

The main aim of this work is the improvement of these two solvers in order to allow the simulation of complex, multidimensional reactors. In the previous works ([9] and [1]), only simple geometries and flow field have been tested and many aspects about the stability and the accuracy of the adopted methodology have not been taken into account.

In the present work, the most important critical issues have been deeply analyzed and fixed and the simulations of an industrial reactor for the oxidation of the ethylene have been carried out during an internship in BASF.

In the following a short description about the organization of the present thesis is reported.

In **Chapter 1** a general overview of the catalyticFOAM framework is provided. In particular three different tools are briefly described: OpenFOAM®, OpenSMOKE and CatalyticSMOKE. The first one is a CFD framework, which is able to discretize and solve the transport equations on complex

structured and unstructured meshes. The others two are kinetic libraries that allow the solver the possibility to simulate complex kinetic schemes. OpenSMOKE is able to manage the gas-phase, instead CatalyticSMOKE handling the heterogeneous kinetic schemes.

In **Chapter 2** the first version of catalyticFOAM [8] are analyzed. The main criticalities that affect the solver have been studied in order to obtain a code able to work both in isothermal and adiabatic conditions, exploiting detailed or global kinetic schemes. The main issues that have been studied are the energy balance and the operator splitting order of equations. In the previous work [9] the solver has been tested only in isothermal conditions with a detailed kinetic scheme for the oxidation of hydrogen. The introduction of the energy balance equation is not a trivial operation due to the strong non linearity of the system under investigation. The purpose of this section is the identification of the best coupling between the species and energy balances.

The catalyticFOAM framework is based on the operator splitting technique for the efficient coupling between microkinetic modeling and CFD. It allows the separation of the reactive term from the transport one in order to select the best numerical methodology to solve each of them. In this context, the second important issue that it has been taken into account is the order of the equations within the operator splitting scheme itself. In particular the influence of the position of the stiff term (that corresponds to the reactive term) has been investigated in order to find the best solution in term of stability of the algorithm and accuracy of the solution. Finally the new version of the solver has been tested for complex catalytic reactive systems in order to verify the effectiveness of the revisions introduced.

In **Chapter 3** the catalyticFOAM multiRegion solver is analyzed. In a previous work [1] this tool has been used for the simulation of multi-region domain, studying only the steady-state solution. The solver was not able to ensure the convergence at the interphase between the different domains during the transient. This issue is crucial for the correct modeling of the system, because the steady-state solution is strongly influenced by the evolution of the system during the transient. In order to overcome these criticalities the entire framework of the solver was modified, following a more physical approach able to describe the interface coupling of neighboring regions in an accurate way. In particular, to handle multiple regions and their interaction, a partitioned approach is adopted: the governing equations are solved separately on each of the coupled regions, imposing appropriate boundary conditions (mixed boundary conditions) at the interface between two different phases. To make the coupling effective, the procedure must be iterated

until convergence is reached (PIMPLE Loop). All the features described above are tested in this Chapter, by performing simple numerical tests of increasing complexity to prove the validity and effectiveness of the segregated numerical approach proposed.

Eventually, in order to investigate the reliability of the solver, a validation is performed through the simulation of fuel-rich $H_2$ combustion over Rh catalyst in an annular reactor. The simulation results are compared with experimental data in order to study the capability of the solver to reproduce the physics of both inter-phase interaction and intra-phase phenomena inside the solid catalyst.

In **Chapter 4** different packed beds made by three different unit structures (spheres, cylinders and rings) have been analyzed in order to allow the simulation of an industrial reactor of ethylene oxide that has be studied in Chapter 5. These structures are generated though the DEM (Discrete Element Method) approach. The DEM is a modeling technique capable of describing the mechanical behavior of assemblies of structures through an explicit numerical scheme in which the interaction of the particle is monitored contact by contact and the motion of particle is modeled particle by particle. The final configuration generated is made by the unit elements assembled in a random way. In order to test the reliability of the structures obtained a comparison with the void fraction of the real catalytic packed beds of the ethylene oxide has been carried out. Moreover, a deep analysis of the pressure drops on the beds analyzed has been carried out. The results have been compared both with experimental data and with correlations available in the literture.

In **Chapter 5** an industrial reactor of ethylene oxidation has been simulated in order to test the predictive ability of the two solvers (catalyticFOAM and catalyticFOAM multiRegion) studied respectively in Chapter 2 and Chapter 3. The investigated process is high exothermic and, hence, it has carried out in non-adiabatic multitubular fixed-bed catalytic reactor. In order to simulate this reactive system, the three structures (spheres, cylinders and rings) generated by the DEM methodology, described in Chapter 4, are used.

Simulations have been carried out both in isothermal and adiabatic conditions in a range of inlet temperature (432-550 K) in order to test the realistic operating industrial conditions. The three packed beds have the same catalytic area, hence, analyzing the levels of conversions at steady-state it is possible to define the shape that guarantee the best exchange of mass and heat at the interface between bulk phase and catalytic surface.

Eventually, the same simulations have been carried out with the improved version of catalyticFOAM multiRegion able to characterize also the solid phase. With this solver it is possible to investigate the profile inside the solid phase in order to study if the onset of pore diffusion regime can modify the efficiency of the catalyst.

# 2 The CatalyticFOAM solver

The starting points of this thesis were two different versions of catalyticFOAM that have been built up in previous works [9]-[1]. Although these two solvers are used to model different reacting system, they have the same general structure. In particular catalyticFOAM is the sum of three different tools: OpenFOAM, OpenSMOKE and CatalyticSMOKE. In this Chapter a general overview of these tools has been carried out with the aim to highlight the specificity of each of them.

## 2.1 The OpenFOAM® framework

The aim of this section is to introduce the main features of OpenFOAM® as support code for CFD simulations and its practical use.

OpenFOAM® is a C++ library created in 1993 and it is an object-oriented numerical simulation toolkit for continuum mechanics. Its popularity is increasing in the last years because OpenFOAM is released under General Public License (GPL), including the possibility to have at disposal the whole code and eventually modify it as needed. It is capable to support all the typical features of C++ programming, e.g. creation of new types of data specific for the problem to be solved, construction of data and operations into hierarchical classes, handling of a natural syntax for user defined classes (i.e. operator overloading) and it easily permits the code re-use for equivalent operations on different types [10].

OpenFOAM® is not meant to be a ready-to-use software, even if it can be used as a standard simulation package. Rather, it offers a support in building user specific codes. Like the widest part of CFD software, OpenFOAM® provides tools not only for the finite volumes calculations, but also for pre and post processing. A schematic of the library structure is given in Figure 2

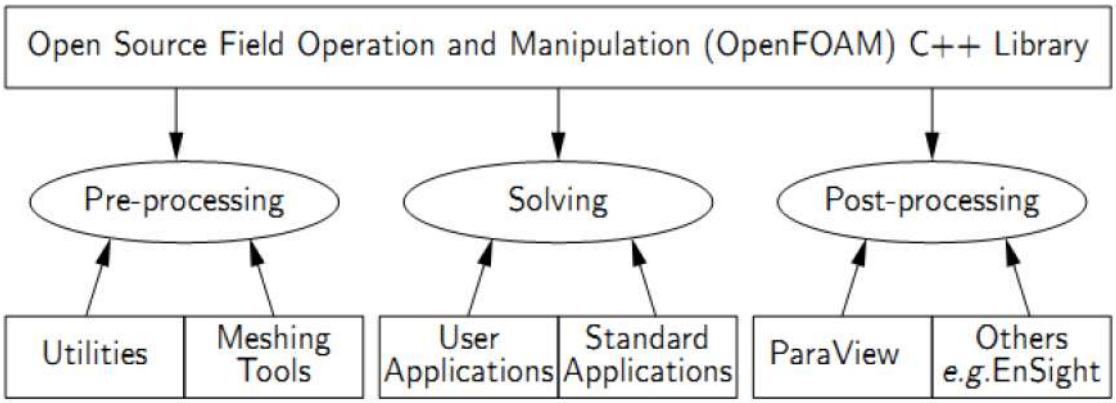


Figure 2: OpenFOAM® library structure

Pre-processing tools enable the set-up of the simulations by the generation of the computational mesh, only with the corresponding initial and boundary conditions. Post-processing utilities allow one to view and analyze simulations results. The computational part is based on solvers, applications designed to solve specific classes of engineering problems, e.g. aerospace, mechanics, chemistry.

The latest OpenFOAM® version (2.1.1) includes over 80 solver applications and over 170 utility applications that perform pre-and post-processing tasks, e.g. meshing, data visualization, etc.

In the following it will be present the structure and organization of an OpenFOAM® case. In general the sequence of work in OpenFOAM® can be divided into three consecutive steps:

- ✓ *pre-processing*: firstly it is necessary to set-up the problem;
- ✓ *processing*: the simulation is performed by a solver;
- ✓ *post-processing*: results are displayed with specific application for data analysis and manipulation.

### 2.1.1 Pre-processing

The basic directory structure for the set-up of an OpenFOAM® case is represented in Figure 3.

.

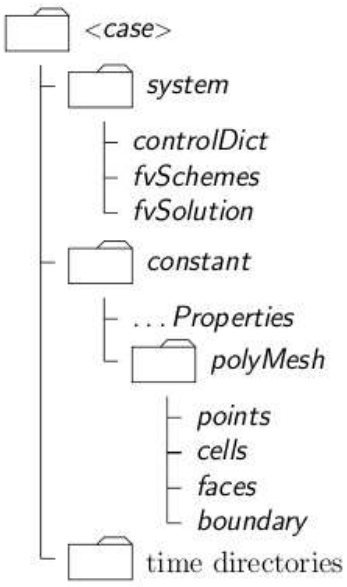


Figure 3: Directory structure for the set-up of an OpenFOAM® case

The case folder includes:

- ✓ The *polyMesh* folder providing a full description of the case mesh.
- ✓ The *constant* directory containing information about physical properties.
- ✓ The *time* directories containing individual data files for each field (e.g. temperature, pressure, compositions) at different times of simulation.
- ✓ The *system* directory for setting numerical parameters associated with the solution procedure.

It is necessary to pay great attention to the creation of the computational mesh in order to ensure a valid and accurate solution.

OpenFOAM® provides a mesh generation utility called *blockMesh* that creates parametric meshes with specified grading and arbitrary curved edges. The mesh is generated from a dictionary file named *blockMeshDict* located in the *constant/polyMesh* directory. The utility reads this dictionary, generates the mesh and creates the mesh data.

In order to easily generate elaborate meshes it is possible to use a variety of software, such as *GAMBIT* [11], a mesh generation software owned by Ansys FLUENT®, which writes mesh data to a single file. OpenFOAM® provides a tool for the conversion of GAMBIT meshes to OpenFOAM® format.

Initial and boundary conditions for a certain number of fields are required in order to start the simulation. These data are stored in the *0* folder: each file contains for every variable the initial

conditions for the internal field and the declaration of each boundary condition. The latter has to be chosen from a list of pre-built standard conditions [12].

The *system* directory contains at least the following three files: *controlDict, fvSchemes* and *fvSolution*. In the first one run control parameters are set, including start/end time, time step and other specifications. The *fvSchemes* file contains the discretization schemes used in the solution. Typically one has to assign the discretization methods for gradient, divergence etc. In the *fvSolution* file algorithms for the solution of each equation are selected and tolerances for each variables are set.

### 2.1.2 Processing and post-processing

During the calculations the solver iterates the numerical procedure and periodically writes results at intermediate times. It is possible to choose how often taking note of the results (setting the *writeInterva l= timeIntervalBetweenSuccessiveRecords* in the *controlDictionary* file) and/or how many time folders to write (setting the *purgeWrite* ≠ 0 in the *controlDictionary* file). It is also possible to choose between two different format of writing files:

- ✓ *writeFormat* = BIN: faster writing operation, output files unreadable with text editor tool, but observable through sampling and plotting or classical post processing.
- ✓ *writeFormat* = ASCII: slower writing operation, output files readable with text editor tool as well as observable with more classical methods.

There are some tricks to make the simulations faster. For example it is possible to run a simplified and lightened form of the solver (*simpleFoam*) just to get the stationary field for velocities and take it as starting point: in this way the Navier-Stokes equations are already at a stationary point.

OpenFOAM® is supplied with the post-processing utility *ParaView* [13] an open source multi-platform data analysis and visualization application which provides a lot of useful tools for these scope.

The widest part of complex engineering systems is described by one or more Partial Differential Equations (PDEs). Since the majority of these equations does not have an analytical solution, it is necessary to solve them with numerical methods [14].

In the following the fundamentals of numerical procedures of discretization and solution will be presented.

The purpose of any discretization practice is to transform one or more PDEs into the resulting system of algebraic equations to allow the numerical solution. The discretization process consists of splitting of the computational domain into a finite number of discrete regions, called control volumes or cells. For transient simulations, it is also required to divide the time domain into a finite number of time-steps. Finally, it is necessary to re-write equations in a suitable discretized form.

The approach of discretization adopted by OpenFOAM® is the Finite Volume Method (FVM) [15]. The main features of this method are listed below:

- ✓ The governing equations are discretized in the integral form.
- ✓ Equations are solved in a fixed Cartesian coordinate system on the computational mesh. Solution can be evaluated both for steady-state and transient behaviors.
- ✓ The control volumes can have a generic polyhedral shape: together they form an un-structured mesh ([16] [17]).

In the following it will be provide a description of discretization of domain, time and equations.

### 2.1.3 Domain discretization

The discretization via FVM entails the subdivision of the domain in control volumes or cells. These have to completely fill the domain without overlapping. The point in which variables are calculated is located in the centroid of the control volume of each cell, defined as:

$$\int_{V_P} (x - x_p) dV = 0 \tag{2.1}$$

where $x_p$ stands for the coordinate of the centroid, as shown in Figure 4.

The domain faces can thus be divided in two classes: internal faces, between two control volumes, and boundary faces, which coincide with the boundaries of the domain. A simple example of domain discretization is showed in Figure 4.

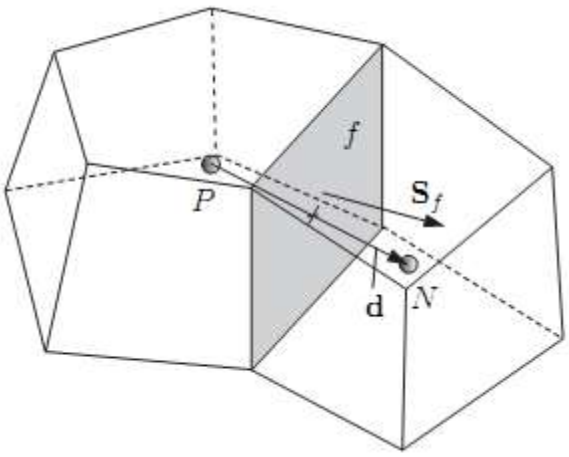


Figure 4: Example of finite volume discretization

In Figure 4 the point *P* and *N* represents the centroid of the cells of the geometric domain. The vector *d* represents the distance between the two centroids. The vector *Sf* is the surface vector outgoing from the generic flat face *f*.

### 2.1.4 Equations discretization

Let us consider the standard form of the transport equation of a generic scalar field $\phi$:

$$\frac{\partial p\phi}{\partial t} + \nabla(\rho U\phi) - \nabla(\Gamma\nabla\phi) = 0 \tag{2.2}$$

where $U$ is the velocity vector and $\Gamma$ is the generic diffusion coefficient (e.g. thermal conductivity). For the sake of clarity the source term has been neglected.

The finite volume method requires that Eq. (2.2) is satisfied over the control volume $V_P$ in the integral form:

$$\int_t^{t+\Delta t}\left[\frac{\partial}{\partial t}\int_{V_P}\rho\phi dV + \int_{V_P}\nabla(\rho U\phi)dV - \int_{V_P}\nabla(\rho\Gamma\nabla\phi)dV\right]dt = 0 \tag{2.3}$$

The discretization of each term of Eq. (1.3) is achieved by applying the Gauss theorem in its general form:

$$\int_V \nabla\phi dV = \oint_{\partial V}\phi dS \tag{2.4}$$

Having in mind that each cell is bounded by a list of flat faces, it is possible to re-write the integral of Eq. (1.4) as a sum over all faces. The combination of Eq. (1.3) and (1.4) leads to:

$$(\nabla\phi)V_P = \sum_f S_f \phi_f \tag{2.5}$$

where $V_P$ is the volume of the cell, $S_f$ is the surface of the cell and $\phi_f$ is the flux of the generic scalar $\phi$ through the face *f*.

### 2.1.5 Time discretization

In transient problems it is fundamental to adopt numerical methods to handle temporal integration. Let us consider the first term of Eq. (1.3):

$$\int_t^{t+\Delta t}\left[\frac{\partial}{\partial t}\int_V \rho\phi dV + \int_V \psi(\phi)dV\right]dt \tag{2.6}$$

where $\psi(\phi)$ is a generic non linear function.

The time integration can be evaluated in three different ways in OpenFOAM®:

- ✓ **Euler implicit:** the time term is Hartmann discretized in an implicit way [18], thereby taking current values $\phi^n$:

$$\int_t^{t+\Delta t} \psi(\phi)dt \cong \psi_D(\phi^n)\Delta t \tag{2.7}$$

where $\psi_D(\phi^n)$ is the discretized form of the spatial quantity $\psi(\phi)$ and *n* indicates the new computed value. This method provides first order accuracy, guarantees boundedness and is always stable [19].

- ✓ **Explicit:** the spatial term is discretized in explicit way, which means that old values of $\phi$ are used:

$$\int_t^{t+\Delta t} \psi_D(\phi^n)dt \cong \psi_D(\phi^0)\Delta t \tag{2.8}$$

where $\phi^0$ are the old values of $\phi$. This method is first order accurate and the solution depends only on previous times. The main disadvantage is that this method becomes unstable when too big time steps are adopted for the integration.

- **Crank-Nicholson:** a trapezoid rule is used to discretize the temporal integral:

$$\int_t^{t+\Delta t} \psi_D(\phi)dt \cong \psi_D\left(\frac{\phi^n + \phi^0}{2}\right)\Delta t \tag{2.9}$$

This method is second order accurate and stable, but does not guarantee boundedness of the solution [20].
In the rest of this dissertation the Euler implicit method has been adopted.

### 2.1.6 Boundary conditions

In order to complete the formulation of the discretized problem one has to set boundary conditions. First of all, it is important to separate physical and numerical conditions:

- **Physical conditions:** these conditions are derived from engineering interpretation of the true system behavior. These conditions are set during the creation of a mesh. Each physical condition is the union of several numerical conditions. Here we provide some significant examples:
  - ✓ Inlet: the velocity profile at inlet is assigned and, for consistency, pressure gradient is set to zero.
  - ✓ Outlet: the pressure profile is assigned and velocity gradient is set to zero.
  - ✓ Symmetry plane: in 2D cases it is necessary to specify the symmetry plane of the system. The related boundary condition implies that the components of the gradient normal to the surface are set to zero.
- **Numerical conditions:** these conditions provide a suitable expression for the value of variables at boundaries. Their values are specified with the initial conditions. Specifically, the most important conditions are Dirichlet (or fixed value) and Neumann (or fixed gradient).

### 2.1.7 Algebraic linear system

OpenFOAM® implements different algorithms for the solution of linear algebraic systems of equations. Algorithms are selected by specifying the following features:

- ✓ *Preconditioner*: allow one to choose a method for the preconditioning of the system [12]. This improves the conditioning of the problem and save computational time.
- ✓ *Linear solver*: specifies which solver has to be used. Here it is possible to cite Krylov subspace solvers and GAMG [12], which evaluate the solution on a coarse grid and then refine it on a finer mesh.
- ✓ *Smoothers*: improve computational speed reducing the number of iterations required to reach the convergence.

## 2.2 The kinetic library

In this section a detailed description of the kinetic library is provided. A general introduction is reported in 1.2.1 The gas-phase kinetic is handled by the *OpenSMOKE* library, described in 1.2.2, while the heterogeneous kinetic mechanism is implemented in the *CatalyticSMOKE* library, illustrated in 1.2.3.

### 2.2.1 General overview

In the chemical industry the need to control reactions at the molecular level quickly increased within the requirement of more energy efficient and selective processes. In order to achieve this goal during most of the 20th century the approach consisted in proposing a rate equation and fitting it with experimental data to obtain the most suitable rate constants. Even though this method leads to powerful results, these models give satisfying results only in a narrow range of operating conditions [21].

In recent years kinetic models have been reinterpreted thanks to the possibility of modeling in detail the surface chemistry. Indeed, the aim of kinetic modeling is to provide valuable tools for the design of chemical reactors under a wide range of conditions and for the analysis and optimization of catalytic processes [22].

During the last years the attention has been focused on kinetic models that try to incorporate the basic surface chemistry involved in the catalytic reaction [23]. This new perspective leads to the development of a new rational design of the catalyst based on predictive capability of first-principles models, without any experimental input. Anyway this approach still presents many challenges to overtake, in order to have a full description and control of all chemical transformations.

In order to provide a predictive ability to the heterogeneous kinetics model, it has been useful to employ some specific libraries. In particular, the kinetic scheme handling relies on two libraries, one for the homogeneous and the other for the heterogeneous phase.

## 2.3 The OpenSMOKE library

The gas-phase is entirely managed by the *OpenSMOKE* library. This has been written in C++ by the *CRECK* modeling group at Politecnico di Milano and provides an efficient handling of thermodynamic, transport and kinetic data.

In order to use the *OpenSMOKE library* two steps are required:

- ✓ the first one is the interpretation of the input files: in this phase the interpreter program reads information from files, checks if these are correct and consistent, elaborates data and prints them in binary files. The input files contain respectively thermodynamic, transport and kinetic information and are written in the standard CHEMKIN® format [24].
- ✓ the second one is the computation of desired properties: binary files are read, data are saved in the Random Access Memory (RAM) to improve the speed of access and the requested properties are calculated by calling the required functions.

The structure of the *OpenSMOKE* library is described In Figure 5.

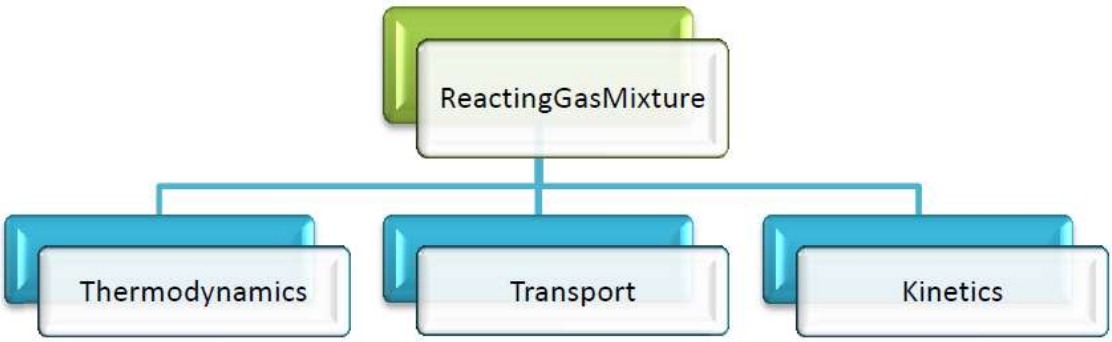


Figure 5: Schematization of the object-oriented library OpenSMOKE

The main class is the *ReactingGasMixture* class, which contains species data, e.g. molecular weight and species names, and a number of useful functions, e.g. conversion from molar to massive fractions and computation of the mean molecular weight of the gas mixture. Furthermore, it includes references to:

- ✓ the *Thermodynamic* class, which contains functions for the computation of thermodynamic properties such as enthalpy, entropy and specific heats.
- ✓ the *Transport* class, which provides methods for the calculation of diffusivities, viscosity and thermal conductivities.
- ✓ the *Kinetics* class, which comprises all the necessary functions for the computation of reaction rates, formation rates and heats of reaction.

## 2.4 The CatalyticSMOKE library

For the handling of the heterogeneous kinetic scheme the most appropriate tool is the *CatalyticSMOKE* library. The main purposes of this tool are:

- ✓ to provide an efficient handling of traditional kinetic schemes based on the SURFACE CHEMKIN® standard format;
- ✓ to give the possibility to implement non-standard kinetic schemes, such as mechanisms based on Unity Bond Index-Quadratic Exponential Potential (UBI-QEP) framework [25].

The organization of this tool is based on the *OpenSMOKE* library structure. Thus, two applications are required: the first one to read and interpret input files, the second to compute the desired properties. In the following, we provide a description of the entire library.

### 2.4.1 Input file

The input file has to be written in the SURFACE CHEMKIN® format [24]. The main features of this format are:

- ✓ broad generality: the SURFACE CHEMKIN® standard is adopted by the widest part of the scientific community;
- ✓ flexibility: there is no limit to the number of materials, catalytic sites, adsorbed species and surface reactions in a single kinetic scheme;

- ✓ possibility to take into account standard, stick and coverage-dependent reactions;
- ✓ intuitive and easy-to-use interface.

One of the main tasks of this interpreter is that it is able to read and process data for UBI-QEP schemes. This feature has been coded as an extension of the standard CHEMKIN® format and it was one of the main purposes of a previous work [9].

It is thus possible to adopt both classic kinetic mechanisms and UBI ones, because semi-empirical methods provide an efficient approach for the detailed description of microkinetic behavior of reacting systems ([26] - [27]).

### 2.4.2 CatalyticSMOKE Library structure

The kinetic parameters stored in the binary file can be read by the *CatalyticSMOKE* library. The structure of this computational tool is described in Figure 6

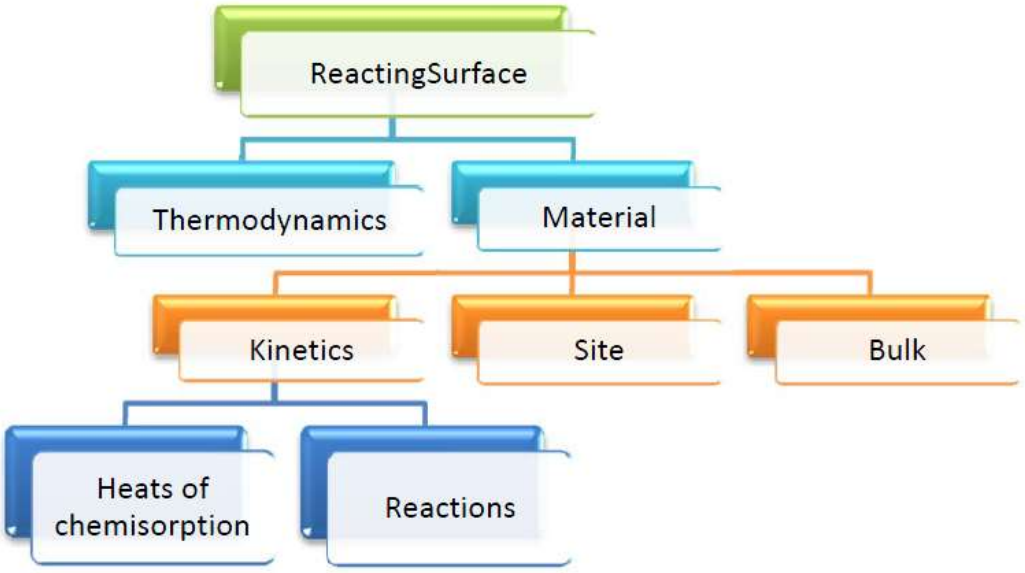


Figure 6: Schematization of the structure of the CatalyticSMOKE library

The main class is *ReactingSurface* and contains references to *Thermodynamics* and *Material* classes. The former provides information on the thermodynamic properties, the latter contains the material properties and is linked to the classes *Site*, *Bulk* and *Kinetics*, which contains information about the kinetic scheme adopted and manages the calculations of heats of chemisorption. For this reason, it is linked to the *Reactions* class, which comprises all the reaction parameters and methods.

In order to exploit the potentiality of C++ language and in particular of object-oriented design, each component of the *CatalyticSMOKE* library is arranged as a class. Specifically, each class has its own methods and can be called by hierarchically superior classes. The function that computes the reaction rates is one of the most used of the *CatalyticSMOKE* library. It can be recalled from the main program by pointing to the main class. The function executes a loop over the materials considered in the kinetic scheme. Since the single material can be composed by one or more active elements, the computation of the reaction rates is accomplished for each kind of site. The information about the kinetic schemes are contained in the *Kinetic* class, while the properties of each site, e.g. site density, are grouped in the *Site* class. The reaction rate evaluation in made by recalling each *Reaction* object, which contains all the necessary data, e.g. activation energy, pre-exponential factor.

# 3 Improvements in catalyticFOAM

In the previous works of thesis the solver catalyticFOAM has been partially tested and some important aspects have not been already investigated, such as the energy balance and the operating splitting technique. For these reasons, this Chapter will provide a more accurate analysis and testing of these aspects. In particular the solver will be tested in adiabatic conditions with simple cases and the results will be compared with equilibrium calculations.

Thereafter a numerical and methodological analysis of the operating technique will be carried out in order to define the most appropriate order of equations.

Finally the solver will be tested with more complex geometries and reactive systems, both in isothermal and adiabatic conditions in order to have a wide perspective of the solver.

## 3.1 The operator splitting approach

The operator splitting methods are commonly used for the numerical computation of reactive flows. Indeed, in case of reacting systems, strong non-linearities are present in the equations. The diffusion and convection terms are slightly non-linear, and therefore they can be easily lagged or linearized without large losses of accuracy in the solution [19].

Nevertheless the source term due to the reaction is highly non-linear: indeed the widest part of kinetic constants are expressed in the Arrhenius' form and the reaction rate is proportional to concentrations at the power of the respective reaction order. For this reason in order to solve the problem it is necessary to adopt specific algorithms.

Nowadays, available CFD codes encounter several difficulties in the solution of these problems, especially in case of the use of detailed microkinetic description of the surface chemistry. For all the reasons presented above, it is compulsory to rely on numerical techniques that allow to overtake these difficulties and obtain a satisfactory and accurate solution.

The numerical scheme adopted consists in the splitting of the equations into sub-equations, and integrating each one separately and sequentially. Typically, each sub-equation describes only one part of the physics of the problem. The results of the integration at each sub-step are combined to

approximate the final solution with high accuracy [28]. This methodology is applied only for the material balance equation and energy balance equation.

Let us consider the generic transport equations:

$$\frac{d\boldsymbol{\varphi}}{dt} = \boldsymbol{M}\left(\boldsymbol{\varphi}, t\right) + \boldsymbol{S}\left(\boldsymbol{\varphi}\right) \tag{3.1}$$

where $\boldsymbol{\varphi}$ comprehend the entire set of species composition and the temperature. Therefore it is a vector of NS+1 variables written as $\boldsymbol{\varphi}$=[$\omega_1$, $\omega_2$,… $\omega_{NS}$, T]. Furthermore $\boldsymbol{M}$ denotes the transport processes due to diffusion and convection, and $\boldsymbol{S}$ denotes the source term due to chemical reactions..

As already mentioned, the $\boldsymbol{S}$ term is stiff and highly non-linear in concentrations and temperature. The $\boldsymbol{M}$ term instead presents a low stiffness and a quasi-linear nature. Instead of solving the entire system, the splitting method provides the splitting of these equations in two systems of equations, the first taking into account only the reaction term and the second one considering only the transport term. The resulting system can be represented in this way:

$$\begin{cases} \dfrac{d\boldsymbol{\varphi}_1}{dt} = \boldsymbol{S}\left(\boldsymbol{\varphi}\right) \\ \dfrac{d\boldsymbol{\varphi}_2}{dt} = \boldsymbol{M}\left(\boldsymbol{\varphi}, t\right) \end{cases} \tag{3.2}$$

---

$$\frac{d\boldsymbol{\varphi}}{dt} = \boldsymbol{M}\left(\boldsymbol{\varphi}, t\right) + \boldsymbol{S}\left(\boldsymbol{\varphi}\right) \tag{3.3}$$

The Jacobian matrix associated to the whole PDEs system that takes into account the reaction is block-unstructured and sparse (Figure 7**).** The Jacobian matrix has the dimension of $N_c \; x \; NU$, where $N_c$ is the total number of computational cells and $NU$ is the number of unknowns, given by the sum of species and temperature. The blocks have dimension equal to $NU \; x \; NU$.

The Jacobian matrix associated to the reactive step becomes a diagonal blocks matrix. Indeed the rate of production of each cell depends only on the conditions of the cell itself. This implies that the PDEs system can be turned into a group of decoupled Ordinary Differential Equations (ODEs) system. The resulting numerical problem is constituted by a system of weakly non linear PDEs and a group of non-linear ODEs system (Figure 7).

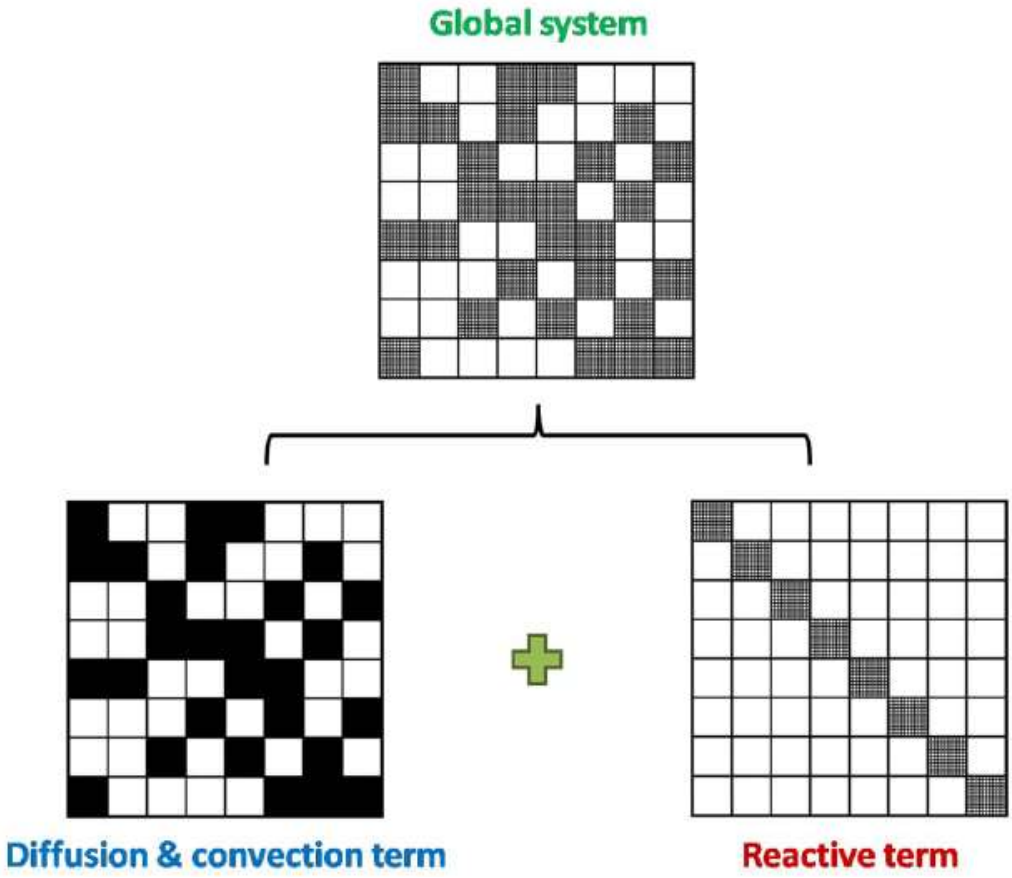


Figure 7: Structure of the system in CatalyticFoam

Among this type of computational methods, two classes of splitting schemes can be distinguished: one is based on the Strang splitting scheme [28], and the other is based on staggered time steps.

1. For each time step Δt, schemes based on Strang splitting require two reaction sub-steps of length Δt/2 and one transport sub-step of length Δt.

2. Schemes based on staggered time steps require a single transport sub-step of length $\Delta t$ and a single reaction fractional step of length $\Delta t$. As the computational cost scales with the number of reaction sub-steps that need to be performed, these methods result much more computationally feasible when dealing with complex chemical systems and will thus be chosen as the method of choice in this work. This method computes the predictor value integrating the transport equations PDEs system on a time step Δt in order to obtain first-guess values of temperature and massive fractions. Then the ODEs system is solved using the obtained values as initial conditions. Once again integration is performed over the same Δt. The systems solved are stiff, decoupled and dimensioned NS + 1.

The second class of splitting scheme will be applied in the solution of the following problems.

## 3.2 The Energy balance equation

In the previous work [9], the catalyticFOAM solver has been tested only in isothermal conditions. Therefore the first important step was the introduction of the energy balance equation into the system. In particular the source term, due to the heat of reaction associated to the surface chemistry, has been tested in order to compute the temperature field inside the reactor:

$$c_p \frac{\partial(\rho \mathrm{T})}{\partial \mathrm{t}} + c_p \nabla\left(\rho \mathbf{U} \mathrm{T}\right) - \lambda \nabla^2 T = \sum R_j \Delta H_j \tag{3.4}$$

where T is the temperature, $c_p$ is the specific heat of the gas mixture and $\Delta H_j$ is the heat of reaction of the *j*th reaction. The energy dissipation due to the viscosity of the fluid is neglected. Furthermore the pressure term is ignored [29].

### 3.2.1 Methodology

Considering the methodology proposed in the last paragraph, it is necessary to identify for each equation the predictor and the corrector term associated to the material and energy balance equations.

The predictor value will be given by the solution of the PDE´s system made by transport of species and energy. With the segregated approach they are solved decoupled in the following form:

$$\begin{cases} \dfrac{d(\rho \omega_i)}{dt} + \nabla\left(\rho U \omega_i\right) - \nabla\left(\rho D_i \nabla \omega_i\right) = 0 \\ c_p \dfrac{\partial(\rho T)}{\partial t} + c_p \nabla\left(\rho T\right) - \lambda \nabla^2 T = 0 \end{cases} \tag{3.5}$$

The corrector factor takes into account the variations of species composition and heat owed to chemical reactions. Since reactions take place both in the gas and adsorbed phase, it is required to discriminate the cells close the catalyst (catalytic cells) from the other ones (homogeneous cells).

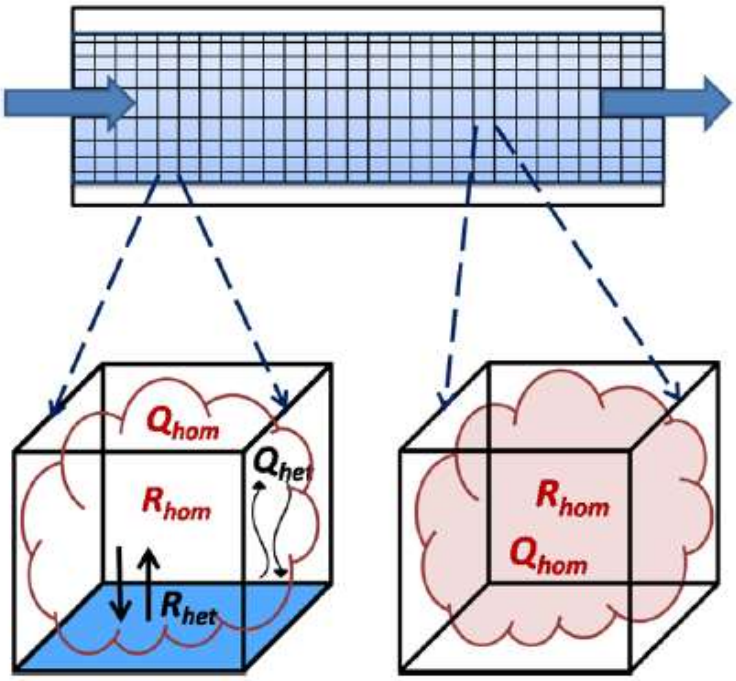


Figure 8: Catalytic and non-catalytic cells

As shown in Figure 8, in the homogeneous cells take place only the gas phase reactions, while in the catalytic cells involve the heterogeneous reactions too.

The predictor values for a homogeneous cell are calculated by solving the following system of equations:

$$\begin{cases} \dfrac{d(\rho\omega_i)}{dt} = \sum_{j=1}^{NR} R_j^{hom} \nu_{ij} MW_i \\ c_p \dfrac{\partial(\rho T)}{\partial t} = Q^{hom} \end{cases} \tag{3.6}$$

where $R_j^{hom}$ is the homogeneous reaction rate and $Q^{hom}$ is the net heat of production of the gas phase species. The mass balance of the *i*th species is written for each component of the gas mixture.

For the catalytic cells the expression of the predictor system has to take into account additional terms. Indeed in these cells the gas adsorbs on the catalytic surface: adsorbed species react through a number of elementary steps and desorb into the gas phase. Therefore, to describe the evolution of the catalytic surface it is necessary to:

- Add the heterogeneous reaction term to gas phase balances. This takes into account the adsorption and desorption reactions at the catalytic surface.

- Introduce additional term to satisfy the total mass balance in the gas-phase. Since this solver has to be able to describe transient behavior, the mass balances of the gas phase have to include the sum of the production rates over each component due to chemisorption reactions.
- Consider site conservation balances of the adsorbed species [30]. These include both surface and chemisorption reactions.

Mathematically the ODEs system becomes:

$$\begin{cases} \dfrac{d\omega_i}{dt} = \dfrac{R_i^{hom} MW_i}{\rho} + \dfrac{1}{\rho V_{cell}} \left[ \displaystyle\sum_{k=1}^{NCF} \alpha_{cat}^{(k)} A_{face}^{(k)} \left( R_{ik}^{het} MW_i - \omega_i \sum_{i=1}^{NC} R_{ik}^{het} MW_i \right) \right] \\ \dfrac{dT}{dt} = -\dfrac{1}{\rho c_p} \displaystyle\sum_{i=1}^{NCF} H_i{}^{hom} R_i^{hom} + \dfrac{1}{\rho c_p V} \sum_{k=1}^{NCF} \alpha_{cat}^{(k)} A_{face}^{(k)} \sum_{i=1}^{NC} R_{ik}^{het} MW_i \left( H_{ik}{}^{het} - H_i{}^{hom} \right) \\ \Gamma_{site} \dfrac{\partial \vartheta}{\partial t} = \displaystyle\sum_{j=1}^{NCF} R_j^{sur} \nu_{ij} \end{cases} \tag{3.7}$$

where $R_j^{sur}$ is the production rate of the ith surface species and $\Gamma_{site}$ denotes the catalyst site density, $A_{face}^{(k)}$ is the area of the cell of the catalytic surface, $V_{cell}$ is the volume of that cell and $NCF$ is the Number of Catalytic Faces of the cell. The mass balance of the *i*th gas species is written for each component of the gaseous mixture. The site conservation equation is written for each adsorbed species including the free catalytic sites for each catalytic face.

In order to account for the surface coverage of the reactor wall, a new parameter has been introduced: $\alpha_{cat}^{(k)}$ , calculated as the ratio of the effective catalytic area over the geometric surface.

### 3.2.2 Case study: hydrogen combustion in adiabatic conditions

The solver catalyticFOAM has been tested in the case of hydrogen combustion. To reduce and simplify the mesh, a 2D geometry has been considered. In particular the mesh is made by a channel with inside a cylinder that represents the catalytic surface. This geometry has been chosen because this mesh allows to test the behavior of the solver with unstructured grids made by mixed elements (both triangle-shape and rectangle-shape cells). A more refined grid around the reactive surface (Figure 9) has been taken into account in order to well characterize the strong

normal gradients of temperature and compositions in this area. Table 1 shows the dimensions of the 2D mesh:

| | |
|---|---|
| Channel Length | 4 cm |
| Channel Width | 1 cm |
| Cylinder Radius | 3 mm |

Table 1: Dimensions of the mesh

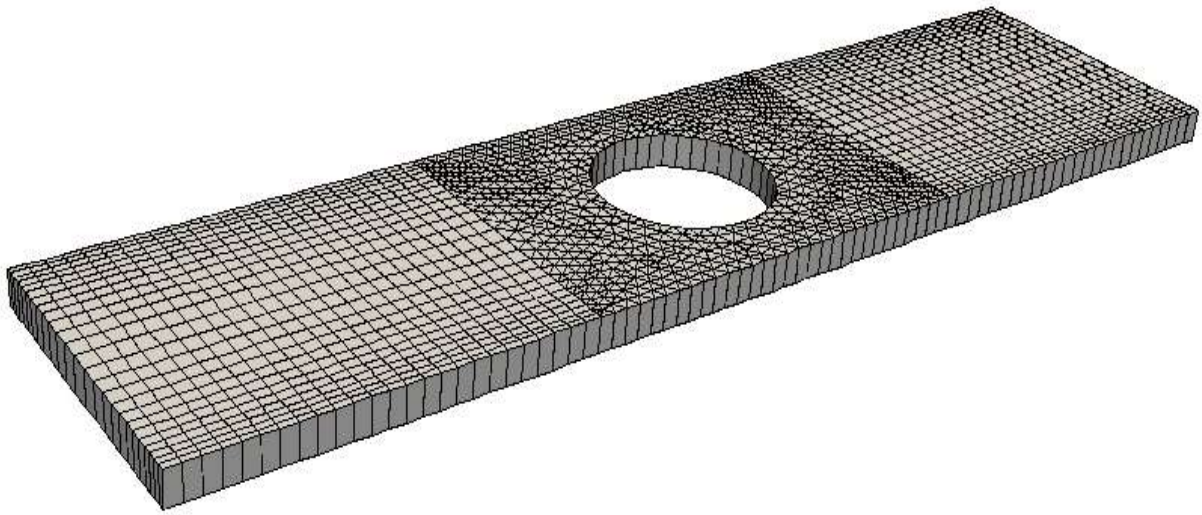

Figure 9: Detail of the mesh

The operating conditions are shown in Table 2:

| **OPERATING CONDITIONS** | |
|---|---|
| $H_2$ Mass Fraction | 2.96e-3 |
| $O_2$ Mass Fraction | 1.18e-2 |
| $N_2$ Mass Fraction | 9.86e-1 |
| Pressure | 1 atm |
| Inlet Temperature | 473 K |
| Flow Velocity | 0.2 m/s |

Table 2: Operating conditions hydrogen combustion

Figure 10 shows the results of the simulation, in particular compositions and temperature fields will be considered.

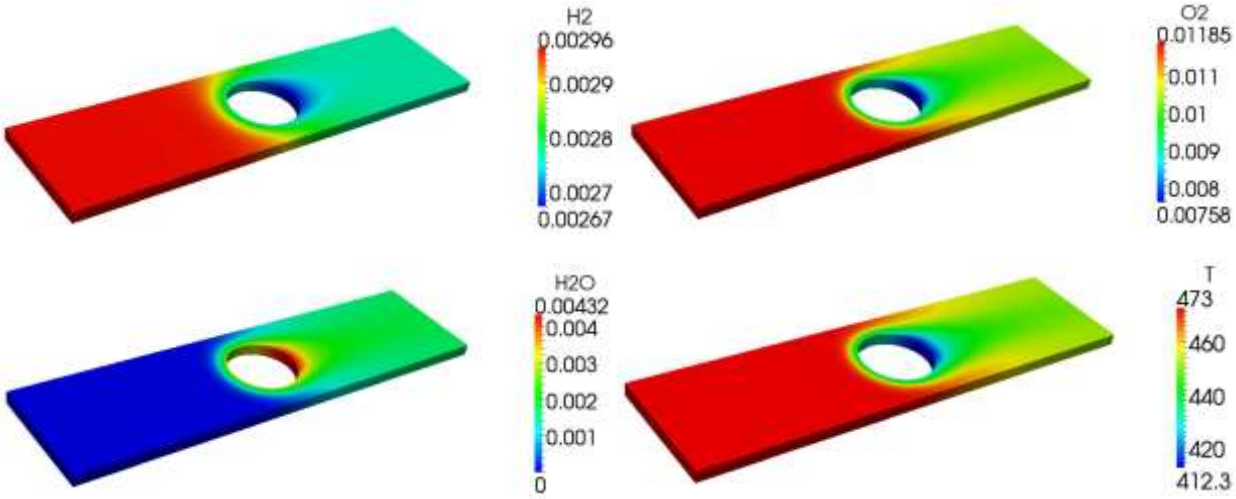


Figure 10: Composition and temperature fields

The oxidation of hydrogen is not interested by equilibrium but, in proximity of the reactive surface, the limiting reactant (in this case oxygen) will be completely converted into the product. In order to verify the fields of composition and temperature, Stanjan [31] has been used in order to evaluate the conditions at thermodynamic equilibrium. In the following section, the expected results for a complete conversion of oxygen have been presented.

| **EXPECTED RESULTS** | |
|---|---|
| $H_2$ Mass Fraction | 1.46E-03 |
| O2 Mass Fraction | 0 |
| $H_2O$ Mass Fraction | 1.33e-1 |
| Outlet Temperature | 636 K |

Table 3: Expected results in equilibrium conditions – Stanjan

The same reactive system in isothermal conditions has been simulated in the previous work [9] with an excellent agreement also with experimental data. A partial validation of the equations could be possible considering a reactor with a length of reactor and an amount of reactive surface enough to reach the equilibrium conditions. In this way the results provided by the CFD simulation have to be the same of the ones of Stanjan at equilibrium conditions. With this simple approach the identification of possible macroscopic error is possible. Figure 10 shows that both composition and temperature fields are very distant from the expected results. In particular, observing the temperature fields, it seems that the reaction takes endothermic paths that for an exothermic reaction, as the oxidation of hydrogen is, are completely unfeasible.

## 3.3 Improvements in the energy balance

As shown by the previous results, the structure of the energy balance clearly produces an unfeasible result, even if the equations are written correctly. The simplest way to overcome this issue is to write in a different way the balance. Usually the best solution is to work up the equation as less as possible in order to minimize this effect.

The result is the following:

$$\frac{dT}{dt} = -\frac{1}{\rho c_p}\sum_{i=1}^{NCF} H_i{}^{hom} R_i^{hom} - \frac{1}{\rho c_p V}\sum_{i=1}^{NC} H_i \left[ \rho V_{cell} \frac{d\omega_i}{dt} + \sum_{k=1}^{NCF} \alpha_{cat}^{(k)} A_{face}^{(k)} \omega_i \sum_{i=1}^{NC} R_{ik}^{het} MW_i \right] \tag{3.8}$$

In appendix C it is possible to see how the new energy balance equation has been obtained in detail.

### 3.3.1 Case study: hydrogen combustion with the new energy balance

The previous cases was then analyzed with the new formulation of the energy balance equation.

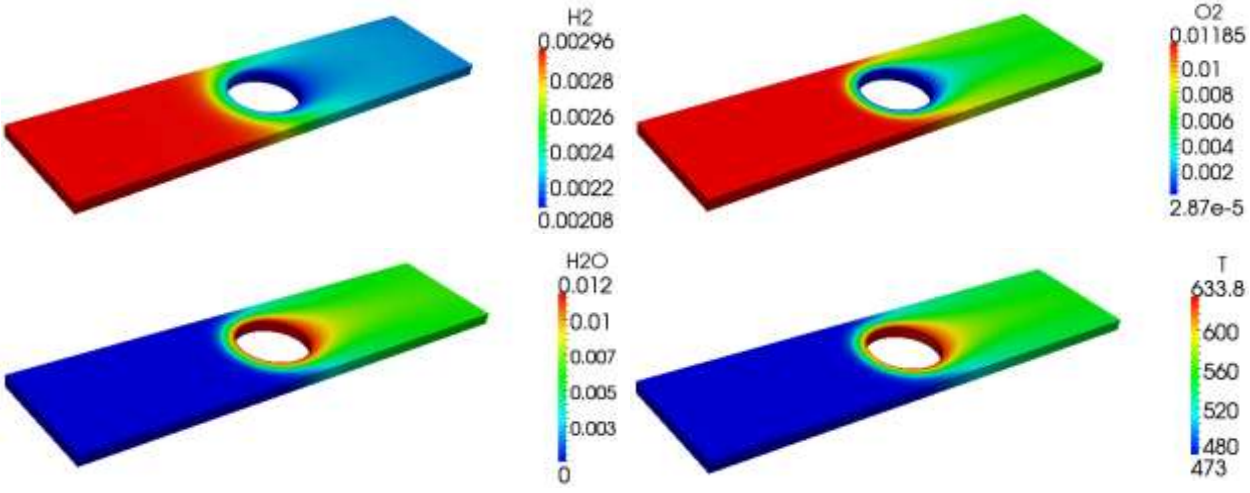


Figure 11: Composition and temperature fields - new energy balance equation

Figure 11 shows that near the reacting surface the oxygen conversion is complete and the thermodynamic equilibrium is reached and verified. Here the results have been compared with an excellent agreement with the one provided by Stanjan at equilibrium conditions (Table 3). In this

case there is a good accordance both for temperature and composition fields. The adiabatic temperature is only two degree below the expected one and also the production of water is slightly lower than the 1.33E-2 predicted. This is a first index of the better coupling between the new energy balance equation and the material one. Nevertheless, the solver has to be tested with several reacting systems and geometries in order to affirm that the correct configurations of the equations has been found

Since the investigated geometry shows an axis of symmetry, it is important to check if also the numerical solution depicts the same trend.

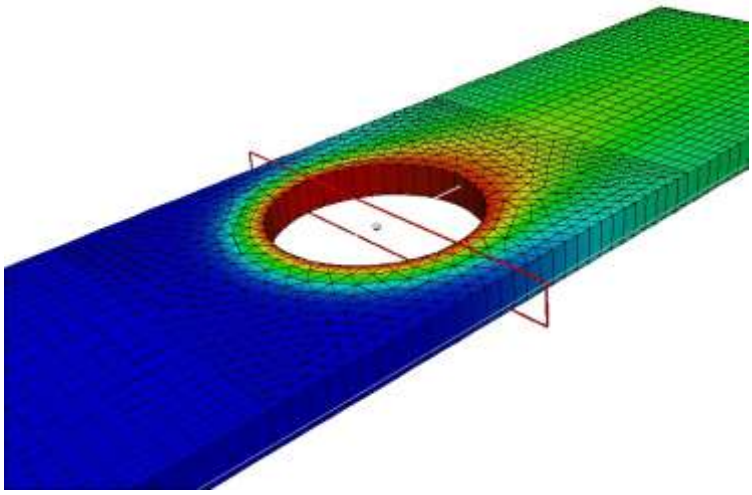

Figure 12: Detail of the plane used for the plots

In Figure 13, temperature and water mass fraction profiles have been presented. Both temperature and $H_2O$ mass fraction profiles are exactly symmetrical along the radial coordinate. In particular the maximum value of temperature is reached on the reactive surface where the importance of the reactions is much stronger. The same trend is shown also by the product, in this case water.

As already said the solver has to be tested with several reacting systems (see Paragraph 3.4 and 3.6) but it is possible to affirm that the new energy balance equation has introduces an higher numerical stability into the system.

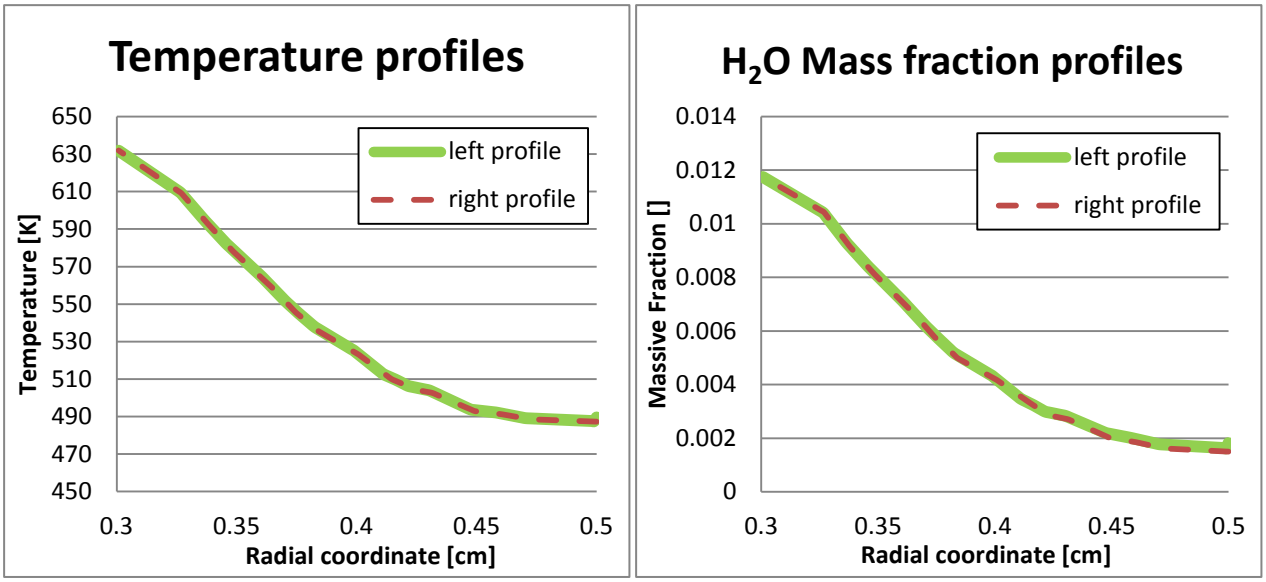


Figure 13: Temperature and water profile along the radial coordinate

### 3.3.2 The importance of the operator splitting technique

There are mainly two advantages in the using of operator splitting technique:

- first, each operator can be solved using specific tailored solver. This is particularly pragmatic since black boxes can be easily incorporated in existing software;
- second advantage is associated with CPU requirements.

In this section the operator splitting technique has been used in order to analyze a simple linear system. Specifically the results of several splitting schemes have been compared with the results provided by a fully couples approach in order to highlight differences between them.

Considering the following first order linear equation

$$\frac{dz}{dt} = Az + Bz, \qquad z(0) = z_o \tag{3.9}$$

Where A and B are linear operators. First order (with respect of Δt) method are define in this way:

$$\begin{cases} \dfrac{dz^{*}}{dt} = Az^{*}, & z^{*}(0) = z_0 \qquad on[0,\Delta t] \\ \dfrac{dz^{**}}{dt} = Bz^{**} & z^{**}(0) = z^{*}(\Delta t) \quad on[0,\Delta t] \end{cases} \tag{3.10}$$

The final value is then taken as $z^{**}(\Delta t)$. This scheme will be denoted by (*A*–*B*) splitting.

(*B*–*A*) splitting is of course defined by reversing *A* and *B*. Making the assumption that B is a stiff operator (for instance chemical kinetics) while A is a non-stiff one (for instance diffusion), Sportisse has demonstrated that the two splitting schemes don't provide the same results [32].

Figure 14 represents a simple case of air pollutions [33].Here it is possible to understand that (A-B) and (B-A) schemes are not symmetric.

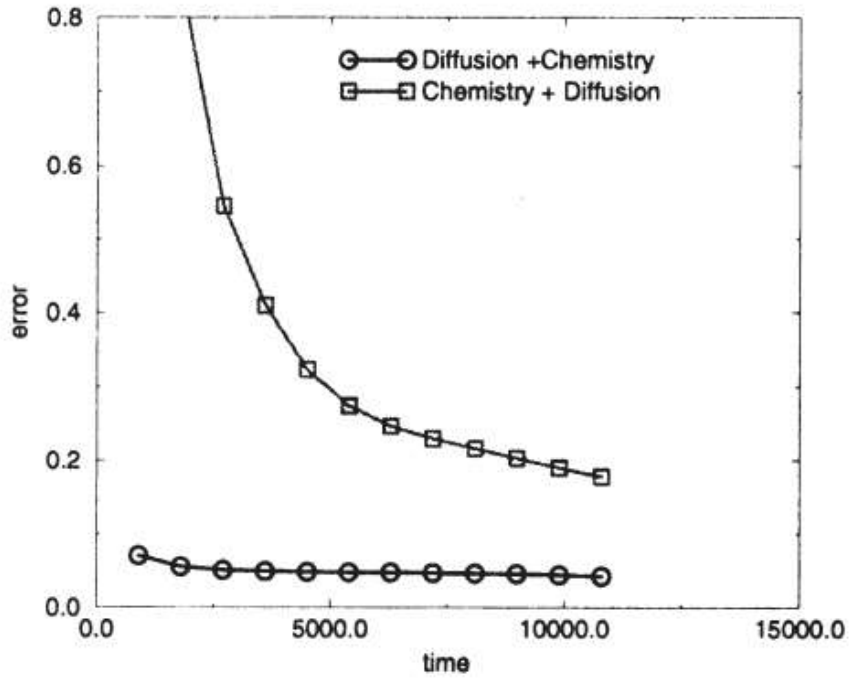


Figure 14: Behavior of error in time for A-B and B-A splitting schemes

With the (A-B) scheme, where the reactive term is solved as the second one, the error due to the operation splitting technique is always lower to the one given by the (B-A) scheme.

The main point is that the stiff operator (chemical kinetics) has always to terminate the splitting process (due to its stabilizing effect). In the following section, with a simple example of a system of two equations, it will be possible to explain the causes of this statement.

### 3.3.2.1 Mathematical analysis of the operator splitting technique

In this paragraph an ODE system will be taken into account in order to demonstrate the influence of the equations order in the operator splitting technique [33]. A model function is usually used in order to consider a simpler structure of the same problem. In fact, in this case, the system includes both a non stiff operator that represents the convection and diffusion term and a stiff operator that, instead, represents the generation term due to the kinetic of reaction.

$$\begin{cases} \dfrac{dx}{dt} = \dfrac{-x+y}{\varepsilon} - x, & x(0) = x_0 \\ \dfrac{dy}{dt} = \dfrac{x-y}{\varepsilon}, & y(0) = y_0 \end{cases} \tag{3.11}$$

The following study is able only to define the accuracy of the different operator splitting orders but not the stability of those methods.

Sportisse, in his work [33], suggested that the system showed in Equation (3.11) presents a stiff behavior. In order to verify this sentence, an analysis of the eigenvalues of the system has been provided:

$$J = \begin{bmatrix} \dfrac{\partial(dx/dt)}{\partial x} & \dfrac{\partial(dx/dt)}{\partial y} \\ \dfrac{\partial(dy/dt)}{\partial x} & \dfrac{\partial(dy/dt)}{\partial y} \end{bmatrix} = \begin{bmatrix} -\dfrac{1}{\varepsilon} - 1 & \dfrac{1}{\varepsilon} \\ \dfrac{1}{\varepsilon} & -\dfrac{1}{\varepsilon} \end{bmatrix} \tag{3.12}$$

The eigenvalues of this matrix can be calculated analytically. The results are:

$$\begin{cases} \lambda_1 = \dfrac{-\varepsilon + \sqrt[2]{\varepsilon^2 + 4} + 2}{2\varepsilon} \\ \lambda_2 = \dfrac{-\varepsilon - \sqrt[2]{\varepsilon^2 + 4} + 2}{2\varepsilon} \end{cases} \tag{3.13}$$

$\varepsilon$ is still a small number, so if $\varepsilon \to 0$ the results is that the first eigenvalue will be a very high number cause by the $\varepsilon$ find at the denominator. The second one, instead, will tend to 1/2. In this way the stiff behavior of the system has been demonstrated. Now it is possible to investigate the solutions provided with the two splitting schemes in order to demonstrate the thesis suggested by Sportisse of the less accuracy of the solution obtained with the A-B scheme.

At now, the stiff and non stiff operators have not been identified yet. In order to achieve the results, an analysis of the eigenvalues of the different term of the system has been necessary. In fact, considering the two sub-system:

$$sub-system\,1:\begin{cases}\dfrac{dx}{dt}=\dfrac{-x+y}{\varepsilon}, & x(0)=x_0\\ \dfrac{dy}{dt}=\dfrac{x-y}{\varepsilon}, & y(0)=y_0\end{cases} \tag{3.14}$$

$$sub-system\,2:\begin{cases}\dfrac{dx}{dt}=-x, & x(0)=x_0\\ \dfrac{dy}{dt}=0, & y(0)=y_0\end{cases} \tag{3.15}$$

Table 4 shows the eigenvalues that are respectively:

| | $\lambda_1$ | $\lambda_2$ |
|---|---|---|
| Sub-system 1 | $0$ | $-2/\varepsilon$ |
| Sub-system 2 | $-1$ | $0$ |

Table 4: Eigenvalues of the two sub-systems

This means that sub-system 1 represents the stiff term. In this case the difference between the eigenvalues of the system is extremely high (ε is considered as a very small number). Sub-system 2 represents the non-stiff term (the eigenvalues present the same magnitude).

At this point the solution of the system will be calculated using two different approaches:

- MOL: well known as method of line. It will be considered as the fully coupled approach;
- Operator splitting technique: both A-B and B-A operator splitting order.

For convenience the stiff step is solved in the lumped basis [34].

### 3.3.2.2 MOL - Method of line

In order to obtain the analytical solution, the following change of variable is needed:

$$U=x+y \Rightarrow x=U-y \tag{3.16}$$

thus with simple algebraic rearrangements:

$$\begin{aligned}
&\frac{dx}{dt} = \frac{dU}{dt} - \frac{dy}{dt} = \frac{-U + y + y}{\varepsilon} - U + y \\
&\frac{dU}{dt} = \frac{dy}{dt} + \frac{2y - U}{\varepsilon} + y - U \\
&\frac{dy}{dt} = \frac{U - y - y}{\varepsilon} = \frac{U - 2y}{\varepsilon} = -\frac{2y - U}{\varepsilon}
\end{aligned} \tag{3.17}$$

The resulting system is:

$$\begin{cases} \dfrac{dU}{dt} = y - U \\ \dfrac{dy}{dt} = \dfrac{U - 2y}{\varepsilon} \end{cases} \tag{3.18}$$

Under the hypothesis of $\varepsilon \ll 1$:

$$\varepsilon \frac{dy}{dt} = U - 2y \simeq 0 \Rightarrow y = \frac{U}{2} \tag{3.19}$$

And introducing this value in the system it is possible to obtain the value of $U$:

$$\begin{cases} \dfrac{dU}{dt} = \dfrac{U}{2} \\ y = \dfrac{U}{2} \end{cases} \Rightarrow \frac{dU}{U} = \frac{dt}{2} \Rightarrow U = U_0 \, \mathrm{e}^{-1/2t} \tag{3.20}$$

The solution of the system in the lamped basis is the following:

$$\begin{cases} U = U_0 e^{-1/2t} \\ y = \dfrac{U_0}{2} e^{-1/2t} \end{cases} \tag{3.21}$$

And finally, reintroducing the variable $x$ into the system:

$$x = U - y \;\Rightarrow\; x = U_0 e^{-1/2t} - \frac{U_0}{2} e^{-1/2t} = \frac{U_0}{2} e^{-1/2t} \tag{3.22}$$

The analytic solution in the hypothesis of $\varepsilon \ll 1$ is reached:

$$\begin{cases} x = \dfrac{x_0 + y_0}{2} e^{-1/2t} \\ y = \dfrac{x_0 + y_0}{2} e^{-1/2t} \end{cases} \Rightarrow\; x = y = \frac{x_0 + y_0}{2} e^{-1/2t} \tag{3.23}$$

### 3.3.2.3 A-B operator splitting scheme

Solving the non stiff term as the first one, the reduced system is the following:

$$\begin{cases} \dfrac{dx^*}{dt} = -x^* & x^*(0) = x_0 \\ \dfrac{dy^*}{dt} = 0 & y^*(0) = y_0 \end{cases} \tag{3.24}$$

Solving for $x$ and $y$:

$$\begin{cases} x^*(t) = x^*(0)e^{-\Delta t} = x_0 e^{-\Delta t} \\ y^*(t) = y^*(0) = y_0 \end{cases} \tag{3.25}$$

And introducing one again the variable $U$:

$$U = x + y = x_0 e^{-\Delta t} + y_0 \tag{3.26}$$

With the step B, the system that has to be solved is the following:

$$\begin{cases} \varepsilon \dfrac{dx^{**}}{dt} = -x^{**} + y^{**} & x^{**}(0) = x^*(\Delta t) = x_0 e^{-\Delta t} \\ \varepsilon \dfrac{dy^{**}}{dt} = -y^{**} + x^{**} & y^{**}(0) = y^*(\Delta t) = y_0 \end{cases} \tag{3.27}$$

With simple algebraic rearrangements:

$$\begin{cases} \dfrac{dU^{**}}{dt} = 0 & U^{**}(0) = U^*(\Delta t) = x_0 e^{-\Delta t} + y_0 \\ \varepsilon \dfrac{dy^{**}}{dt} = U^{**} - 2y^{**} & y^{**}(0) = y^*(\Delta t) = y_0 \end{cases} \tag{3.28}$$

Under the same hypothesis seen before, $\varepsilon \ll 1$, the calculation of $y^{**}$ is possible:

$$y^{**} = \frac{U^{**}}{2} \tag{3.29}$$

reintroducing this solution into the system the solution in the lamped based is calculated:

$$\begin{cases} y^{**} = \dfrac{U^{**}}{2} \\ U^{**}(t) = U^{**}(0) = x_0 e^{-\Delta t} + y_0 \end{cases} \Rightarrow \begin{cases} y^{**} = \dfrac{x_0 e^{-\Delta t} + y_0}{2} \\ U^{**} = x_0 e^{-\Delta t} + y_0 \end{cases} \tag{3.30}$$

Eventually:

$$\begin{cases} x^{**} = U^{**} - y^{**} = \dfrac{U^{**}}{2} = \dfrac{x_0 e^{-\Delta t} + y_0}{2} \\ y^{**} = \dfrac{x_0 e^{-\Delta t} + y_0}{2} \end{cases} \Rightarrow \; x^{**} = y^{**} = \frac{x_0 e^{-\Delta t} + y_0}{2} \tag{3.31}$$

Also in this case $x^{**} = y^{**}$. The fully coupled solution and the one given with the A-B operator splitting technique provide the same results. A-B splitting scheme can be considered as a good approximation of the entire system solved all together.

### 3.3.2.4 B-A operator splitting scheme

Solving the stiff term as the first one, the reduced system is the following:

$$\begin{cases} \dfrac{dU^{**}}{dt} = 0 & U(0) = U_0 \\ \varepsilon \dfrac{dy^{*}}{dt} = U^{*} - 2y^{*} & y(0) = y_0 \end{cases} \tag{3.32}$$

Under the hypothesis of $\varepsilon \ll 1$:

$$U^{*} = 2y^{*} \Rightarrow y^{*} = \frac{U^{*}}{2} \tag{3.33}$$

The solution of the system for the stiff term is:

$$\begin{cases} U^{*}(t) = \cos t = U_0 = x_0 + y_0 \\ y^{*} = \dfrac{U^{*}(t)}{2} = \dfrac{U_0}{2} = \dfrac{x_0 + y_0}{2} \end{cases} \Rightarrow x = U - y \Rightarrow x(\Delta t) = \frac{x_0 + y_0}{2} \tag{3.34}$$

Solving the system for the non-stiff term:

$$\begin{cases} \dfrac{dx^{**}}{dt} = -x^{**} & x^{**}(0) = x^{*}(\Delta t) = x_0 e^{-\Delta t} \\ \dfrac{dy^{**}}{dt} = 0 & y^{**}(0) = y^{*}(\Delta t) = \dfrac{x_0 + y_0}{2} \end{cases} \tag{3.35}$$

And eventually:

$$\begin{cases} x^{**}(\Delta t) = \dfrac{x_0 + y_0}{2} \mathrm{e}^{-\Delta t} \\ y^{**}(\Delta t) = \dfrac{x_0 + y_0}{2} \end{cases} \quad \Rightarrow \quad x^{**} \neq y^{**} \tag{3.36}$$

In this case $x \neq y$. The solution given by the operating splitting scheme B – A doesn't satisfy the algebraic constraints.

In few words it is better to loose accuracy at the beginning and then project the evolution onto the simplified model than to be close to the exact solution after the first step but without being close to the reduced model thereafter. Such results can be easily extended to second-order methods [32]. The method ending with the stiff operator is always more accurate than the other one.

### 3.3.2.5 Evaluation of the local error

The local error is the error that results when a single step is performed with exact "input data". For the two cases presented before (A-B and B-A schemes) the evaluation of the local error is presented in order to compare these results with the ones given by the classic method explained in paragraph 2.3.1.

If the stiff term is solved as the last one (A-B schemes) the local error is the following:

$$\begin{aligned} x_{exact} &= \frac{x_0 + y_0}{2} e^{-\Delta t/2} \\ x_{A-B} &= \frac{x_0 e^{-\Delta t/2} + y_0}{2} \end{aligned} \tag{3.37}$$

$$\varepsilon_{A-B} = x_{exact} - x_{A-B} = e^{-\Delta t/2}\left(\frac{x_0}{2} + \frac{y_0}{2}\right) - \frac{x_0}{2} e^{-\Delta t} - \frac{y_0}{2} \tag{3.38}$$

with a Taylor expansion around $\Delta t = 0$

$$\begin{aligned}
\varepsilon_{A-B} &\simeq \varepsilon(\Delta t=0)+\left.\frac{\partial \varepsilon}{\partial \Delta t}\right|_{\Delta t=0}(\Delta t-0)+\vartheta(\Delta t^2)= \\
&=\left(\frac{\cancel{x_0}}{\cancel{2}}+\frac{\cancel{y_0}}{\cancel{2}}\right)-\frac{\cancel{x_0}}{\cancel{2}}-\frac{\cancel{y_0}}{\cancel{2}}+\frac{x_0+y_0}{2}\left(\frac{\partial}{\partial \Delta t}e^{-\Delta t/2}\right)\Bigg|_{\Delta t=0}-\frac{x_0}{2}\left(\frac{\partial}{\partial \Delta t}e^{-\Delta t/2}\right)\Bigg|_{\Delta t=0}= \\
&=-\frac{1}{2}e^{-\Delta t/2}\Bigg|_{\Delta t=0}\frac{x_0+y_0}{2}+\frac{x_0}{2}e^{-\Delta t}\Bigg|_{\Delta t=0}= \\
&=-\frac{1}{2}\cdot 1\cdot\frac{x_0+y_0}{2}+\frac{x_0}{2}\cdot 1=\frac{-x_0-y_0}{4}+\frac{x_0}{2}=\frac{2x_0}{4}-\frac{2x_0}{4}-\frac{y_0}{4}=\frac{x_0-y_0}{4}
\end{aligned} \tag{3.39}$$

And for these reasons the local error for the A - B scheme is:

$$\varepsilon_{A-B}=\left(\frac{x_0-y_0}{4}\right)\Delta t+\vartheta(\Delta t^2) \tag{3.40}$$

Computing the same parameter for the B - A scheme where the stiff term is solved as the first one it is possible to verify if the local error between the two schemes is the same as computed with the classic method in paragraph 2.3.1.1.

For the B – A scheme:

$$\begin{aligned}
x_{exact} &= \frac{x_0+y_0}{2}e^{-\Delta t/2} \\
x_{B-A} &= x_{exact}=\frac{x_0+y_0}{2}e^{-\Delta t}
\end{aligned} \tag{3.41}$$

$$\varepsilon_{B-A}=x_{exact}-x_{B-A}=\frac{x_0+y_0}{2}\left(e^{-\Delta t/2}-e^{-\Delta t}\right) \tag{3.42}$$

again with a Taylor expansion around $\Delta t = 0$

$$\begin{aligned}
\varepsilon_{B-A} &\simeq \varepsilon(\Delta t=0)+\left.\frac{\partial \varepsilon}{\partial \Delta t}\right|_{\Delta t=0}(\Delta t-0)+\vartheta(\Delta t^2)= \\
&=\frac{x_0+y_0}{2}\left(-\frac{1}{2}e^{-\Delta t/2}+e^{-\Delta t}\right)\Bigg|_{\Delta t=0}= \\
&=\frac{x_0+y_0}{2}\left(-\frac{1}{2}+1\right)=\frac{x_0+y_0}{4}
\end{aligned} \tag{3.43}$$

The final result is:

$$\varepsilon_{A-B} = \left( \frac{x_0 + y_0}{4} \right) \Delta t + \vartheta(\Delta t^2) \tag{3.44}$$

As it possible to see the results provided tor the two splitting schemes are not the same.

This seems to be a rather disappointing result since we have only first-order local errors (on the contrary to the usual analysis). The former study has however to be performed with ($x_0$, $y_0$) being the current value of the splitting process. The key property of splitting (A–B) is that ($x_0$, $y_0$) (except for the first iteration) satisfies a constraint: the computed solution is in the vicinity of the reduced model x = y (splitting B-A presents an opposite behavior). This aspect brings to say that (outer a transient phase) we have (up to first-order in e) $x_0 = y_0$ for the splitting (A–B).

The reason why the scheme (B-A) has a loss of accuracy is that since the dynamical behavior justifies that the initial slow–fast model can be approximated up to some orders in $\varepsilon$ by integrating successively the fast and then the slow operators

## 3.4 The operator splitting technique in catalyticFOAM

The effect of the operator splitting order on the catalyticFOAM simulations has been investigated. In the latest version of the solver, the user can choose the order of equations easily changing a string in the solverOptions dictionary.

```
AlfaCatalyst 0.75;

massFractionsTolerance 1.e-9;

diffusivityCorrection "semi-implicit";
massDiffusionContributionInEnergyEquation on;

strangAlgorithm "TransportReactionMomentum";
// strangAlgorithm "ReactionTransport";

inletBoundaries  ("inlet");
outletBoundaries ("outlet");

conversionSpecies ("H2" "O2");
```

Figure 15: Detail of the solverOption dictionary

Figure 15 shows where it is possible to shift from the splitting algorithm "TrasportReactionMomentum" that correspond to the (A-B) scheme presented by Sportisse [33] to "ReactionTransport" that correspond to the (B-A) scheme.

Following the two Splitting Schemes are presented more in detail.

***TransportReactionMomentum***: in this case, the first equations that have to be solved are the transport equations of species and energy. These equations are quasi-linear and have a low stiffness degree. The solution of this system defines the predictor values of temperature and mass fractions. A segregated approach can be adopted solving the equations decoupled. Following, the corrector factors have to be computed solving the source term of mass and energy starting from the predictor variables. This step defines the corrector values of temperature and mass fraction.

Finally, the momentum equation is solved by means of the PISO procedure [35]. This procedure allows to simplify the problem decoupling the Navies Stokes equation resolution by the continuity equation resolutions. These methods are made in three steps:

- Firstly, the Navier-Stokes equations are solved assuming a constant pressure field. Its value is assigned at the previous step. This stage is called momentum predictor and an approximated value of the velocity field is obtained.
- Using predicted velocity it is possible to solve the continuity equation and consequently get the correct pressure field: this step is called pressure solution.
- The velocity field is corrected in an explicit manner making it consistent with the new pressure field. This is the explicit correction stage.

The PISO loop is iterated till the tolerance for the pressure-velocity system is reached. The correction of velocity actually consists of two parts: an adjustment due to the change in the pressure gradient and another one due to the variation of the neighboring velocities. In the PISO algorithm, velocity is corrected explicitly: this means that the second correction is neglected and the whole error is assumed to be due to the error in the pressure term. This assumption is not true and makes it necessary to iterate the calculus procedure to achieve the correct solution. In other words, the PISO loop consists of an implicit momentum predictor.

In Figure 16 a scheme of the sequence of equations is presented for the TransportReactionMomentum order:

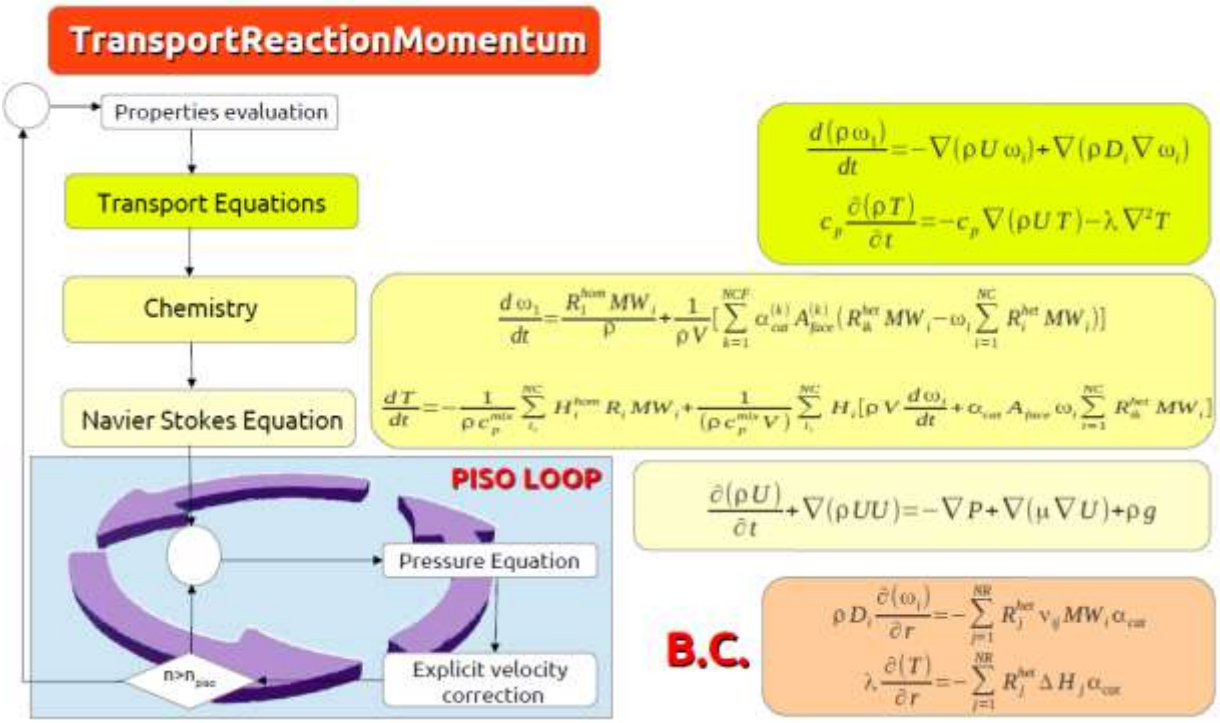


Figure 16: Structure of TRM operator splitting order

***ReactionTransport:*** the main difference from the previous order is that the predictor value of the system is given from the resolution of the source term and the corrector one by the resolution of mass and energy transport equations. The Navies Stokes equations are solved between these two steps [Figure 17]. At the end, a PISO loop is always necessary to calculate the pressure field and thus to correct the velocity field inside the reactor.

In the nest sections in order to demonstrate the higher stability and accuracy of the TransportReactionMomentum order over ReactionTransport ones, several cases, with different geometries and/or reacting systems in different conditions of temperature and flow velocity, have been investigated.

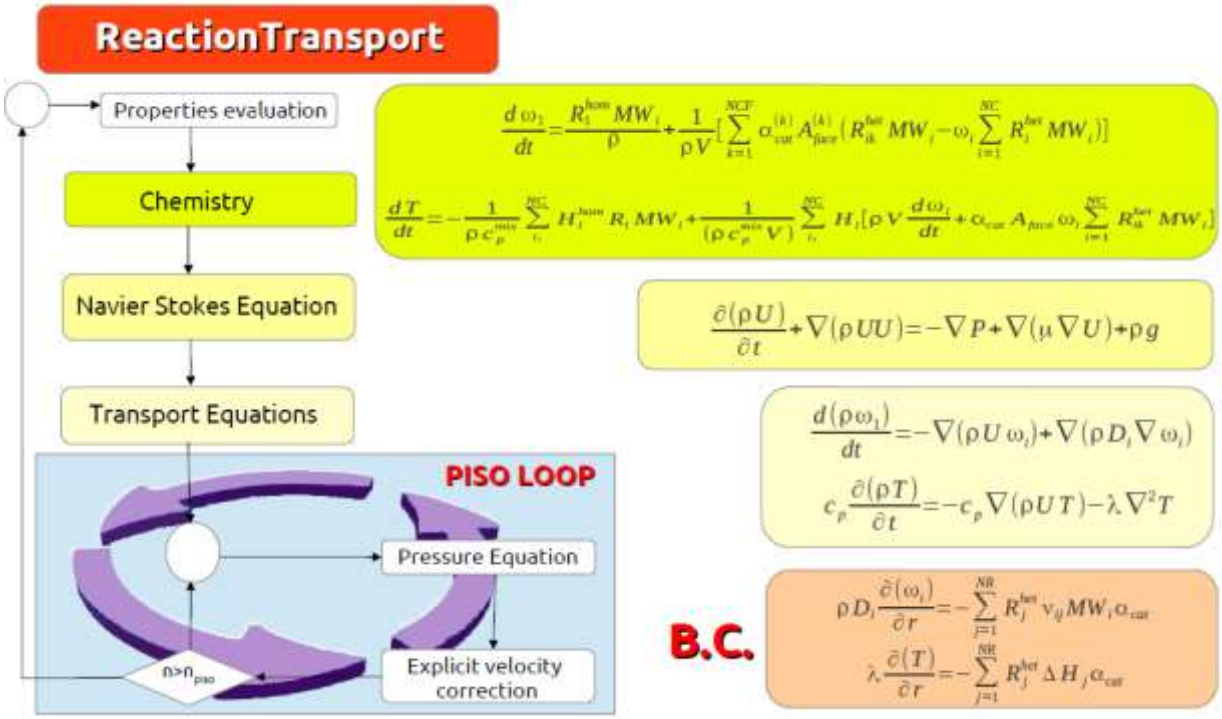


Figure 17: Structure of RT operator splitting order

### 3.4.1 Case study: hydrogen combustion in adiabatic conditions

The first example is a simple 2D geometry in which the axial symmetry has been exploited in order to simulate only a small portion of the reactor; in particular only 5° of the whole reactor has been simulated. In this way it is possible to achieve a computational time 72 times lower than the one necessary for the 3D simulation. The system is made by a tube with inside two spheres covered by the catalyst as shown in Figure 18.

The dimensions of the reactor are presented below in Table 5:

| | |
|---|---|
| Cylinder Length | 5 cm |
| Cylinder Radius | 0.5 cm |
| Catalytic Sphere Radius | 0.3 cm |

Table 5: Dimensions of the mesh

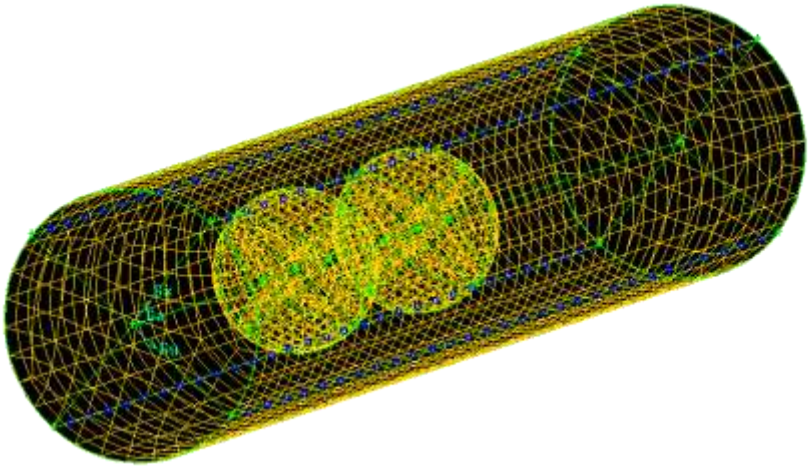

Figure 18: 3D mesh

The centers of the catalytic spheres are located respectively 1.5 and 2.6 cm after the inlet of the reactor.

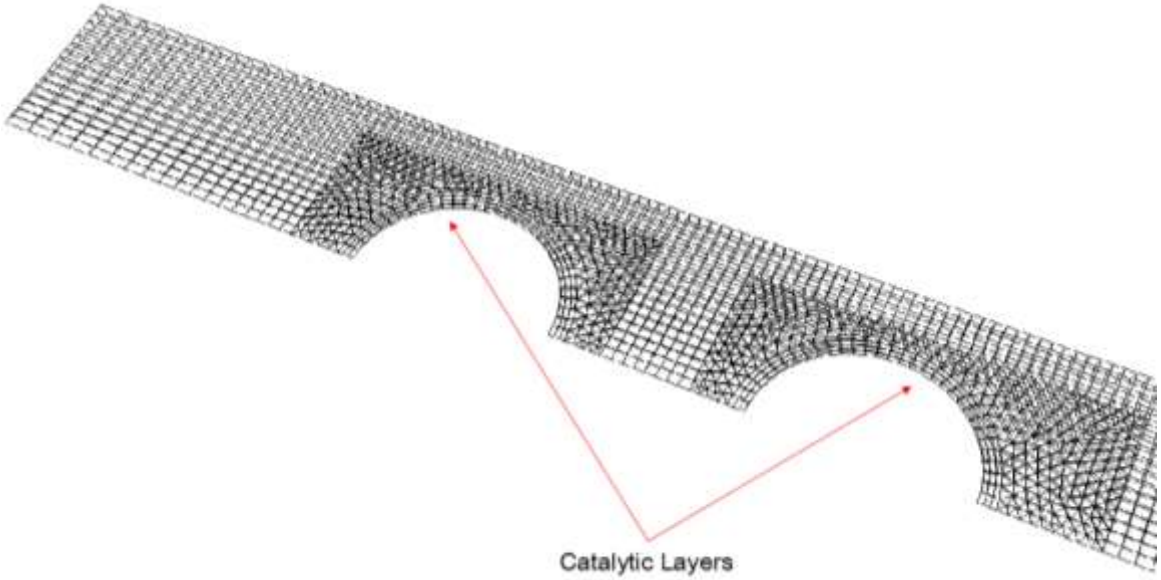


Figure 19: 2D mesh

The mesh was optimized with a higher cells density near the reacting surface using appropriate boundary layers (Figure 19). This is particularly important because the zone close to the catalyst is interested by strong normal gradients, both of temperature and concentrations. The overall mesh is made by 2,152 cells with 62 catalytic cells.

The hydrogen oxidation over rhodium catalyst using a UBI microkinetic model [26] with nitrogen as inert diluent was investigated. This kinetic scheme is made by 18 reactions and 5 adsorbed

species, as reported in Appendix B. The system has been studied in adiabatic condition in order to verify also the temperature reached by the system. Conditions and compositions of the feed are depicted in Table 6.

| **OPERATING CONDITIONS** | |
|---|---|
| $H_2$ Mass Fraction | 0.299% |
| $O_2$ Mass Fraction | 1.180% |
| $N_2$ Mass Fraction | 98.50% |
| Pressure | 1 atm |
| Temperature | 973 K |
| Flow Velocity | 0.08 m/s |

Table 6: Operating conditions hydrogen combustion

The results of the simulation have been compared with data provided by STANJAN at equilibrium conditions and presented in Table 7.

| **EXPECTED RESULTS** | |
|---|---|
| $H_2$ Massi Fraction | 0.149% |
| $O_2$ Massi Fraction | 0.000% |
| $N_2$ MassiFraction | 98.50% |
| H2O Massi Fraction | 1.334% |
| Temperature | 1124 K |

Table 7: Expected results at equilibrum condition - Stanjan

The two simulations are carried out using a Courant Number Co of 0.05. This parameter is used in order to compute the time step for the run and it is define as:

$$Co = \frac{|U| * \delta t}{\delta x} \quad \rightarrow \quad \delta t = \frac{Co * \delta x}{|U|}$$

where $\boldsymbol{U}$ is the velocity of the flow inside the cell, $\delta x$ is the smallest dimension of the cell related to the mesh and $\delta t$ is the time step. This parameter has to be chosen, at least, minor of 1.

### 3.4.2 Simulation with Reaction Transport

The simulation results for the ReactionTransport operator splitting order show clear errors in the resolutions of the equations (Figure 20). As it is well know the oxidation of hydrogen is an exothermic reaction and thus, the decreasing of the temperature in one point of the reactor (with no exchange of heat with the external environmental) under the inlet value is absolutely unfeasible. This is particularly true near the reacting surface where the increase of temperature would be much stronger (Figure 21).

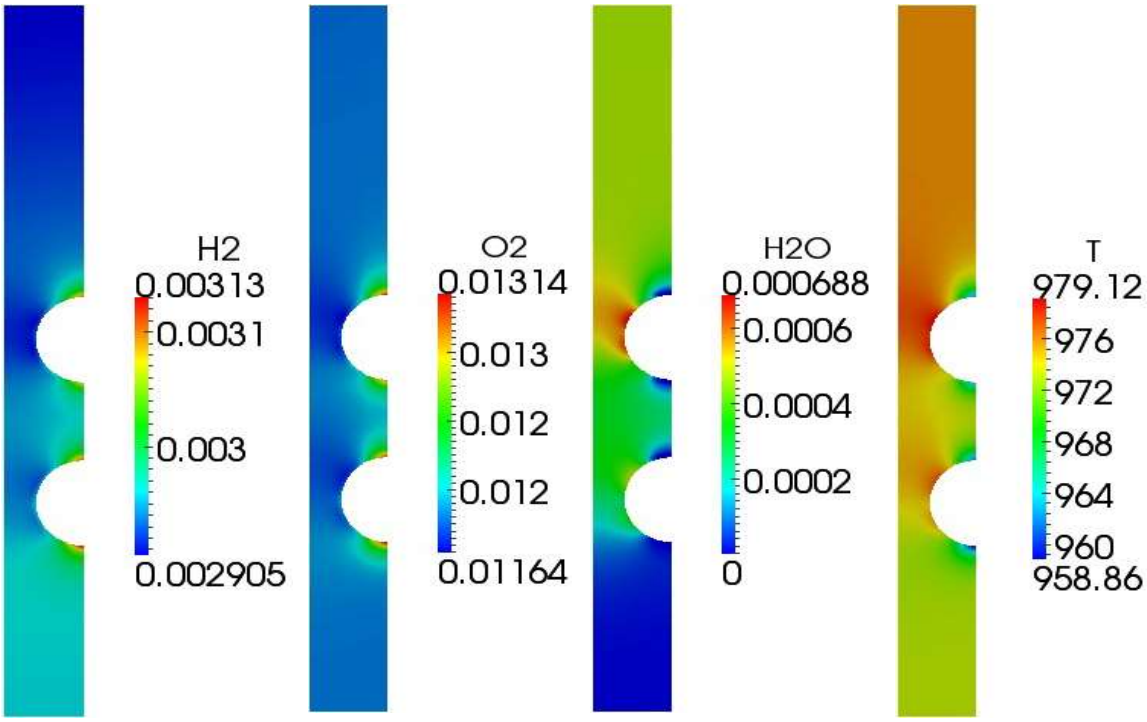


Figure 20: Composition and temperature fields for RT operator splitting order

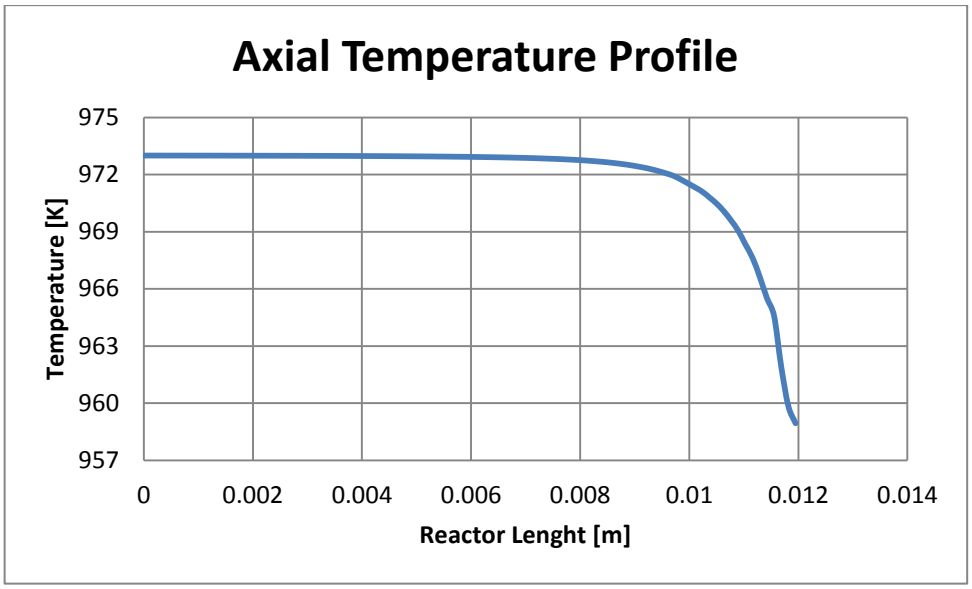


Figure 21: Axial temperature profile - RT operator splitting order

Furthermore, the profiles of reactants and products species have an opposite behavior as the expected ones. Figure 22-Figure 24 show the axial profile of $H_2$, $O_2$ and $H_2O$ from the inlet of the reactor to the first reacting wall: the massive fractions of reactants increase gradually until the maximum value is reached on the catalyst. Production of water (Figure 24) is very low, even if the reaction takes place at very high temperature, and it presents a profile with a maximum, other no sense for the simulation.

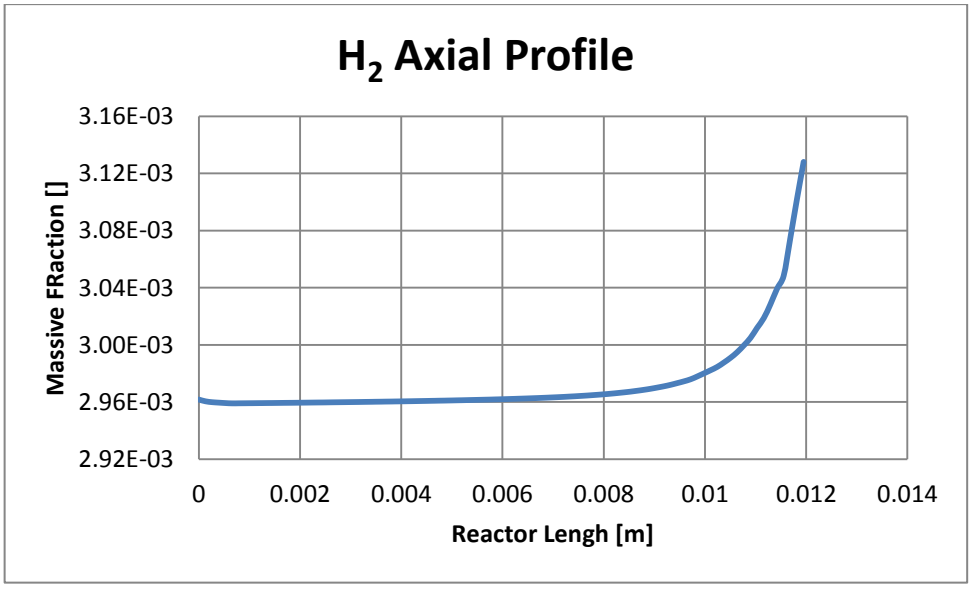


Figure 22: Hydrogen axial profile - RT operator splitting order

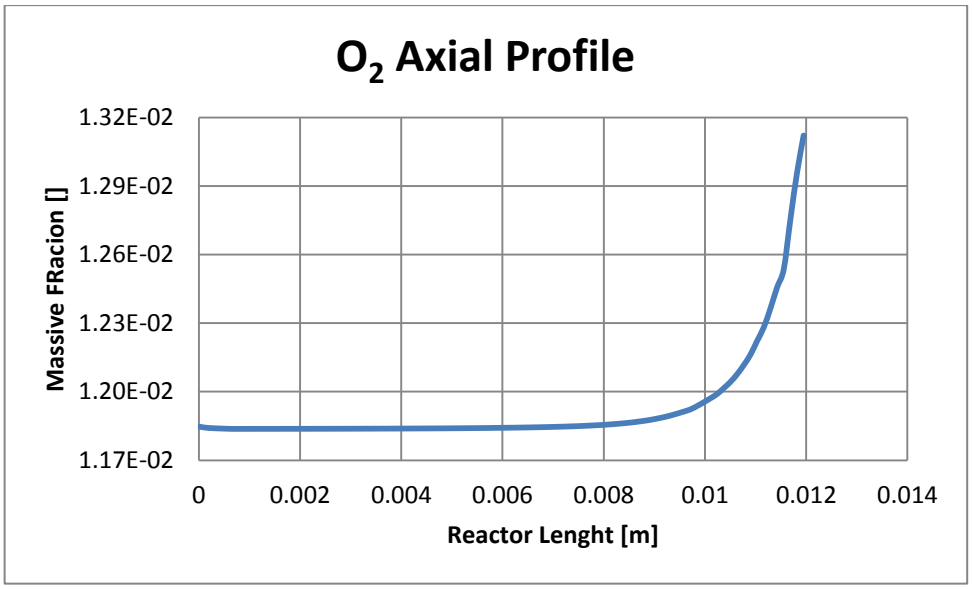


Figure 23: Oxygen axial profile - RT operator splitting order

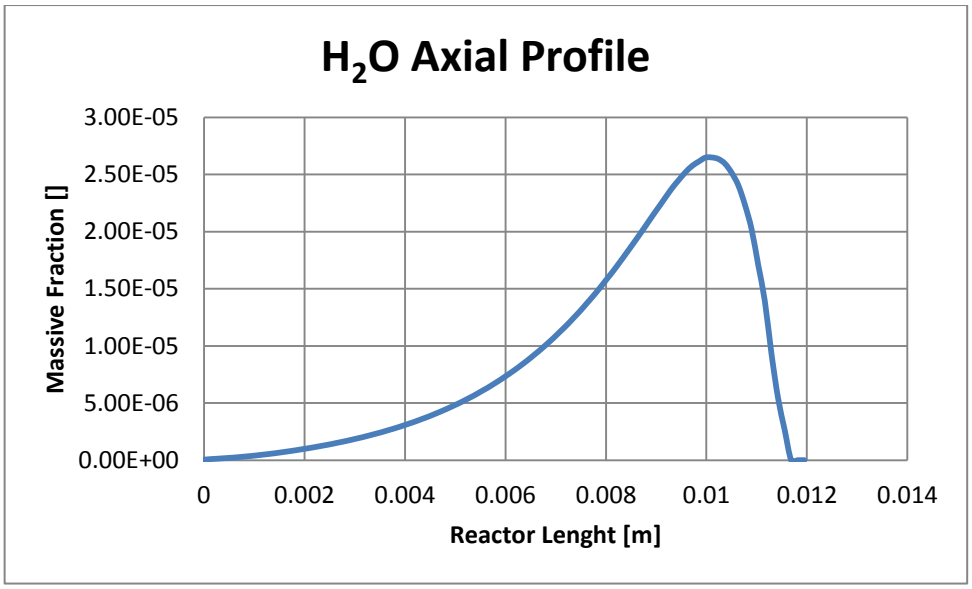


Figure 24: Water axial profile - RT operator splitting order

Moreover, it has been studied if this problem was due by the time step adopted for the simulation. For this reasons the same run was carried out with three different values of Courant Number: 0.2, 0.05 and 0.01 (Figure 25).

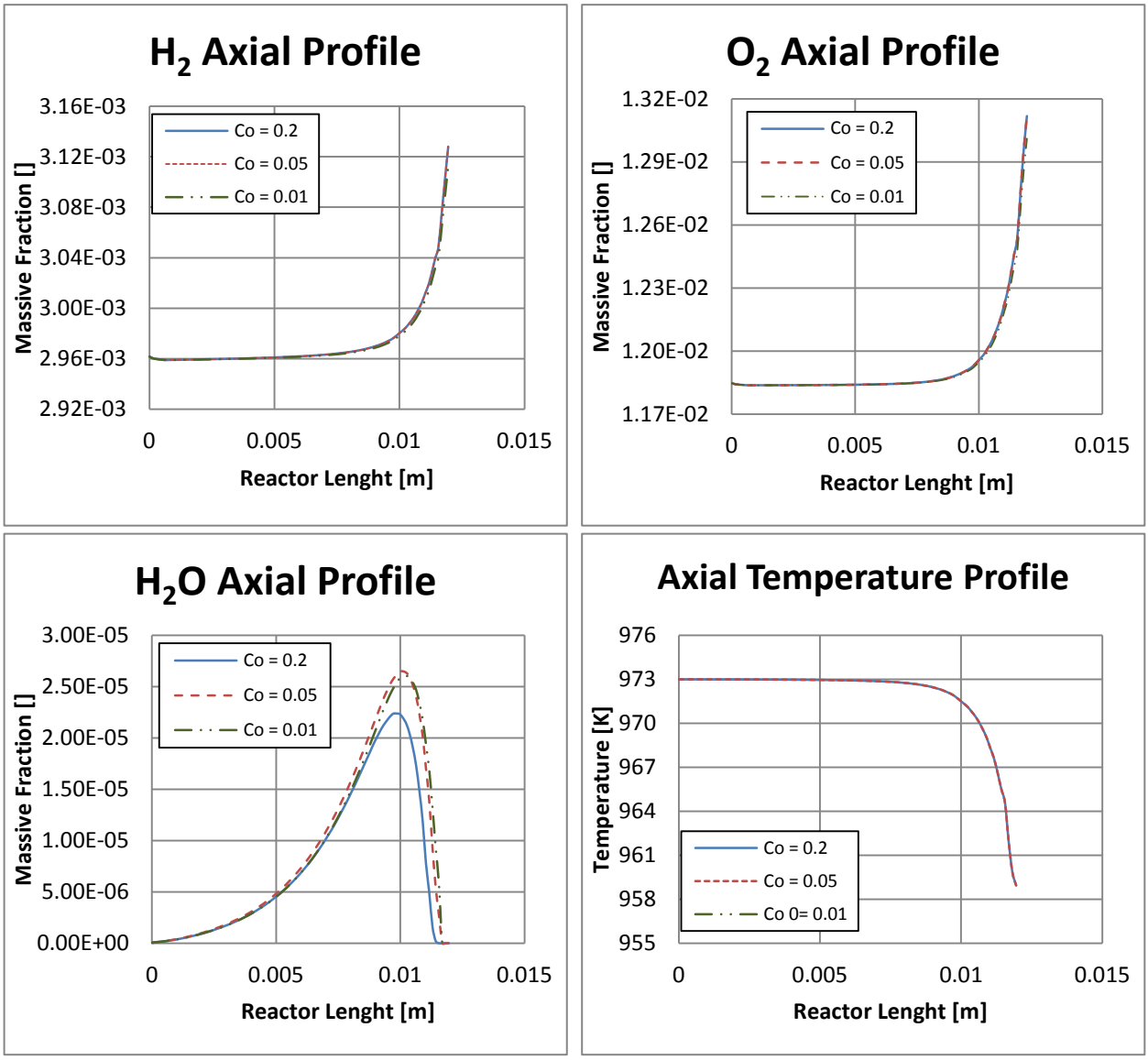


Figure 25: Compositions and temperature profiles at different Co number - RT operator splitting order

The same trends are obtained also with a smaller time step. With a Couran Number of 0.01, the $\Delta t$ of integration related to transport term is 5e-6 s, sufficiently accurate in order to well describe the phenomena.

As it possible to see, the results for the simulation where the reaction term is solved as the first one they are always in disagreement with the expected results provided by Stanjan at equilibrium conditions. Moreover the results, especially for the profile of reactants and product, are complete unfeasible. This is the first evidence that the theory developed by Sportisse about the stabilizing effect of the reaction term if solved as the last one is correct [32].

### 3.4.3 Simulation with Transport Reaction Momentum

This thesis is further supported by the results with TransportReactionMomentum splitting order that are in excellent agreement with the expected results reported in Table 7. As it possible to see in Figure 26-Figure 27, the endothermic behavior of the previous simulation completely disappeared. The adiabatic temperature is reached close to the reactor where the reactants are completely consumed.

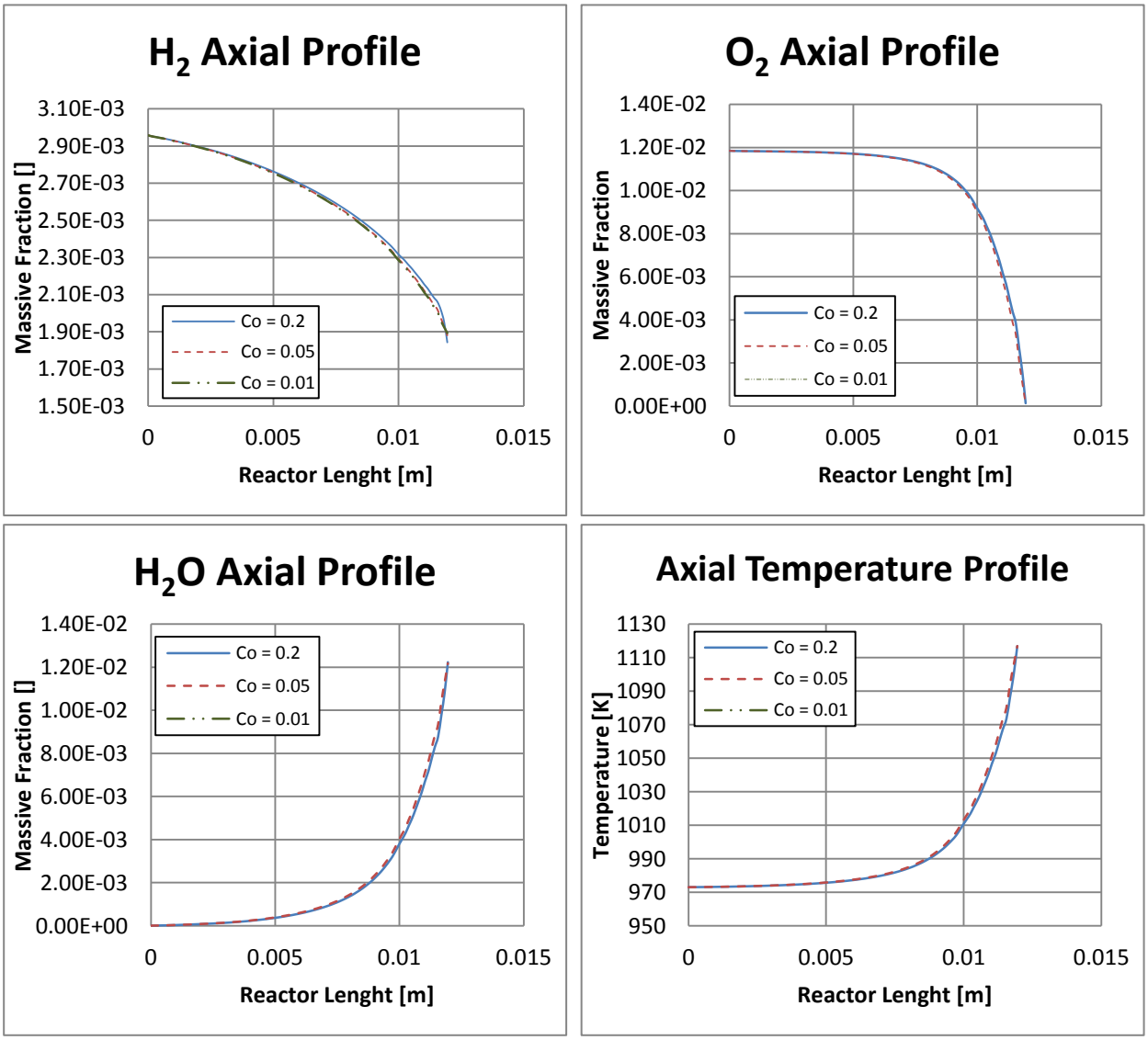


Figure 26: Compositions and temperature profiles at different Co number - TRM operator splitting order

The profiles of $H_2$ and $O_2$ are in agreement with the expected ones: indeed, the mass fraction, from the inlet value, gradually decreases approaching the catalytic surface until reaching a value near zero on it. Moreover the mass fraction of water increases and amount to the maximum value

on the rhodium surface. Here the oxygen conversion is complete and also the hydrogen residual reaches the value of Stanjan at equilibrium conditions.

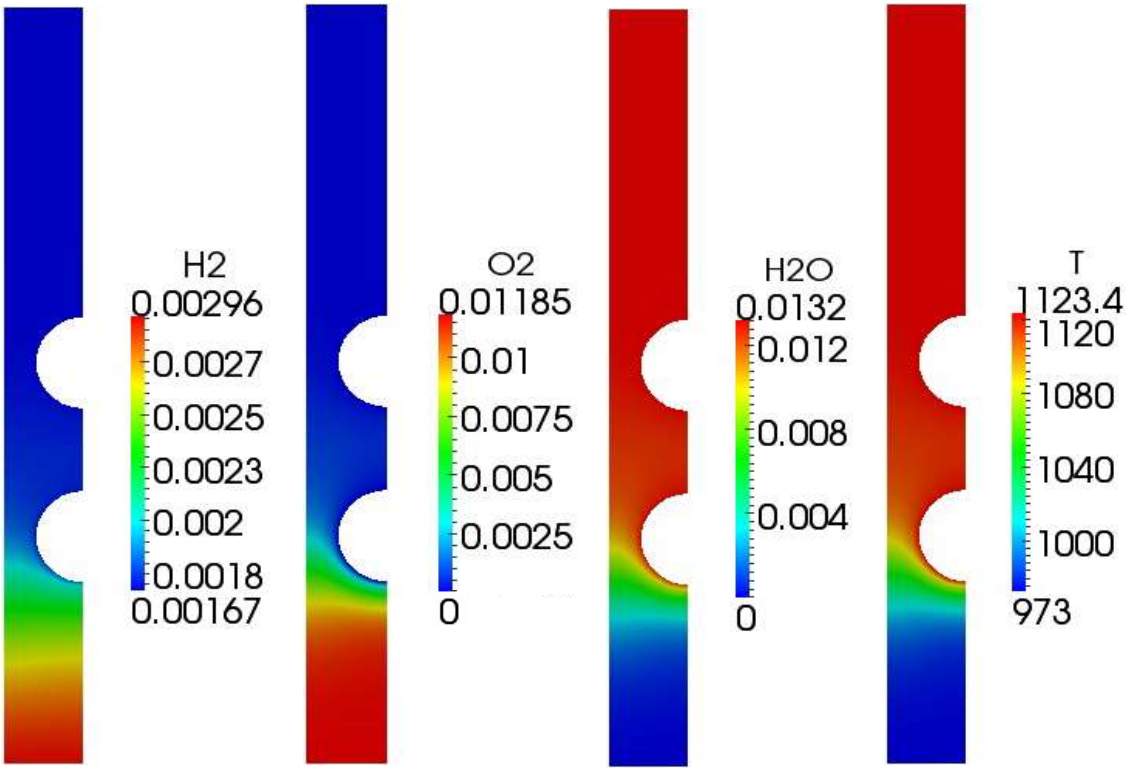


Figure 27: Composition and temperature fields for TRM operator splitting order

As a first approach, it would be easy to think that the computational time for the same case with the two splitting orders will be the same. However the reality is very different. Adopting the three different $Co$, the computational time required by a TransportReactionMomentum simulation is always lower than the ReactionTransport one. Figure 28 represents the clock time, i.e. the total time that the processor needs in order to complete the simulation (it is the sum of the CPU time, I/O time and the communication channel delay).

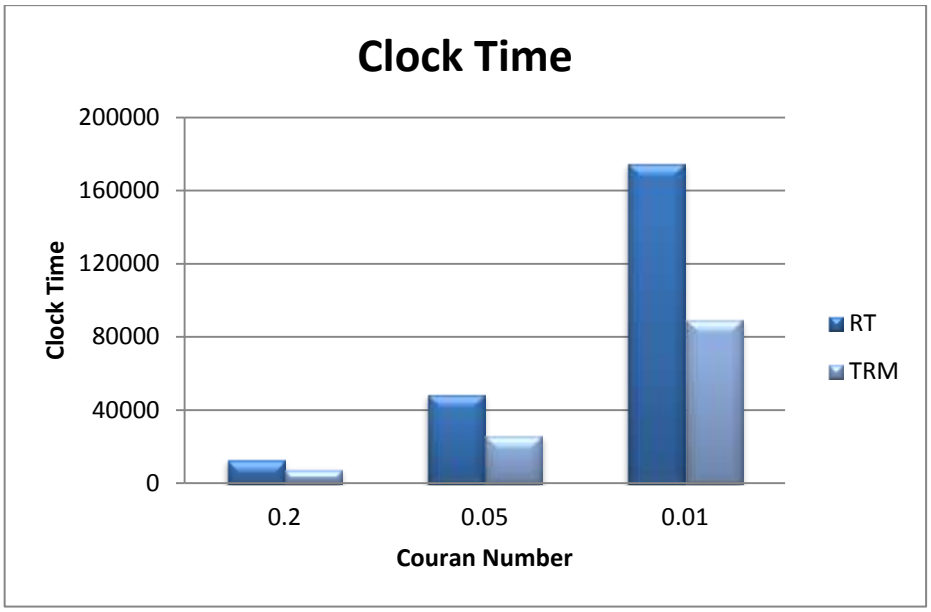


Figure 28: Computational effort at different Couran number

The computational time for ReactionTrasport order at each Couran Number is double than the one necessary for a TransportReactionMomentum simulation.

## 3.5 Complex Reacting systems

The systems that have been taken into account are the well known processes of Steam reforming (SR) and Reverse Water Gas Shift (RWGS) over rhodium catalyst. The UBI kinetic scheme, used for both the systems is made by 82 surface reactions, 16 species and 13 adsorbed species (see Appendix B) [26].

The experimental tests were performed in a short-contact time annular reactor (Figure 29). The reactor consisted of a catalyst-coated alumina tube coaxially inserted into a quartz-tube. The dimensions are shown in Table 8. Inside the alumina tube, a sliding thermocouple was inserted, in order to measure catalyst temperature profiles [36]. The catalyst weight was of the order of 10 mg (4% $Rh/\alpha\text{-}Al_2O_3$), and the Rh dispersion for the aged-catalyst was estimated, from CO and $H_2$ chemisorption experiments, to be 5%. For this rig, this corresponds to a Rh specific surface of 600 $cm^2/cm^3$ [26].

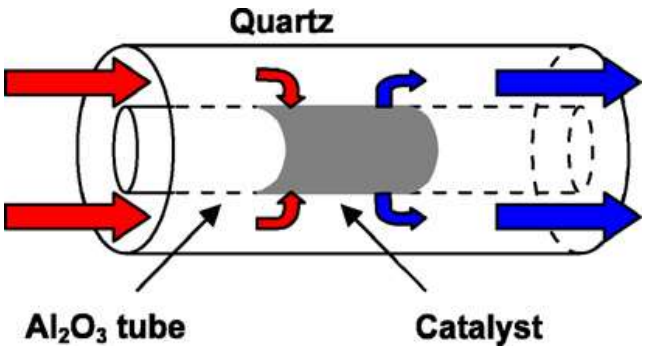


Figure 29: Scheme of an annular reactor

| Reactor Geometry | |
|---|---|
| Inner Radius | 0.20 cm |
| Outer Radius | 0.25 cm |
| Reactor Lenght | 2.2 cm |

Table 8: Geometry of the mesh

The spatial discretization of the geometrical domain was simplified in order to reduce the computational effort. Specifically, thanks to the symmetry of the annular reactor, it is possible to consider only one slice of this reactor. This is very convenient because this allows to consider a 2D mesh instead of a 3D one. The 2D mesh is obtained considering the slice of a cylinder with a width of 5°. The number of required cells is thus 72 times lower than the one required for a 3D grid. A schematic view of the mesh is presented in Figure 30.

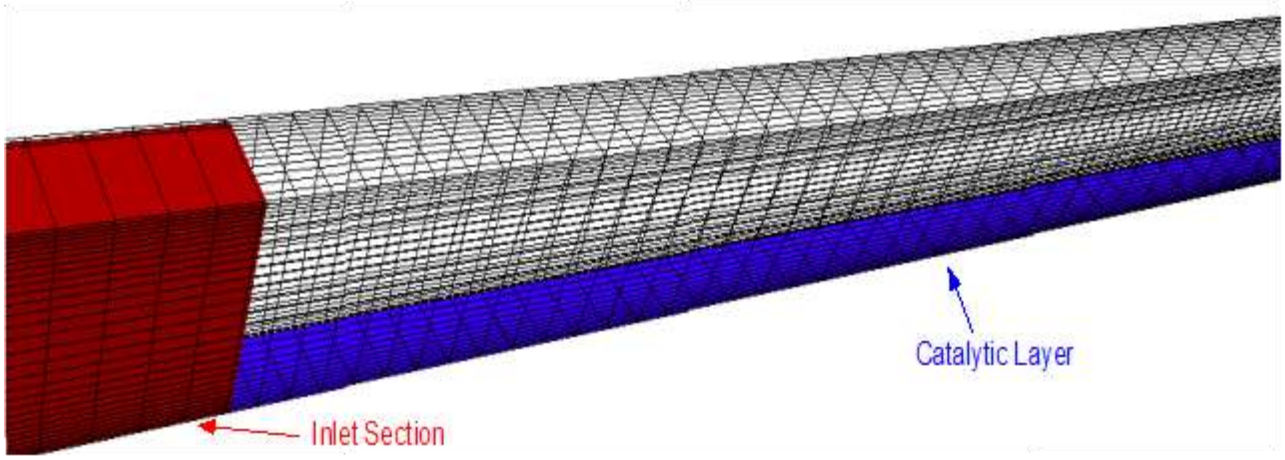


Figure 30: Particular of the 2D mesh

The simulations are performed over an optimized mesh composed by 135 units in axial direction and 30 units in the radial one for an overall amount of 4050 cells.

In addition the grid is refined with a specific grading, i.e. the length of each cell of the mesh is not constant. The expansion ratio of the cells is calculated as the ratio among the length of the first and the last cell along one edge of a block. This enables the mesh to be graded, or refined, in specified directions for a specific factor. The introduction of a non-constant step grid allows one to describe certain areas of the system in a more detailed way. In this case, since the zone close to the catalyst is interested by strong normal gradients, the mesh is highly refined near the catalytic wall in the radial direction. A further grading was introduced in the axial direction to provide a proper description of the rapid consumption of reactants at the reactor inlet.
For the temporal discretization a Courant number of 0.05 is adopted.
For a comprehensive understanding of the two reactive systems, simulations with a wide range of temperature have been carried out (300°C – 800°C) in isothermal conditions under atmospheric constant pressure.

### 3.5.1 Steam reforming

The first reaction considered is the following:

$$CH_4 + H_2O \rightarrow CO + H_2$$

The composition of the feed is reported in Table 9:

| **FEED COMPOSITION** | |
|---|---|
| $CH_4$ Mole Fraction | 1.00% |
| $H_2O$ Mole Fraction | 2.00% |
| $N_2$ Mole Fraction | 97.00% |
| Flow Rate | 0.01724 mol/min |

Table 9: Feed composition - Steam reforming:

Figure 31 and Figure 32 show the average composition on the outlet patch as a function of the reactor temperature:

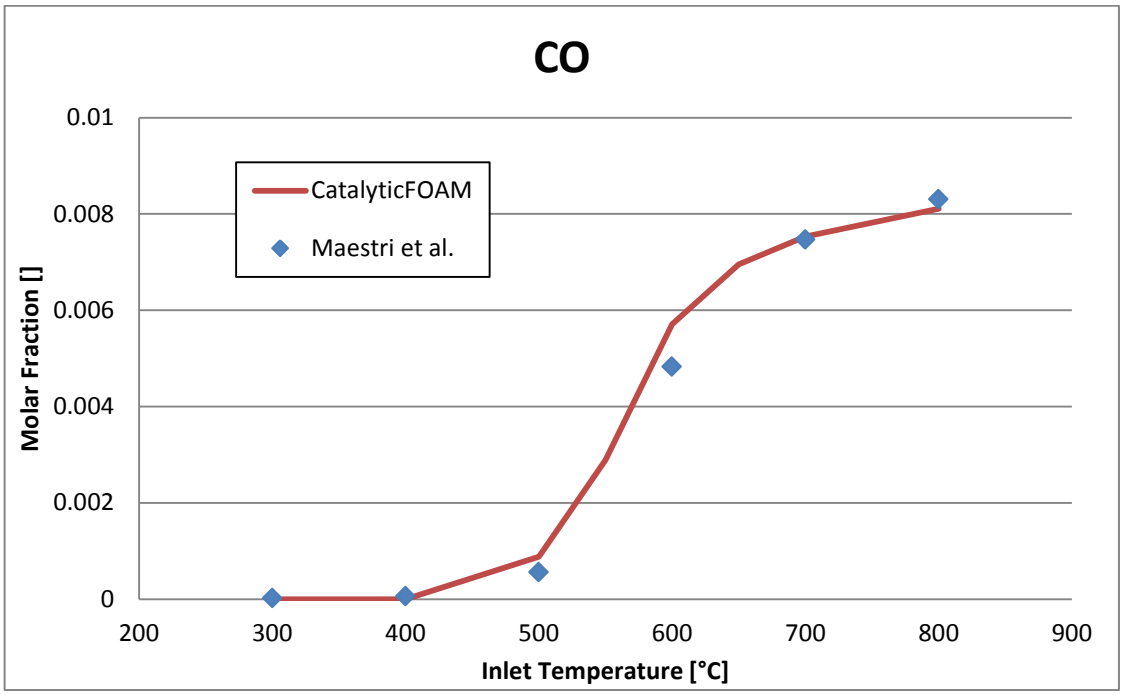


Figure 31: CO mole fraction at the exit of the reactor versus the temperature

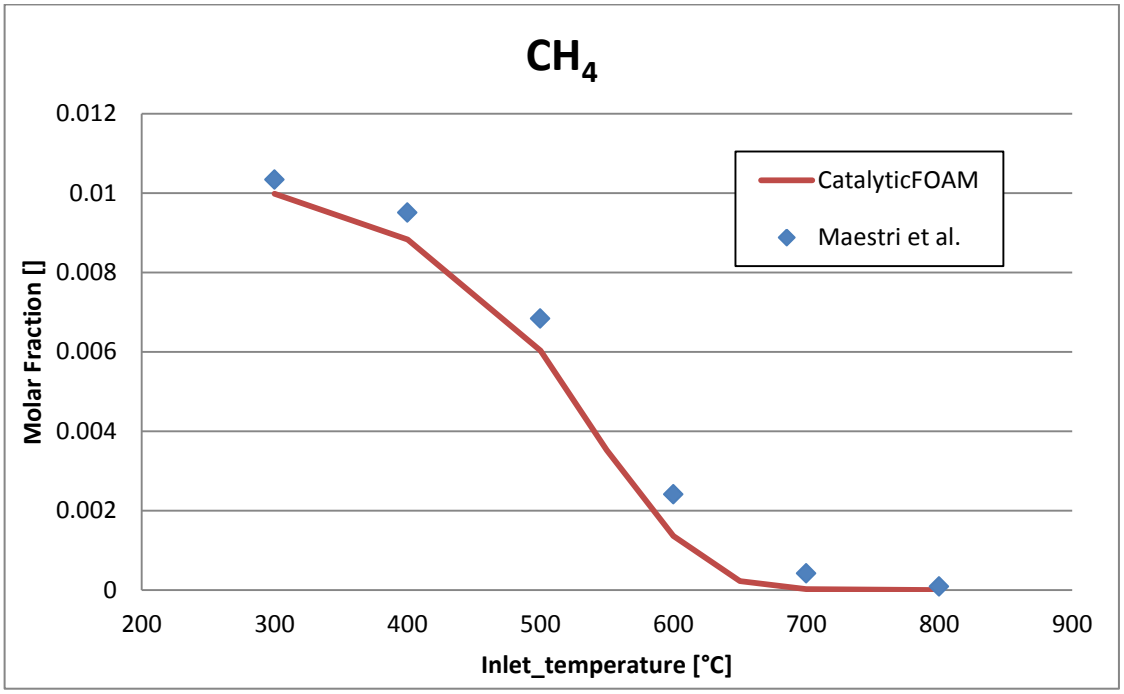


Figure 32: $CH_4$ mole fraction at the exit of the reactor versus the temperature

Figure 31 and Figure 32 show a good agreement between the experimental data and the numerical simulations in the wide range of temperature investigated.

### 3.5.2 Revers water gas shift

The second system investigated is the reaction of Revers Water Gas Shift between $CO_2$ and $H_2$. The reaction is the following:

$$CO_2 + H_2 \rightarrow CO + H_20$$

The new composition of the feed is reported in Table 10:

| FEED COMPOSITION | |
|---|---|
| $CO_2$ Mole Fraction | 1.09% |
| $H_2$ Mole Fraction | 1.02% |
| $N_2$ Mole Fraction | 97.89% |
| Flow Rate | 0.01321 mol/min |

Table 10: Inlet feed composition - revers water gas shift:

Figure 34 show the comparison between experimental data and the numerical simulations also for this reactive system.

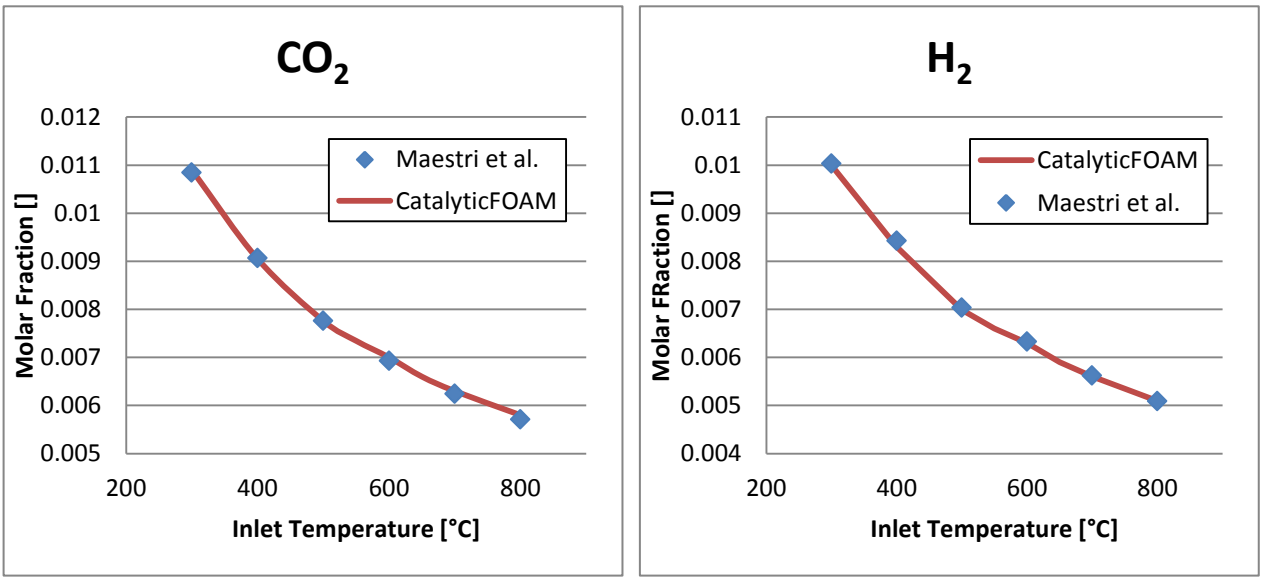


Figure 33: $CO_2$ and $H_2$ mole fraction at the exit of the reactor versus the temperature

As expected, the behavior of reactants and products (Figure 33 and Figure 34) is the same because of the stoichiometric composition of the feed. $CO_2$ and $H_2$ are consumed in the same way and moreover the amounts of $H_2O$ and CO increase properly.

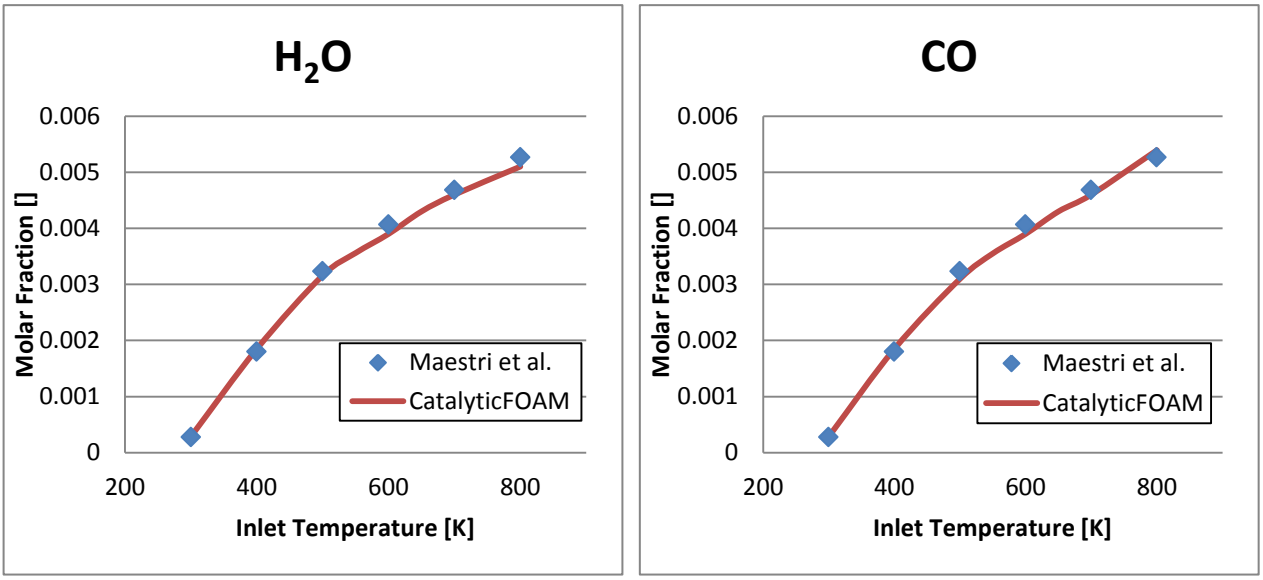


Figure 34: $H_2O$ and CO mole fraction at the exit of the reactor versus the temperature

## 3.6 Adiabatic cases

Here the same reactive systems shown in Paragraph 2.4. have been tested in adiabatic conditions. In these cases the comparison of the results will be done with data at equilibrium conditions provided by Stanjan at equilibrium conditions. In this case only one value of inlet temperature will be taken into account (800 °C) both for steam reforming and revers water gas shift.

As already said the composition of the feeds is the same presented in Table 9 and Table 10.

### 3.6.1 Steam Reforming

The expected results are presented in Table 11:

| EXPECTED RESULTS STEAM REFORMING | |
|---|---|
| $CH_4$ Mass Fraction | 0.0% |
| $H_2O$ Mass Fraction | 0.474% |
| CO Mass Fraction | 0.797% |
| $CO_2$ Mass Fraction | 0.243% |
| $H_2$ Mass Fraction | 0.384% |
| Temperature | 1006.2 K |

Table 11: Expected results Steam Reforming in adiabatic conditions

Figure 35 shows the temperature reached in adiabatic conditions at the outlet of the reactor with an inlet temperature of 800 °C. As it possible to see this value presents an excellent agreement with the value provided by the database, difference is less than 1°C.

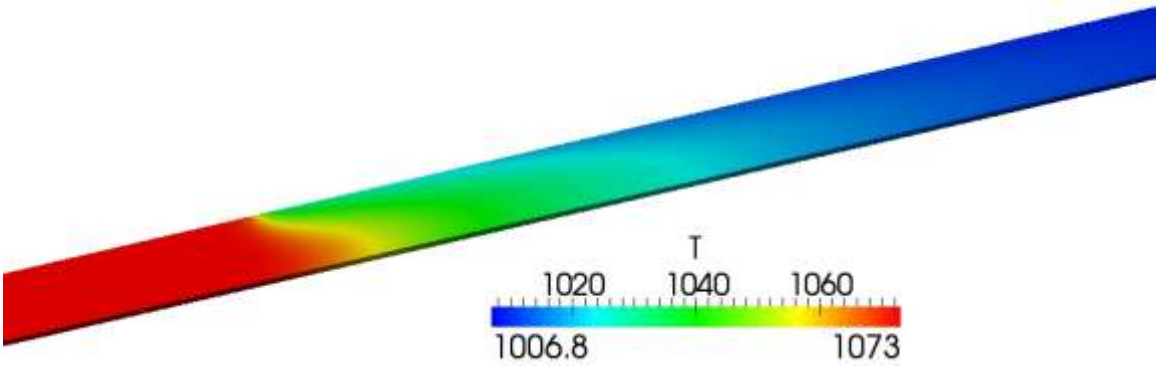


Figure 35: Temperature field for steam reforming case

About the composition at the outlet of the reactor, the results are presented in Table 12:

| SIMULATION RESULTS STEAM REFORMING | |
|---|---|
| $CH_4$ Mass Fraction | 0.0% |
| $H_2O$ Mass Fraction | 0.474% |
| CO Mass Fraction | 0.792% |
| $CO_2$ Mass Fraction | 0.250% |
| $H_2$ Mass Fraction | 0.290% |

Table 12: Composition at the outlet patch of the reactor - SR

The mass fractions of reactants and product present an excellent agreement with the results provided by Stanjan at equilibrium conditions. This means that both the mass and energy balance are well characterized.

### 3.6.2 Revers water gas shift

The expected results are presented in Table 13:

| EXPECTED RESULTS REVERS WATER GAS SHIFT | |
|---|---|
| $CO_2$ Mass Fraction | 0.800% |
| $H_2$ Mass Fraction | 0.417% |
| $H_2O$ Mass Fraction | 0.331% |
| CO Mass Fraction | 0.515% |
| Temperature | 1067.7 K |

Table 13: Expected results Revers water gas shift in adiabatic conditions

Also in this case a perfect agreement between simulation and expected results (Table 14) is provided. The adiabatic temperature of 1067.7 K is correctly verified (Figure 36).

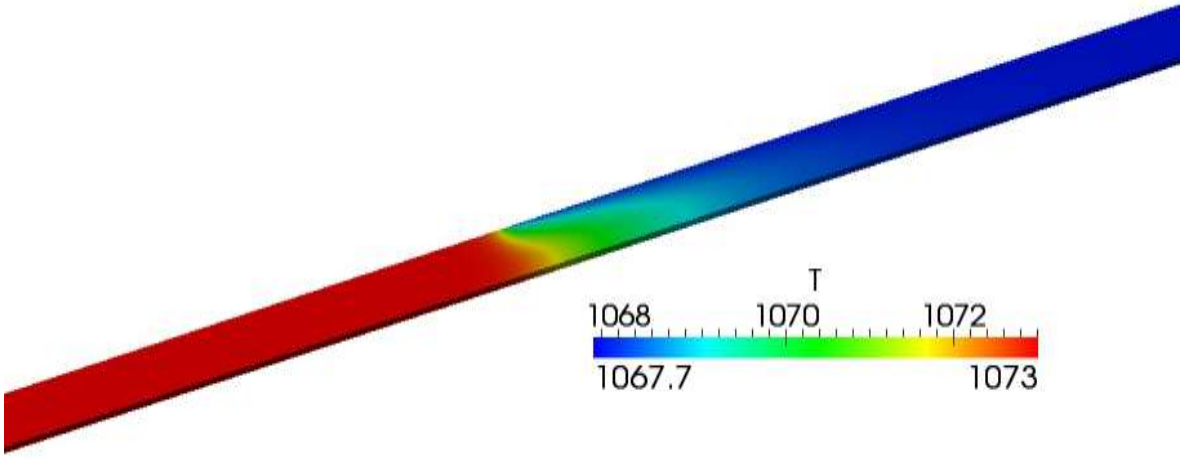


Figure 36: Temperature field for revers water gas shift case

| SIMULATION RESULTS REVERS WATER GAS SHIFT | |
|---|---|
| $H_2O$ Mass Fraction | 0.327% |
| CO Mass Fraction | 0.510% |
| $CO_2$ Mass Fraction | 0.770% |
| $H_2$ Mass Fraction | 0.370% |

Table 14: Composition at the outlet patch of the reactor- RWGS

The same behavior seen in the last paragraph is proposed again here. $H_2O$, $H_2$, CO and $CO_2$ are once again in a good agreement with the results at equilibrium condition that it is represented by the complete conversion of methane.

## 3.7 Conclusions

A new version of the energy balance equations has been written in order to overcome the convergence problem of the solver that affected the old one. The new equations has been tested with different reactive systems and geometries characterized by progressive complexity with good agreements.

The analysis of Operator Splitting order of equations has demonstrated that the investigated splitting orders are not equal in the resolutions of the system and in the calculation of the local error. Furthermorer, the stiff terms, represented by the reactive term, has always to terminate the splitting process in order to increase the accuracy of the results. Evidences of these issues have been provided both by literature through the works of Sportisse [33] and with simulations results of simple reacting systems.

Moreover, the solver was tested with complex reaction systems (SR and RWGS) and microkinetic schemes in different conditions (isothermal and adiabatic cases). The simulation results gave an excellent agreement both with data provided in literature and with the results at thermodynamic equilibrium.

# 4 Improvements in catalyticFOAM multiRegion

In this Chapter the development of the multi-region solver is described, from the mathematical model to the details about its numerical structure and its implementation.

In the first part, the mathematical model is presented, including the main numerical issues related to the solution of the governing equations in complex catalytic systems. Secondly, the numerical structures adopted to overcome the intrinsic issues of a segregated approach for the interface coupling is presented, as well as the final architecture of the solver, with particular attention to the solution process in each phase.

In a second part of the Chapter, several tests on the built numerical architecture are presented and discussed. In particular, in order to test the validity of the adopted coupling strategy, diffusion-reaction isothermal cases with different geometries are carried out.

Eventually, a case study of fuel rich combustion of $H_2$ on Rh in annular reactor is presented through a comparison between the numerical results and the experimental data. In order to save the CPU time the solver has been parallelized and a description of the performance of the system is provided.

## 4.1 Introduction

One of the aims of this Thesis is to develop a powerful numerical tool able to predict the behavior of catalytic heterogeneous reacting systems, taking into account both inter and intra-phase phenomena, as well as detailed kinetic schemes.

In order to properly model this system, it is necessary to address different phenomena, such as heat and mass transfer occurring both in the gas and solid phase (intra-phase phenomena) and between them (inter-phase phenomena). Moreover the velocity and pressure fields due to the fluid flow in the reactor and surface reactivity have to be calculated. The most important phenomena taking place in a catalytic reaction can be summarized as shown in Figure 37:

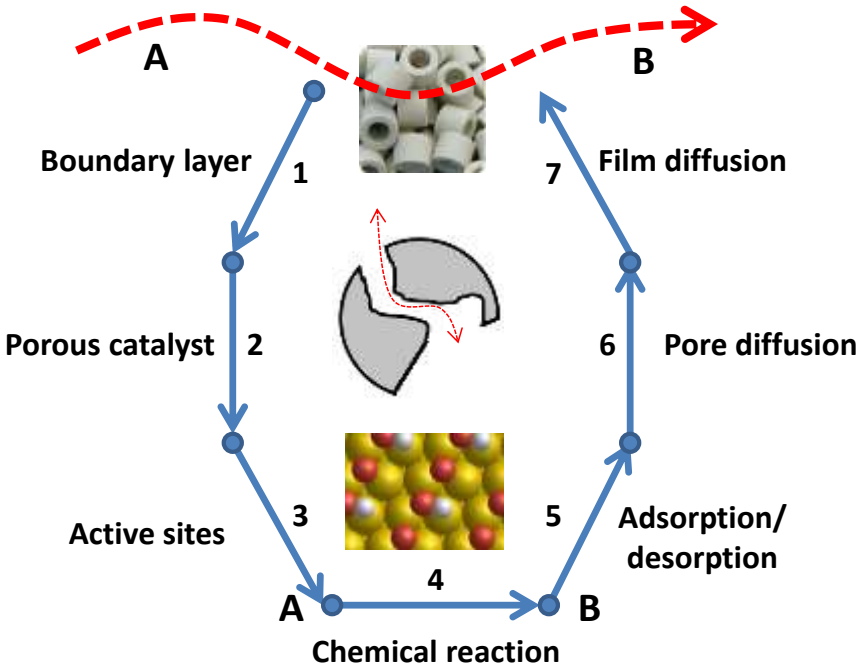


Figure 37: Individual steps of a simple, heterogeneous catalytic fluid-solid reaction A->B carried out on a porous catalyst.

1. Film diffusion: the reactants diffuse from the bulk phase to the boundary layer surrounding the solid phase;
2. Pore diffusion: the reactants diffuse from the boundary layer to the solid phase through the catalyst pores;
3. Adsorption: the reactants physically or chemically adsorb on the solid surface. If the adsorption is chemical, a free active site is necessary for the adsorption to take place;
4. Surface reaction: the adsorbed species react between each other or with gas-phase species;
5. Desorption: the reaction products desorb from the catalytic surface;
6. Pores back-diffusion: the reaction products diffuse from inside the catalyst to the boundary layer surrounding the solid;
7. Film back-diffusion: the reaction products diffuse from the boundary layer to the bulk.

In analogy with mass transfer, a similar phenomenology can be considered for heat transfer.

The presence of diffusive limitation within the catalytic layer affects the performance of the whole catalytic process. As shown in **Error! Reference source not found.**, three different rates controlling egimes can establish by varying the operative conditions:

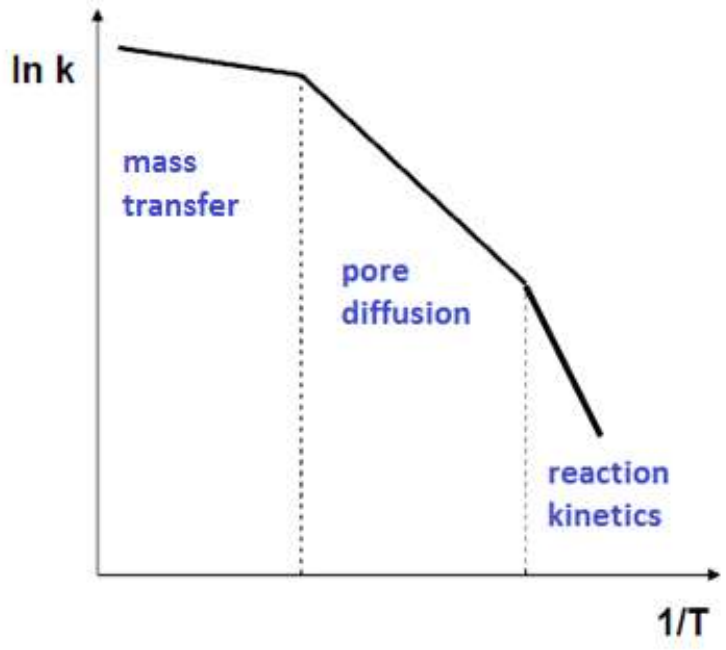


Figure 38: Influence of the temperature on the rate controlling regimes

The rate limiting mechanism can be determined based on the differences in activation energies for the reaction, pore diffusion, and mass transfer regime. At low temperatures, the chemical reaction rate is relatively slow if compared with the diffusion rate and, thus, the catalytic system works under kinetics controlled regime. As the temperature increases, the rate of the kinetic step becomes higher than the diffusion rate and the control of the overall rate shifts from chemical to pore diffusion. Finally, at high temperatures, both chemical and pore diffusion rates are sufficiently faster than bulk mass transfer, making to become it the rate determining step.

Therefore, it is important to develop a solver able to describe in detail the transport phenomena in and around the catalyst to account for the different controlling regimes.

## 4.2 State of the art

Within the OpenFOAM® framework the only available multiple-region partitioned solver is the *chtMultiRegionFoam* solver. This solver is able to describe only heat transfer problems using the OpenFOAM® internal libraries for coupling handling. On the other hand, neither libraries nor solvers for mass-transfer coupling existed in OpenFOAM®, as well as no convergence criteria were implemented for the coupling of multiphase system.

In a previous work [1], a numerical tool able to describe the behavior of catalytic heterogeneous reactors via a *first principles approach* has been implemented. It allows for the dynamic solution of reacting flows over solid catalysts through the development of a multi-region structure in order to investigate complex systems with an arbitrary number of different domains with their own properties. The solver was based on a segregated approach for physical coupling of neighboring regions, involving the solution of the governing equations on each domain and the achievement of the convergence on the boundary conditions interface through an iterative loop called PIMPLE loop (merged PISO-SIMPLE algorithm,[37, 38]).

Calonaci and Furnari [1] proposed the solver's architecture shown in Figure 39:

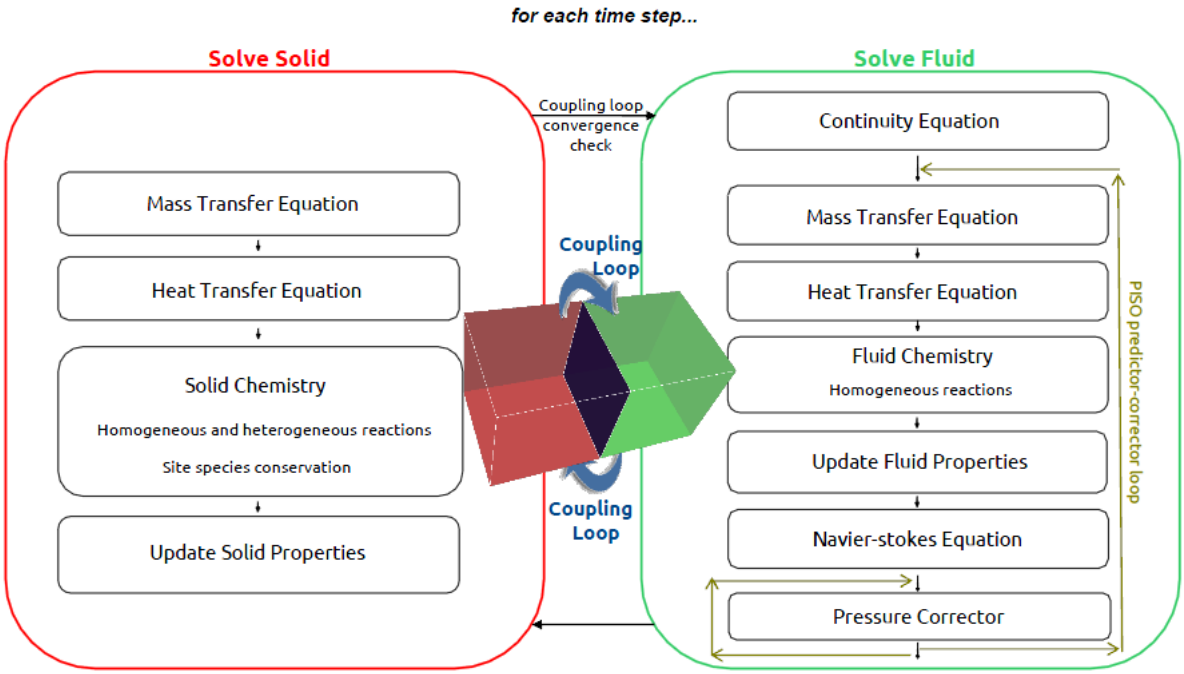


Figure 39: Schematization of CatalyticFOAM solution procedure in a previous work [1]

This tool has been tested for the solution of a 1-D conjugate heat/mass transfer problems and the results showed a good agreement between the analytical solution for steady state and the numerical ones. On the contrary, the proposed procedure presented problem of stability if tested in other conditions. In this work, to overcome these criticalities, the architecture of the previous solver has been modified following a more physical approach able to describe the interface coupling of neighboring regions in an accurate way. A deep analysis of these issues will be provided in the section 4.4.

# 4.3 Mathematical model

The equations used to model the system are the general equations of conservation of mass, energy, continuity, and momentum. In this paragraph it will be shown as these equations have been solved into a mathematical model, with the aim to describe the whole range of phenomena occurring in both the fluid and the solid regions. The latter have been considered as a porous matrix including both the solid catalytic volume and the fluid contained inside its pore. This system, inherently heterogeneous, has been modeled considering a pseudo-homogeneous simplification using modified transport properties that take into account the transport in the porous phase.

The equations that have to be solved are the following:

- **Navier-Stokes Equations**

For a correct description of the flow field it is necessary to solve the Navier-Stokes equations for the momentum transport under the hypothesis of Newtonian fluids:

$$\frac{\partial(\rho U)}{\partial t} + \nabla(\rho UU) = -\nabla p + \nabla(\mu \nabla U) + \rho g \tag{4.1}$$

where

μ is the dynamic viscosity, $g$ is the gravity acceleration and is the pressure.

In the hypothesis of absence of convective flux inside the catalytic solid pores, there is no need to solve the Navier-Stokes equation in the solid phase. The micro-fluxes that involve the solid domain are characterized as a merely diffusion mechanism.

Being the density field interconnected with the velocity and pressure fields, it is necessary to add the continuity equation:

$$\frac{\partial \rho}{\partial t} + \nabla(\rho U) = 0 \tag{4.2}$$

For compressible fluids it is requested the knowledge of the pressure field, described by the equation of state. Since the technological interest is focused on processes where the flowing phase is gaseous, the ideal gas approximation is adopted:

$$\rho = \frac{p \cdot MW}{R \cdot T} \tag{4.3}$$

- **Species transport equations**

Both in the solid and fluid regions the transport equation of species is written under the hypothesis of Fickian diffusion:

- ✓ *Fluid phase*

$$\frac{\partial(\rho\omega_i)}{\partial t} + \nabla(\rho U \omega_i) = \nabla(\rho \wp_i \nabla \omega_i) + \sum_{j=1}^{NR} \nu_{i,j} R_j^{\text{homo}} MW_i \tag{4.4}$$

- ✓ *Solid phase*

$$\frac{\partial(\rho^G \omega_i)}{\partial t} = \nabla(\rho^G \wp_{i,eff} \nabla \omega_i) + \sum_{j=1}^{NR} \nu_{i,j} R_j^{het} MW_i \tag{4.5}$$

where $\omega_i$ is the mass fraction of the *i*-th component, $\wp_i$ and $\wp_{i,eff}$ represent respectively the diffusivity in the fluid phase and the effective diffusivity in the solid phase of the *i*th species, $\rho^G$ is the density of the gas inside the catalyst pores, $MW_i$ is the molecular weight for the i-th species, $R_j^{\text{homo}}$ and $R^{het}_j$ are respectively the velocity of homogeneous and heterogeneous j-th reaction, $\nu_{i,j}$ is the stoichiometry coefficient of the i-th component.

- **Energy transport equation**

To describe the temperature field, the solution of the energy balance is required.

- ✓ *Fluid phase*

$$c_p \frac{\partial(\rho T)}{\partial t} + c_p \nabla(\rho U T) = \nabla(\lambda \nabla T) - \Delta \mathrm{H}_{R,j} R_j^{\text{homo}} \tag{4.6}$$

- ✓ *Solid phase*

$$c_p \frac{\partial(\rho^S T)}{\partial t} = \nabla(\lambda_{eff} \nabla T) - \Delta \mathrm{H}_{R,j} R_j^{het} \tag{4.7}$$

where $T$ is the temperature, $c_p$ is the specific heat of the gas mixture. $\lambda$ and $\lambda_{eff}$ represent, respectively, the thermal conductivity in the fluid phase and the effective thermal conductivity in the solid one, $\Delta H_{R,\mathrm{j}}$ is heat of reaction. The energy dissipation due to the viscosity of the fluid is neglected. Furthermore the pressure term can be ignored [29].

- **Reactive term in different phases**

To model properly the multiphase system, it is necessary to mathematically describe all the phenomena taking place both in the solid and in the fluid phase. All the species can:

- lead to homogeneous reactions in the fluid phase;
- adsorb on the catalytic surface and lead to heterogeneous reactions;
- react in the fluid phase inside the solid pores.

As previously stated, homogeneous reactions taking place inside the catalyst pores will be reasonably neglected. Naturally, the reaction creates a concentration gradient which makes new reactants move from the fluid to the solid phase until a steady state is reached. All the reactions will be accompanied by heat generation or subtraction.

- In the fluid phase:

$$\begin{cases} \dfrac{\partial(\rho\omega_i)}{\partial t} = \sum_{j=1}^{NR} R_{\mathrm{hom},j}\upsilon_{i,j}MW_i \\ c_p\dfrac{\partial(\rho T)}{\partial t} = \sum_{j=1}^{NR} R_{\mathrm{hom},j}\Delta H_j \end{cases} \tag{4.8}$$

- In the solid phase:

$$\begin{cases} \dfrac{\partial(\rho^G\omega_i)}{\partial t} = \sum_{j=1}^{NR_{het}} R_{\mathrm{het},j}\upsilon_{i,j}MW_i a_{cat} \\ c_p^s\dfrac{\partial(\rho^S T)}{\partial t} = \sum_{j=1}^{NR,het} R_{\mathrm{het},j}\Delta H_j a_{cat} \end{cases} \tag{4.9}$$

where $R_{\hom,i}$ is the homogeneous reaction rate for the i-th specie $\left[\frac{kmol}{m^3 s}\right]$ and $R_{het,i}$ is the heterogeneous surface reaction rate in $\left[\frac{kmol}{m^2 s}\right]$, which needs to be multiplied by the specific catalytic area $a_{cat}\left[\frac{m_{cat}^2}{m_{cat}^3}\right]$.

Furthermore, site conservation balances have to be written as follows:

$$\Gamma_{site}\frac{\partial \vartheta_i}{\partial t} = R_{i,surf} \tag{4.10}$$

where $\vartheta_i$ is the site fraction of the ith species, $\Gamma_{site}$ is the sites density and $R_{i,surf}$ is the production rate of the ith surface species. More details about the equation are provided in Appendix D.

- **Boundary conditions**

The transport equations of total mass, mixture momentum, individual species mass fraction and mixture energy require boundary conditions to be specified for pressure, velocity vector, species mass fractions and temperature.

The usual boundary conditions for pressure and velocity are imposed. In particular, the pressure value is fixed at the outlet boundaries and a zero-gradient condition is imposed at the inlets and at the walls. For the velocity filed, the no-slip conditions are assumed at the walls. At the inlet the velocity profile is assigned, while at the outlet boundaries the flow is assumed to be fully-developed and zero-gradient conditions are then imposed.

Boundary conditions for the gas-phase species mass fraction and temperature are summarized in the following:

*Inert walls*

The mass flux of the individual species k is set equal to zero:

$$\nabla \omega_k\big|_{inert} = 0 \tag{4.11}$$

According to the physics of the particular problem under investigation, on inert walls the temperature can be prescribed through a generic function of time $T_{inert}(t)$ or calculated to take into account the heat transfer with the external environment (at temperature $T_{env}(\mathrm{t})$):

$$T\big|_{inert} = T_{inert}(t) \tag{4.12}$$

$$\left(\lambda \nabla T\right)\big|_{inert} = U\left[T\big|_{inert} - T_{env}(t)\right] \tag{4.13}$$

where $U$ is the global heat transfer coefficient.

*Interface walls*

To solve the mass and energy transport equations in both regions it is necessary to impose appropriate boundary conditions that guarantee the continuity of the mass and energy flux through the interface and the same value of the field variable (temperature and mass fraction) on both interface sides.

These equations are shown in Eq. (4.14) and Eq. (4.15):

$$\begin{cases} \lambda_{eff,I} \left.\dfrac{\partial T_{SOLID}}{\partial x}\right|_{(I)} = \lambda_{fluid,I} \left.\dfrac{\partial T_{FLUID}}{\partial x}\right|_{(I)} \\ T_{SOLID,I} = T_{FLUID,I} \end{cases} \tag{4.14}$$

$$\begin{cases} \wp_{ieff,I} \left.\dfrac{\partial C_{i,SOLID}}{\partial x}\right|_{(I)} = \wp_{ifluid,I} \left.\dfrac{\partial C_{i,FLUID}}{\partial x}\right|_{(I)} \\ C_{iSOLID,I} = C_{iFLUID,I} \end{cases} \tag{4.15}$$

*Inlet boundaries:*

At inlet boundaries, Danckwerts' conditions are set for gas-phase species, i.e. the total mass flux for each species k (accounting for diffusion and convection) is specified. If composition gradients exist at the boundary, these conditions allow diffusion into the computational domain, therefore giving a more accurate description than classic Dirichlet conditions:

$$\left(\rho U \omega_k\right)\big|_{inlet} - \left(\rho \Gamma_k \nabla \omega_k\right)\big|_{inlet} = \left(\rho U \omega_k\right)_0 \tag{4.16}$$

where the term on the right side is the prescribed total mass flux. In analogy for the temperature:

$$\left(\rho U \hat{H}\right)\Big|_{inlet} - \left(\lambda \nabla T\right)\Big|_{inlet} = \left(\rho U \hat{H}\right)_0 \tag{4.17}$$

*Outlet boundaries*

At the outlet boundaries the mass flux of the gas-phase species and the heat flux to be equal to zero:

$$\nabla \omega_k \big|_{outlet} = 0 \tag{4.18}$$

$$\nabla T \big|_{outlet} = 0 \tag{4.19}$$

# 4.4 Numerical methodology

After that the adopted mathematical model has been presented, it is necessary to address the numerical issues related to its solution and to develop a solver which can handle the computational structure defined.

The architecture of the solver is summarized in Figure 40.

The main difference from the previous structure consists in the decoupling of the chemical step from the PIMPLE loop. Indeed, in agreement with the physics of the system, when a reactant arrives on the catalyst, the convergence at the interface values is immediately achieved and, only at this moment, the reaction takes place. Therefore, the reaction step has to be taken into account only after reaching the convergence within the PIMPLE loop.

The introduction of multiple regions and particularly the modeling of a solid phase with its own properties and variable fields require an accurate characterization of the interface between the different regions. In this respect the communication among neighbor domains, identified by different characteristic times and distinctive lengths, is not a trivial task.

Initially, the geometric domain is discretized by the creation of the computational mesh, one for each region. Then temperature, pressure, velocity and species concentrations are initialized in the whole domains.

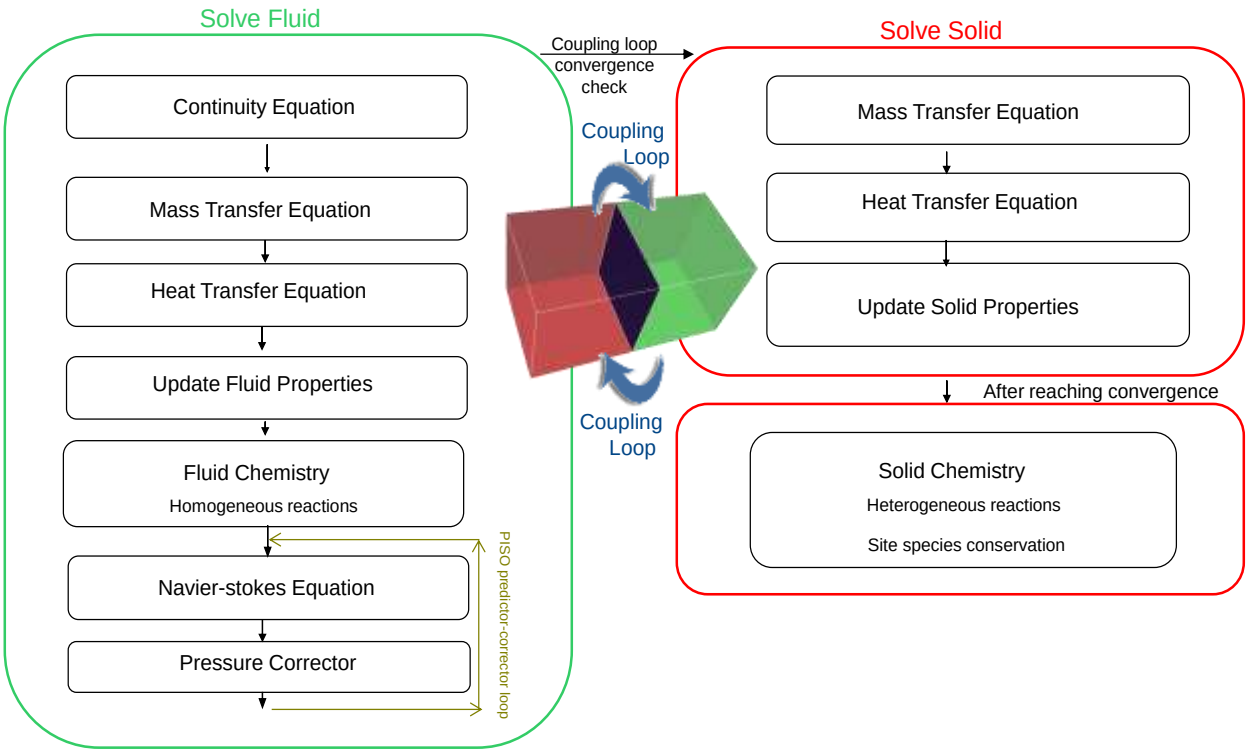


Figure 40: Schematization of CatalyticFOAM solution procedure in the fluid and solid phase

The iterative procedure begins with the solution of the characteristic equations for the fluid region. According to the operator splitting technique, described in Chapter 2, the reactive term has been separated by the transport term following the more stable order of equations: "*Transport-Reaction-Momentum*". It means that, first of all, the heat and mass transport equations of each species are solved imposing the boundary conditions of the fluid side, as shown in Eq.(4.14) and Eq.(4.15). Then the homogeneous reactions are solved. At this moment, the PISO loop starts: the Navier-Stokes and the continuity equations are solved and the velocity field is corrected explicitly.

Once updated the boundary conditions of the solid side, the solution of the equations in the solid region follows the same approach already used for the fluid domain. The mass and energy transport equations are solved and the side fluid interface values are updated. For this reason, an iterative procedure, named PIMPLE loop and widely described in the following paragraph, is necessary to guarantee the interface convergence.

Once the convergence criteria are satisfied, the ODE system of the heterogeneous reactions is solved. The whole procedure is iterated till the reaching of the end time.

### 4.4.1 PIMPLE loop structure

According to literature [39], there are two possible approaches to impose the interface boundary conditions shown in Eq. (4.14) and Eq. (4.15):

- **Monolithic**: this approach involves a single coupled system of equations on a single matrix taking into account both the phases involved. When dealing with multiple regions with different properties, this approach can work just for loose inter-equation coupling. Furthermore, the management of the constitutive equations, the storage of field variables and all post-processing operations would become harder with a single matrix approach, as well as parallel processing handling [40];
- **Partitioned**: this approach involves governing equations solved separately on each of the coupled regions, imposing appropriate boundary conditions on both ends. To make the coupling effective, the procedure must be iterated until convergence is reached. If this can be seen as a negative aspect in terms of computational time, the advantage of this approach is that it works on multiple meshes even for stiff inter-equation coupling.

Since the equation system describing the heterogeneous catalytic reactors shows stiff inter-equation coupling, the partitioned approach has been chosen to ensure numerical stability to the whole solver.

The physical conditions previously shown (Eq. (4.14) and Eq. (4.15)) have thus been converted into a single mathematical condition, according to what reported below (Eq. (4.20) and Eq. (4.21)). The implemented partitioned approach can be summarized as:

- Constitutive governing equations are solved in each zone with the appropriate boundary conditions. These conditions are called “Mixed” [41], as opposed to Dirichlet/Neumann BCs, which impose different conditions on different parts of the domain’s boundary [39].
- While solving for the neighboring region, the conditions are updated with the variables values in the freshly solved coupled cell, and this procedure is iterated until convergence is reached.

$$\begin{cases} \lambda_{eff,I} \left.\dfrac{\partial T_{SOLID}}{\partial x}\right|_{(I)} = \lambda_{fluid,I} \left.\dfrac{\partial T_{FLUID}}{\partial x}\right|_{(I)} \Rightarrow T_{I,OWN} = \dfrac{\dfrac{\lambda_{OWN} \cdot T_{OWN}}{\Delta_{OWN}} + \dfrac{\lambda_{NBR} \cdot T_{NBR}}{\Delta_{NBR}}}{\dfrac{\lambda_{OWN}}{\Delta_{OWN}} + \dfrac{\lambda_{NBR}}{\Delta_{NBR}}} \\ T_{SOLID,I} = T_{FLUID,I} \end{cases} \tag{4.20}$$

$$\begin{cases} \wp_{ieff,I} \left.\dfrac{\partial C_{i,SOLID}}{\partial x}\right|_{(I)} = \wp_{ifluid,I} \left.\dfrac{\partial C_{i,FLUID}}{\partial x}\right|_{(I)} \Rightarrow C_{I,OWN} = \dfrac{\dfrac{\wp_{i,OWN} \cdot C_{i,OWN}}{\Delta_{OWN}} + \dfrac{\wp_{i,NBR} \cdot C_{i,NBR}}{\Delta_{NBR}}}{\dfrac{\wp_{i,OWN}}{\Delta_{OWN}} + \dfrac{\wp_{i,NBR}}{\Delta_{NBR}}} \\ C_{iSOLID,I} = C_{iFLUID,I} \end{cases} \tag{4.21}$$

The iterative numerical methodology of the partitioned approach is summarized below:

1. Solving the fluid phase governing equations with the proper boundary conditions (called mixed conditions);
2. Solving the chemistry in the gas phase;
3. Updating of the interface boundary conditions (temperature and concentration) for the solid sides on the basis of the new fluid phase values:

$$\begin{cases} C^{j}_{I,solid} = \dfrac{\dfrac{\wp_{i,fluid} \cdot C^{j}_{i,fluid}}{\Delta_{fluid}} + \dfrac{\wp_{i,solid} \cdot C^{j-1}_{i,solid}}{\Delta_{solid}}}{\dfrac{\wp_{i,fluid}}{\Delta_{fluid}} + \dfrac{\wp_{i,solid}}{\Delta_{solid}}} \\ T^{j}_{I,solid} = \dfrac{\dfrac{\lambda_{fluid} \cdot T^{j}_{fluid}}{\Delta_{fluid}} + \dfrac{\lambda_{solid} \cdot T^{j-1}_{solid}}{\Delta_{solid}}}{\dfrac{\lambda_{fluid}}{\Delta_{fluid}} + \dfrac{\lambda_{solid}}{\Delta_{solid}}} \end{cases} \tag{4.22}$$

4. Solving the characteristic equations of mass/heat transfer on solid cells with the interface boundary conditions estimated at the step 3;
5. Updating of the interface boundary conditions for fluid sides on the basis of the new solid phase values estimated at point 4:

$$\begin{cases} C^{j}_{I,\,fluid} = \dfrac{\dfrac{\wp_{i,\,fluid}\cdot C^{j}_{i,\,fluid}}{\Delta_{fluid}} + \dfrac{\wp_{i,solid}\cdot C^{j}_{i,solid}}{\Delta_{solid}}}{\dfrac{\wp_{i,\,fluid}}{\Delta_{fluid}} + \dfrac{\wp_{i,solid}}{\Delta_{solid}}} \\ T^{j}_{I,\,fluid} = \dfrac{\dfrac{\lambda_{fluid}\cdot T^{j}_{fluid}}{\Delta_{fluid}} + \dfrac{\lambda_{solid}\cdot T^{j}_{solid}}{\Delta_{solid}}}{\dfrac{\lambda_{fluid}}{\Delta_{fluid}} + \dfrac{\lambda_{solid}}{\Delta_{solid}}} \end{cases} \tag{4.23}$$

6. Checking for convergence: residuals of mass fractions/temperature interface values have to be lower than user defined absolute and relative tolerances:

$$\left|T_{fluid,I} - T_{solid,I}\right| \le absTol_{T} \qquad \left|\frac{T_{fluid,I} - T_{solid,I}}{T_{fluid,I}}\right| \le relTol_{T} \tag{4.24}$$

$$\left|\omega_{i\,fluid,I} - \omega_{i\,solid,I}\right| \le absTol_{\omega_i} \qquad \left|\frac{\omega_{i\,fluid,I} - \omega_{i\,solid,I}}{\omega_{i\,fluid,I}}\right| \le relTol_{\omega_i} \tag{4.25}$$

7. If the convergence is not reached, the procedure restarts from point 1. The solver employs the interface value calculated at the step 5 to solve the transport equation for the fluid region starting from the initial temperature and mass fractions evaluated at the previous time step.
8. If the convergence criteria are satisfied in a user defined maximum number of iterations the solver computes the chemistry inside the solid phase, otherwise a convergence failure is registered. This can occur if the convergence criteria imposed are too severe, if the system modeled is too numerically unstable or the discretization time is too coarse for the system itself.
9. Moving to the next time step

In this way the interface values of each domain are updated at each iteration, but the number of transport loop remains the same. This issue is crucial in order to ensure the correct implementation of the operator splitting technique and minimize the local error between the coupling and the uncoupling procedure.

The final structure of the PIMPLE loop has been shown in the Figure 41

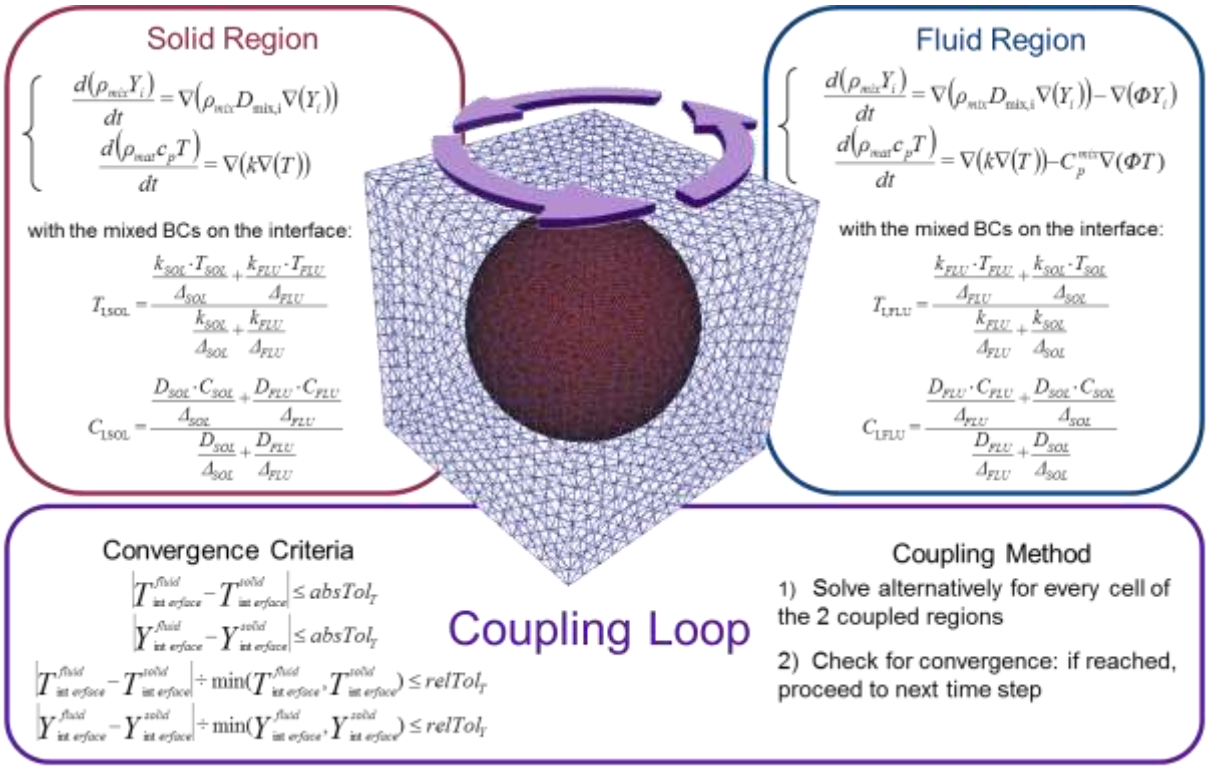


Figure 41: PIMPLE loop structure

# 4.5 Domain description

An accurate modeling of the catalytic system has to take into account the competition between the transport phenomena and the chemical kinetics in order to identify the rate determining step of the whole process. This issue is important not only for the optimization of the catalyst design, but also for the minimization of the total cost of the process.

The domain of the whole catalyst system is split into two different regions:

- Fluid region, containing only the gas phase (i.e. only the gas phase reaction can occur);
- Solid region, which has been considered as a porous pseudo-homogeneous phase (only heterogeneous reaction occur inside it). Due to the high third body concentration and the low gaseous volumes inside the solid pores, the homogenous reactions are heavily inhibited.

Due to the complexity of catalysts morphology, the solid phase is characterized by isotropic and constant properties in the whole catalytic volume.

The catalytic bed is characterized by the following parameters:

- the void fraction ε: it is the volume of voids over the total volume of the cell. This parameter allows to take into account the gaseous phase inside the pores;
- the effective catalytic surface per unit of volume of catalyst : it can be often found in the literature as a characteristic parameter of a catalytic geometry.

  When this parameter is not known, it is still possible to estimate it if other physical properties of the catalyst are available. For example, in the case of supported catalysts, it is possible to compute it as:

$$a_{cat} = \frac{W_{cat} \cdot \xi \cdot \delta}{MW \cdot \Gamma_{site} \cdot V} \tag{4.26}$$

  where:

  - ✓ $\xi$ is the fraction of the active phase over the total catalyst mass $\left[ kg_{active} / kg_{cat} \right]$;
  - ✓ $\delta$ is the fraction of active sites available over the total active sites $\left[ kmol_{availableActive} / kmol_{TotActive} \right]$;
  - ✓ $\Gamma_{sites}$ is the density of sites per unit area $\left[ kmol_{availableSites} / m^2 \right]$;
  - ✓ $W_{cat}$ is catalyst loading $\left[ kg \right]$ ;
  - ✓ is the volume of catalyst $\left[ m^3 \right]$;
  - ✓ is the molar weight of active phase $\left[ kmol_{Active} / kg_{Active} \right]$.

As already mentioned, the solid phase is characterized by effective properties of diffusivity and thermal conductivity that are taken into account for transport limitations in the catalytic phase and incomplete use of the catalyst volume. Different models can be used to estimate the effective diffusivity:

- Parallel pore model developed by Wheller [42].

  In this model the porous material is considered to be a bundle of capillaries through which species diffuse. The volume available for diffusion is the pore volume. An additional factor is introduced to account the fact that the pores are not straight, but rather follow a tortuous path. The effective diffusivity is given by the following equation:

$$\wp_{A,e} = \frac{\varepsilon_P}{\tau} \cdot \frac{\wp_{A,M} \cdot \wp_{A,K}}{\wp_{A,M} + \wp_{A,K}} \tag{4.27}$$

where:

- ✓ $\wp_M$ is the molecular diffusivity [$m^2/s$];
- ✓ $\wp_K$ is the Knudsen diffusivity [$m^2/s$];
- ✓ $\varepsilon$ is the void fraction of the catalyst [-];
- ✓ $\tau$ is the tortuosity factor [-].

Because of the difficulty in obtaining experimental measurement of tortuosity, this data has been considered as an adaptive parameter. The parallel pore model works better for catalyst with a unimodal pore size distribution that has a narrow range of pore diameters.

- Random pore model developed by Wakao-Smith [43].

  This model is able to take into account micro-morphology features such as pore sizes, pore orientation, interconnections and dead ends. Wakao and Smith proposed this model for predicting diffusivity at constant pressure in bidisperse porous media. This represents the diffusion flux as being the sum of that through macropores and micropores. The model gives the effective diffusivity for isobaric diffusion with the following equation:

$$\wp_{effective} = \varepsilon_M{}^2 \cdot \wp_M + \frac{\varepsilon_\mu{}^2 \cdot (1 + 3 \cdot \varepsilon_M)}{1 - \varepsilon_M} \cdot \wp_\mu \tag{4.28}$$

  where:

- ✓ $\varepsilon_M$ is the porosity of the macropores;
- ✓ $\varepsilon_\mu$ is the porosity of the micropores.

The Random pore model diffusivity prediction is generally higher than those evaluated experimentally. Hayes et al. [44] reported a diffusivity evaluated with RPM eight times higher than the experimental value. For these reasons catalyticFOAM multiRegion uses the parallel pore model to evaluate the effective diffusivity inside the solid domain.

### 4.5.1 Generation of a conformal mesh with the OpenFOAM® utilities

The structure of the solver has been optimized in order to exploit the OpenFOAM® framework. The introduction of multiple regions requires an accurate description of both the domains, solid and fluid, mainly in nearness of the interface. The interface boundary conditions, imposed to solve the problem, require that the numbers of cells at the interface have to be equal for each region. In this manner the solver is able to interact with both the domains and it allows a correct coupling between them. An example of conformal mesh is shown in Figure 42.

In order to reproduce this type of geometries, the mesh generation utility, *blockMesh*, supplied with OpenFOAM®, has been used. The mesh is generated from a dictionary file named *blockMeshDict* located in the *constant/polyMesh* directory of the case.

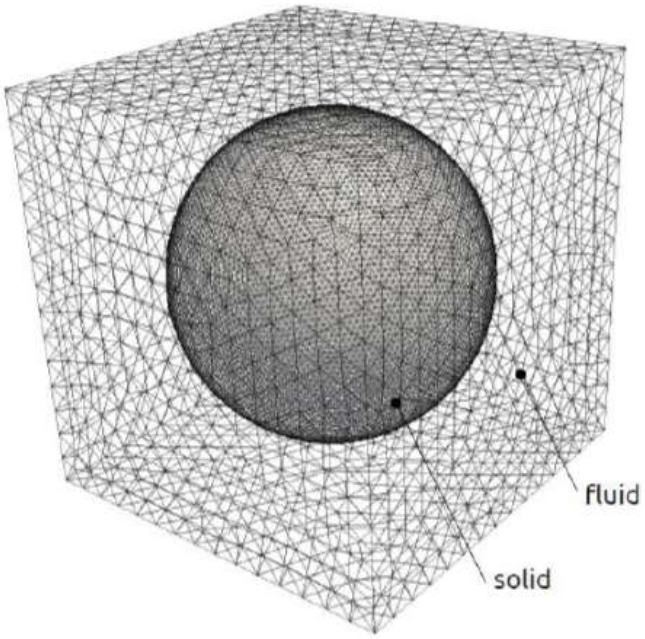


Figure 42: Mesh separation for multiphase representation

*blockMesh* reads this dictionary, generates the mesh and writes out the mesh data in *points*, *faces*, *cells* and *boundary* files in the same directory. The principle behind *blockMesh* is to decompose each domain geometry into a set of one or more 3D, hexahedral blocks. Edges of the blocks can be straight lines, arcs or splines. Each block of the geometry is defined by 8 vertices, one at each corner of a hexahedron, sorted according to the right-hand rule. An example of *blockMeshDict* is shown in Figure 43.

In order to split a mesh into multiple regions a command already implemented in the OpenFOAM® environment can be used:

```
splitMeshRegions -cellZones -overwrite
```

This function automatically creates inside each of the OpenFOAM® case folders (*0, constant* and *system*) a number of sub-folders equal to the number of regions considered, each called with the name assigned during the mesh generation.

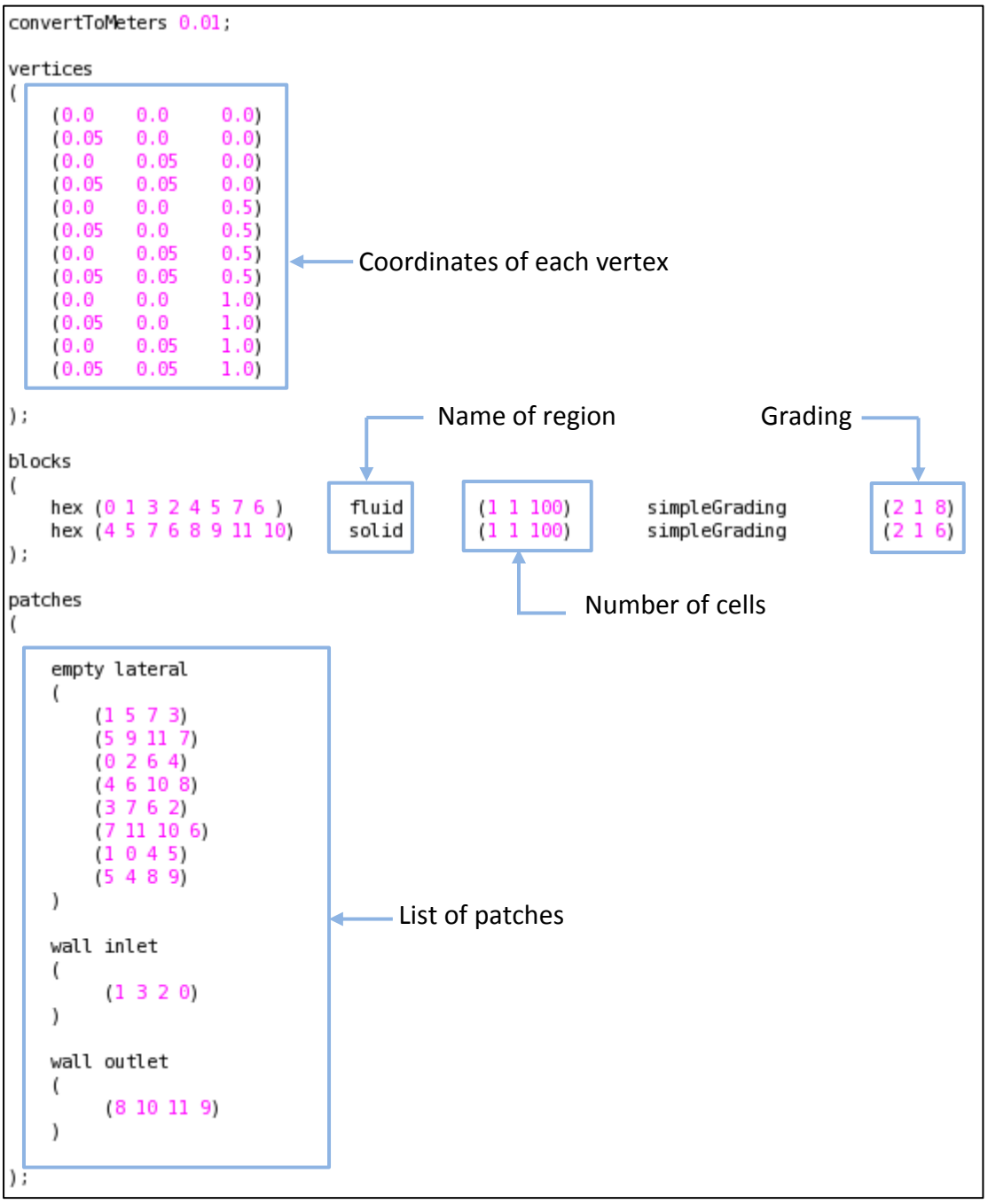


Figure 43: example of the blockMeshDict for a multi-region mesh

### 4.5.2 The Diffusion Number

The critical issue in the simulations of multi-region solver is the choice of the integration time step of the transport equation. It has to be sufficiently small in order to characterize the faster phenomena and to ensure numerical stability to the procedure. On the other hand, it cannot be too much small because the computational effort would be unreasonable. To guarantee the correct trade-off between these two features a new dimensionless number, the Diffusion Number, has been identified:

$$Di = \frac{\delta t \cdot \wp_{i,eff}}{\delta x^2} \tag{4.29}$$

where $\delta t$ is the time step, $\wp_{i,eff}$ is effective diffusivity in the solid region of the ith species and $\delta x$ is the smaller cell size in the solid domain.

Each component has a different value of effective diffusivity and it is necessary to ensure the condition $Di$<1 in each cells of the domain. Therefore it is chosen based on the worst case: the maximum corresponding to the combined effect of highest effective diffusivity and smallest cell size.

Within the OpenFOAM® framework it is possible to choose the time step for the integration of the transport equation for the fluid region through a different dimensionless number, the Courant Number that is defined as:

$$Co = \frac{|U| \cdot \delta t}{\delta x} \tag{4.30}$$

where $\delta t$ is the time step, $|U|$ is the magnitude of the velocity through the cell and $\delta x$ is the cell size in the direction of the velocity.

In agreement with the Eq.(4.29) and Eq.(4.30), it is possible to identify two different values of the time step respectively for the solid region and for the fluid one, as explained in Eq. (4.31):

$$\begin{cases} \delta t_{FLUID} = \dfrac{Co \cdot \delta x}{|U|} \\ \delta t_{SOLID} = \dfrac{Di \cdot \delta x^2}{\wp_{i,eff}} \end{cases} \tag{4.31}$$

On the basis of these two relations, the solver is able to select the minimum value of the integration time step ensuring temporal accuracy and numerical stability.

To demonstrate the effect of the Diffusion Number, the combustion of hydrogen in a simple solid slab has been simulated imposing different value of Di. The computational domain is shown in Figure 44.

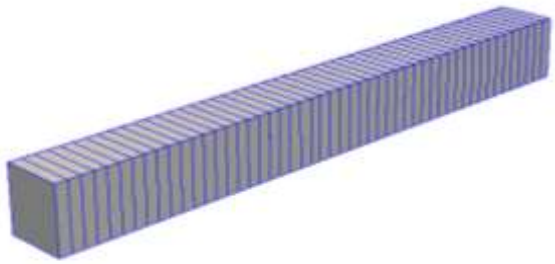

Figure 44: Computational domain of a solid slab

The problem has been investigated in a 1D mesh solving only the mass transfer equation and the reactive step just for the solid region. The slab is 1 cm long. The profile of hydrogen inside the solid phase has been calculated setting a fixed value of the $H_2$ mass fraction on the wall.

The characterization of the hydrogen profile within the solid domain is a critical issue because it is the specie with the highest effective diffusivity inside the kinetic scheme.

In Figure 45 and Figure 46 the results of the simulations have been presented. The Diffusion Number has been modified acting respectively on:

- ✓ Integration time step at constant dimension cell (Figure *45*);
- ✓ Dimension of cell at constant integration time step (Figure 46).

Figure *45* shows the effect of the integration time step on the concentration profile of $H_2$ inside the solid domain. The cell number of the mesh are 50 and the Di has been changed in a wide range (from 0.5 to 50) in order to work with different value of integration time step (from $3.4 \cdot 10^{-8}$ to $3.4 \cdot 10^{-6}$ s).

As it is possible to see in Figure 45, at higher value of Di the hydrogen shows an unfeasible profile. This effect depends on the integration time step that is higher than the characteristic diffusion time of hydrogen inside the domain. Decreasing the Di the profile shows a more and more feasible trends and only when Di is about one ($\leq$ 1) the solution is independent by the integration time step.

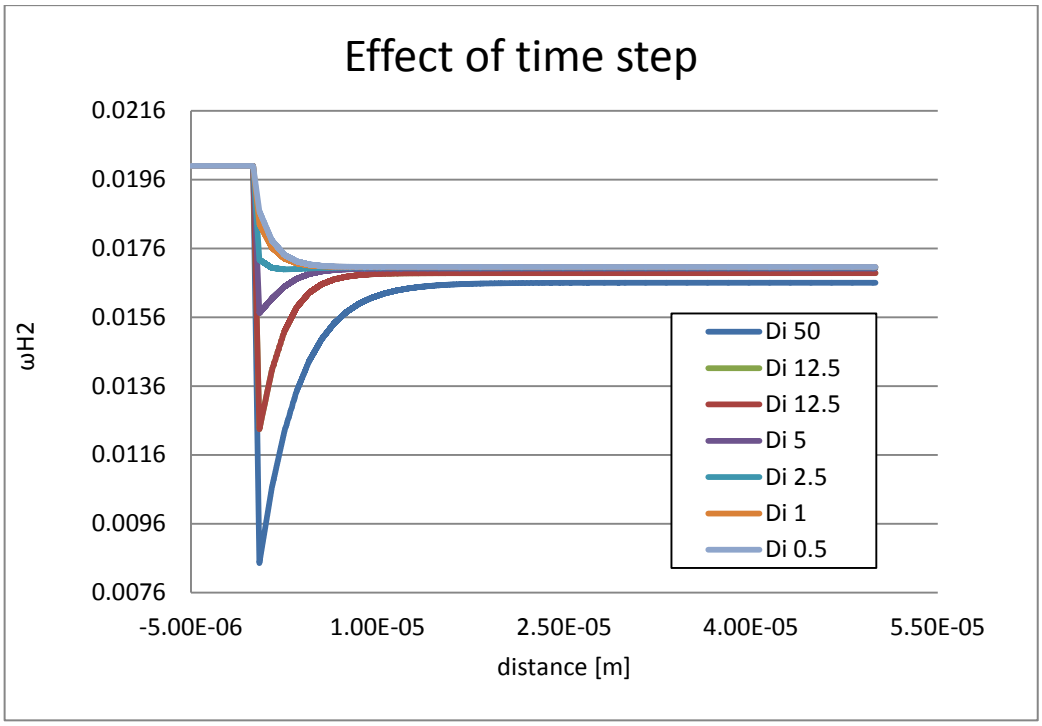


Figure 45: Time step effect on axial concentration profile

The second issue tested has been the influence of the minimum cell size on the $H_2$ profile. In particular two computational grids, made by 50 and 250 cells, have been studied.

With a constant length of the slab, increasing the number of cells, the dimension of the cell itself progressively decreases. Hence, working with a fixed time step, the Diffusion number increases as shown in Eq. (4.29)

The operative conditions are summarized in Table 15.

| **OPERATIVE CONDITIONS** | |
|---|---|
| number of cells | Di |
| 50 | 0.5 |
| 250 | 12.5 |
| integration time step | 3.38E-8 s |

Table 15: Operative conditions

As shown in Figure 46 the profiles inside the solid region are exactly overlapping. This means that it is possible to relax the Di condition without losing accuracy, but this involves an almost linear increase of the computational effort.

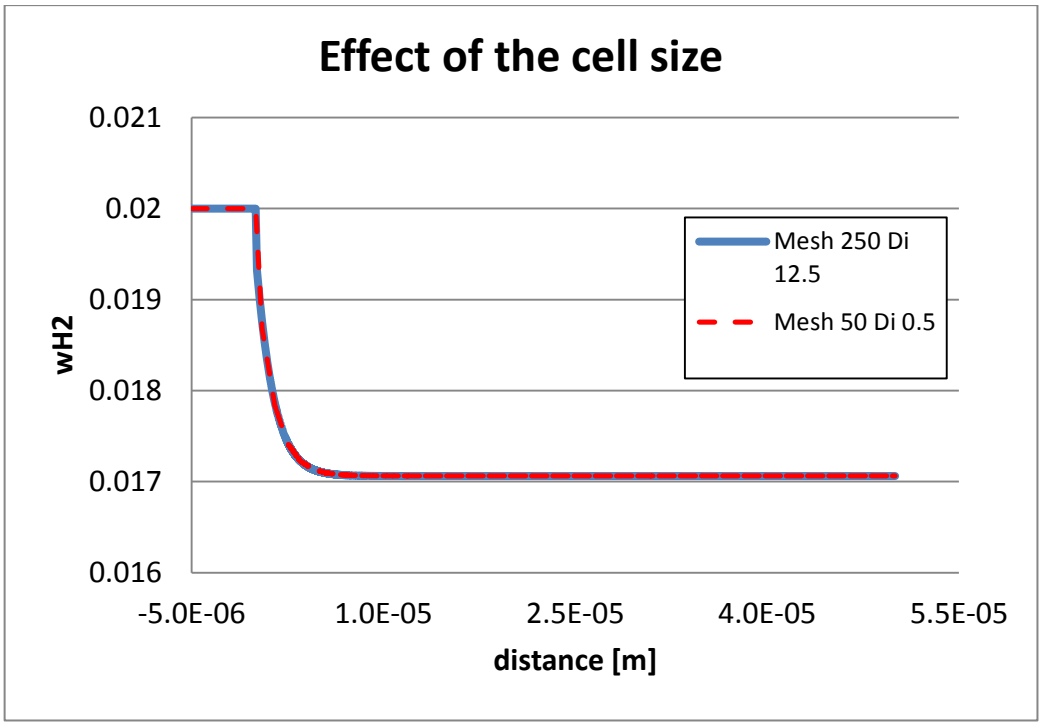


Figure 46: Cell size effect on axial concentration profile

## 4.6 Validation of the computational tool

The aim of this section is the validation of the coupling methodology used in the multiRegion solver. The segregated numerical approach has been tested by performing simple numerical tests of increasing complexity.

### 4.6.1 Conjugate Mass Transfer in a reacting environmental

The numerical prediction of catalyticFOAM multiRegion solver has been compared with the analytic solutions of a diffusion-reaction problem in two parallel slabs in isothermal condition, with fixed reactant concentration at the domain boundaries and first order heterogeneous reaction $A \rightarrow B$ inside the domain. **Error! Reference source not found.** shows the computational omain:

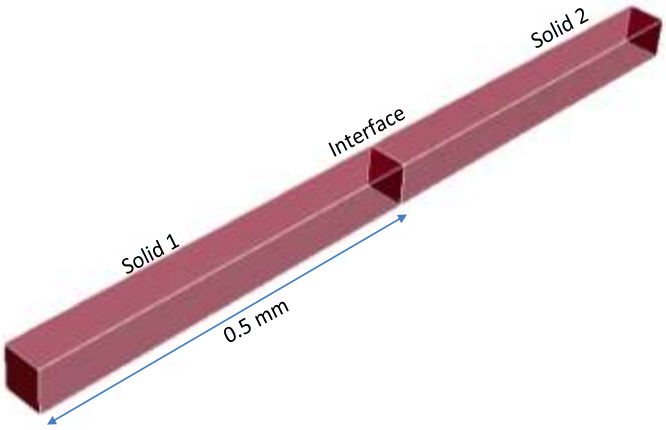


Figure 47: Computational domain of the two parallel slabs

The mathematical model that describes the system is summarized in the Eq. (4.32).

$$\begin{cases} \rho \dfrac{\partial \omega_{A,1}}{\partial t} = \rho \cdot \wp_{eff,1} \dfrac{\partial^2 \omega_{A,1}}{\partial x^2} + R_{het} a_{cat} \\ \rho \dfrac{\partial \omega_{A,2}}{\partial t} = \rho \cdot \wp_{eff,2} \dfrac{\partial^2 C_A}{\partial x^2} + R_{het} a_{cat} \end{cases} \tag{4.32}$$

where $\wp_{eff,1}$, $\wp_{eff,2}$ and $\omega_{A,1}$, $\omega_{A,2}$ [-] are the effective diffusivity and the mass fraction on the specie A respectively inside the Solid 1 and Solid 2, $\rho$ is the density of the mixture inside the pore of both solids, $R_{het}$ is the velocity of the heterogeneous reaction and $a_{cat}$ is effective catalytic surface per unit of volume of catalyst

The boundary conditions are shown in the Eq (4.33).

$$\begin{cases} \omega_{A,1}(0,t) = 0.05 \\ \omega_{A,2}(L,t) = 0.05 \\ \omega_{A,1}(I,t) = \omega_{A,2}(I,t) \\ \wp_{eff,1} \left. \dfrac{\partial \omega_{A,1}}{\partial x} \right|_I = \wp_{eff,2} \left. \dfrac{\partial \omega_{A,2}}{\partial x} \right|_I \end{cases} \tag{4.33}$$

where $I$ is the axial coordinate of the interface between the two solids as highlighted in **Error! eference source not found.**. From Eq. (4.33) it is possible to obtain an analytical solution, as shown in the Eq. (4.34)

$$\omega_A = \omega_A^s \frac{\cosh\left(\sqrt{\left(\frac{k}{\wp_{eff}}\right)}x\right)}{\cosh\left(\sqrt{\left(\frac{k}{\wp_{eff}}\right)}L\right)} \tag{4.34}$$

The numerical results of multiRegion solver have been compared with the analytical solutions in different conditions of:

- ✓ Kinetic rate (Figure 48);
- ✓ Effective diffusivity in two slabs (Figure 49).

Figure 48 shows an excellent agreement with the analytical solution in all the conditions investigated. This means that the coupling procedure between the solid regions is able to describe the physic of the system.

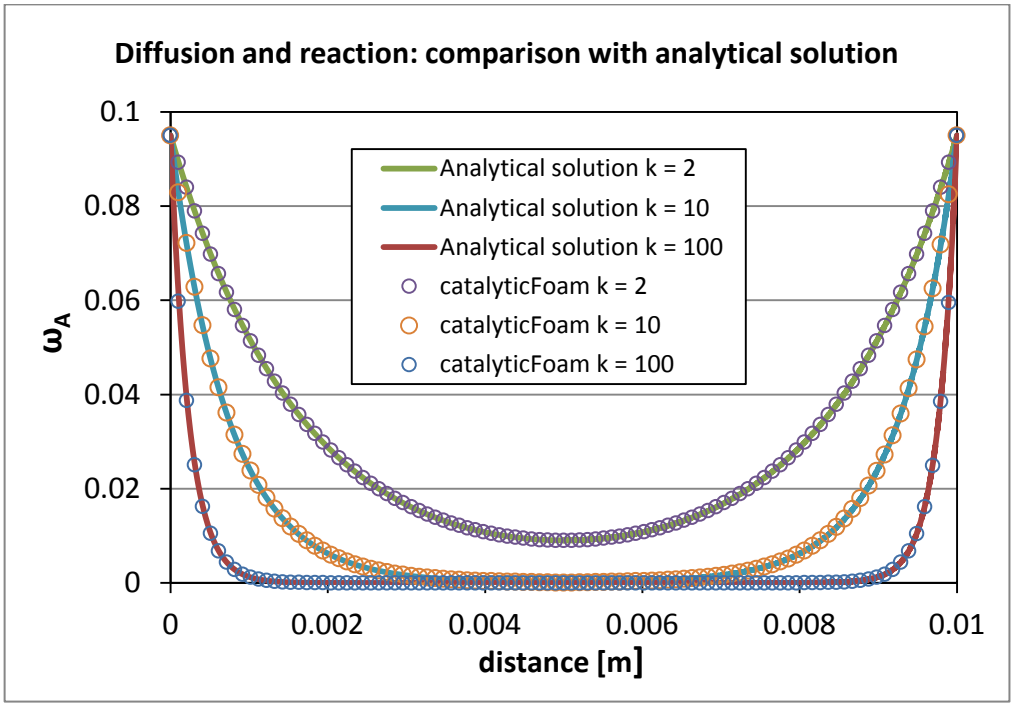


Figure 48: Effect of the kinetic rate on the concentration profile inside the solids at equal effective diffusivity in the two solids

Figure 49 shows the comparison between the numerical solution and the analytic one for different diffusivity in the two slabs. In this case the profile has a discontinuity at the interface that it is correctly reproduced by catalyticFOAM multiRegion.

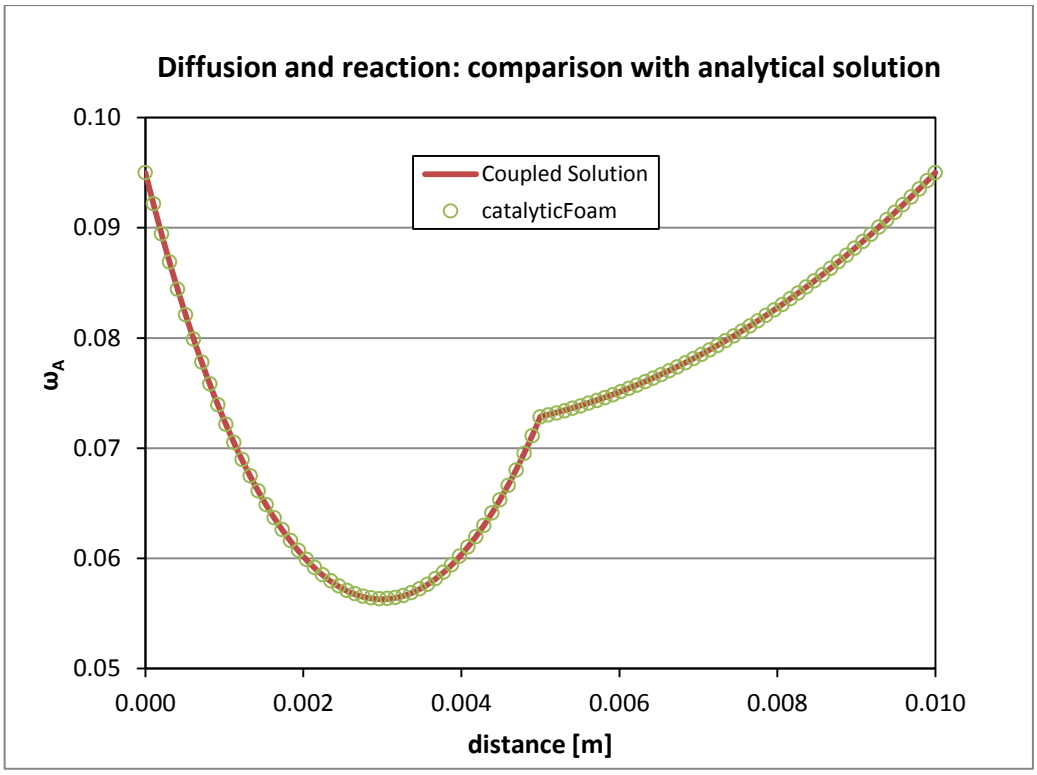


Figure 49: Effect of the different effective diffusivity in the two solids on the concentration profile

## 4.6.2 Diffusion-reaction in a channel with sphere

The mesh of a second representative case is shown in Figure 50. It is a cylindrical channel in which the reactants move at the inlet velocity equal to 0.1 m/s. Inside the channel there is a solid sphere of catalytic material that allows reactants to adsorb and react. To save CPU time the symmetry of the mesh has been exploited, in fact only 1/8 of the whole structure has been simulated.

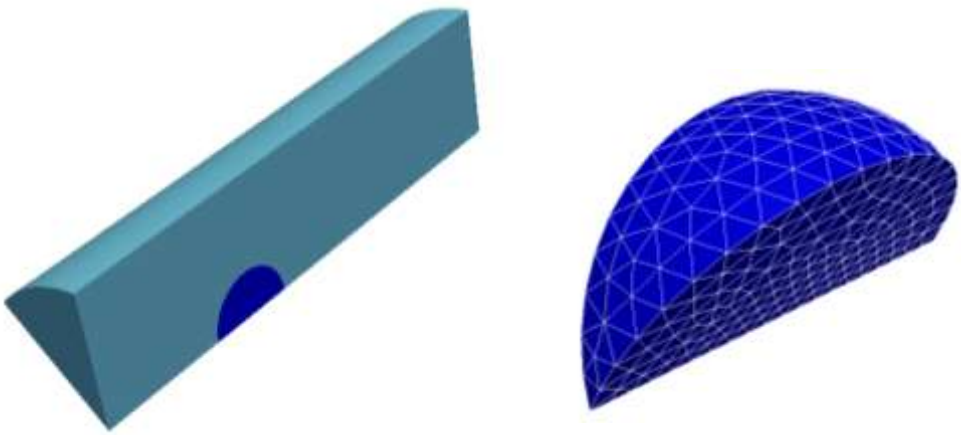

Figure 50: Computational grid of a channel with sphere

The reaction investigated is the oxidation of ethylene on silver catalyst supported on $\alpha$-$Al_2O_3$. The simulations have been carried out using a kinetic scheme provided in literature [45] and described in Chapter 5. The diffusive coefficients in the fluid phase are calculated according to the composition, temperature and pressure of the mixture, while the effective diffusivity in the solid phase is computed with the parallel pore model analyzed in section 4.5.

A correct physical description of the system should include:

- Null velocity field on the walls (both of the channel and of the sphere);
- Poiseuille velocity profile in laminar flow, with maximum value along the symmetry axis once the profile is fully developed;
- Velocity increase across the sphere due to the section restriction;
- Velocity reduction in the zone immediately behind the obstacle.

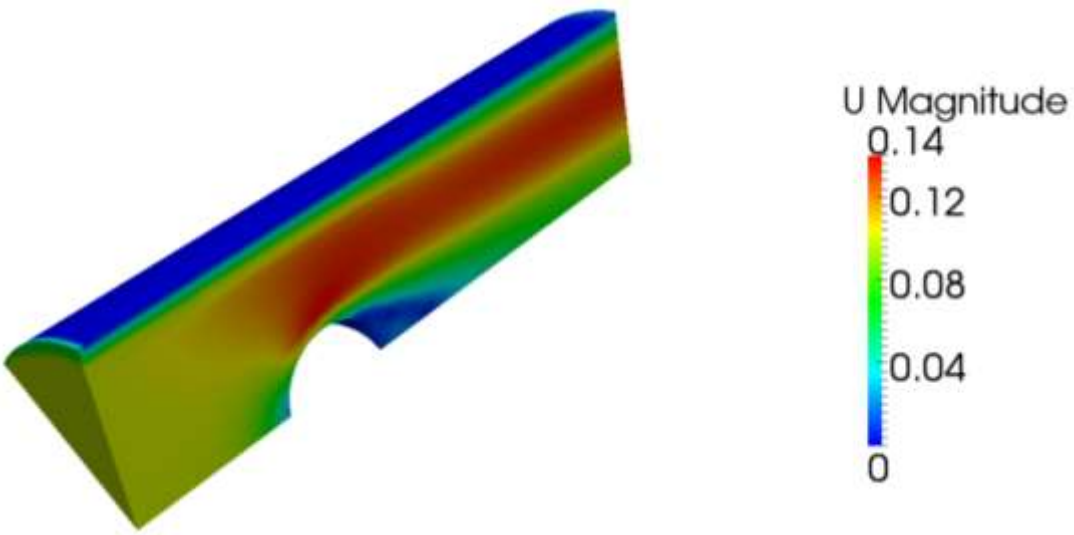


Figure 51: Velocity profiles in the computational domain

As it is possible to see in Figure 51 , the velocity profiles correctly describe the system as mentioned above.

The main aim of this section is to study the profile of reactants and product inside the catalytic sphere in order to understand the governing regime. In the following the results of the simulation have been reported.

**$O_2$ solid profile**

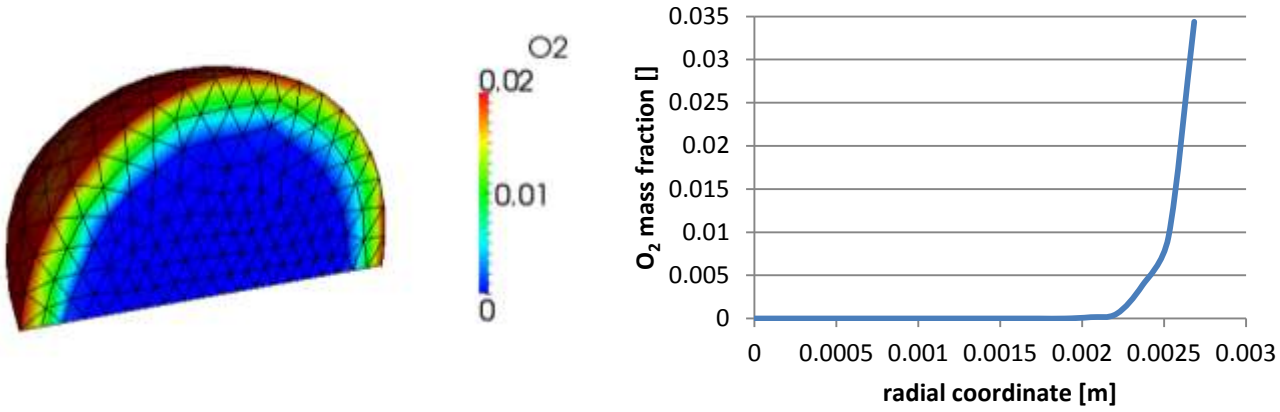


**$C_2H_4$ solid profile**

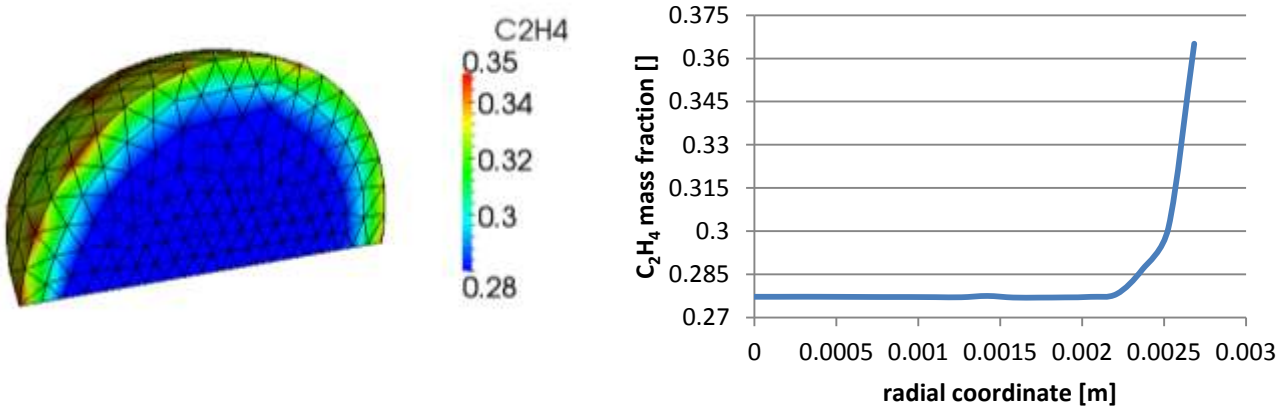


**$C_2H_4O$ solid profile**

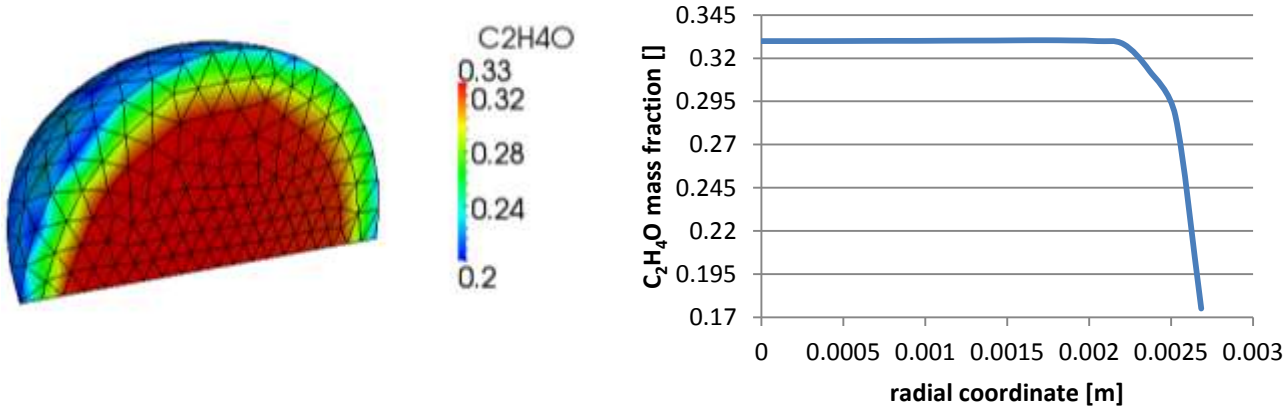


Figure 52: Profile of reactants and products within the solid domain

As shown in Figure 52 the solid is affect by strong normal gradient that reduce the efficiency of the catalyst. The reaction takes place only in a small layer of the catalyst, close to the surface of the sphere. The volume interested by the reaction is about the 70% of the whole volume.

In this test the potential of catalyticFOAM multiRegion is emphasized. Without imposing any impermeability condition inside the domain, the solver is able to take into account the diffusive limitations in order to highlight incomplete usage of catalyst. These issues are very important from an industrial point of view because in this way it is possible to understand if the investigated catalyst needs an "egg shell" structure or not in order to reduce the purchasing costs.

## 4.7 Show case: fuel rich combustion of $H_2$ on Rh

In order to validate the reliability of the tool, it is now necessary to test its predictive ability. In this section the $H_2$ combustion on Rh in an annular isothermal reactor is presented and discussed. The results of the simulation have been compared with the experimental data provided in literature [46]. This case is an ideal bench test for catalyticFOAM multiRegion because it is possible to evaluate how the onset of three different regimes (chemical, pore diffusion and mass-transfer regime) can affect the reactivity of the system. The simulation has been carried out exploiting detailed microkinetic model of $H_2$ combustion. This kinetic scheme consists of 18 reactions and 5 adsorbed species, and it is reported in Appendix B. A sketch of the catalytic reactor is given in Figure 53.

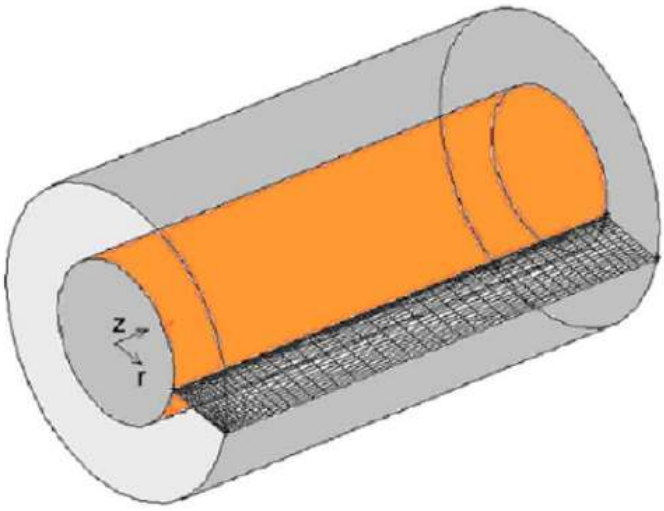


Figure 53: Sketch of the annular catalytic reactor, adapted in the simulation

The $Rh/\alpha\text{-}Al_2O_3$ catalyst is deposited over the surface of the inner wall of the reactor (colored in orange), forming a uniform and well adherent catalytic layer (1.5 cm long, 50 µm thick).
The operating conditions and the geometric parameters of the reactor are reported in Table 16.

| **OPERATING CONDITIONS** | |
|---|---|
| $H_2$ Mole Fraction | 0.01 |
| $O_2$ Mole Fraction | 0.04 |
| $N_2$ Mole Fraction | 0.95 |
| **REACTOR GEOMETRY** | |
| Inner radius | 0.235 cm |
| Outer radius | 0.450 cm |
| Reactor length | 1.5 cm |
| $a_{cat}$ | 31,672 $m^2_{cat}/m^3_{cat}$ |

Table 16: Simulation parameters

### 4.7.1 Computational grid

The spatial discretization of the geometrical domain was simplified to reduce the computational effort. Specifically, exploiting the symmetry of the annular reactor, it is possible to consider only one slice of this reactor. This is very convenient because this allows one to consider a 2D mesh instead of a 3D one. The 2D mesh is obtained considering the slice of a cylinder with a width of 5°. The number of required cells is thus 72 times lower than the one required for a 3D grid. A schematic view of the overall mesh is presented in Figure 54.
The grid is refined with a specific grading, i.e. the length of each cell of the mesh is not constant. The expansion ratio of the cells is calculated as the ratio among the length of the first and the last cell along one edge of a block. This enables the mesh to be graded, or refined, in specified directions for a specific factor. The introduction of a non-constant step grid allows one to describe certain areas of the system in a more detailed way. In the case considered, this is particularly important because the zone close to the catalyst is interested by strong normal gradients, both from the fluid and from the solid side. The mesh is thus highly refined near the catalytic wall in the radial direction. Furthermore, particular attention has to be given to the cells dimensions at the

coupled interface; their size in the radial direction must not differ much from one side to the other. In this way it is possible to ensure numerically stability of coupling partitioned scheme without the need of many PIMPLE loop iterations.

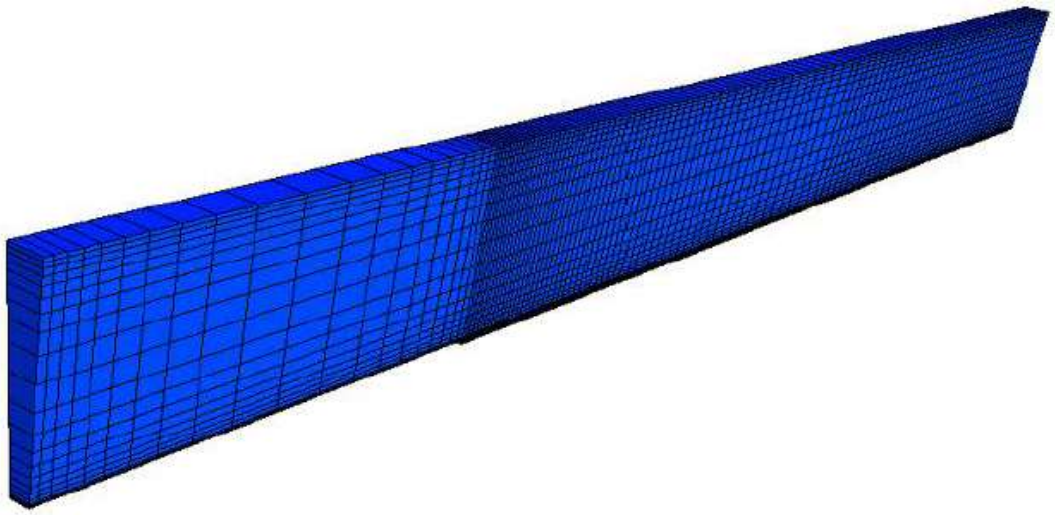

Figure 54: 2D mesh used for the numerical simulation

### 4.7.2 Comparison with the previous solver

The solver developed in the previous work [1], as mentioned in the paragraph 4.2, was not able to correctly simulate the transient in the resolution of diffusion and reaction problems.
This criticality has been demonstrated with two simulations of hydrogen combustion considering the annular reactor that has already presented in the section 4.7 (Figure 55 and Figure 56) in which the behavior of the two coupling structure of the PIMPLE loop has been compared.

As Figure 55 shows, the convergence at the interface between two domains is not reached both for species and temperature profiles even if a high number of PIMPLE loop iterations have been considered.

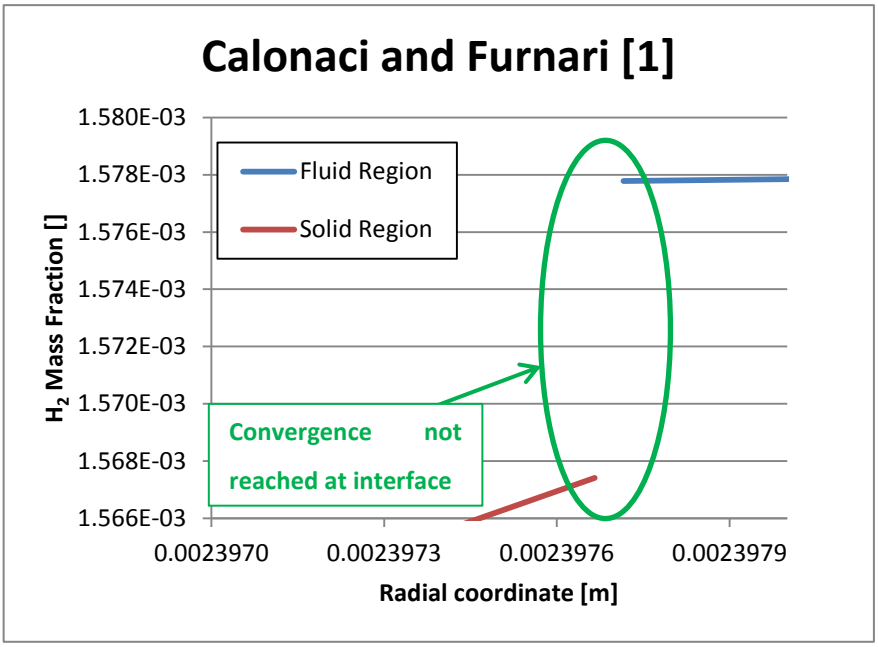


Figure 55: Convergence at the interface - Calonaci and Furnari [1]

Figure 56, instead, shows that with the new structure of the PIMPLE loop the convergence is correctly achieved. This is a really important issue because the transient strongly influences the steady state solutions differently from the assumption of Calonaci and Furnari [1].

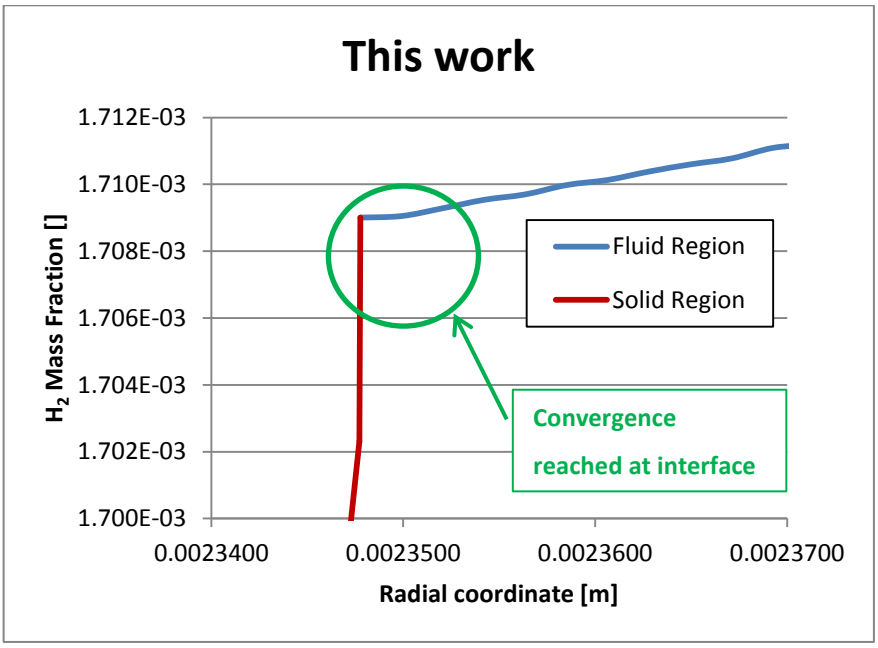


Figure 56: Convergence at the interface - this work

In Figure 57, the number of PIMPLE loop iterations necessary to achieve the convergence at interphase has been shown. As already said the previous solver is not able to ensure this aim and,

after some millisecond of simulations, it reaches the maximum number of PIMPLE loop iterations set by the user.

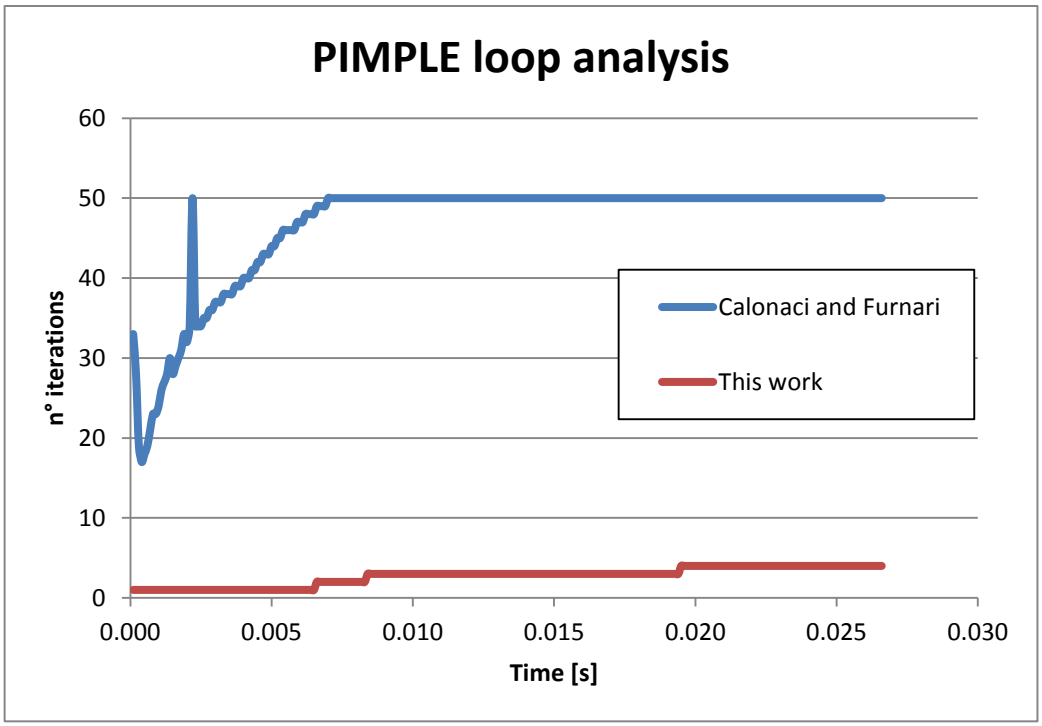


Figure 57: Comparison of the two solvers in the PIMPLE loop

The new coupling procedure is more stable than the previous one because not only it is able to achieve the convergence, but it ensures this condition with a low number of PIMPLE loop iterations.

The right characterization of the interface phenomena is an essential step forward in the modeling of the system. In this way it is possible to ensure not only the stability of the procedure of coupling but also the reproducibility of results.

### 4.7.3 Parallelization of the CatalyticFOAM multiRegion

As explained in section 4.5, the need to work with a detailed mesh to correct modeling not only the fluid region, but also the solid region, leads to severe demands on computational resources. In order to save CPU time, the parallelization of the code has been carried out.

The method of parallel computing used by OpenFOAM® is known as domain decomposition, in which the geometry and the associated fields are broken into pieces and allocated to separate processors for solution. The process of parallel computation involves:

- ✓ decomposition of mesh and fields;
- ✓ running the application in parallel;
- ✓ post-processing of the decomposed case.

The parallel running uses the public domain *openMPI* implementation of the standard message passing interface (MPI).

The mesh and fields are decomposed using the *decomposePar* utility. The underlying aim is to break up the domain with minimal effort but in such a way to guarantee a fairly economic solution. The geometry and fields are broken up according to a set of parameters specified in a dictionary named *decomposeParDict,* that must be located in the *system* directory of the case of interest.

The user has a choice of four methods of decomposition, specified by the method keyword as described below.

- ✓ Simple: simple geometric decomposition in which the domain is split into pieces by direction, *e.g.* 2 pieces in the $x$-direction, 1 $y$ in etc.
- ✓ Hierarchical. Hierarchical geometric decomposition which is the same as simple except the user specifies the order in which the directional split is done, *e.g.* first in the $y$-direction, then the $x$-direction, etc.
- ✓ Scotch: scotch decomposition which requires no geometric input from the user and attempts to minimize the number of processor boundaries. The user can specify a weighting for the decomposition between processors, through an optional *processorWeights* keyword which can be useful on machines with differing performance between processors.
- ✓ Manual: manual decomposition, where the user directly specifies the allocation of each cell to a particular processor.

The *decomposePar* utility is executed by typing

```
decomposePar –region <name of the region>
```

On completion, a set of subdirectories will have been created, one for each processor, in the case directory. The directories are named *processor N* (where N = 0,1,2…) represents a processor number and contains a time directory, containing the decomposed solid and fluid field descriptions, and a *constant/polyMesh* directory containing the decomposed mesh description for both the regions.

The simulation then runs in parallel on the separate sub-domains, and the communication between the processors occurs through the MPI protocol. The discretized governing equations are solved in each sub-mesh with the appropriate boundary conditions (inner iteration). Once all sub-meshes have been calculated, information on the interpolation boundaries is transferred between the different sub-meshes in an explicit manner (outer iteration). This strategy allows to solve several sub-meshes simultaneously using different processors. The processors communicate once per outer iteration. Thus, in general the communication work is notably lower than the calculation work.

A satisfactory computational efficiency can be achieved only if the mesh is correctly decomposed, i.e. if the computational costs of the different sub-meshes are comparable.

In general, for homogeneous architectures, i.e. identical processors (as used for all the parallel computations performed with catalyticFOAM), an effective load balancing can be achieved by assigning to each processor a similar number of cells.

The architecture of the solver proposed in the section 4.4 is not able to run catalyticFOAM multiRegion in parallel due to a problem of synchronization of processors during the PIMPLE loop. Indeed, when in a generic processor the number of iterations needed to ensure the convergence at the interphase becomes greater than 1 the solver fails. In order to overcome this problem, the structure of the PIMPLE loop has been modified. In particular, the convergence is ensured setting a fixed number of iterations. The same procedure is adopted in the solver *chtMultiRegionFOAM,* already implemented in the OpenFOAM® framework. This structure has been introduced to simplify the problem but in future the solver will be generalized removing this assumption introducing the same structure of the PIMPLE loop of the serial version.

It is interesting to understand how a wrong choice of the number of iterations can affect the reproducibly of the results. This issue has been tested for the combustion of hydrogen in the annular reactor presented in the section 4.7 and the results are shown in the Figure 58.

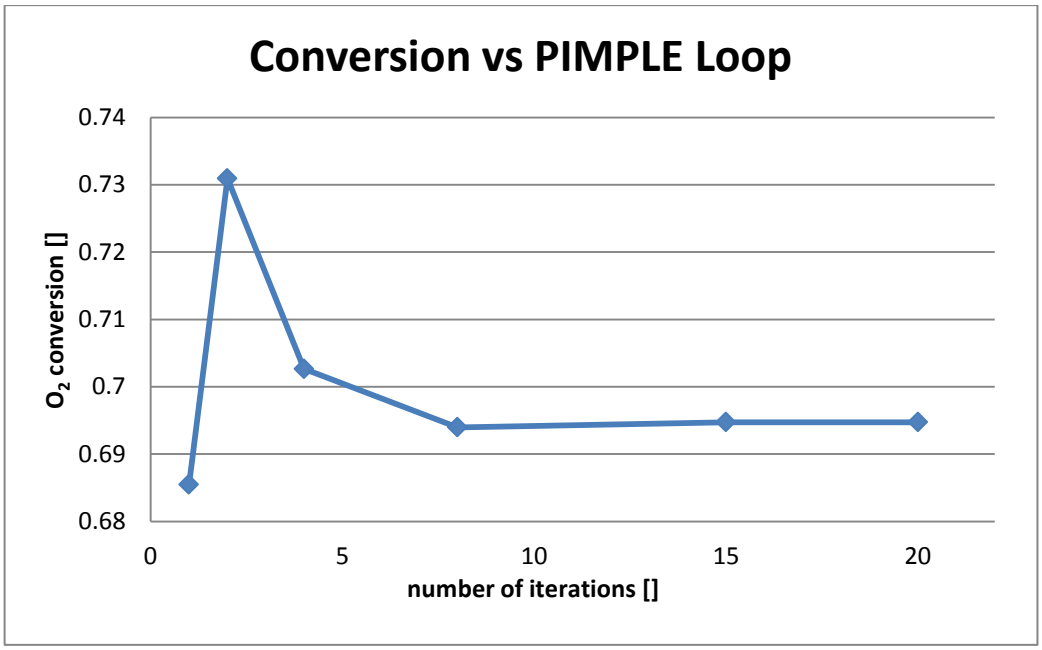


Figure 58: Influence of the number of iterations of the PIMPLE loop on the conversion of oxygen

As it is possible to see, a wrong set of iterations within the PIMPLE loop can strongly influence the quality and the accuracy of the solution. The results shown in Figure 58 demonstrate that the approach used in the previous work [1] was not correct. Working with a single iteration of PIMPLE loop is not possible to reach convergence at interface and thus to obtain satisfactory results at steady state conditions only once the minimum number of iterations that can guarantee the convergence is reached, the results don't change anymore.

Another important point that needs to be focused is the influence of the number of the PIMPLE loop iterations on the CPU time. As shown in Figure 59, increasing the number of iterations the CPU time increases in a linear manner. In particular it is interesting to see that if the number of iterations becomes four times higher (from 5 to 20), the simulation time becomes about two times larger.

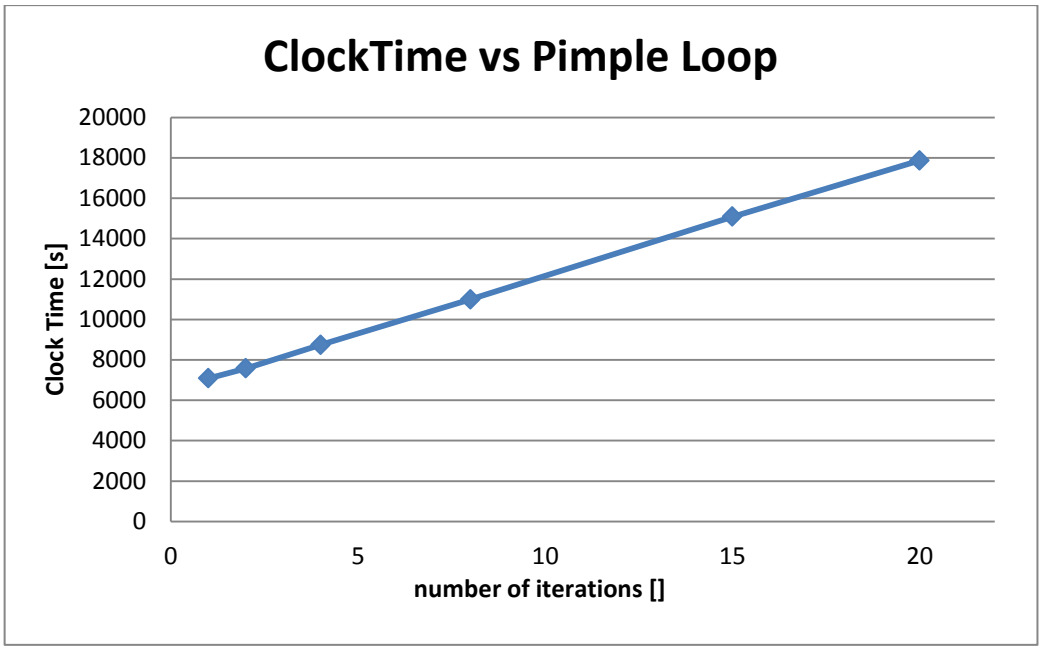


Figure 59: Influence of the PIMPLE loop iterations on the time of simulation

The parallel performances of the catalyticFOAM multiRegion code have been assessed for the reacting systems discuss in section 4.7. An Infiniband platform was used for running all the simulations. In its current configuration, it is made up of 16 nodes, each of them having 36 GB of RAM memory and 12 Intel® Xeon® X5675 (12Mb cache, 3.06 GHz, 6.40 GT/s Intel® QPI) processors. The scaling properties are measured by the parallel speed-up $S_p$ and efficiency $\eta_c$ which are defined as:

$$S_p = \frac{t_s}{t_p} \tag{4.35}$$

$$\eta_c = \frac{S_p}{p} \tag{4.36}$$

where $t_s$ and $t_p$ are the total wall times required to solve the problem with 1 and $p$ processors, respectively. The integration of the chemical step (which requires most of the computational time) does not involve communication between the different sub-domains, thus resulting in satisfactory parallel performances of the catalyticFOAM multiRegion code. Figure 60 reports the speed-up and the efficiency which are achieved using an annular reactor of 7420 cells (1200 solid cells).

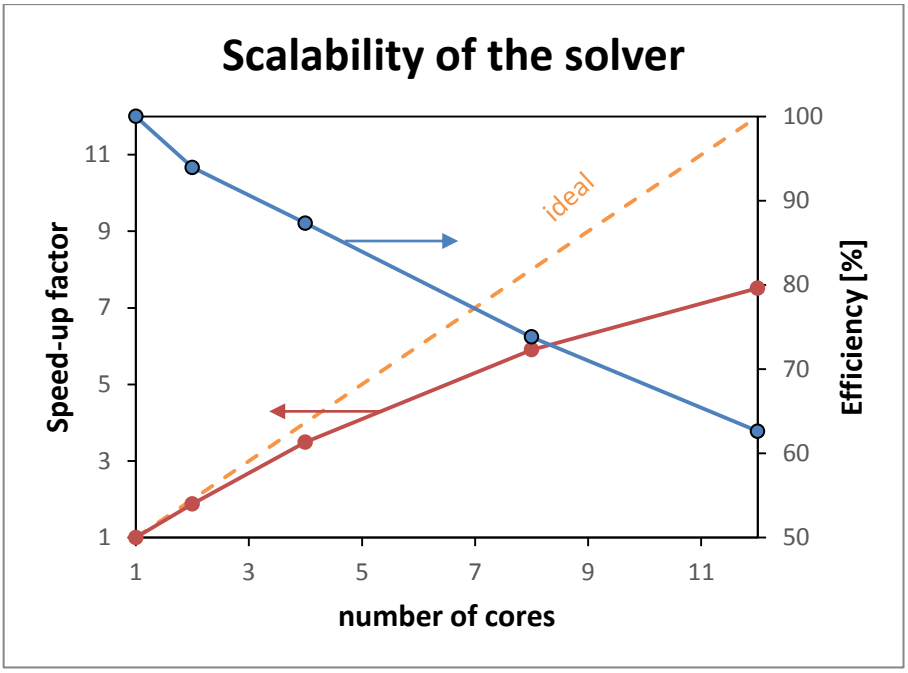


Figure 60: Example of scalability test on the code using an annular reactor

As expected, the efficiency decreases with the number of processors. It is register a good scalability until 8 processors. The overall performance can be considered quite satisfactory considering the low number of cells of the grid, especially considering the generality of the code and the possibility to work on arbitrarily complex meshes.

## 4.8 Comparison with experimental data

Always considering the annular reactor described above, It is possible to compare the steady state conversion profiles at different temperatures with the experimental data retrievable in literature [46].

The new architecture of the solver is able to model intra-phase phenomena in both gas and solid phase, as well all inter-phase phenomena between them. This allows taking into account diffusive limitations inside the catalyst, which was not possible to consider in previous work [9], where the catalyst morphology was neglected. The effective diffusivity for each species has been computed using the parallel pore model described in section 4.5. In particular the porosity has been determined with experimental analysis. On the contrary, the tortuosity is an adaptive parameter. As widely reported in literature this value is included in a range between 1 and 10. Knowing the

catalyst used in the process ($\alpha$-$Al_2O_3$ on Rh) it has been chosen the value that best fit the experimental trend in the middle temperatures range [423K-573K], in which the tortuosity has the stronger influence on the oxygen conversion. In Table 17 are shown the results of the sensitivity analysis.

| | $O_2$ CONVERSION | |
|---|---|---|
| Tortuosity Value | 473 K | 523 K |
| 4 | 74.27% | 83.44% |
| 5 | 72.89% | 82.60% |
| 6 | 69.77% | 81.85% |

Table 17: Influence of the tortuosity value on the oxygen conversion results

Comparing these trends with the experimental data shown in Figure 61 it is clear that the tortuosity value that fits in the best way the results is 6.

Thus, the parameters that have been used in the following simulation are reported Table 18:

| **OPERATIVE PARAMETER** | |
|---|---|
| $\varepsilon$ | 0.55 |
| $\tau$ | 6 |

Table 18: Operative parameter for the simulation of annular reactor

The results simulated using the multi-region approach are shown in Figure 61, together with an analysis of concentration profiles in the fluid and solid phase with variation of regime from chemical to mass-transfer controlled. Moreover, a comparison with the results of the same reactive system obtained with catalyticFOAM has been carried out.

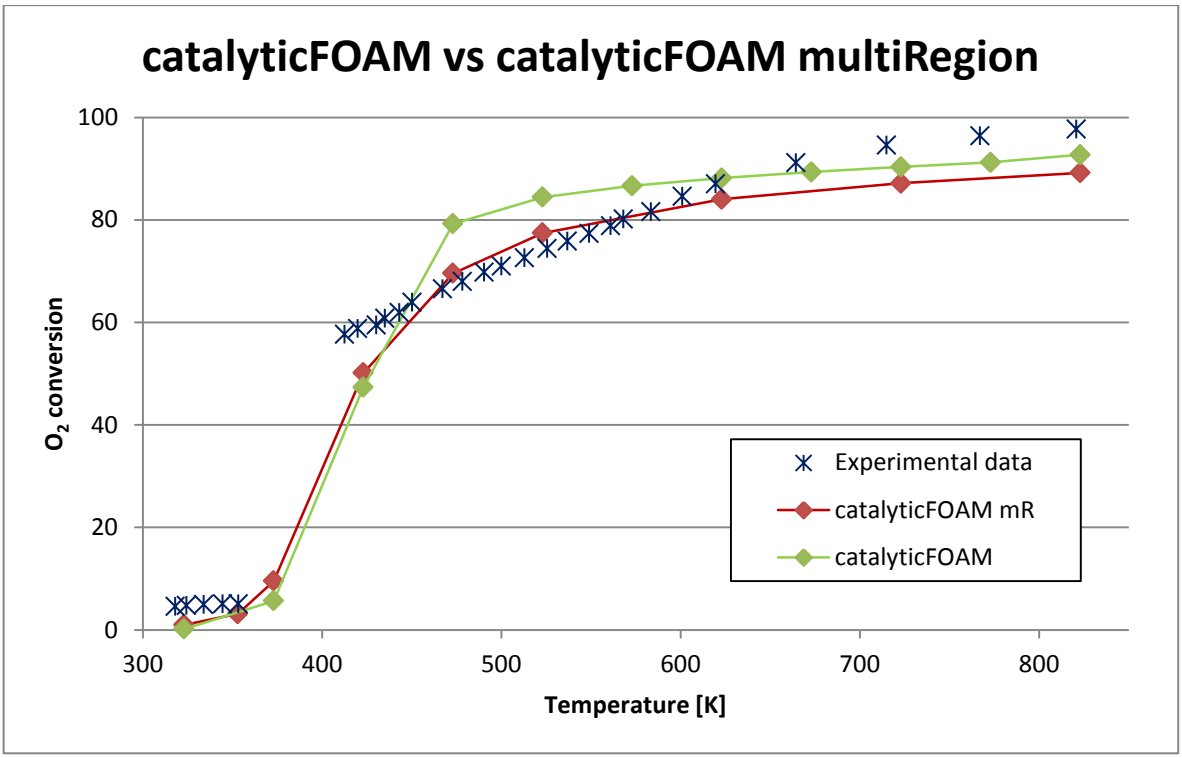


Figure 61: Conversion of $O_2$ vs. temperature for a flow rate of 0.274 Nl/min

The results of the two solvers are the same at low temperatures (under 400K). At high temperatures (about 800K) the difference between the two predictions is only of 2%. Thus in range of temperature [323K-423K] and [623K-823K], it is possible to affirm that both the models are able to predict the chemical and mass transfer regime. At intermediate temperature (range between 400K and 800K) catalyticFOAM overestimate the oxygen conversion, instead catalyticFOAM multiRegion is in good agreement with the experimental trend. It is evident the importance that the correct modeling of these phenomena has in order to reproduce the actual physical behavior of the system. With the multi-region approach is possible to take into account the diffusive limitation inside the solid washcoat that leads to a reduction of the reactivity of the system. CatalyticFOAM is not able to model this phenomenon and for this reason at medium temperature it is possible to observe a conversion gap between the predictions of the two solvers. To demonstrate the validity of this statement it is interesting to analyze the concentration profiles in the solid region with variation of regime from chemical to mass-transfer controlled. The results are shown in Figure 62.

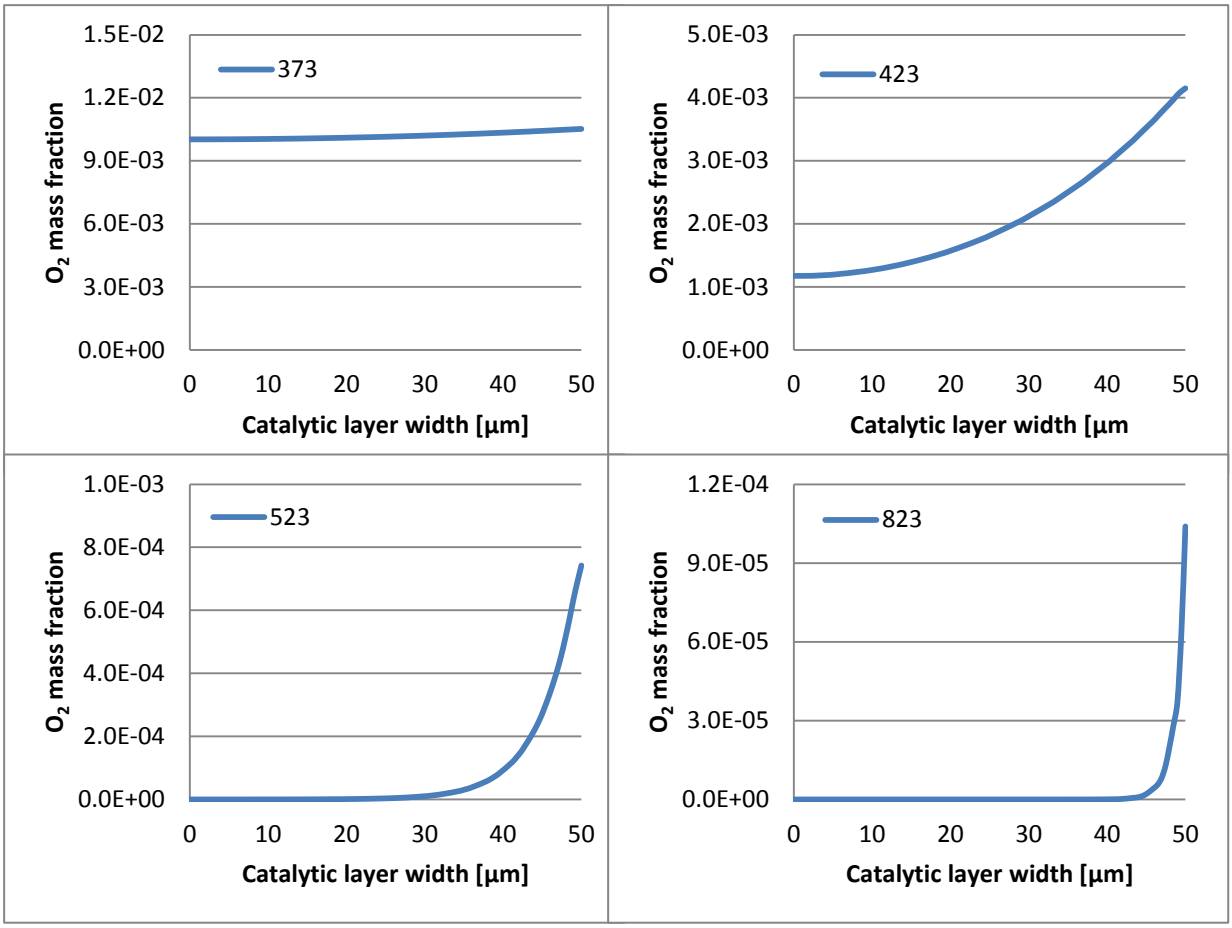


Figure 62: $O_2$ mass fraction along radial reactor direction in the solid phase at different temperatures

It is thus possible to confirm the strong influence of diffusive intra-phase limitations inside the 50 µm thick catalytic solid phase in the middle range of temperatures, making the actual profile of concentration inside the solid phase due to intra-phase diffusive limitations, correctly predicted by the solver developed. At higher temperatures, on the other hand, the oxygen mass fraction profile decrease immediately after the surface of the catalytic layer, making its fraction practically zero after the first few micrometers of the layer. This happens because the mass transfer phenomenon becomes the rate determining step. The presence of strong gradients in a few micrometers of thickness close to the surface of the catalytic layer make it necessary for the mesh to be very detailed in that zone in order to reproduce the profiles shown before. If the chosen mesh is, on the contrary, not enough refined in this zone, the mass transfer regime cannot be described properly. On the other hand, the mass fraction profiles in the fluid phase are characterized by lower gradients and don't require, at first instance, a very refined mesh. Nevertheless, it is important for the cells on both sides of the interface to have similar dimensions. In the fluid cells

close to the solid-fluid interface a geometrical subdivision as refined as their solid counterparts is required, in order to assure numerical stability of the coupling procedure adopted and descripted in section 4.4. A detail of the computational grid is shown in Figure 63 to clarify this concept.

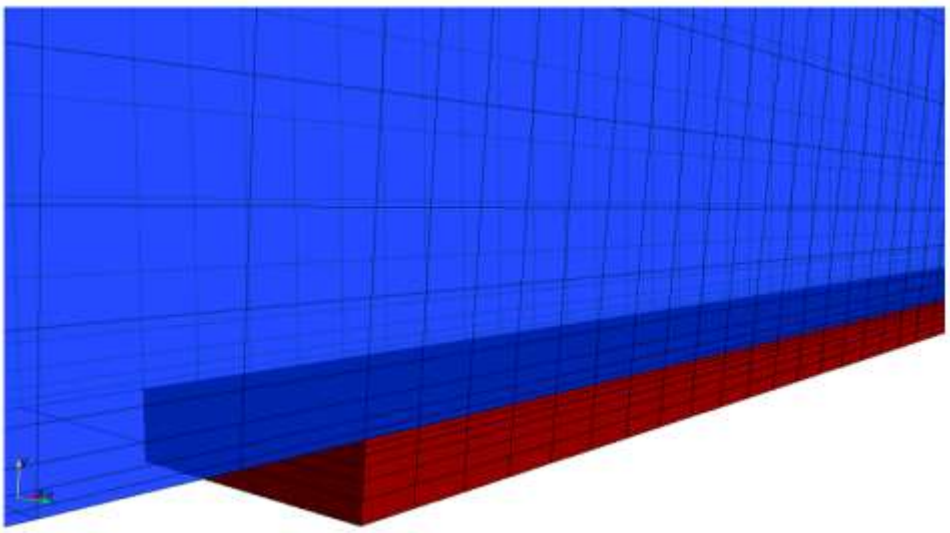

Figure 63: Importance of radial grading, specifically at the interface

As it is possible to see in Figure 61, the experimental data show an enhanced conversion with respect to the model predictions at high temperature. The reasons of this discrepancy are discussed by Maestri and co-workers [46]: the “conversion enhancing mechanism” observed in the experimental data is not due to the homogeneous gas phase chemistry, as the fraction of H* which is predicted to desorb in the gas phase at 500°C is orders of magnitude lower than the one identified as necessary to trigger gas-phase chemistry. The main hypothesis is that, downstream the catalytic bed, Rh evaporation and redeposition occurred. This brought to the creation of zones of low catalytic activity outside the catalytic bed. Even if at low temperatures these contributions are negligible, at higher temperatures a rise of the oxygen conversion is observable. This assumption has been investigated by considering two sections with low catalytic activity upstream and downstream the catalytic bed, as shown in Figure 64. A catalytic layer of 0.2 cm is then added upward the main bed. Another one is added downstream, with a length of 0.7 cm. The catalytic activity of these beds is lowered to 1% of that of the main bed.

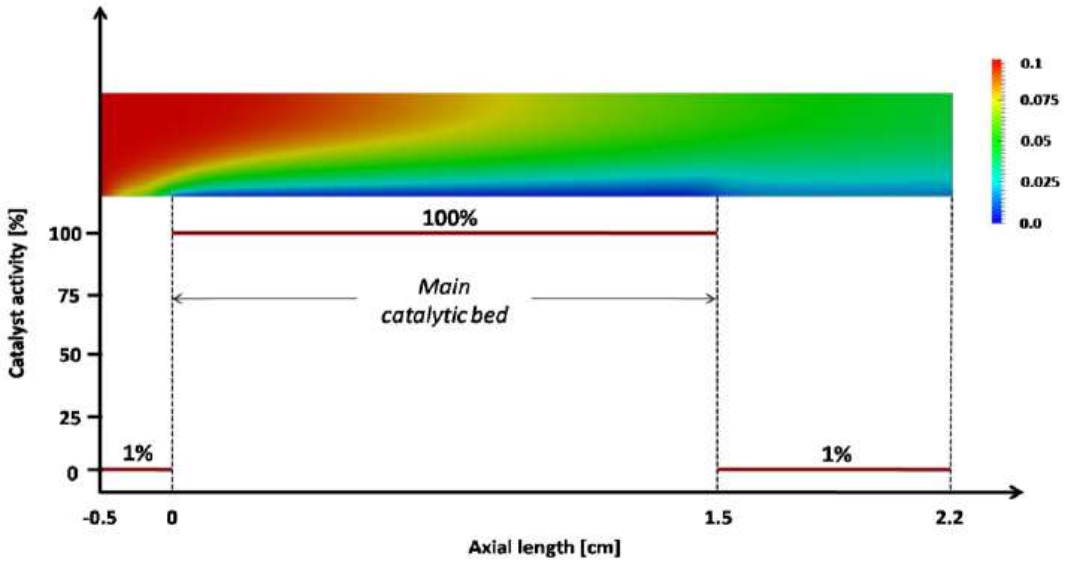


Figure 64: Activity of the catalytic bed vs. axial reactor length.

In Figure 65 the new results based on this hypothesis are shown. The additional low activity sections beside the main bed, which work in chemical regime due to the low amount of catalyst, lead to an increase of conversion. At low temperatures, on the other hand, the contribution is almost negligible. This produces a good agreement with the experimental data at high temperature.

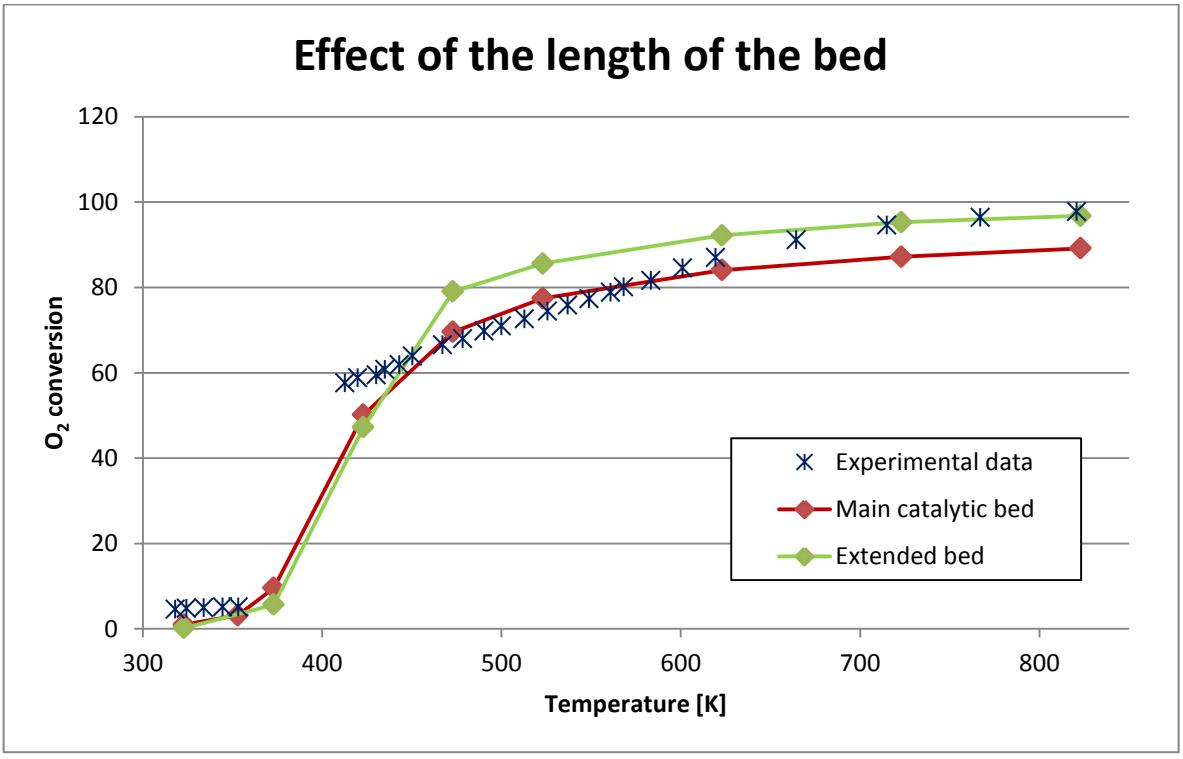


Figure 65: $O_2$ conversion vs. temperature for different catalytic bed at 0.274Nl/min

In the middle range of temperatures the solver overestimates the experimental trend. This disagreement is due to the tortuosity factor that, as already said is an adaptive parameter. In fact, its value has been identified through fitting of experimental data with the short length reactor.

## 4.9 Conclusions

In this chapter several aspects about the development of the catalyticFOAM multiRegion solver have been discussed. In the first section of the chapter the mathematical model has been presented together with the numerical strategies necessary for its solution. In particular a segregated approach has been adopted to impose the interface boundary condition through an iterative procedure, named PIMPLE loop. This Loop allows the correct coupling between different regions. To describe with the right level of accuracy all the phenomena that occur within the solid domain a dimensionless number (*Diffusion Number*) has been introduced.

In the second section of the chapter several cases have been carried out in order to test the effectiveness of the procedure proposed. The solver solution has been compared with the analytical one and the results are in excellent agreement.

Eventually, a validation of the developed solver has been presented through a comparison between the numerical results and the experimental data. In particular, the importance of the description of intra-phase phenomena inside the catalytic solid phase has proven to be critical in order to accurately predict the conversion profiles in the considered system.

# 5 Set up and validation of different packed bed

In this chapter several packed beds characterized by different unit structure with different geometries have been analyzed. In order to achieve this purpose a mathematical model, based upon DEM (discrete element method) has been used. This method is able to describe the mechanical behavior of assemblies of spheres or other structures through an explicit numerical scheme in which the interaction of the particles is monitored contact by contact and the motion of the particles modeled particle by particle. In order to achieve this result a computational tool based on the DEM methodology has been used. DEM (discrete element method) is a modeling technique capable of describing the mechanical behavior of assemblies of spheres and other structures. It is based on the use of an explicit numerical scheme in which the interaction of the particle is monitored contact by contact and the motion of the particle modeled particle by particle. In this work previously developed computational modeling framework has been used. This tool has been provided by BASF.

The feasibility of the results will be tested calculating the void fraction and the pressure drops in different conditions, in particular with different values of the inlet flow velocity. The outcome will be compared with both correlations and data provided in literature. The same packed beds will be exploited in the next chapter in order to validate CatalyticFOAM with complex geometries.

## 5.1 The DEM methodology

The Discrete Element Methods are a family of numerical methods for computing the motion of a large number of particles of micrometer-scale size and above. Though DEM is very closely related to molecular dynamics, the method is generally distinguished by its inclusion of rotational degrees-of-freedom as well as state full contact and often complex geometries (including polyhedra).

In this work a computational tool based on these methods has been used in order to generate random packed beds characterized by different structures. These beds will be used as the basic

geometry for the simulation of the oxidation of ethylene that will be taken into account in the following chapter. As it is well known this process is carried out in a multi-tubular rector where the catalyst usually fills these tubes.

The computational effort required by these methods is relatively high. This fact limits either the length of a simulation or the number of particles. This is particularly true when powders has been taken into account, so when the dimensions of the unit structures are really low and the numbers of particles extremely high. For the cases treated in this work, with dimensions much larger (some millimeters), it is possible to simulate also the entire reactor length that can reaches 6 to 12 meters. Several DEM codes, in fact, as do molecular dynamics codes, take advantage of parallel processing capabilities (shared or distributed systems) to scale up the number of particles or length of the simulation.

### 5.1.1 The mathematical model

A DEM code is based on the resolution of the second Newton law of motion. Moreover it is able to provide the random spatial orientation of all particles inside the reactor. The forces which act on each particle are computed from the initial data and the relevant physical laws and contact models. The forces that usually are taken into account are:

- *friction:* when two particles touch each other;
- *contact plasticity*: when two particles collide;
- *gravity* and the force of attraction between particles due to their mass, which is only relevant in astronomical simulations;
- *attractive potentials*: such as cohesion, adhesion, electrostatic attraction.

All these forces are added up to find the total force acting on each particle. An integration method is employed to compute the change in the position and the velocity of each particle during a certain time step from Newton's laws of motion. Then, the new positions are used to compute the forces during the next step, and this loop is repeated until the simulation ends.

More in detail, the approach used in this work is based on a finite number of discrete, semi-rigid spherical or polygon particles interacting by means of contact or non-contact forces and every

single particle of the system is described by Newton´s equations of motion related to transitional and rotational motions [47]. These equations, which are based on the forces and torques originated from its interaction with neighboring, can be given by:

$$\begin{cases} m_i \dfrac{d\mathbf{v}_i}{dt} = \sum_j \mathbf{f}_{ij} + m_i \mathbf{g} \\ I_i \dfrac{d_i}{dt} = \sum_j \boldsymbol{\tau}_{ij} \end{cases} \tag{5.1}$$

where $m_i$, $I_i$, $\boldsymbol{v}_i$ and $\omega_i$ are the mass, moment of inertia, translational velocity and angular velocity of the i-th particle respectively. The forces involved are the gravitational force, $m_i \boldsymbol{g}$ ($\boldsymbol{g}$ is the gravitational acceleration), and the interaction force $\boldsymbol{f}_{ij}$ between particles $i$ and $j$, which depends on the deformation of particle $i$. For simplicity, in most cases, the interparticle forces only include elastic and dampling parts and particles are supposed to be non-deformable. The torque acting on particle $i$ by particle $j$, $\boldsymbol{\tau}_{ij}$, stem from the contact force and causes particle $i$ to rotate or slow down the relative rotations between particle $i$ and $j$. Wall is treated as a particle of infinite size.

The components of the forces and the torques acting on a particle $i$ are:

- normal elastic forces,
- normal damping forces,
- tangential elastic forces,
- tangential damping forces,
- Columbian friction forces;
- Torque by tangential forces;
- Rolling friction torque;

In this way, the trajectory, velocity, angular velocity, transient forces and torques of all particles in the system can be traced by solving equations (5.1)

## 5.1.2 Steps of a DEM simulation

The first step that has been needed in a DEM simulation is the definition of the basic structure of the bed. It is possible to setup them using a CAD software able to produce an STL file. This file format is also known as Standard Tessellation Language and describes a raw unstructured triangular surface by the unit normal vertices (ordered by the right-hand rule) of the triangles

using a three dimensional Cartesian coordinate system. Several open source and non-commercial software can be used in order to complete this procedure. An example is MeshLab®. At this point it is possible to choose between two types of simulations:

- Fixed number of particles;
- Fixed length of the packed bed (the number of particle will be determined during the simulation);

Then is necessary to generate the geometry of the tube where the particles have to fall down and package randomly. Here it is important to adopt only the correct diameter of the reactor because during the meshing phase it is possible to change the length. This structure must have an enlargement in upper part in order to allow to the unit structure to enter in an easier way in the reactor. From this moment, the DEM code has to begin to solve the balances of forces in order to calculate the position of equilibrium of each unit that will establish the final bed. The software proceeds iteratively until the velocity of each particle reaches a value around zero that means that they have achieved their equilibrium position (the accuracy is due by the tolerance given by the user). Figure 66 clearly shows the final results of a simulation.

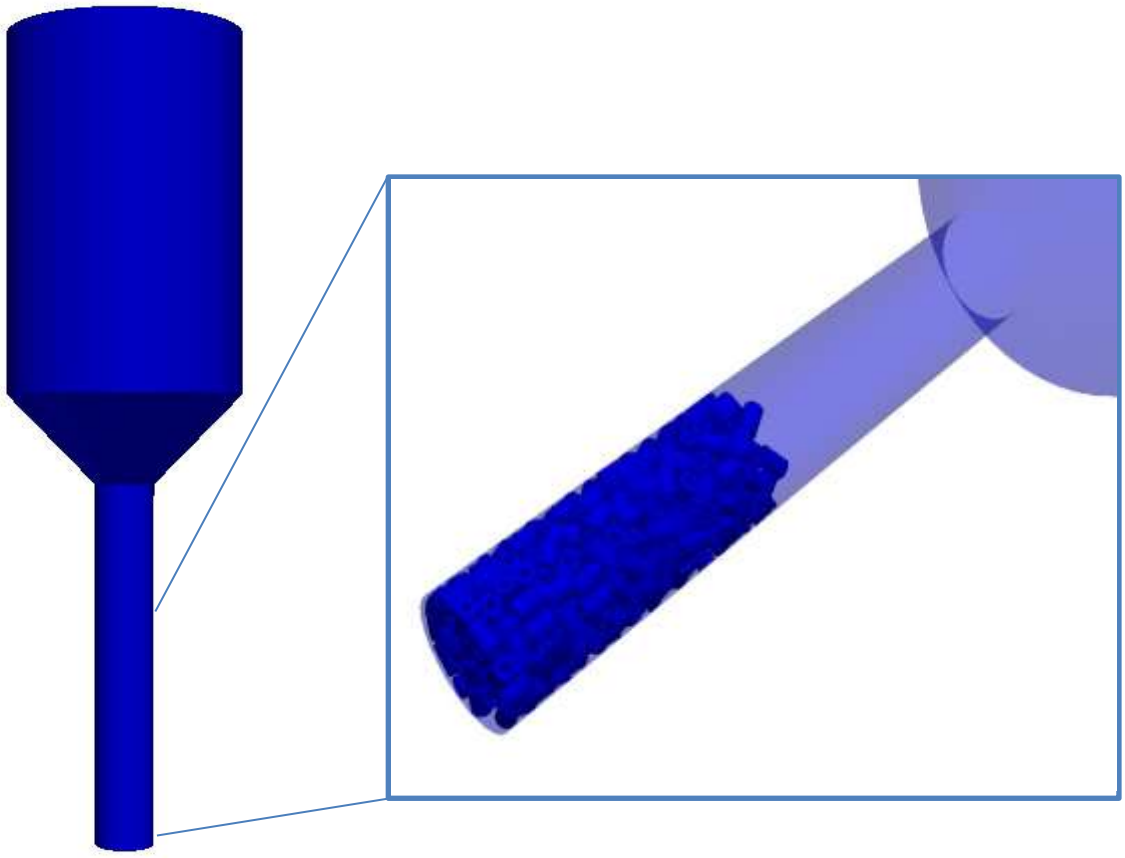

Figure 66: Result of a DEM simulation

A DEM-simulated packing geometry is exported into a text file of multiple columns containing the information regarding dimensions and positions of all particles in the packing.

The DEM field is a very dynamic world because in order to decrease the computational effort necessary to solve these types of problems, a lot of new algorithms are being developed. For example an interesting theory was developed by Tokoro et al (2005) [48]. Generally the equations of motion of particles are solved using the second-order Adams-Bashforth method, which estimates the values of contact force in the following calculation time by linear extrapolation, or by multi-step methods such as the predictor-corrector method. Inspired by these two conventional methods, this new theory propose a Contact Force Prediction Method that makes a larger time step possible. This method uses the predicted values of contact force at every contact point, which are exact solutions or numerical solutions of differential equations that represent two particle contacts.

Several commercial and open source software can be exploited in order to setup these beds:

- *SDEC:* Spherical Discrete Element Code [49].
- *Yade:* Yet Another Dynamic Engine (historically related to SDEC), modular and extensible toolkit of DEM algorithms written in C++. Tight integration with Python gives flexibility to simulation description, real-time control and post-processing, and allows introspection of all internal data. Can run in parallel on shared-memory machines using OpenMP [50].
- *LAMMPS* is a very fast parallel open-source molecular dynamics package with GPU support also allowing DEM simulations [27].
- *LIGGGHTS* is a code based on LAMMPS with more DEM features such as wall import from CAD, a moving mesh feature and granular heat transfer. Further a coupling to CFD is available [51].
- *MechSys:* it uses both spherical elements and sphero-polyhedra to model collision of particles with general shapes. Both elastic and cohesive forces are included to model damage and fracture processes. Parallelization is achieved mostly by POSIX threads. There is also a module dealing with the coupling between DEM and the Lattice Boltzmann Method (LBM) [52].

## 5.2 Simulation results: basic structures

In this work three different geometries were investigated as shown in Figure 67

- Cylinders;
- Rings;
- Spheres.

Figure 67: Basic structures of the beds

The dimensions of the three structures are reported in Figure 68:

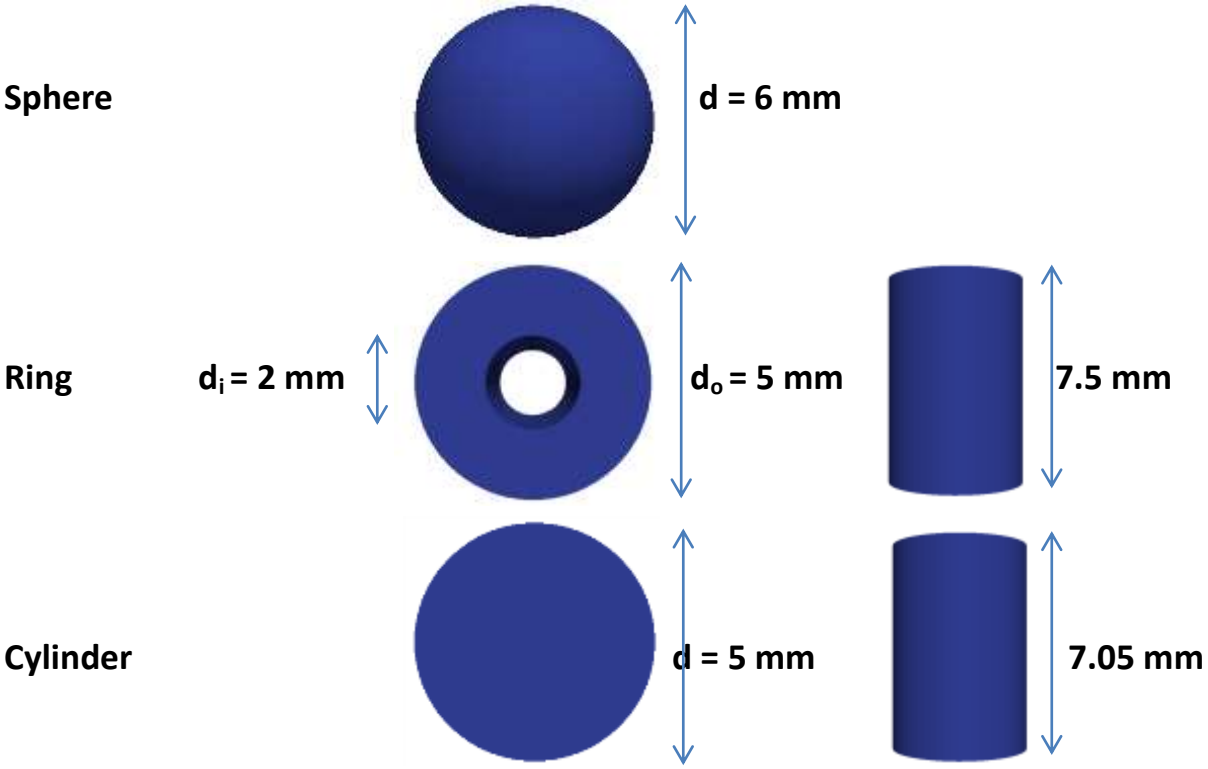


Figure 68: Dimensions of the basic structures

Usually a DEM code is able to treat only spherical particles. If a shape other than a sphere is required, it has to be built by assembling spheres [53]. Taking into account the example of a ring,

this is generated by only placing particles on the surface of it which is defined by the diameter and number of particles on the surface (Figure 69). The number of particles on the surface has an impact on the roughness. Since the spheres are staggered on the surface, “valleys” and “hills” can be found. However, the smoothness of the surface can be adjusted by the relative positions of the spheres and their diameters. A smoother surface can be achieved by more spheres with smaller diameters for the composition of one cylinder. This adds to the numerical complexity of the packing simulation.

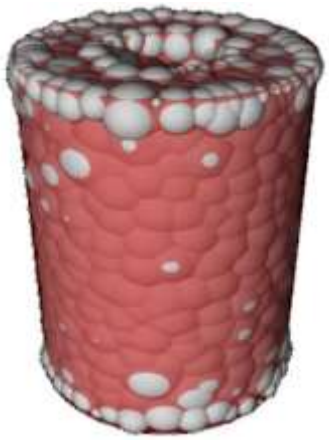

Figure 69: Ring structure in a DEM simulation

### 5.2.1 Simulation results: resulting beds

Known the dimensions of the three basic structures, the total number of rings, cylinders and spheres has been calculated in order to achieve the same catalytic area that amount to $5.655 \cdot 10^{-3}$ $cm^2$.

The first analysis involves only short packed beds with a length between 1.0 and 2.0 cm. The aim of this section, in fact, is just to validate the methodology and increase the CPU time with a bed characterized by higher length is useless to this objective.

| | $A_{single\ element}$ | N |
|---|---|---|
| Sphere | 0.000113097 | 50 |
| Ring | 0.000188024 | 30 |
| Cylinder | 0.000157080 | 36 |

Table 19: Number of particles for each bed

The aim of this work is to estimate the behavior of the three packed beds in different conditions. Considering the same available catalytic area, the results of the simulation presented in Chapter 5 will be dependent on the fluid dynamics around the particles and the capability of spheres, rings and cylinders of transfer mass and energy at the interface between reactive surface and bulk phase at different temperatures.

The results of the three simulations are random packed beds and they are presented in Figure 70:

Figure 70: Short packed beds

Current computational power allows DEM simulation of an entire packed bed containing thousands of particles. However, the number of particles that can be modeled in CFD is significantly less and is limited by available computational resources. For a typical commercial scale packed bed such as the cases conducted in this work, only a small section of the entire packed bed is included in the CFD model to fit the available computational resources.

In order to estimate the pressure drops of the three packed bed, increasing the length of those has been necessary. The number of unit structure of rings, cylinders and spheres are respectively 300, 360, 500 that correspond to a length of the bed between 10 and 12 cm (Figure 71). The chosen section should have a packing porosity that is the closest to that in the corresponding entire packed bed. With a length of 2 cm, this cannot be ensured.

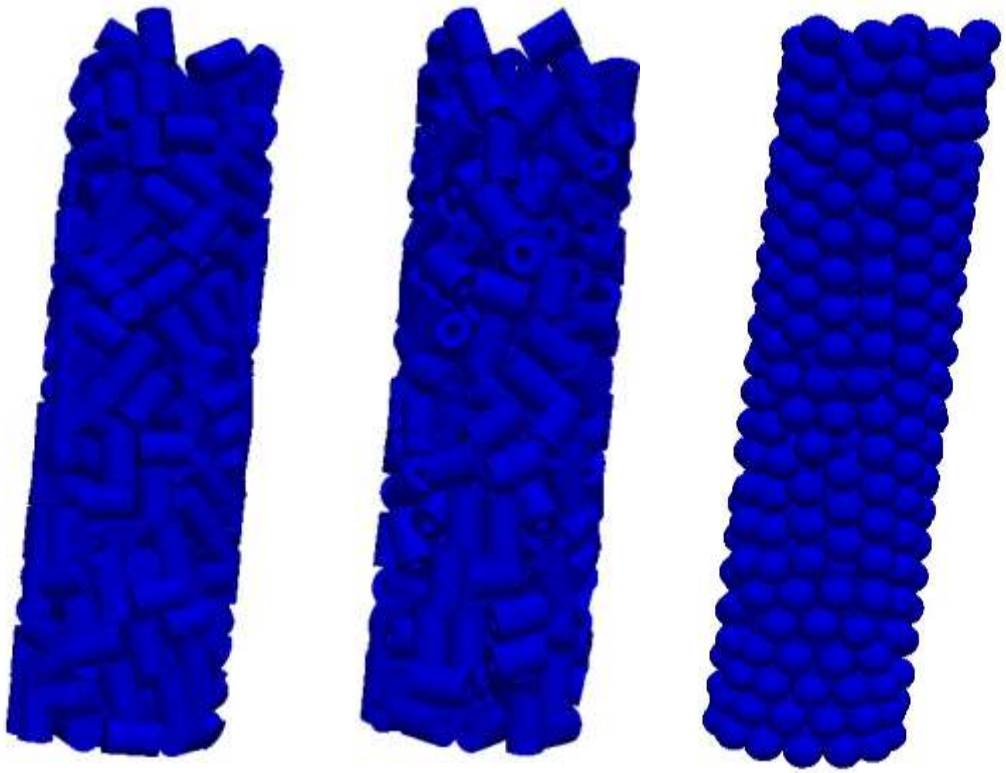

Figure 71: Long packed beds

### 5.2.2 Meshing phase

The results of a DEM simulation is still a STL file. At this point it is possible to obtain the mesh both for the tube and the packed beds using a meshing tool as snappyHexMesh (in Appendix A how this toll works will be explained). In Figure 72 the results for different levels of refinement for the packed bed made by rings will be presented:

Higher is the refinement, more realistic and smoother are the surfaces. Figure 72 shows the same case with three different levels of accuracy:

Figure 72: snappyHexMesh - different levels of refinement of the mesh

Observing these three structures it is possible to note that using a higher level of refinement and then a higher number of cells, it is possible to have a more accurate definition of the surface of the

ring. Particles contact each other, and some also contact the tube wall. At these points of contact, mesh cells become highly skewed, which results in a poor-quality mesh and often causes a convergence and stability problems in CFD simulation. In order to overcome this problem increase the level of the mesh in this zone is strongly suggested.

Figure 73 shows a slice of the mesh for the ring structure in order to understand the degree of detail near the catalyst.

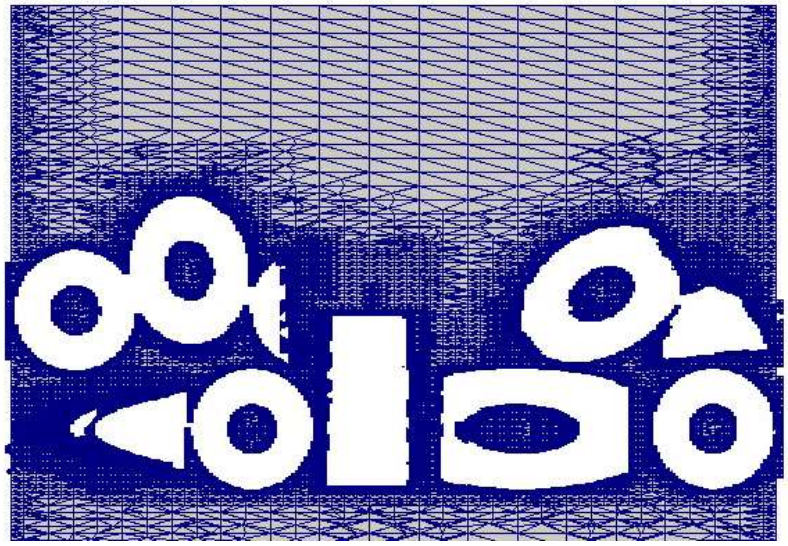

Figure 73: Detail of the mesh around the rings

# 5.3 Pressure drops calculation

The ability to *a priori* predict the void fraction and the pressure drop in a packed bed would significantly improve the reactor design, with possible optimization of catalyst performance, catalyst design, and the resulting process pressure drop. This is also particularly important because this parameter strongly influences the energy requirements of supply pumps and compressor.

For this reason the calculation of pressure drops will be provided in order to verify the consistency of the packed beds obtained with the DEM simulation.

### 5.3.1 CFD simulations

In order to drastically reduce the computational time for the calculation of the pressure drops, a basic solver of OpenFOAM has been used: simpleFOAM. This tool is able to compute velocity and pressure fields inside the tube neglecting the transient but only predicting the steady state conditions. This solver works with constant values of density and viscosity that have to be setup in the *constant/transportProperties dictionary*. The outlet pressure was set to 15 atm. Different simulations with different inlet velocities, between 0.2 and 1 m/s, have been carried out.

First of all the convergence of the mesh has to be verified (Figure 74). In particular, these types of structures present a high dependence of the results with the number of cells of the mesh. The analysis has been carried out with a bed made by cylinders and a velocity of 1 m/s.

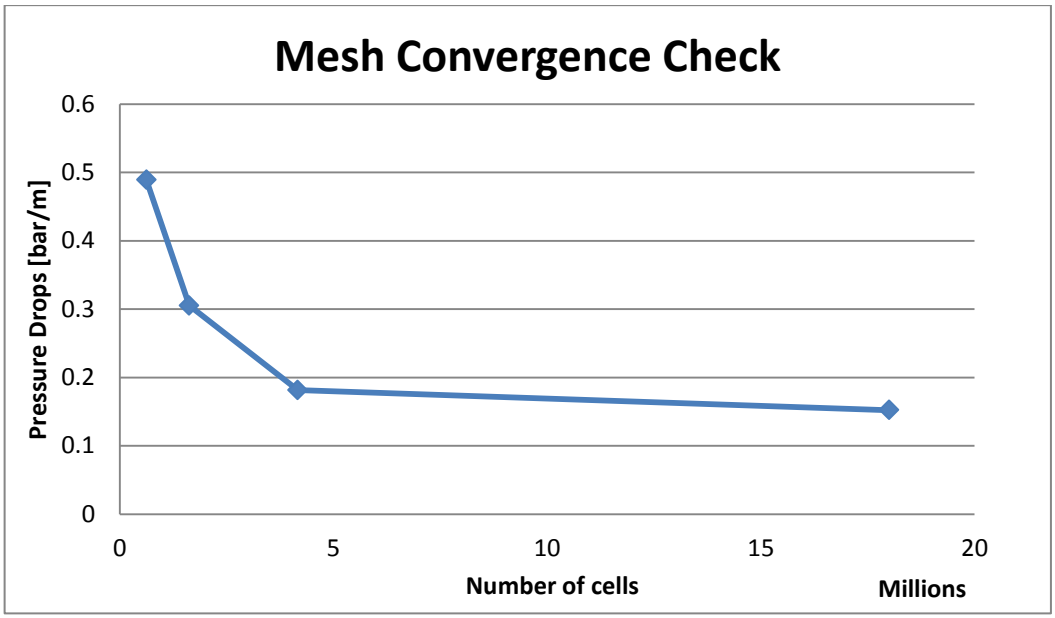


Figure 74: Mesh convergence check

In order to guarantee the convergence of the mesh a refinement level of 4 with snappyHexMesh is necessary. The corresponding number of cells is about 15-20 millions. The simulations that have been carried out in this chapter present this degree of detail.

No simulations between 4 and 18 millions of cells have been provided because these two simulations correspond to level of refinement 3 and 4 of snappyHexMesh. Thus, develop a mesh characterize by an intermediate number of cells was not possible. In the following tables (Table

20-Table 22) the results of the simulation at different velocity will be provided. As it is well known, the pressure drops increase with the square of the velocity.

| Spheres | | | | | |
|---|---|---|---|---|---|
| | **U=0.2 m/s** | **U=0.4 m/s** | **U=0.6 m/s** | **U=0.8 m/s** | **U=1.0 m/s** |
| **$P_{in}$ [Pa]** | 1519971.75 | 1520160.75 | 1520464.5 | 1520862.75 | 1521376 |
| **$P_{out}$ [Pa]** | 1519870.5 | 1519870.5 | 1519870.5 | 1519870.5 | 1519870.5 |
| **ΔP [Pa]** | 101.25 | 290.25 | 594.00 | 992.25 | 1505.25 |
| **ΔP/m [bar/m]** | **0.00804** | **0.02304** | **0.04714** | **0.07875** | **0.11946** |

Table 20: Spheres pressure drops

| Cylinders | | | | | |
|---|---|---|---|---|---|
| | **U=0.2 m/s** | **U=0.4 m/s** | **U=0.6 m/s** | **U=0.8 m/s** | **U=1.0 m/s** |
| **$P_{in}$ [Pa]** | 1520100 | 1520545.5 | 1521207 | 1522071 | 1523185 |
| **$P_{out}$ [Pa]** | 1519870.5 | 1519870.5 | 1519870.5 | 1519870.5 | 1519870.5 |
| **ΔP [Pa]** | 229.50 | 675.00 | 1336.50 | 2200.50 | 3314.250 |
| **ΔP/m [bar/m]** | **0.02250** | **0.06618** | **0.13108** | **0.21573** | **0.32493** |

Table 21: Cylinder pressure drops

| Rings | | | | | |
|---|---|---|---|---|---|
| | **U=0.2 m/s** | **U=0.4 m/s** | **U=0.6 m/s** | **U=0.8 m/s** | **U=1.0 m/s** |
| **$P_{in}$ [Pa]** | 1519971.75 | 1520187.75 | 1520518.5 | 1520957.25 | 1521504 |
| **$P_{out}$ [Pa]** | 1519870.5 | 1519870.5 | 1519870.5 | 1519870.5 | 1519870.5 |
| **ΔP [Pa]** | 101.25 | 317.25 | 648.00 | 1086.75 | 1633.50 |
| **ΔP/m [bar/m]** | **0.01125** | **0.03525** | **0.07200** | **0.12075** | **0.18150** |

Table 22: Ring pressure drops

As it possible to see (Figure 75) the basic structure that provides the higher pressure drops is the cylinder. The geometries of spheres and rings allow the flow to pass through the bed in an easier way with a lower value of pressure drops.

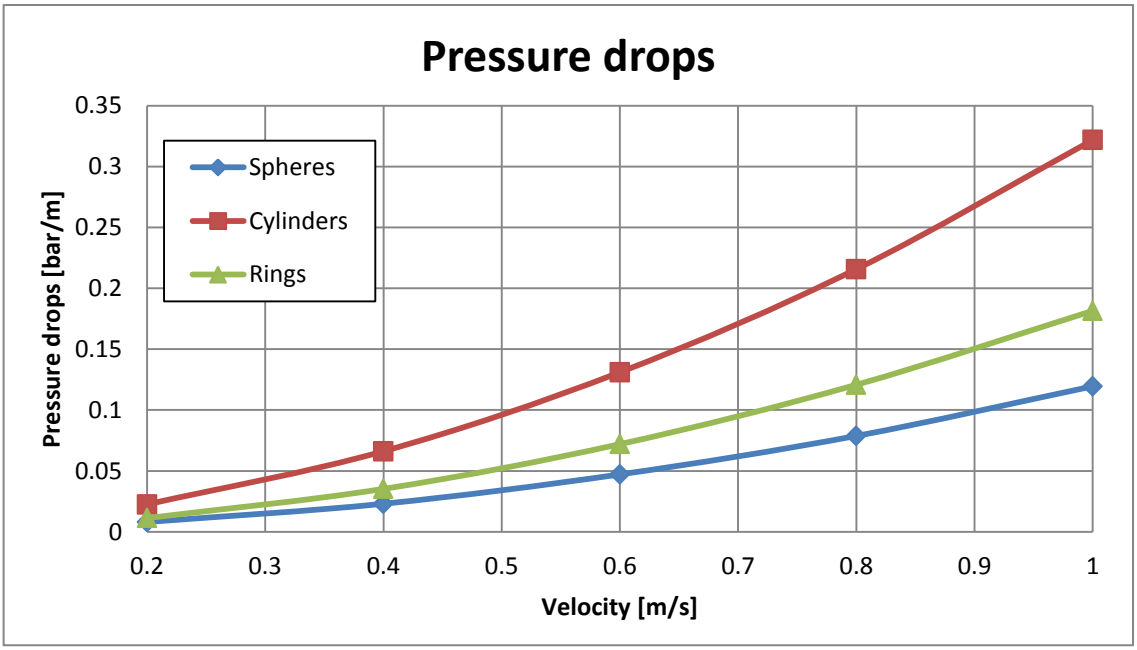


Figure 75: Trends of the pressure drops for the three packed beds

A graphical representation of the pressure drops for each bed are presented in Figure 76-Figure 78. These results have been obtained with an inlet velocity of 1 m/s.

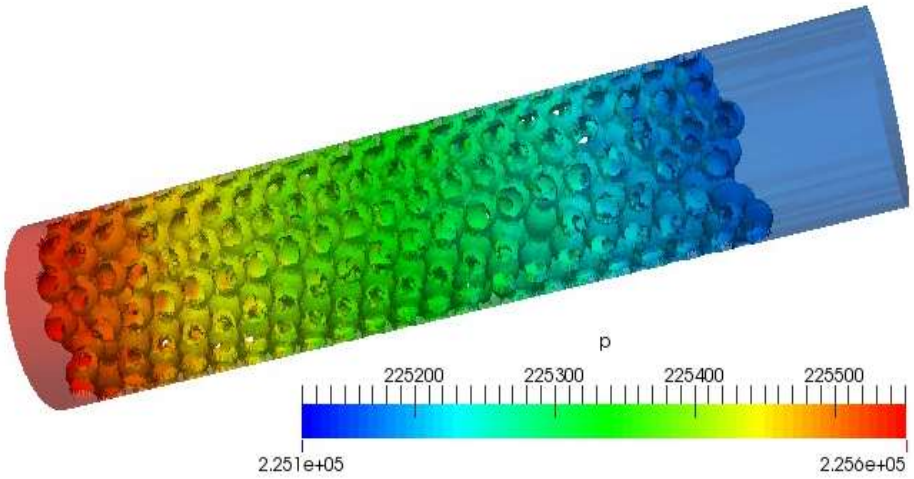


Figure 76: Spheres pressure drops (v=1m/s)

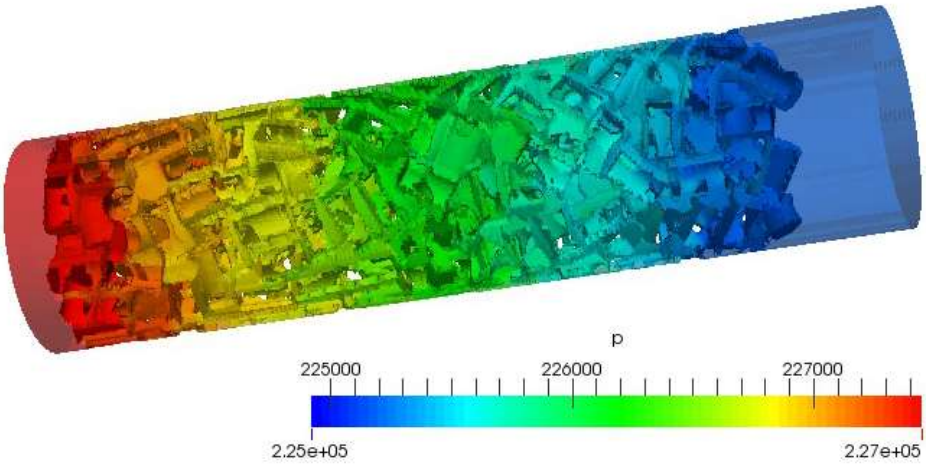


Figure 77: Cylinders pressure drops (v=1m/s)

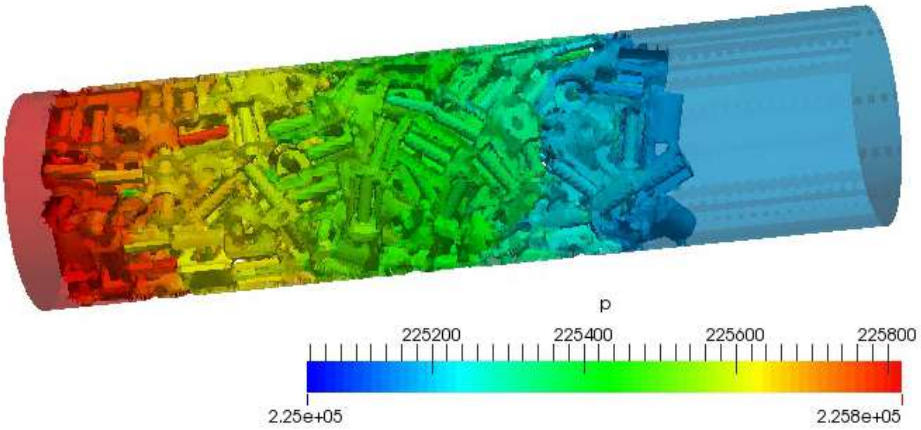


Figure 78: Rings pressure drops (v=1m/s)

## 5.3.2 Literature correlations – Void fraction

A parameter that is really important for a packed bed is the void fraction. In order to check the result of the DEM simulation, the void fraction calculated with the CFD simulation has to tend asymptotically with the one estimated with literature correlations.

For a packed bed, the most widely used correlations for the estimation of this parameter are probably Dixon's correlations. They depend by the ratio between the tube diameter $d_t$ and the hydraulic diameter of sphere and cylinder $d_{hyd}$.

Dixon correlations for spheres and cylinders are reported in Table 24 and Table 24 [54]:

| | |
|---|---|
| $\left(d_t / d_{hyd}\right) > 2$ | $\varepsilon = 0.4 + 0.05\left(d_t / d_{hyd}\right)^{-1} + 0.412\left(d_t / d_{hyd}\right)^{-2}$ |
| $1+\sqrt{3}/2 \leq \ (d_t / d_{hyd}) \leq 2$ | $\varepsilon = 0.528 + 2.464\left[\left(d_t / d_{hyd}\right)^{-1} - 0.5\right]$ |
| $\left(d_t / d_{hyd}\right) < 1+\sqrt{3}/2$ | $\varepsilon = 1 - 0.667\left(d_t / d_{hyd}\right)^{-3}\left[2\left(d_t / d_{hyd}\right)^{-1} - 1\right]^{0.5}$ |

Table 23: Dixon correlation for spheres

| | |
|---|---|
| $\left(d_t / d_{hyd}\right) > 1.67$ | $\varepsilon = 0.36 + 0.1\left(d_t / d_{hyd}\right)^{-1} + 0.7\left(d_t / d_{hyd}\right)^{-2}$ |
| $1.43 \leq \ (d_t / d_{hyd}) \leq 1.67$ | $\varepsilon = 0.677 - 9\left[\left(d_t / d_{hyd}\right)^{-1} - 0.625\right]^2$ |
| $\left(d_t / d_{hyd}\right) < 1.43$ | $\varepsilon = 1 - 0.763\left(d_t / d_{hyd}\right)^{-2}$ |

Table 24: Dixon correlation for cylinders

For rings the calculation is more complex because the evaluation of $\varepsilon_{sc}$ is necessary. This is the void fraction of bed of hollow cylinder corrected to solid cylinder basis.

| | |
|---|---|
| $\left(b_i / b_e\right) < 1.43$ | $\varepsilon = 1 - \left[\left[1 + 2\left(\frac{b_i}{b_e} - 0.5\right)^2\left(1.145 - \frac{d_{hyd}}{d_t}\right)\right] * \left[1 + \left(\frac{b_i}{b_e}\right)^2\right] * (1 - \ \varepsilon_{sc})\right]$ |

Table 25: Dixon correlation for rings

Where $b_i$ is the inner diameter of the ring, $b_e$ is the external diameter. $d_{hyd}$ and $d_t$ still represent respectively the hydraulic diameter of the particle and the diameter of the external tube.

### 5.3.3 Literature correlations – Pressure drops

In order to check the accuracy of the previous CFD simulations, it is necessary to find some literature correlations in order to estimate the pressure drops and the void fraction of the three packed beds.

The pressure drops have been calculated exploiting two different correlations: the Ergun equation and the Eisfeld equation.

The most familiar correlation for pressure drop through a packed bed is the Ergun equation [55]:

$$\psi = \frac{A}{Re_{dp}} \frac{(1-\varepsilon)^2}{\varepsilon^3} + \frac{B}{Re_{dp}^{2-n_{max}}} \frac{(1-\varepsilon)^{3-n_{max}}}{\varepsilon^3} \tag{5.2}$$

where $\psi$ is the dimensionless pressure drop or friction factor:

$$\psi = \frac{\Delta P}{\rho U^2} \frac{d_p}{L} \tag{5.3}$$

$Re_{dp}$ is the particle Reynolds number and is calculated as following:

$$Re_{dp} = \frac{\rho U d_p}{\mu} \tag{5.4}$$

$A$ and $B$ are parameters that depend from the geometry of the bed, $n_{max}$ was calculated by Ergun and its value is 2.

The Ergun equation consists of two terms, corresponding to the Ergun constants $A$ and $B$. The first term is nominally considered the turbulent term, representing the contribution to pressure drop from expansion and contractions. The second term, called the laminar term, represents contributions from form drag. According to Ergun, the advantage of this equation was that void fraction sufficiently characterized tube packing. This allows the parameters $A$ and $B$ to be universal, dimensionless constants ($A$ =150, $B$=1.75). Ergun further argued that these parameters were independent of catalyst particle geometry and tube size. However, all of Ergun's data were obtained with large tube-to-particle diameter ratios, *D*/*d* > 10. Much research has been conducted to identify more accurate Ergun constants $A$ and $B$ for different particle geometries and particle-to-tube diameter ratios. A widely used set of Ergun constants is from Handley and Heggs [56] as shown in Table 26:

| | $A$ | $B$ |
|---|---|---|
| Cylinder | 368 | 1.248 |
| Sphere | 458 | 1.28 |

Table 26: Ergun coefficients

Nevertheless Ergun equation is not able to take into account another parameter that is also very important during the estimation of pressure drops: the wall effect. In fact, any packing is bounded by confining walls, so that an influence of the tube-to-particle diameter ratio $D/d_p$ on the pressure drop is to be expected. On the one hand these external boundaries offer an additional

resistance due to the wall friction. On the other hand they force the particle to order in such a way that a region of increased void fraction is formed. For this reasons a more accurate correlation has been investigated in order to validate the results given by simulations. For geometry as cylinders and rings the most appropriate one is the Eisfeld correlation [55].

$$\psi = \frac{K_1 A_w^2}{Re_{dp}} \frac{(1-\varepsilon)^2}{\varepsilon^3} + \frac{A_w}{B_w} \frac{1-\varepsilon}{\varepsilon^3} \tag{5.5}$$

$$A_w = 1 + \frac{2}{3(D/d_p)(1-\varepsilon)}, \quad B_w = \left[ k_1 \left( \frac{d_p}{D} \right)^2 + k_2 \right] \tag{5.6}$$

This is an Ergun-type equation where the contribution of the conflicting wall to the hydraulic radius is accounted analytically by the coefficient $A_w$. Additionally, the function $B_w$ has been introduced, describing empirically the porosity effect of the walls at high Reynolds number [53]. The parameters $K_1, k_1$, and $k_2$ have been fitted for three types of shapes: sphere, cylinder and general geometries [57] (Table 27), $d_p$ is the hydraulic radius which is defined as the diameter of a sphere of equivalent surface area.

| | $K_1$ | $k_1$ | $k_2$ |
|---|---|---|---|
| Spheres | 154 | 1.15 | 0.87 |
| Cylinders | 190 | 2.00 | 0.77 |
| Other geometries | 155 | 1.42 | 0.83 |

Table 27: Eisfeld coefficients

## 5.3.4 Results and comparisons – void fraction

The correlations used in this work are the first of Table 23: Dixon correlation for spheres and Table 24: Dixon correlation for cylinders because the ratio $d_t/d_{hyd}$ is respectively 5.69 for spheres and 5.33 for cylinders. The comparisons between the CFD results and the correlation are reported in Table 28:

| | Bed porosity | Expected porosity |
|---|---|---|
| Cylinder | 0.38 | $\varepsilon = 1 - \frac{Nd^3}{D^2 H} = 0.37$ |
| Sphere | 0.42 | $\varepsilon = 1 - \frac{2Nd^3}{3D^2 H} = 0.44$ |

Table 28: Comparison between effective porosity and expected from literaure - spheres and cylinders

In both cases the results provided by the packed beds obtained with the DEM simulation are in good agreement with the literature correlation. In these cases it is possible to confirm that the particles are correctly randomly packed and that the beds are a good representation of reality.

For rings, as verified with the pressure drops, the agreement is not good as in the previous cases

| | Bed porosity | Expected porosity |
|---|---|---|
| Ring | 0.49 | $\varepsilon = 0.52$ |

Table 29: Comparison between effective porosity and expected from literature - rings

As expected the porosity founded with the CFD simulation is higher compared to the one calculated with Dixon correlation. This is usually a minimum asymptotic value that the bed reaches for ratio between tube diameter and particle diameter near 10.

### 5.3.5 Results and comparisons – Pressure drops

The results of the simulations for bed made by spheres give an excellent agreement both with Ergun and Eisfeld correlation (Figure 79). In this case the two correlations estimate the same results because with spheres the wall effect doesn't have a strong influence as for cylinders and rings.

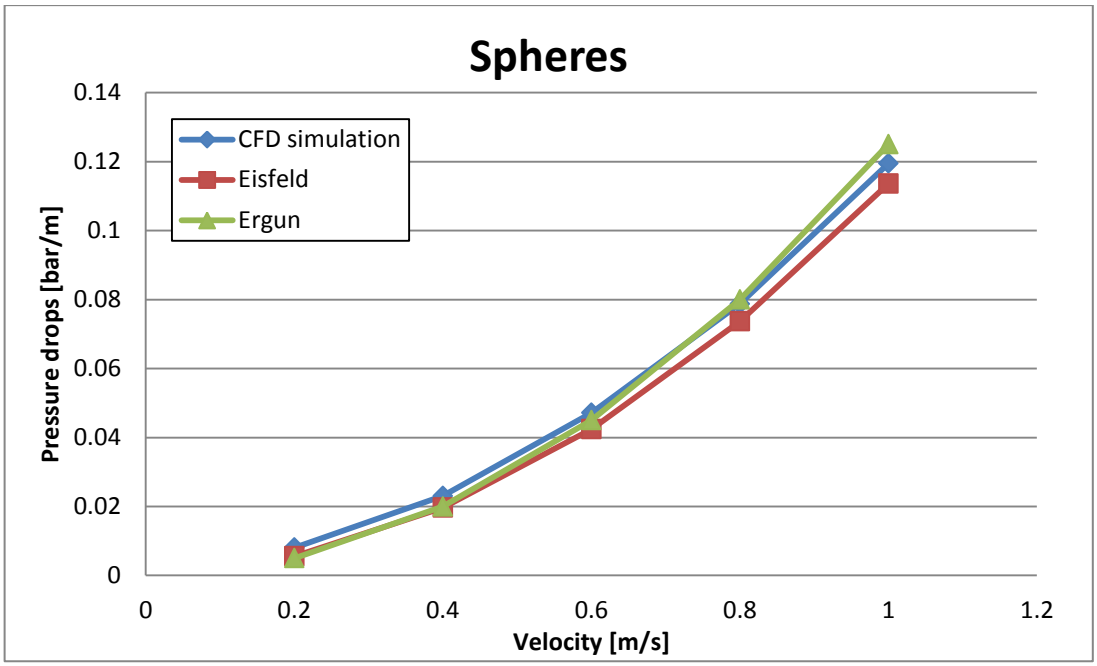


Figure 79: Comparison with literature correlations – Spheres

For cylinders, instead, the satisfactory agreement is reached only between simulation and Eisfeld correlation (Figure 80). Clearly, the wall effect is predicted to increase the pressure drop at low and moderate Reynolds numbers; only for sufficiently high $Re_{dp}$ values and for very small tube-to-particle diameter ratios (under $D/d_p$ <5) pressure drop reduction is obtained.

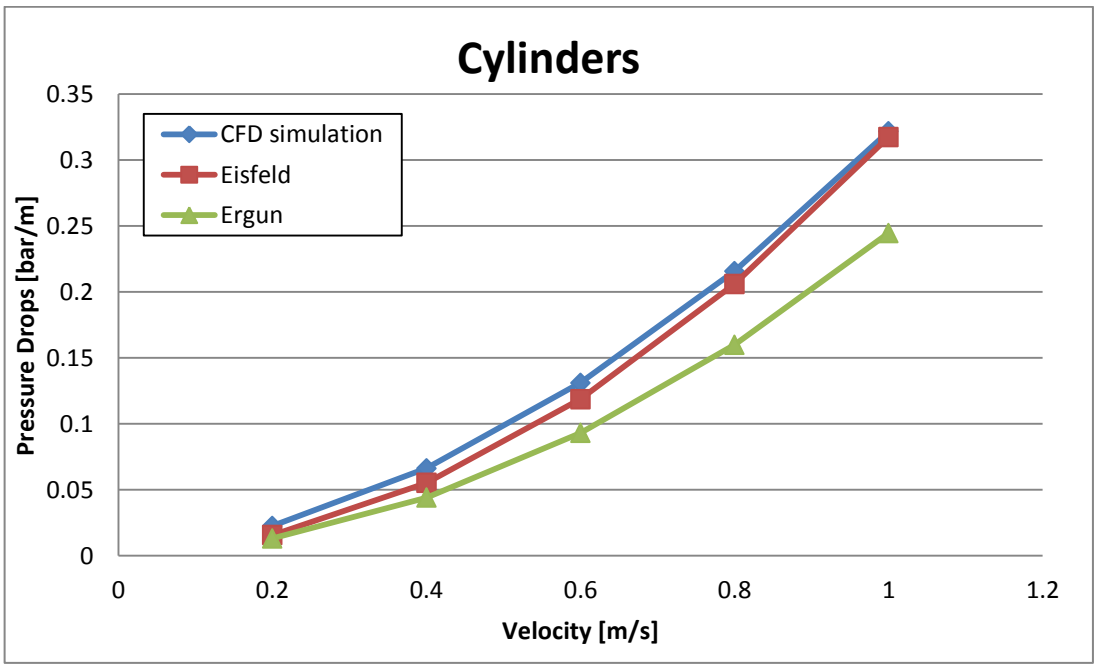


Figure 80: Comparison with literature correlations - Cylinder

Figure 81 well explain this phenomenon known as wall effect: near the surface of the tube, the void fraction increases compared with the one in the center. Here preferential paths for fluid have been created, demonstrated by a parallel increase of the velocity of the fluid. For this reason, a correlation that takes into account the wall effect is necessary in order to well describe the phenomenon. Following the velocity field for packed bed made by rings is presented.

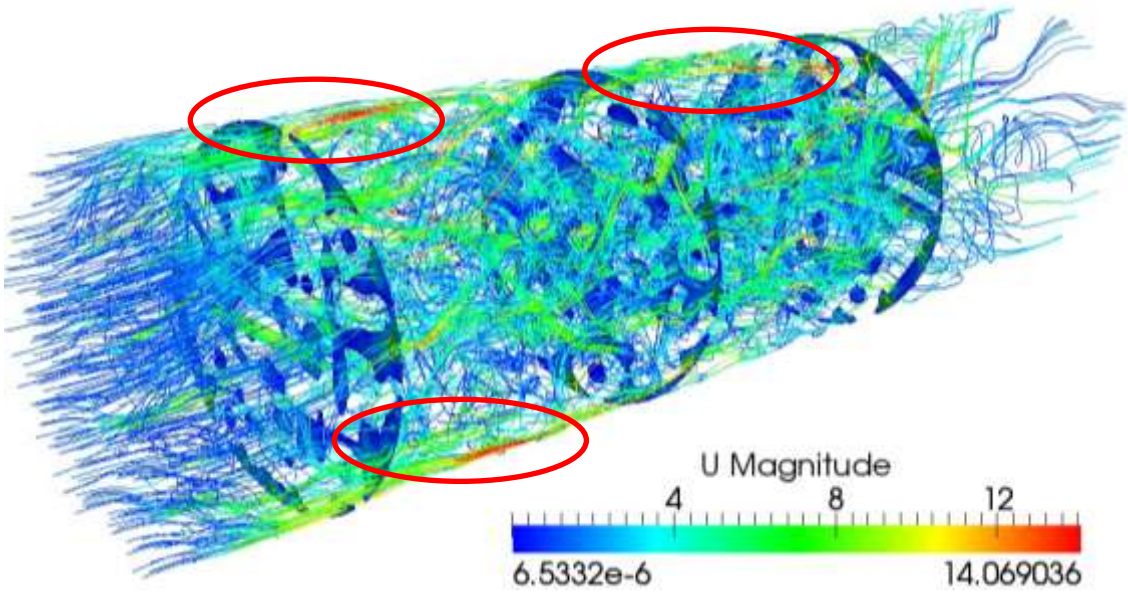


Figure 81: Ring - velocity field

The preferential paths are highlighted in red. As it possible to see, the maximum value of the velocity is reached near the surface of the tube. Observing a radial section (Figure 82) of the tube is more effective in order to understand this point.

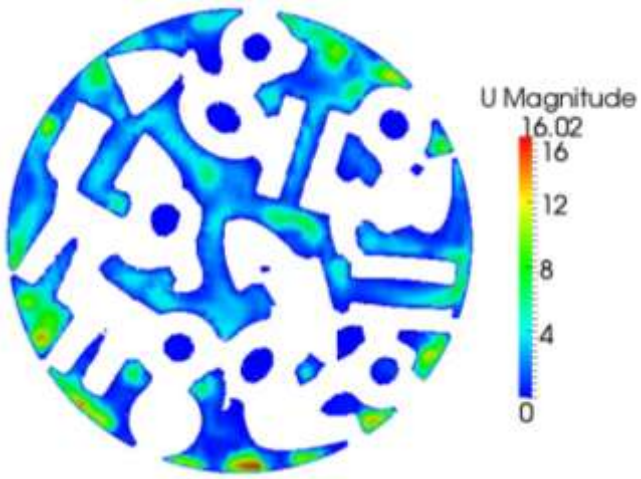


Figure 82: Radial section - velocity field

Finally, as expected, the Ergun correlation for rings (for which the parameters $A$ and $B$ haven't been developed) is very distant from the curve found with the CFD simulations (Figure 83). Also with the Eisfeld correlation the results are not good as in the previous two cases. Here two approaches were possible: use the parameter developed for "all particle geometries" or treat the ring as a cylinder using its parameters. As it possible to see, the second option gives a better agreement with the simulations.

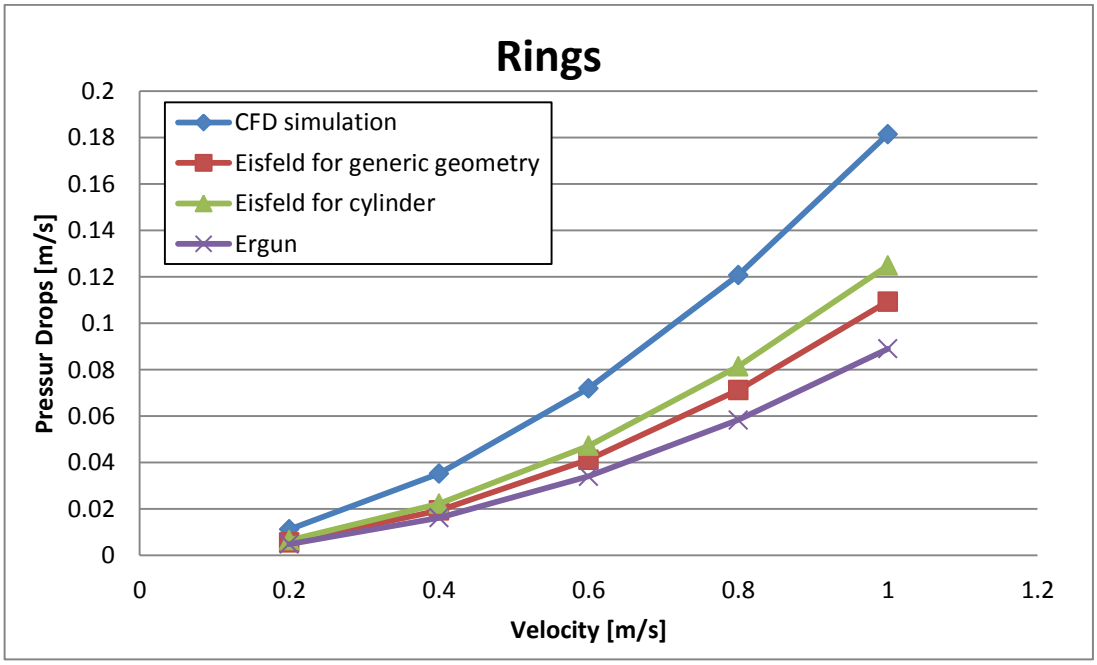


Figure 83: Comparison with literature correlations – Rings

## 5.3.6 Comparison with experimental data

The last step was the validation of the results with experimental data provided in literature. In Ergun's work (1949) [58], the same three geometries with different value of void fraction, caused by different dimension of the external tube, have been investigated. In the following charts, the points represent experimental data while the lines are the numerical calculations.

In this case the charts represent the modified friction factor $\psi' = \psi\,\varepsilon^3/(1-\varepsilon)$ as a function of the Reynolds number [55]. This parameter, in a logarithmic scale, usually presents two different zones: at small values of Reynolds number, $\psi'$ has a linear behavior that becomes a constant value at high Reynolds number.

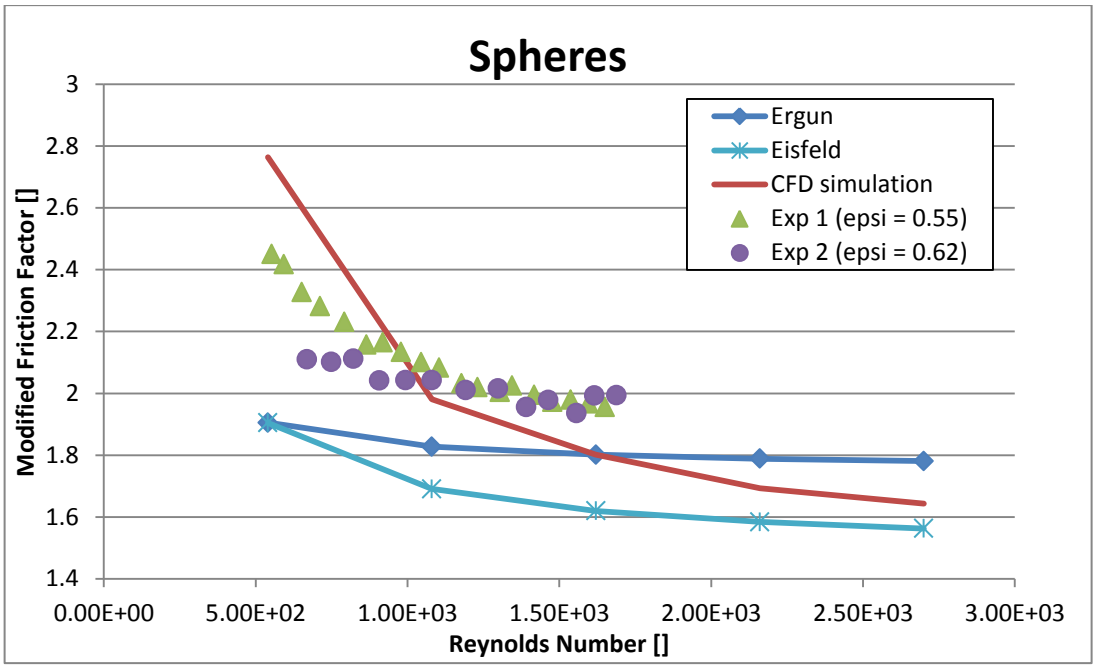


Figure 84: Comparison with experimental data - Spheres

As it possible to see, for spheres and rings the best agreement is reached with the results of the CFD simulation and not with the literature correlation (Figure 84-Figure 85). Usually literary correlations introduces approximations that are bigger that the ones given by the CFD simulation. As it possible to see the difference between Ergun and Eisfeld correlations at low Reynolds number can be represented only by the modified friction factor.

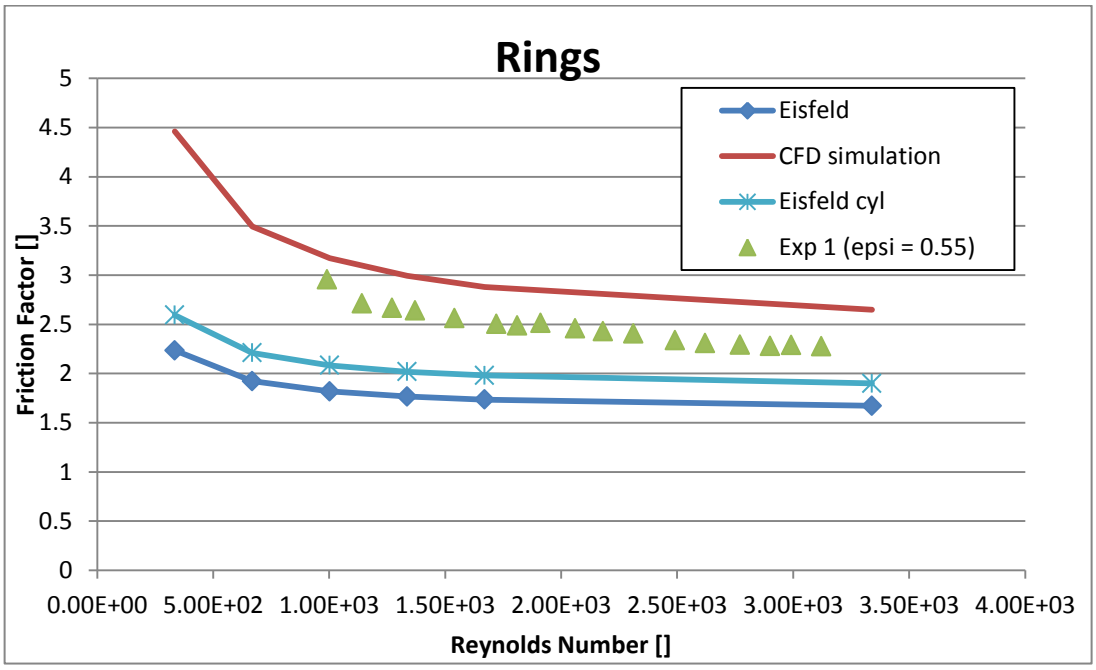


Figure 85: Comparison with experimental data – Rings

Moreover the parameters of all the correlations are fitted based on experimental data, and as it is well known, they are always affected by measurement errors. CFD simulation, instead, since the Navier Stokes equations are solved without introducing approximations, all the phenomena that take place inside the tube are accounted for.

For cylinders the agreement is not good as in the previous cases even if it has already verified that the comparison with literature correlations both for the estimation of the pressure drops and for the void fraction is very satisfactory. For this reason it is possible to interpret the difference between experimental data and CFD simulations, shown in Figure 86, as an error of the article from which the data have been provided. For example, a small error in the estimation of the void fraction for the laboratory scale packed bed can be the cause of these important differences into the comparison.

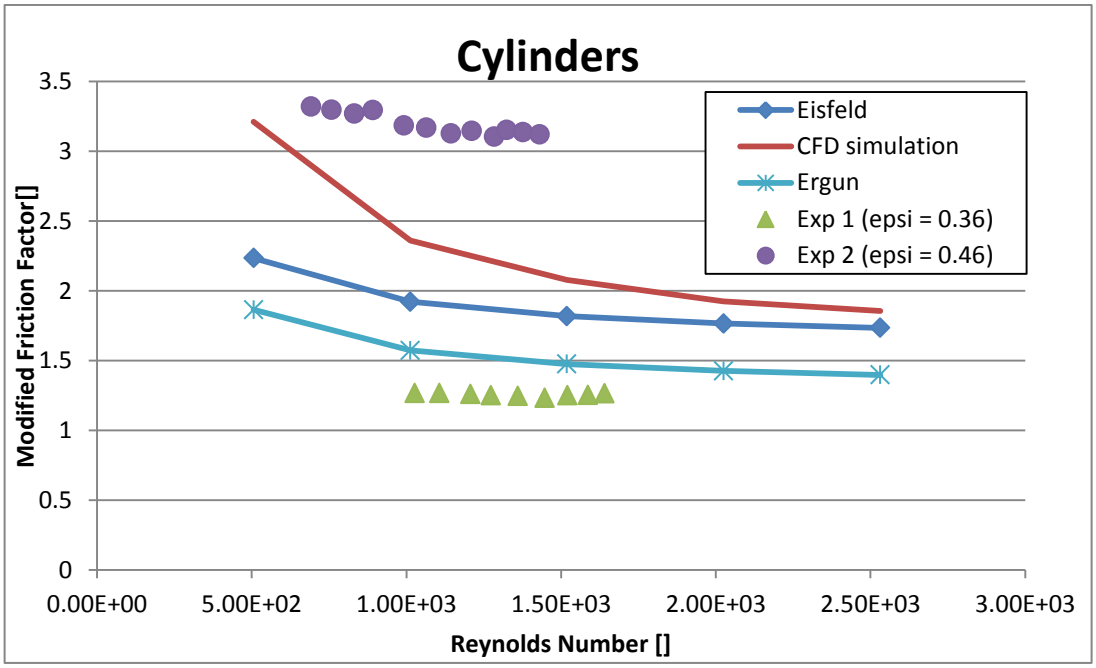


Figure 86: Comparison with experimental data - Cylinders

## 5.4 Conclusions

This analysis has demonstrated that the resulting beds provided with the DEM simulations approximate a real packed bed in a satisfactory way. The comparison of the pressure drops calculated for beds made by spheres and cylinders give satisfactory agreement with the results

provided by the most common literature correlations. In particular for cylinders, it has been demonstrated that the wall effect plays an important role in the establishment of preferential paths near the surfaces of the tube and in parallel in the value of the pressure drops. For rings, the agreement is not good as for the previous cases and the reason is that no correlation has been developed for this particular structure. For instance, taking into account the Eisfeld correlation, using the coefficients for cylinders or “other geometries” is an approximation and an excellent agreement is not expected. Concerning the void fraction, the results of the CFD simulation tend asymptotically to the values provided by Dixon correlations for the three geometries.

# 6 Simulation of the ethylene oxide packed bed reactor

The goal of this chapter is to show the capability of the catalyticFOAM solver to simulate complex geometries as those of a typical industrial reactor. This time, the results have not been compared with experimental data because the real aim is to obtain a qualitative response of the solver and not a quantitative analysis. The three different geometries of the packed beds (spheres, cylinders and rings), described and studied in Chapter 4, have been employed in the study of the ethylene oxidation process. These simulations are the results of a period of internship at the fluid dynamic department of the BASF production plant of Ludwigshafen (DE) under the supervision of Dr Stefan Lipp.

The simulations have been carried out both with and without considering the numerical modeling of the solid phase. The former solver has allowed to analyze the effect of the catalyst geometry on the reactant conversion both in isothermal and in adiabatic conditions. The latter solver has allowed to analyze the importance of the transport phenomena inside the catalyst.

## 6.1 The ethylene oxide process – an introduction

Ethylene oxide, also called oxirane, is the organic compound with the formula $C_2H_4$. It is a cyclic ether and a colorless flammable gas at room temperature, with a faintly sweet odor. It is the simplest epoxide: a three-membered ring consisting of one oxygen atom and two carbon atoms. Because of its special molecular structure, ethylene oxide easily participates in addition reactions (e.g., opening its ring and thus easily polymerizing). Ethylene oxide is isomeric with acetaldehyde and with vinyl alcohol.

The chemical reactivity that is responsible for many of ethylene oxide's hazards has also made it a key industrial chemical. Although too dangerous for direct household use and generally unfamiliar to consumers, ethylene oxide is used industrially for making many consumer products, as well as non-consumer chemicals and intermediates. Ethylene oxide is important or critical to the production of detergents, thickeners, solvents, plastics, and various organic chemicals such

as ethylene glycol, ethanolamines, simple and complex glycols, polyglycol ethers and other compounds. As a poison gas that leaves no residue on items it contacts, pure ethylene oxide is a disinfectant that is widely used in hospitals and the medical equipment industry to replace steam in the sterilization of heat-sensitive tools and equipment, such as disposable plastic syringes.

Industrially, the oxidation of ethylene is carried out in non-adiabatic multi-tubular fixed-bed catalytic reactors. Generally the length of the tubes falls in the range 6 - 12 m with a diameter of 20-50 mm. These reactors can achieve production of 250,000 ton/y.

One of the critical issues of this process is the control of temperature within the tubes due to the large amount of heat released by this exothermic process. For this reason an oil cooled system has to be arranged with the aim to maintain the temperature inside the operative limits avoiding catalyst deactivation, selectivity loss as well as thermal runaway.

## 6.2 Numerical simulation of ethylene oxide packed bed reactor

Two different processes are commonly used for the production of ethylene oxide:

- *Air based process*
- *Oxygen based process* (currently favored)

The first process has the advantage that it does not require an air fractionating plant, but the high discharging of the nitrogen, downstream the reactor, leads to higher ethylene losses. The second process requires an air fractionating plant, but the main advantage is the smaller amount of the waste gas produced, determining an important reduction of the ethylene losses. Despite investment and operating costs for an air fractionating plant, the manufactory costs of the oxygen based process are lower than those of the air based process.

The wide range of the flammability limits of the ethylene/oxygen mixture (3%-90%) limits the content of the $O_2$ and $C_2H_4$ in the reactive mixture, making necessary to employ an inert specie. For the oxygen based process the most common inert diluent is methane. The high heat capacity of the methane allows to reduce and control the hot spot in the reactor which can have important

effect not only on the catalyst deactivation but also on the selectivity. In fact, in the reactor, oxidation reactions of ethylene and ethylene oxide can occur, which are more sensitive to the increase of the temperature than to the partial oxidation reaction (due to higher activation energy) leading a decreasing of the selectivity.

In this work the oxygen based process has been analyzed. The composition of the feed considered for all the simulations are shown in Table 30:

| OPERATING CONDITIONS | |
|---|---|
| **$C_2H_4$ Molar Fraction** | 35.% |
| **$O_2$ Molar Fraction** | 5.0 % |
| **$CH_4$ Molar Fraction** | 60.0 % |
| **Pressure** | 15 atm |
| **Inlet temperature** | 432-490-550 K |
| **Inlet velocity** | 1 m/s |

Table 30: Operating conditions ethylene oxide process

As all the oxidation reactions, the oxidation of ethylene is not controlled by thermodynamics but only by kinetics. For these reasons, in order to ensure high conversions and lower dimensions of the reactor, a pressure of 10-20 atm is necessary. Higher values will not be convenient because the cost related to the compression of gases will be extremely high.

Isothermal simulations have been carried out both with the short and long length packed beds reactors that have been set up and described in Chapter 4. The investigated range of temperature is between 432 K and 550 K. The reasons of this choice will be explained better in the next paragraphs.

The adiabatic simulation are extremely computational expensive and for this reason only one value of inlet temperature has been tested in order to investigate this operating condition.

Finally the solver able to characterize the solid phase has been used for a packed bed made by spheres in order to well describe the intra-phases profiles of reactants and products. This simulation has been carried out in isothermal conditions at 490 K.

### 6.2.1 The kinetic scheme

The epoxidation of ethylene to form the ethylene oxide is one of the most important heterogeneous catalytic oxidation processes. The process employs a silver catalyst supported on $\alpha$-$Al_2O_3$ and promoted by alkalis and halides. A molecular level understanding of this reaction is still lacking since the different reacting species are not easily probed during the reaction. It has been suggested that the surface-mediated addition of ethylene to oxygen is the rate-determining step. As illustrated by Linic at al [45], the process can be illustrated with four elementary steps as reported in the reaction coordinate in Figure 87.

$$step\ 1 \quad O_2 + 2^* \leftrightarrow 2O^*$$

$$step\ 2 \quad C_2H_4 + * \leftrightarrow C_2H_4^*$$

$$step\ 3 \quad O^* + C_2H_4^* \leftrightarrow C_2H_4O^* + *$$

$$step\ 4 \quad C_2H_4O^* \leftrightarrow C_2H_4O + *$$

First the adsorption of the two reactants takes place, then the surface reaction provides the oxametallacycle species, precursor of ethylene oxide, and finally the desorption of the product closes the reaction path.

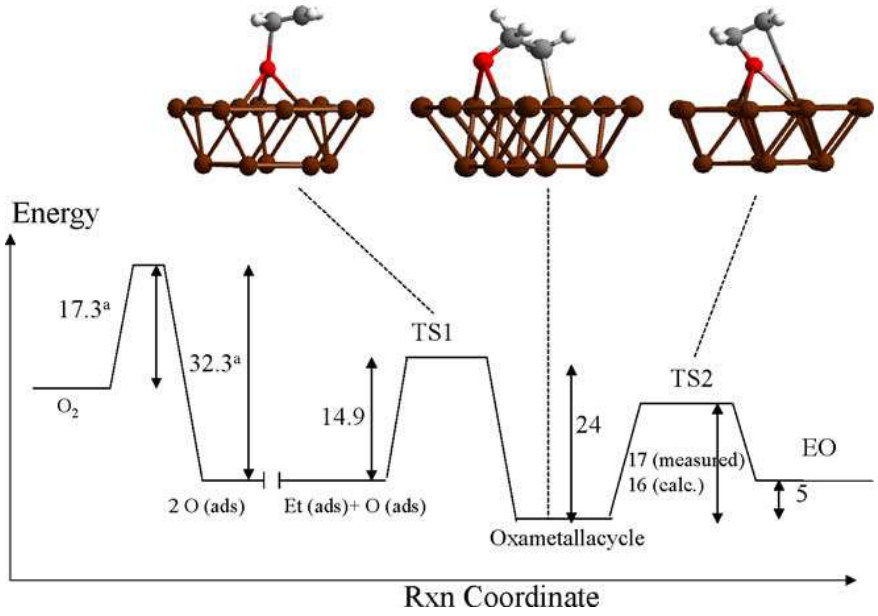


Figure 87: Reaction coordinate for the ethylene oxide process [45]

On the basis of the micro kinetic mechanism proposed above, the same authors have provided a global reaction model for the entire process of synthesis of ethylene oxide:

$$r = k_{overall}(P_{O_2})^n \ (P_{C_2H_4})^m \tag{6.1}$$

where

$$k_{overall} = Ae^{-\frac{E_{att}}{RT}} \tag{6.2}$$

The kinetic parameter as well as the reaction orders of the reactants are reported in Table 31.

| KINETIC MODEL PARAMETERS | |
|---|---|
| A | $9.85 \cdot 10^5$ atm$^2$/(m$^3$ s) |
| Eatt | 15 Kcal/mol |
| m | 0.65 |
| n | 0.71 |

Table 31: Kinetic parameter of the ethylene oxide process [45]

# 6.3 Short packed bed reactor

As already said in Chapter 4, these beds are characterized by a small number of particles and the same catalytic area. The overall lengths are about 1.5 cm.

## 6.3.1 Mesh structure

In this section two different levels of refinement of the mesh have been investigated. In Table 32 the dimensions of the grids have been shown:

| | Level refinment 2 | Level refinment 3 |
|---|---|---|
| Number of cells | 185,626 | 576,311 |
| Number of fluid cells | 144,762 | 385,332 |
| Number of catalytic cells | 40,864 | 190,979 |

Table 32: Number of cells of the short length packed beds reactors

Figure 88 shows the differences in the refinement of the two grids. The spheres in the second one are strongly more detailed and the “bridges” between the particles are completely disappeared. In this way it is possible to better characterize the concentration gradients of reactants and products in proximity of the reacting surface.

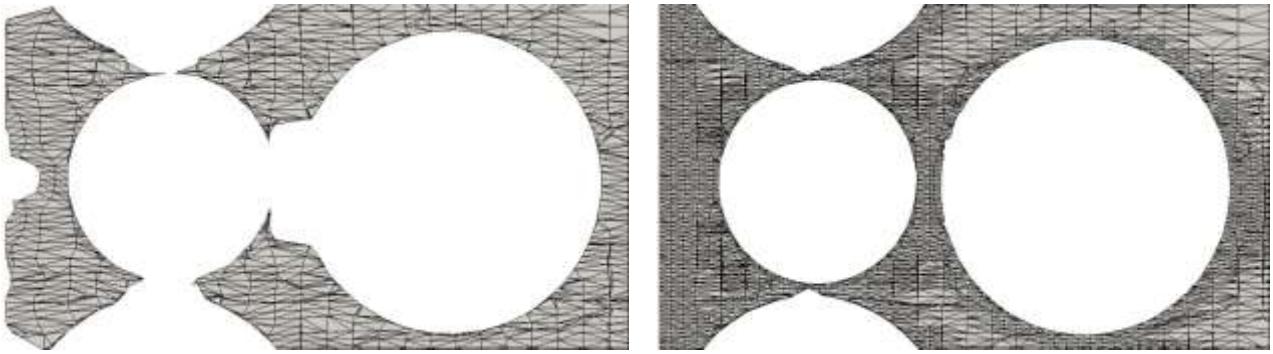

Figure 88: Particular of the meshes with the two levels of refinement

### 6.3.2 Isothermal simulations

The performances of the three different packed beds have been investigated under isothermal conditions at three different temperatures:

- 432 K: this temperature can be considered as a lower temperature limit for this kind of reaction in industrial applications;
- 550 K: this temperature is commonly considered as the upper limit for the process. Above this temperature the side reactions will be the dominant ones;
- 490 K: this temperature has been chosen in order to have a better understanding of the behavior between the lower and the upper limit.

An inlet temperature higher than 550 K is not possible because above this limit the parallel reactions of direct oxidation of ethylene and the oxidation of ethylene oxide into $CO_2$ and $H_2O$ will be the dominant ones and this causes a strong decrease of the selectivity of the expected product, i.e. the ethylene oxide.

These beds are characterized by the same catalytic area, thus the reactivity of the system is controlled by the capacity of the three structures (spheres, cylinders and rings) to transfer mass and heat at the interface between the bulk phase and the reacting wall.

Table 33 shows the reactants conversion for the three reactor configurations at 432 K.

| | $C_2H_4$ Conversion | $O_2$ Conversion |
|---|---|---|
| Cylinders | 3.5 % | 9.3 % |
| Spheres | 3.6 % | 9.7 % |
| Rings | 3.5 % | 9.5 % |

Table 33: Conversion in isothermal conditions - 432 K

As it possible to see in Table 33, the conversions for the three beds are the same. This means that the geometry of the basic structure at low temperature doesn't affect the results of the simulations.

Figure 89 shows the composition fields inside the beds of reactants and product. As it possible to see, the packed bed made by spheres presents some recirculations demonstrated by the lower concentration of ethylene at the end of the catalytic bed.

The ethylene oxide mass fraction in the three beds is more or less the same (about 12%).

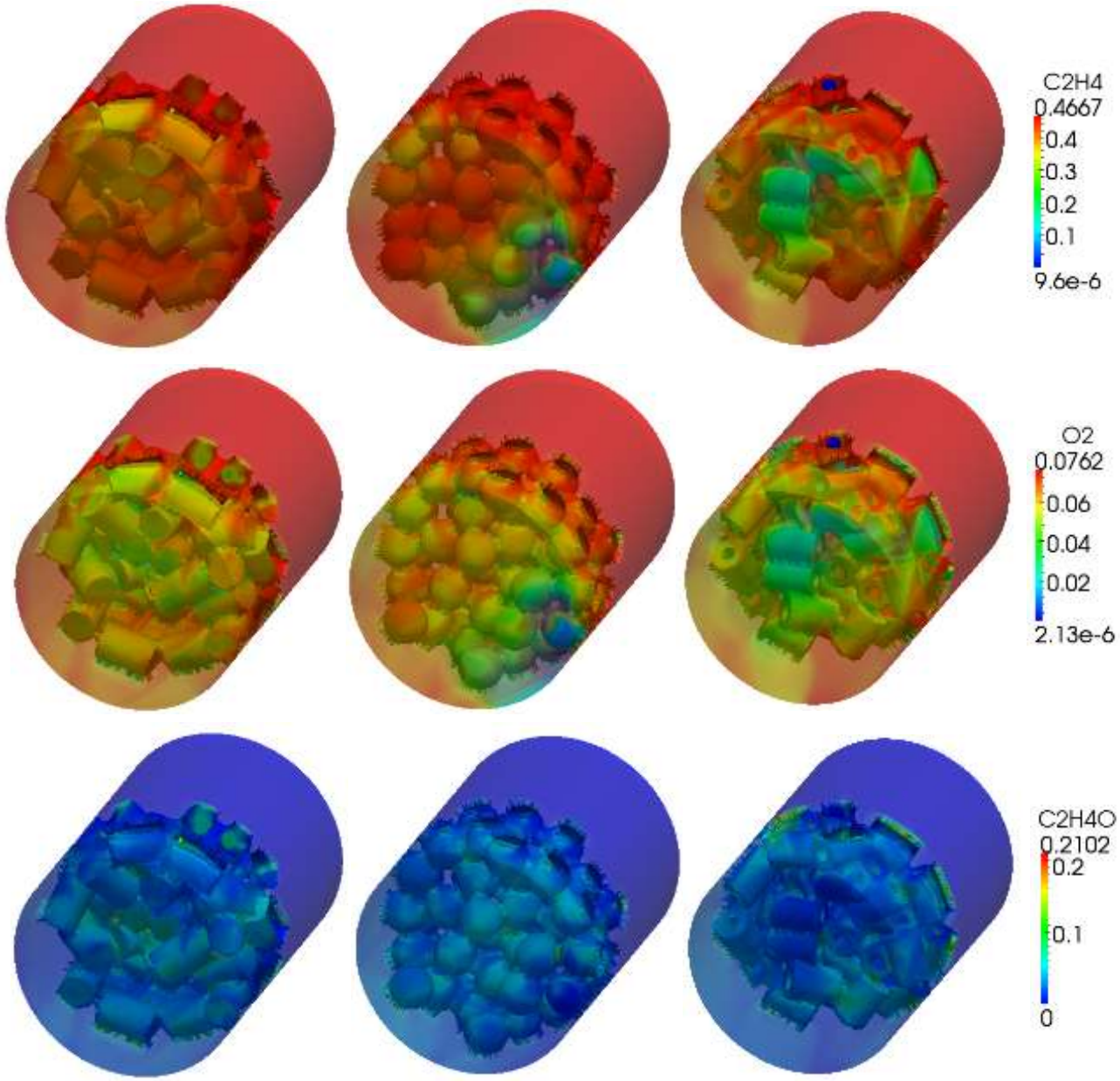


Figure 89: Maps of mass fractions of selected species in the gas phase (isothermal conditions, 432 K

In Figure 90 it is possible to note a problem in the structures of the meshes. In particular for the rings it is very difficult to characterize in a correct way the holes inside them. If the mesh is not refined enough the reactants are not able to go through the cavity (the massive fractions of $C_2H_4$ and $O_2$, in fact, are equal to zero) and the holes will remain full of inert component (methane). The main problem is that this catalytic area doesn't participate to the reaction. The available computational resources don't allow enhancing the number of cells of the mesh but it is obvious that increasing the level of refinement with snappyHexMesh this problem will probably disappear. Aim of this chapter, in fact, is not to compare the results with experimental data (for which it is

necessary to have a very fine grid), but it is to present the potentialities of the solver also in complex geometries. The fact that at low temperatures the conversions reached with the three beds are the same, goes to this direction. At low temperature, as in chemical regime happens, the shape of the catalyst does not influence the results.

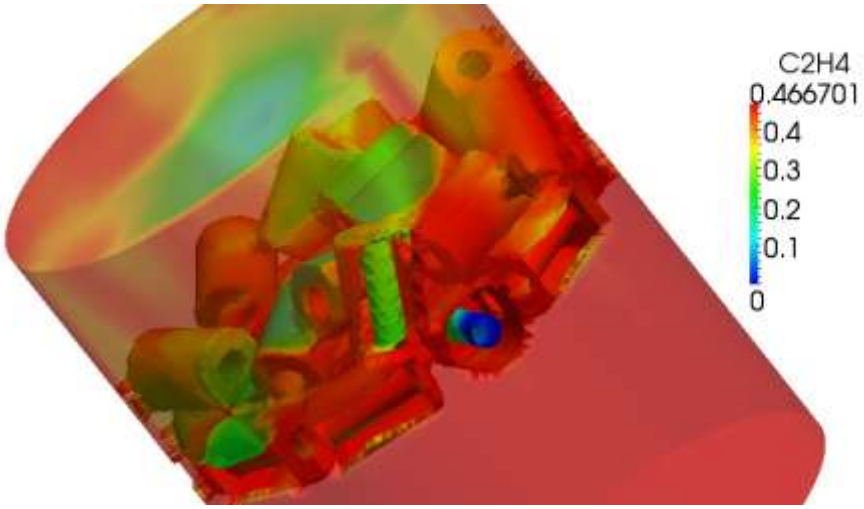


Figure 90: Detail of a hole of a ring - problem in the refinement of the mesh

Table 34 shows the numerical results of the simulations carried out at 550 K.

| | $C_2H_4$ Conversion | $O_2$ Conversion |
|---|---|---|
| Cylinders | 25.0 % | 87.7 % |
| Spheres | 27.0 % | 89.8 % |
| Rings | 22.8 % | 77.6 % |

Table 34: Conversion in isothermal conditions - 550 K

In this case it is possible to note that the geometry of the beds influence the results and thus the conversion of the reactants. Here the structure that is able to transfer in the best way mass and species at the interface of the catalyst ensures the highest level of conversion.

Figure 91 shows the composition fields at 550 K. As it possible to see the average value of the mass fraction of ethylene oxide is higher compared with the one at 432 K. From the compositions fields, it is already possible to assert that the highest value of conversion in these cases is obtained

with the packed bed made by sphere (the average value of the mass fraction of $C_2H_4O$ is higher compared with the other two beds).

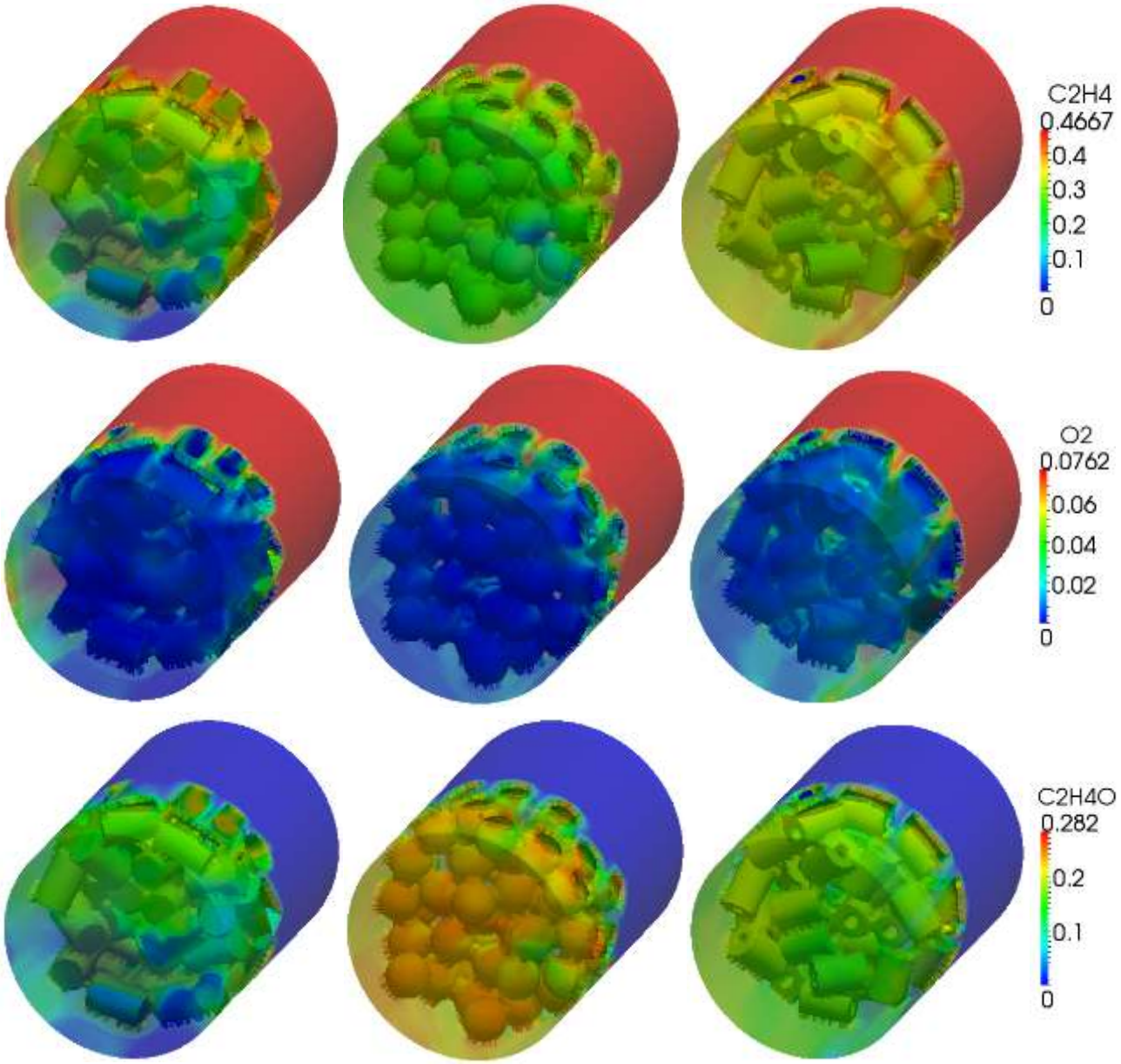


Figure 91: Maps of mass fractions of selected species in the gas phase (isothermal conditions, 550 K)

Figure 92 shows the comparison between the performances of the three catalyst configuration at different temperatures. As it possible to observe, the increase of the temperature not only determines an increasing of the ethylene conversion for any configuration, but, more important it causes an increasing of the differences of the performance between the three catalysts.

The bed made by spheres provides the highest conversion. With the same catalytic area, this structure is the one that can guarantee the best transfer of mass and species at the surface of the

catalyst. The worst conversion belongs to the bed made by rings. As already explained in Figure 90 this fact could be attributed to the small differences in the catalytic area caused by the non-availability of some holes of this structure.

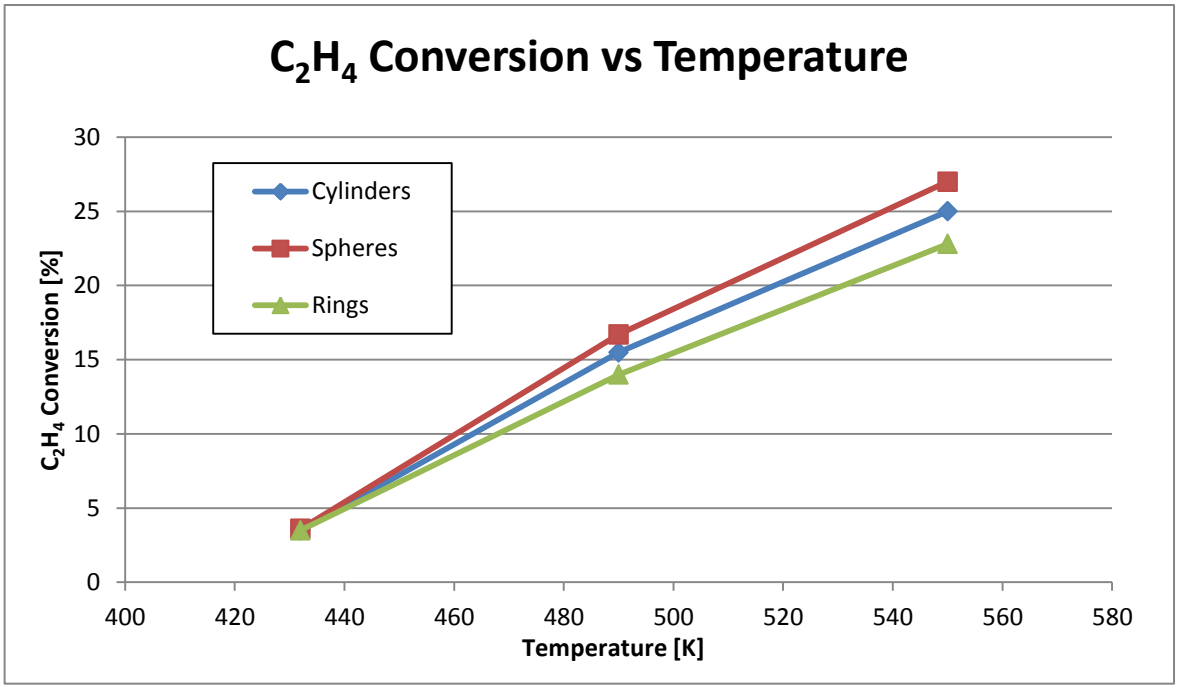


Figure 92: Conversion at different temperatures of the three packed beds

## 6.3.3 Adiabatic simulations

The oxidation of ethylene is an exothermic reaction and as already mentioned one of the main issues is the control of temperature inside the reactor. For this reason it is interesting to test the solver in adiabatic conditions in order to find all the criticalities that could affect these simulations. First of all the case with inlet temperature equal to 432 K that has been analyzed in Paragraph 5.2 is here investigated. The results of the temperature field inside the reactors are the following:

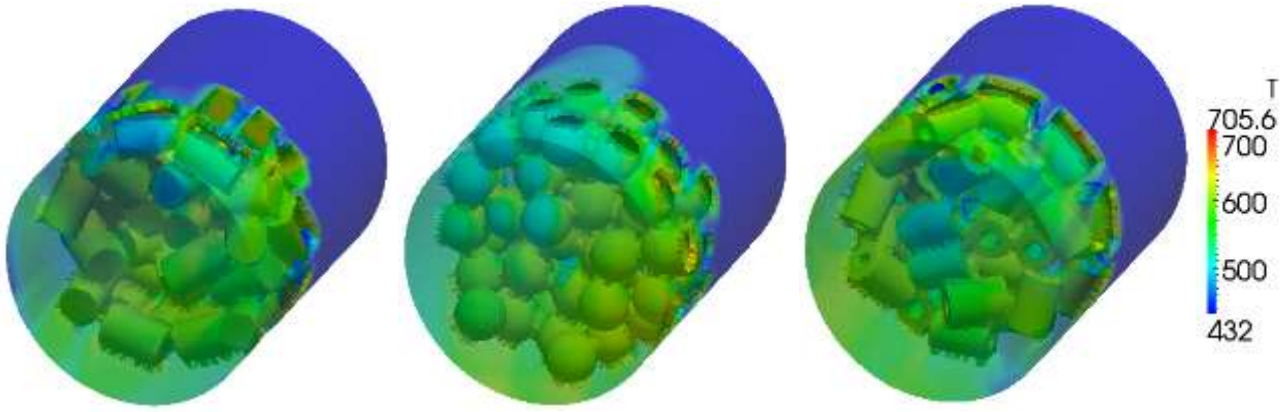


Figure 93: Maps of temperature in the gas phase (adiabatic conditions, 432 K)

Figure 93 shows an important increasing of the temperature inside the reactor with an average temperature of about 600 K. The peaks of 700 K are due by a non-perfect refinement of the mesh near the surface of the tube. Here the catalyst is in contact with the wall of the reactor. At these points of contact, the cells become highly skewed, affecting the quality of the mesh and causing numerical inaccuracies and/or unphysical temperature fields.

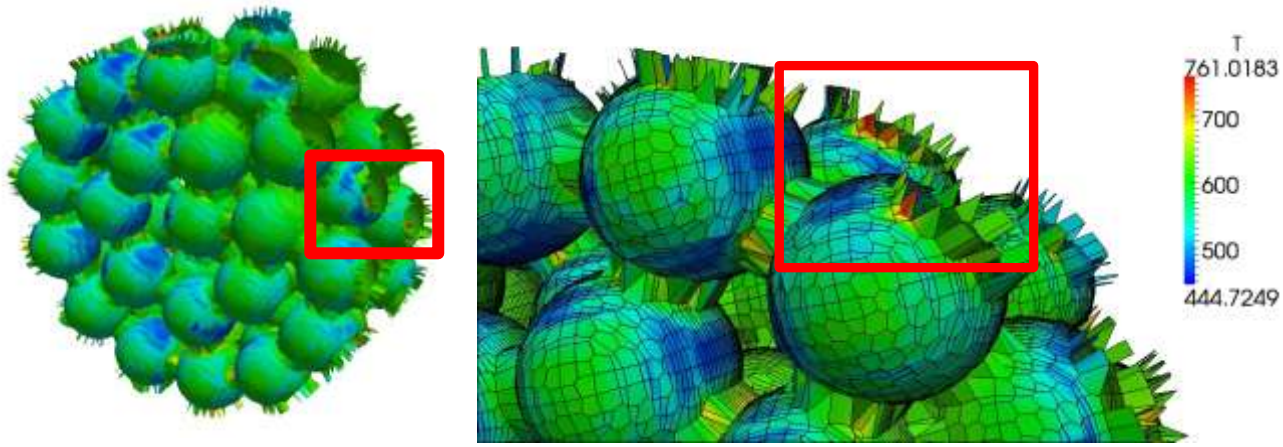


Figure 94: Particular of the cells near the surface of the tube

As it is possible to see in Figure 94, just a few number of cells are interested by this phenomenon and all of them are in contact with the wall of the tubes.

### 6.3.4 Adiabatic simulations with a refined mesh

In order to overcome the problem presented in the last paragraph, a more refined mesh has been developed. In particular the level of the refinement has been increased from level 2 to level 3

using snappyHexMesh. With this choice a new mesh characterized by 160,000 catalytic cells has been achieved (the first mesh was characterized by only 40,000 catalytic cells)

As it is possible to see in Figure 97 with the refined mesh the hot spots near the surface of the tube completely disappeared. The temperature peak is 100°C lower than the one obtained with the less refined mesh. In this way feasible results have been achieved.

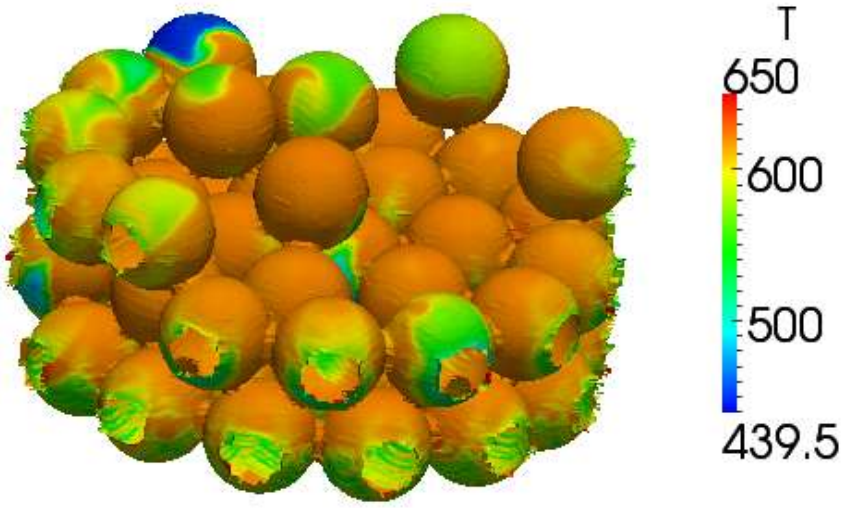


Figure 95: Temperature field with refined mesh

# 6.4 Long packed bed reactor

In order to verify the reliability of the results obtained with the short packed beds, the same simulations at 432 K have been carried out exploiting the extended packed beds. As it has been demonstrated in Chapter 4, with a length of 10 cm the asymptotic behavior of the bed has been achieved: void fraction and pressure drops are the same predicted by literature correlations.

## 6.4.1 Mesh structure

The dimensions of the grids that have been used for the following simulations are shown in Table 35:

| | Spheres | Cylinders | Rings |
|---|---|---|---|
| Number of cells | 776,797 | 622,605 | 347,086 |
| Number of fluid cells | 476,513 | 345,611 | 214,936 |
| Number of catalytic cells | 300,284 | 276,994 | 132,150 |

Table 35: Number of cells of the long length packed beds reactors

In Figure 96 a slice of the packed bed made by sphere are presented. In this case increase the level of the refinement that allows to remove the bridges between the particles is not possible due to the high computational effort already required with this level.

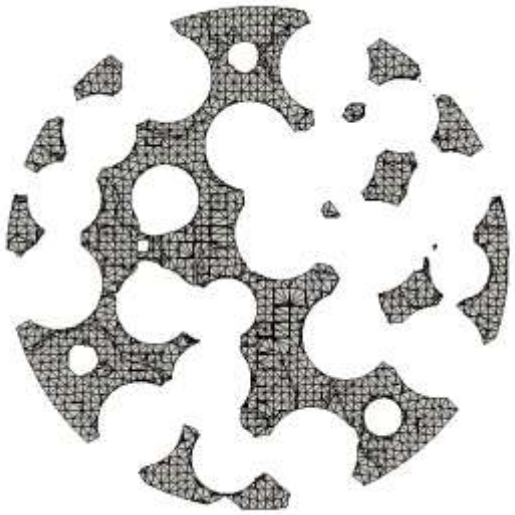

Figure 96: Slice of the long length packed bed made by sphere

These simulations, in fact, are computationally demanding because of the high number of catalytic cells. For these reasons parallel runs on a high number of processors are absolutely necessary in order to complete the simulations saving computational time.

### 6.4.2 Isothermal simulations

In this section the long length packed beds have been exploited to simulate the same case presented in Paragraph 5.3.2 at 432 K. The conversion results of the simulations for the two reactants are shown in Table 36:

| | $C_2H_4$ Conversion | $O_2$ Conversion |
|---|---|---|
| Cylinders | 19.0 % | 66.5 % |
| Spheres | 19.2 % | 68.9 % |
| Rings | 18.7 % | 67.7 % |

Table 36: Long length reactor - conversion at 432 K

The compositions fields of reactants and product are provided in Figure 97-Figure 99:

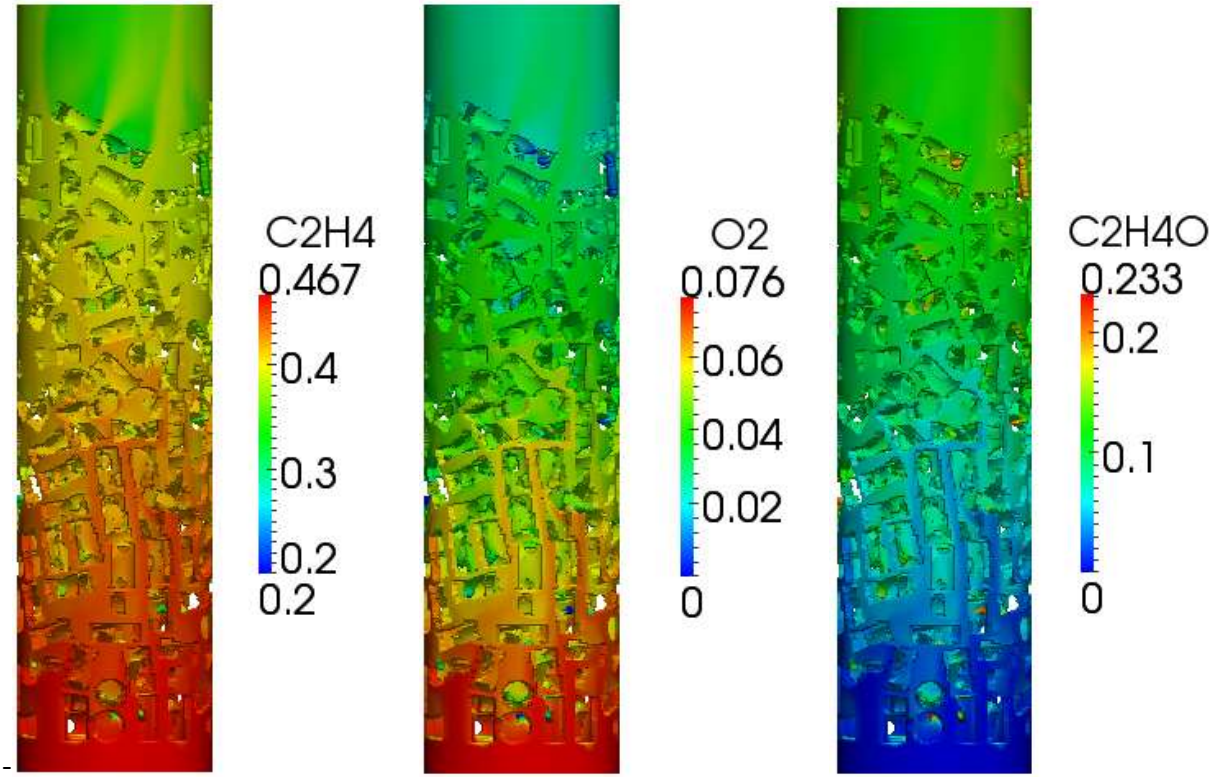


Figure 97: Long length reactor - Cylinders - 432 K

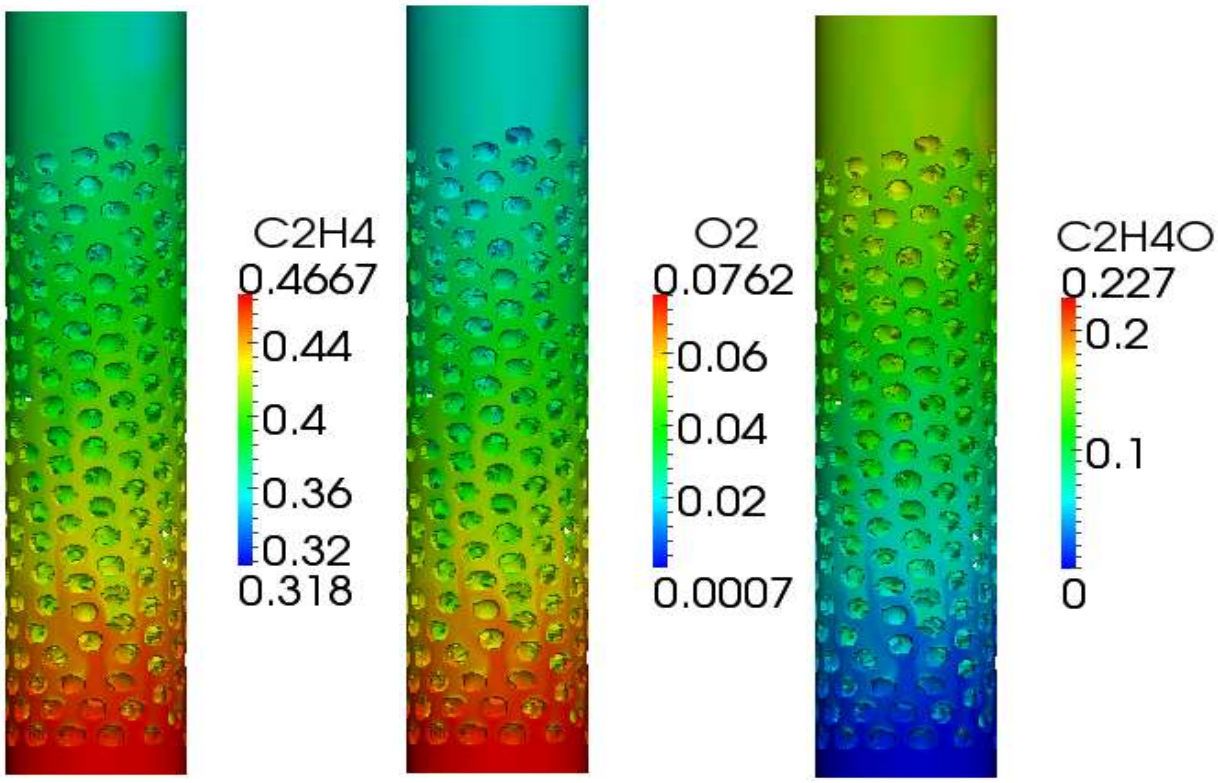


Figure 98: Long length reactor - Spheres - 432 K

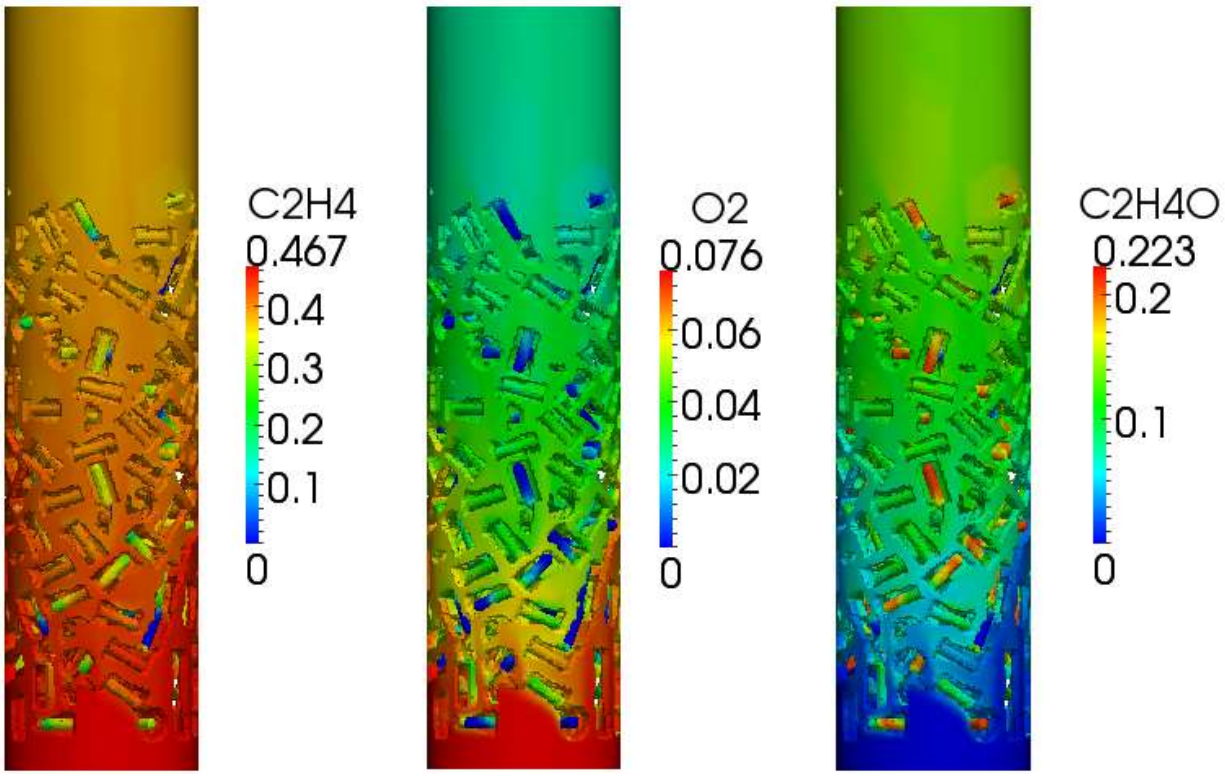


Figure 99: Long length reactor - Rings - 432 K

Table 36 shows that at low temperature the conversions of ethylene obtained with the three beds are substantially the same. This fact has been already verified with the small length packed beds and it is possible because also in these cases the beds are set up to guarantee the same catalytic area. This means that to study the behavior of the three reactive systems it is sufficient to simulate 2 cm of the reactor. In this way the computational effort required is absolutely lower.

From Figure 99 it is possible to see that the same problem of the refinement of the mesh is here present. The holes inside the rings are not refined enough in order to well characterize the flow of the reactants inside them. Also at steady state, holes remain full of methane, the inert species that at the beginning fills the tube.

Differently from the small length packed beds, no simulations at 550 K have been provided because at this temperature the conversion of the limiting reactant is complete in all the three structures due to the higher reactivity of the system at this temperature. For this reason it is not possible to give any consideration about the behavior of the different packed beds at this high temperature.

## 6.5 Multi-Region approach to the packed beds

The spheres packed bed has been investigated also with a multi-region approach. In this case not only the fluid phase has been meshed, but also the catalytic spheres in order to characterize the profile of reactants and products within the solid phase.

### 6.5.1 Mesh for the solid phase

The meshing tool that has been used in order to set up these two different meshes is always *SnappyHexMesh*. In these cases it is necessary to define the level of the refinement both for the fluid phase and the solid one. It is important to remember that the two meshes have to be conformal. In other words, the number of the interface cells between two regions have to be the same, as shown in Figure 100. It is possible to achieve this aim only using the same level of refinement for the two phases.

As for the meshes presented in Chapter 5 (regarding only the fluid phase), the region close to the catalyst has a higher density of cells in order to well characterize the strong grading between the

boundary layer. At the same time, inside the catalytic spheres, the level of refinement is higher near the surface and less detailed in the center, where the reaction has been completely depleted.

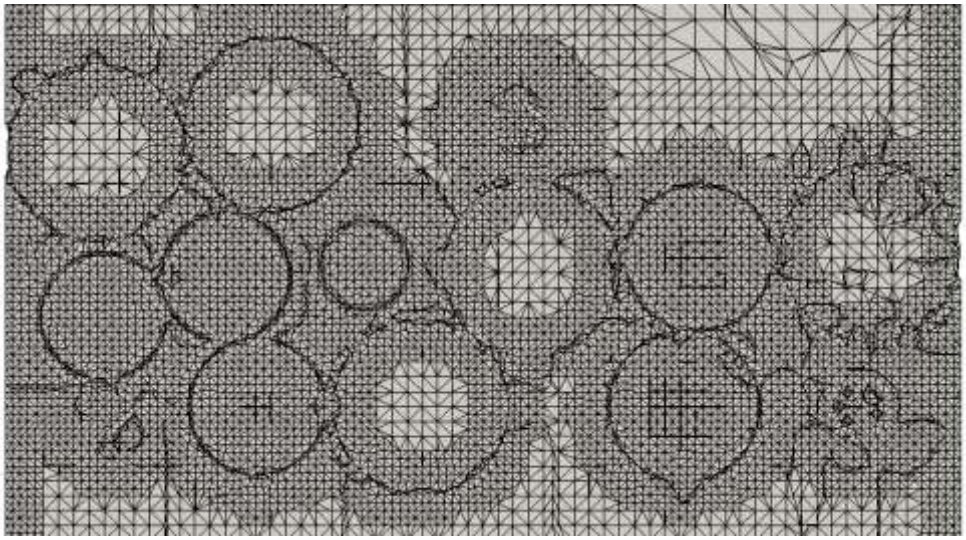

Figure 100: Solid and fluid meshes - Spheres

## 6.5.2 Simulation results

The aim of this section is to understand how the profile within the solid of reactants and products and thus the internal diffusion phenomena can modify the results of the simulations provided with the first solver (in which the numerical modeling of the solid phase is not considered). Observing these trends inside the catalyst it is possible to understand which transport phenomenon is the governing one: chemical, pore diffusion or mass transfer.

Following the simulation at 490 K in isothermal conditions has been presented.

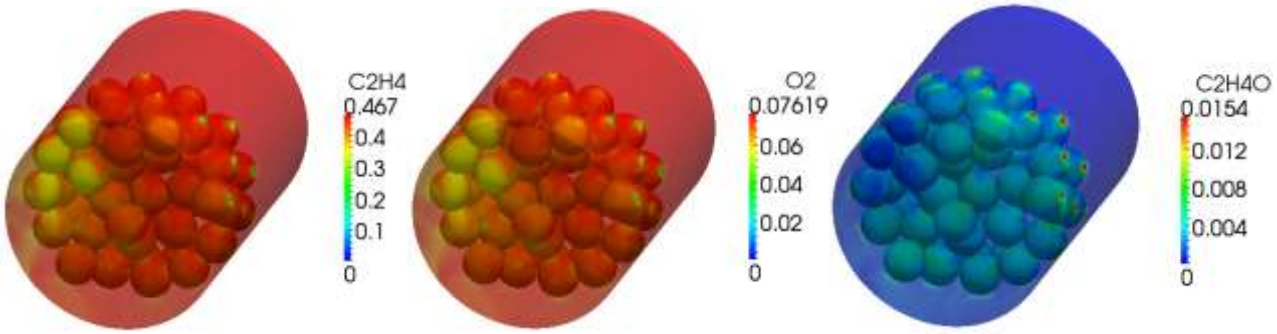


Figure 101: Composition field in gas phase using the multi-region approach

Figure 101 shows the composition fields in the gas phase using the multi-region approach. Here it is already possible to note that the production of ethylene is lower compere with the one calculated in the previous cases (Figure 89 and Figure 91).

A deep analysis of the profiles within the solid phase is now provided in order to understand if the reaction involves all the structure of the catalyst or only the external volume. With a solid sphere of 6 mm the second hypothesis is more realistic.

Figure 102 the composition fields of ethylene and ethylene oxide are presented:

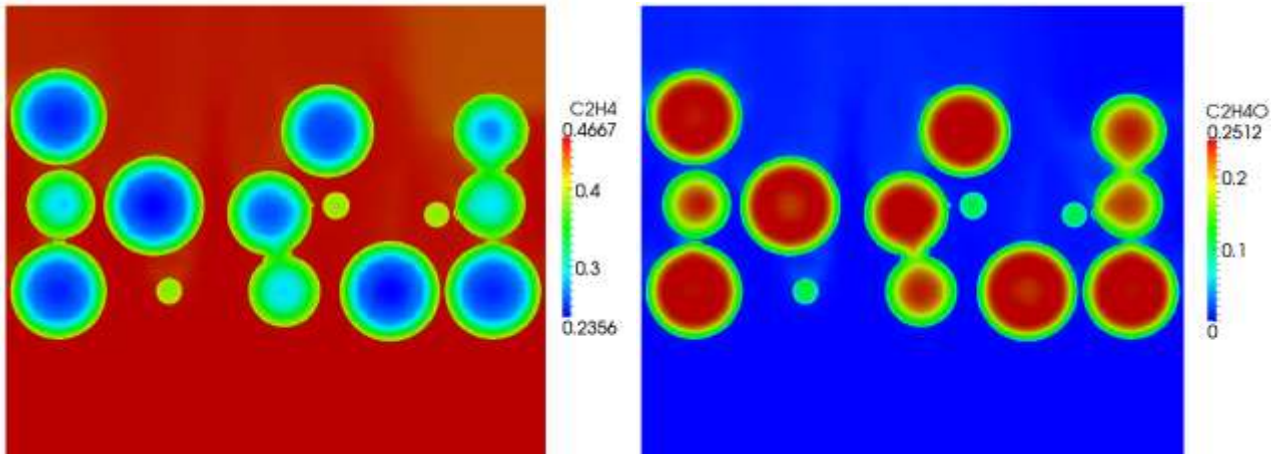


Figure 102: Composition fields of ethylene and ethylene oxide within the fluid and the solid regions

Figure 102 shows that the reaction takes place only in an external layer of the catalyst, close to the surface of the catalytic sphere. The ethylene oxide, instead, has reached the center of the structure as always happen for a product inside a catalyst.

Figure 103 shows the oxygen profile within the solid phase. As it possible to see all the catalytic structure is involved by the reaction of oxidation of ethylene. In this cases the local value of reactants is not costant within the solid phase and a radial profile is highlighted. With the previous solver, instead, the active sites located only on the reactive surface were interested by the same value of oxygen concentration. This difference can explain the lower conversion onbtained with the multiregion approach in the same conditions of temperature and pressure. This value, in fact, is about 2%.

The comparison between the two cases is possible because there is a perfect equivalence between the activity of the catalyst considered as a reactive surface (first approach) or porous volume.

$$\alpha_{catalyticFOAM} \cdot A = \alpha_{multiregion} \cdot V \tag{6.3}$$

It is clear that in this condition of temperature, the governing regime inside the catalyst is the pore diffusion phenomenon.

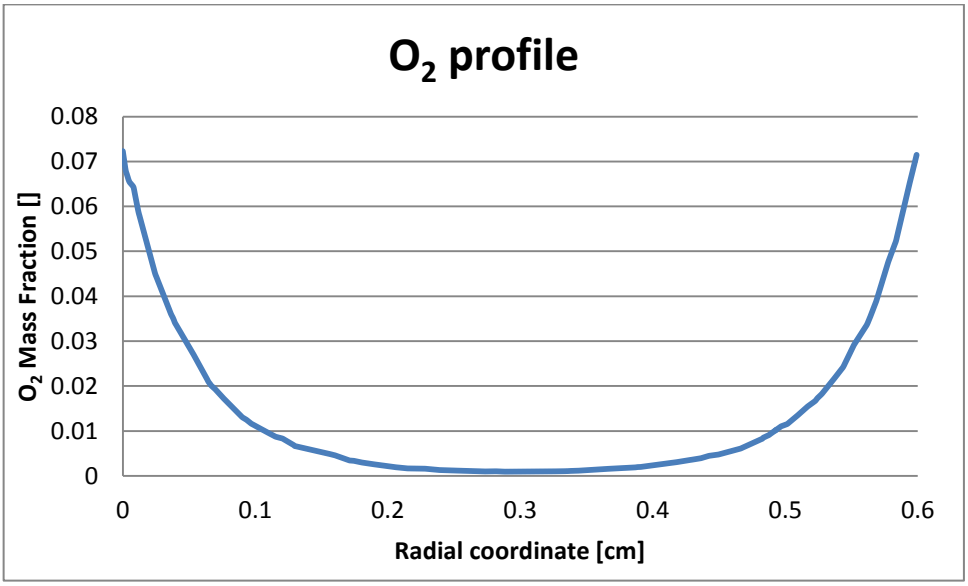


Figure 103: Oxygen profile within the solid phase

# 6.6 Conclusions

In this Chapter the validation of both the solvers with complex geometries has been provided. The process of oxidation of ethylene into ethylene oxide in packed beds reactors are physically represented by these two computational tools (catalyticFOAM and catalyticFOAM multiRegion). In the first cases the main issue that has to be solved is the refinement of the mesh, in particular for adiabatic simulations: the grid has to be strongly refined particularly near the surface of the reactor where catalyst is in contact with the wall of the tube. Simulations with the short length beds and the extended ones have demonstrated that at low temperature the geometries of the beds do not influence the result (conversion) of the runs. At high temperature, instead, the structure that is able to transfer in the best way species at the interface between catalyst and bulk phase is the one that achieve the highest conversion of ethylene.

The multi-region solver has allowed to identify that only a small layer of the catalyst volume is interested by the oxidation reaction. The conversion in this case is lower compared with the one obtain with the first approach. The system is controlled by pore diffusion, phenomenon that catalyticFOAM is not able to characterize and for this reason conversion is over estimated.

# Conclusions

In this work of thesis an extensive and comprehensive optimization of the catalyticFOAM solver has been addressed in order to allow for its successful and efficient applications on relevant industrial cases.

The first code, named catalyticFOAM, is able to investigate catalytic heterogeneous systems with a detailed microkinetic description only of the surface reactivity. The numerical modeling of the solid phase is not considered. Two main issues were investigated during this work.

1. The solver has been tested only for simple geometries in isothermal conditions. The modeling of the temperature field inside the reactor is crucial to identify possible hot spot that can cause deactivation of the catalyst and, hence, increase of the purchasing costs. This issue has been taken into account in this work through an efficient coupling between the material and energy balance. Although the system analyzed is strongly non-linear, the new algorithm is able to guarantee numerical stability of the solution. Different simulations of increasing complexity have been performed in several reactive systems: hydrogen combustion, reverse water gas shift and steam reforming.
2. The second point investigated was the influence of the equation order of the operator splitting technique. In fact, the catalyticFOAM-0.9 solver is based on this methodology for the coupling between microkinetic modeling and CFD. The numerical scheme adopted consists in the splitting of the source term from the transport one and the integration of each of them separately and sequentially. In agreement with the literature, an efficient resolution strategy has been identified. It consists in solving first the transport equations and eventually the reactive term due to its stabilizing effect on the solution.

The second solver, named catalyticFOAM-multiRegion and developed in a previous work [1], presents a detailed description not only of the fluid phase, but also of the solid catalyst. The critical step was found to be the correct description of the interface between the different regions. The original solver was not able to characterize accurately this aspect and the mathematical model was not able to ensure the numerical stability of the solution. In order to overcome these criticalities a more physical analysis of the coupling at the interface has been introduced. In particular, a segregated approach has been adopted, involving an iterative algorithm (PIMPLE

loop) to conjugate neighboring regions. The introduction of multiple phases requires an accurate description of the domains mainly in proximity of the interface. The need to work with very refined meshes leads to an increase of the computational effort. In order to overcome this problem a parallel version of the code has been implemented. The architecture of the parallel solver has been modified to solve the problem of synchronization of the processors during the simulation. Several tests have been performed to validate the new coupling strategy adopted. Diffusion-reaction isothermal cases with different geometries have been carried out and the results showed an excellent agreement with the available analytical solution of the problem. Moreover, the reliability and predictive capabilities of the developed solver have been tested by comparing the numerical results with the experimental data of a fuel rich combustion of hydrogen in an annular reactor. The importance of the description of the intra-phase phenomena inside the catalytic solid phase has proven to be critical in order to accurately predict conversion profiles in the catalytic system considered.

Eventually the two solvers have been use to test relevant industrial cases. A catalytic packed bed reactor for the production of ethylene oxide has been simulated during a period of internship in BASF. The catalytic beds (spheres, cylinders and rings) have been set up with a computational tool based on the DEM methodology. The reliability of the obtained beds has been verified comparing void fraction and pressure drops calculated with CFD simulations and correlations available in the literature. The results of the simulations highlighted the difference and the potentialities of the two solvers.

Future developments will be focused on the improvement of the reliability of the two codes and the extensions of their range of applicability. In particular, the following main objectives can be highlighted

- development of a tool for the reaction path analysis based on actual reaction rate;
- numerical modeling of turbulence;
- identification of improved strategies for speeding-up the computational time both for steady-state and unsteady state problems.

# Appendix A - snappyHexMesh

The *snappyHexMesh* utility generates 3-dimensional meshes containing hexahedra (hex) and split-hexahedra (split-hex) from triangulated surface geometries in Stereolithography (STL) format. The mesh approximately conforms to the surface by iteratively refining a starting mesh and morphing the resulting split-hex mesh to the surface. An optional phase will shrink back the resulting mesh and insert cell layers. The specification of mesh refinement level is very flexible and the surface handling is robust with a pre-specified final mesh quality. It runs in parallel with a load balancing step every iteration.

In order to run snappyHexMesh, the user requires the following:

- surface data: files in STL format, either binary or ASCII, located in *costant/triSurface* sub directory of the case directory;
- a background hex mesh which defines the extent of the computational domain and a base level mesh density; typically generated using the *blockMesh utility*;
- a *snappyHexMeshDictionary*, with appropriate entries, located in the system sub-directory of the case.

At this point the user has to decide the level of refinement of the mesh. With an iterative process this tool is able to generate a grid with different level of detail, more accurate near the surface of the catalyst (defined in the STL) and the boundary of the reactor (Figure 104).

```
// Surface based refinement
// ~~~~~~~~~~~~~~~~~~~~~~~~

// Specifies two levels for every surface. The first is the minimum level,
// every cell intersecting a surface gets refined up to the minimum level.
// The second level is the maximum level. Cells that 'see' multiple
// intersections where the intersections make an
// angle > resolveFeatureAngle get refined up to the maximum level.

refinementSurfaces
{
    catalyst_Topology.stl
    {
        level (3 3);
    }
    reactor_tube
    {
        level (2 2);
    }


}
```

Figure 104: Detail of the snappyHexMeshDict

Here the definition of the level of refining of snappyHexMeshDict is presented. As it has already said before, it is possible to define two levels of detail (minimum and maximum) of the mesh both for the structure of the bed described in the STL file and for the background mesh of the tube. The minimum level is applied generally across the surface; the maximum level is applied to cells that can see intersections that form an angle in excess of that specified by resolveFeatureAngle.

The simple steps that the user has to follow in order to generate the mesh are [59]:

1. **Create the background Hex mesh**: before the execution of snappyHexMesh it is necessay to create a background mesh of hexaedral cell that fill the entire region (Figure 105) this can be done simply by using blockMesh.

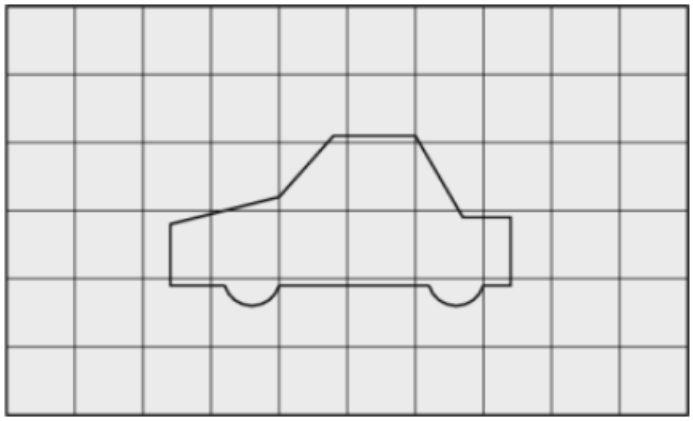

Figure 105: Initial mesh generation in snappyHexMesh meshing process

2. **Cell splitting at feature edges**: Cell splitting is performed according to the specification provided in the snappyHexMeshDict dictionary. The splitting process begins with cells being selected according to specified edge features as illustrated in Figure 106**:**

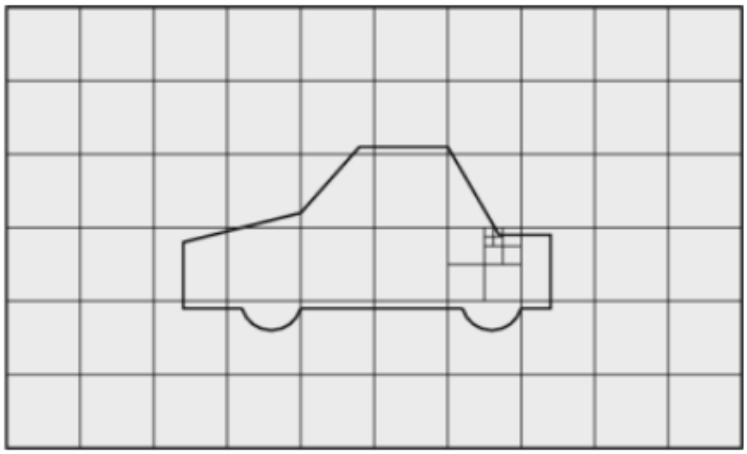

Figure 106: Cell splitting by feature edge in snappyHexMesh meshing process

3. **Cell splitting at the surface**: Following feature refinement, cells are selected for splitting in the locality of specified surfaces as illustrated in Figure 107:

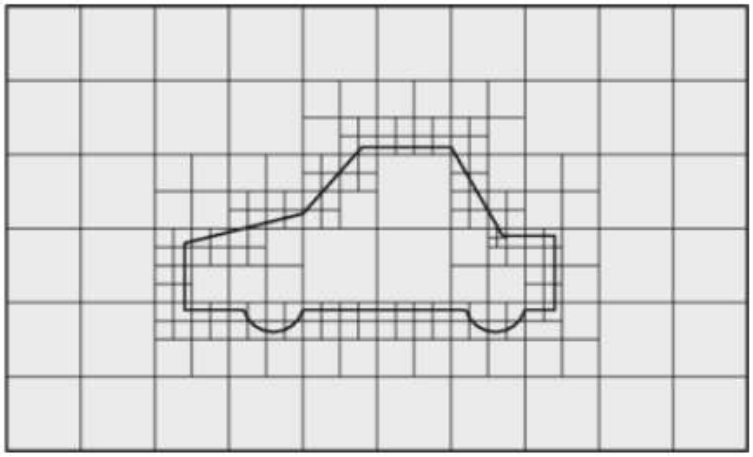

Figure 107: Cell splitting by surface in snappyHexMesh meshing process

4. **Cell removal**: once the feature and surface splitting is complete, a process of cell removal begins. The region in which cells are retained are simply identified by a location vector within the region. Cells are retained if, approximately speaking, 50% or more of their volume lies within the region (Figure 108):

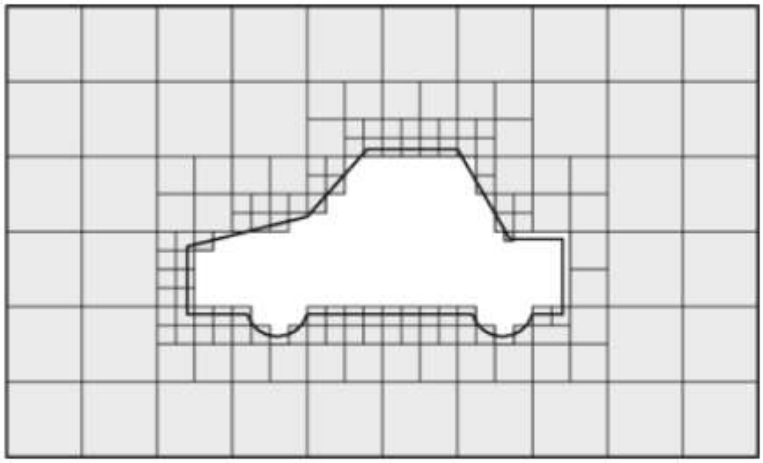

Figure 108: Cell removal in snappyHexMesh meshing process

1. **5 Snapping to surface:** After deleting the cells in the region specified and refining the volume mesh, the points are snapped on the surface to create a conforming mesh ( Figure 109).

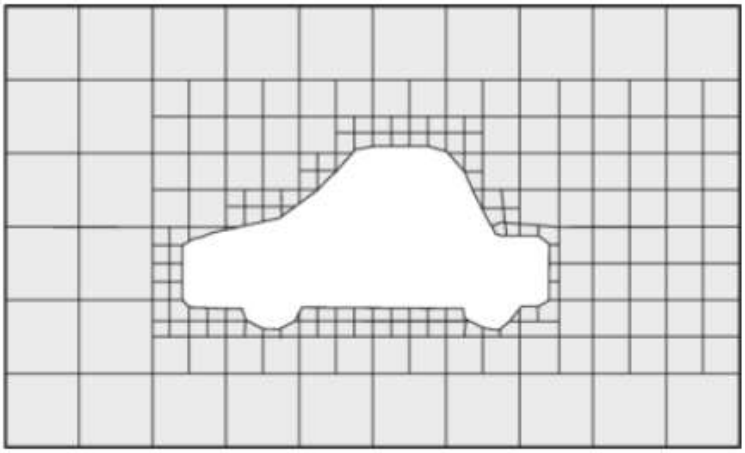

Figure 109: Surface snapping in snappyHexMesh meshing process

# Appendix B – The microkinetic schemes

In this Appendix the kinetic schemes used for the numerical simulations described in the previous chapters are provided.

The UBI-QEP heterogeneous kinetic schemes of $H_2$ and $CH_4$ over rhodium catalyst from (Maestri, Vlachos et al. 2009) are provided in this section. These detailed microkinetic model are able to predict integral data of multiple processes. The parameters of the reaction mechanism been derived according to a multi-scale methodology: activation energies are predicted using the UBI-QEP theory, coverage effects are accounted for using Density Functional Theory(DFT), and pre-exponentials are calculated using transition state theory (TST).

In the input file reported the reactions are written in sequence, followed by the turn over frequency A (unitless and s-1), the exponential beta (-), the bond index (-), the temperature dependence (-), the type of kinetic method (UBI) and the type of reaction. All these parameters are required in order to compute the reaction rates.

## *$H_2$ over Rh in UBI-QEP format*

```
MATERIAL MAT-1

SITE/RH_SURFACE/    SDEN/2.49E-9/
    Rh(s)   H2O(s)  H(s)    OH(s)   O(s)
END

HEATS_OF_CHEMISORPTION / 300 /
    O(s)    /     1.5   /     100.0   /  O(s)  -26                          //
    H(s)    /     1.5   /     61.4    /  H(s)  -2.5                         //
    OH(s)   /     2.0   /     70.0    /  O(s)  -33     /   H2O(s)   25
//
    H2O(s)  /     2.5   /     10.8    /  OH(s)  25       /   H2O(s)  -4.5
//
END

REACTIONS
H2      +Rh(s)   +Rh(s)     =>H(s)    +H(s)     7.73E-01   0.9387  0.5
                                          UBI   2   ADS
H(s)    +H(s)   =>H2        +Rh(s)     +Rh(s)   5.56E+11  -0.4347  0.5
```

```
                                                UBI   2   DES
O2      +Rh(s)   +Rh(s)     =>O(s)      +O(s)   4.81E-02   1.9965  0.5
                                                UBI   2   ADS
O(s)    +O(s)   =>O2        +Rh(s)     +Rh(s)   4.31E12    1.1995  0.5
                                                UBI   2   DES
OH(s)   +Rh(s)  =>H(s)      +O(s)               5.2E10    -0.2659  0.5
                                                UBI   5   SUP
H(s)    +O(s)   =>OH(s)     +Rh(s)              4.69E10   -0.8196  0.5
                                                UBI   5   SUP
H2O(s)  +Rh(s)  =>H(s)      +OH(s)              4.78E12    0.0281  0.5
                                                UBI   5   SUP
H(s)    +OH(s)  =>H2O(s)    +Rh(s)              1.50E10    1.2972  0.5
                                                UBI   5   SUP
H2O(s)  +O(s)   =>OH(s)     +OH(s)              4.15E11   -2.113   0.5
                                                UBI   8   SUP
OH(s)   +OH(s)  =>H2O(s)    +O(s)               1.44E9    -0.2902  0.5
                                                UBI   8   SUP
OH      +Rh(s)  =>OH(s)                         2.66E-1   -0.2891  0.5
                                                UBI   1   ADS
OH(s)           =>OH        +Rh(s)              1.14E13   -0.95    0.5
                                                UBI   1   DES
H2O     +Rh(s)  =>H2O(s)                        7.72E-2    1.4067  0.5
                                                UBI   1   ADS
H2O(s)          =>H2O       +Rh(s)              2.06E13   -1.8613  0.5
                                                UBI   1   DES
H       +Rh(s)  =>H(s)                          1.93E-1    1.5313  0.5
                                                UBI   1   ADS
H(s)            =>H         +Rh(s)              2.4E12     1.3208  0.5
                                                UBI   1   DES
O       +Rh(s)  =>O(s)                          4.46E-2   -1.9236  0.5
                                                UBI   1   ADS
O(s)            =>O         +Rh(s)              9.74E12   -1.9701  0.5
                                                UBI   1   DES
END
```

## *$CH_4$ over Rh in UBI-QEP format*

```
MATERIAL MAT-1

SITE/RH_SURFACE/    SDEN/2.49E-9/
    Rh(s)   H2O(s)  H(s)    OH(s)   CO(s)   C(s)
    CH3(s)  CH2(s)  CH(s)   O(s)    CO2(s)  COOH(s)
    HCOO(s)
END

HEATS_OF_CHEMISORPTION / 300 /
    O(s)   /     1.5   /     100.0   /  O(s)  -26                          //
    H(s)   /     1.5   /     62.3    /  CO(s) -3.7    /  H(s)  -2.5    //
    OH(s)  /     2.0   /     70.0    /  O(s)  -33     /   H2O(s)   25
//
```

```
    H2O(s) /     2.5   /     10.8    /  OH(s)  25       /   H2O(s)  -4.5
//
    CO(s)  /     2.0   /     38.5    /  CO(s) -15       /   H(s)    -3.7
//
    CO2(s) /     2.0   /     5.2
//
    COOH(s)/     2.5   /     62.2
//
    HCOO(s)/     2.5   /     69.2
//
    C(s)   /     1.5   /     159.0
//
    CH(s)  /     2.0   /     151.2
//
    CH2(s) /     2.5   /     109.3
//
    CH3(s) /     2.5   /     42.4
//
    CH4         / 2.0 /    6.0                                              //
END

REACTIONS
H2      +Rh(s)   +Rh(s)      =>H(s)    +H(s)     7.73E-01   0.9387  0.5
                                            UBI   2   ADS
H(s)    +H(s)    =>H2        +Rh(s)     +Rh(s)   5.56E+11  -0.4347  0.5
                                            UBI   2   DES
O2      +Rh(s)   +Rh(s)      =>O(s)      +O(s)   4.81E-02   1.9965  0.5
                                            UBI   2   ADS
O(s)    +O(s)    =>O2        +Rh(s)     +Rh(s)   4.31E12    1.1995  0.5
                                            UBI   2   DES
OH(s)   +Rh(s)   =>H(s)      +O(s)              5.2E12    -0.2659  0.3
                                            UBI   5   SUP
H(s)    +O(s)    =>OH(s)     +Rh(s)             4.69E12   -0.8196  0.3
                                            UBI   5   SUP
H2O(s)  +Rh(s)   =>H(s)      +OH(s)             5.74E11    0.0281  0.55
                                            UBI   5   SUP
H(s)    +OH(s)   =>H2O(s)    +Rh(s)             1.8E9      1.2972  0.55
                                            UBI   5   SUP
H2O(s)  +O(s)    =>OH(s)     +OH(s)             2.08E13   -2.113   0.3
                                            UBI   8   SUP
OH(s)   +OH(s)   =>H2O(s)    +O(s)              7.22E10   -0.2902  0.3
                                            UBI   8   SUP
OH      +Rh(s)   =>OH(s)                        2.66E-1   -0.2891  0.5
                                            UBI   1   ADS
OH(s)            =>OH        +Rh(s)             1.14E13   -0.95    0.5
                                            UBI   1   DES
H2O     +Rh(s)   =>H2O(s)                       7.72E-2    1.4067  0.5
                                            UBI   1   ADS
H2O(s)           =>H2O       +Rh(s)             2.06E13   -1.8613  0.5
                                            UBI   1   DES
H       +Rh(s)   =>H(s)                         1.93E-1    1.5313  0.5
                                            UBI   1   ADS
H(s)             =>H         +Rh(s)             2.4E12     1.3208  0.5
                                            UBI   1   DES
O       +Rh(s)   =>O(s)                         4.46E-2   -1.9236  0.5
                                            UBI   1   ADS
O(s)             =>O         +Rh(s)             9.74E12   -1.9701  0.5
                                            UBI   1   DES
```

```
CO      +Rh(s)  =>CO(s)                          5.00E-1   -2.0000  0.5
                                            UBI   1   ADS
CO(s)           =>CO        +Rh(s)              5.65E12    1.9879  0.5
                                            UBI   1   DES
CO2     +Rh(s)  =>CO2(s)                        3.67E-1   -2.3294  0.5
                                            UBI   1   ADS
CO2(s)          =>CO2       +Rh(s)              7.54E10    2.1831  0.5
                                            UBI   1   DES
CO2(s)  +Rh(s)  =>CO(s)     +O(s)               4.12E09    1.9698  0.9
                                            UBI   5   SUP
CO(s)   +O(s)   =>CO2(s)    +Rh(s)              3.27E09    1.3560  0.9
                                            UBI   5   SUP
COOH    +Rh(s)  =>COOH(s)                       5.34E-1   -1.0767  0.5
                                            UBI   1   ADS
COOH(s)         =>COOH      +Rh(s)              1.12E11    1.6803  0.5
                                            UBI   1   DES
HCOO    +Rh(s)  +Rh(s)      =>HCOO(s)           1.89E-2   -0.5548  0.5
                                            UBI   1   ADS
HCOO(s)         =>HCOO      +Rh(s)  +Rh(s)      3.74E13    0.5548  0.5
                                            UBI   1   DES
CO2(s)  +H(s)   =>CO(s)     +OH(s)              7.99E13    0.0301  0.7
                                            UBI   6   SUP
CO(s)   +OH(s)  =>CO2(s)    +H(s)               7.02E13    0.0301  0.7
                                            UBI   6   SUP
COOH(s) +Rh(s)  =>CO(s)     +OH(s)              1.07E12   -0.4123  0.5
                                            UBI   5   SUP
CO(s)   +OH(s)  =>COOH(s)   +Rh(s)              9.37E11    0.4123  0.5
                                            UBI   5   SUP
COOH(s) +Rh(s)  =>CO2(s)    +H(s)               1.0E10    -0.4424  0.5
                                            UBI   5   SUP
CO2(s)  +H(s)   =>COOH(s)   +Rh(s)              9.99E9     0.4424  0.5
                                            UBI   5   SUP
CO(s)   +H2O(s) =>COOH(s)   +H(s)               3.34E11   -0.2222  0.5
                                            UBI   6   SUP
COOH(s) +H(s)   =>CO(s)     +H2O(s)             1.20E09    0.2223  0.5
                                            UBI   6   SUP
COOH(s) +O(s)   =>CO2(s)    +OH(s)              9.51E10   -0.7192  0.5
                                            UBI   6   SUP
CO2(s)  +OH(s)  =>COOH(s)   +O(s)               1.05E11    0.7192  0.5
                                            UBI   6   SUP
CO2(s)  +H2O(s) =>COOH(s)   +OH(s)              1.78E12   -0.1922  0.5
                                            UBI   6   SUP
COOH(s) +OH(s)  =>CO2(s)    +H2O(s)             5.60E09    0.1922  0.5
                                            UBI   6   SUP
HCOO(s)         =>CO2(s)    +H(s)               3.86E13   -1.1253  0.5
                                            UBI   5   SUP
CO2(s)  +H(s)   =>HCOO(s)                       1.04E09    1.1254  0.5
                                            UBI   5   SUP
CO2(s)  +OH(s)  +Rh(s)=>HCOO(s)  +O(s)          1.09E09    1.4022  0.5
                                            UBI   6   SUP
HCOO(s)+O(s)  =>CO2(s)     +OH(s)  +Rh(s)       3.67E13   -1.4022  0.5
                                            UBI   6   SUP
CO2(s)  +H2O(s) +Rh(s)=>HCOO(s)  +OH(s)         9.24E09    0.4908  0.5
                                            UBI   6   SUP
HCOO(s)+OH(s)=>CO2(s)+H2O(s)     +Rh(s)         1.08E12   -0.4908  0.5
                                            UBI   6   SUP
C       +Rh(s)  =>C(s)                          4.98E-02  -1.8618  0.5
                                            UBI   1   ADS
```

```
C(s)              =>C      +Rh(s)                    1.42E13    1.8618  0.5
                                                UBI   1   DES
CH       +Rh(s)   =>CH(s)                           2.29E-02  -1.0798  0.5
                                                UBI   1   ADS
CH(s)             =>CH     +Rh(s)                   3.08E13    1.0798  0.5
                                                UBI   1   DES
CH2      +Rh(s)   =>CH2(s)                          4.09E-02  -0.4265  0.5
                                                UBI   1   ADS
CH2(s)            =>CH2    +Rh(s)                   1.73E13    0.4265  0.5
                                                UBI   1   DES
CH3      +Rh(s)   =>CH3(s)                          1.35E-01   0.0326  0.5
                                                UBI   1   ADS
CH3(s)            =>CH3    +Rh(s)                   5.22E12   -0.0325  0.5
                                                UBI   1   DES
CH4      +Rh(s)   +Rh(s)   =>CH3(s)     +H(s)      5.72E-01   0.7883  0.5
                                                UBI   4   ADS
CH3(s)   +H(s)    =>CH4         +Rh(s)   +Rh(s)     7.72E10   -0.7883  0.5
                                                UBI   4   DES
CH3(s)   +Rh(s)   =>CH2(s)      +H(s)               2.49E10    0.0862  0.5
                                                UBI   5   SUP
CH2(s)   +H(s)    =>CH3(s)      +Rh(s)              2.57E09   -0.0862  0.5
                                                UBI   5   SUP
CH2(s)   +Rh(s)   =>CH(s)       +H(s)               5.50E10   -0.1312  0.5
                                                UBI   5   SUP
CH(s)    +H(s)    =>CH2(s)      +Rh(s)              7.27E09    0.1312  0.5
                                                UBI   5   SUP
CH(s)    +Rh(s)   =>C(s)        +H(s)               4.58E12   -0.2464  0.5
                                                UBI   5   SUP
C(s)     +H(s)    =>CH(s)       +Rh(s)              2.18E11    0.2464  0.5
                                                UBI   5   SUP
CH3(s)   +O(s)    =>CH2(s)      +OH(s)              2.96E11   -0.1906  0.5
                                                UBI   6   SUP
CH2(s)   +OH(s)   =>CH3(s)      +O(s)               3.38E10    0.1906  0.5
                                                UBI   6   SUP
CH2(s)   +O(s)    =>CH(s)       +OH(s)              2.61e11   -0.4081  0.5
                                                UBI   6   SUP
CH(s)    +OH(s)   =>CH2(s)      +O(s)               3.83E10    0.4081  0.5
                                                UBI   6   SUP
CH(s)    +O(s)    =>C(s)        +OH(s)              4.35e11   -0.5232  0.5
                                                UBI   6   SUP
C(s)     +OH(s)   =>CH(s)       +O(s)               2.30e10    0.5232  0.5
                                                UBI   6   SUP
CH3(s)   +OH(s)   =>CH2(s)      +H2O(s)             1.74E09    0.7208  0.5
                                                UBI   6   SUP
CH2(s)   +H2O(s)  =>CH3(s)      +OH(s)              5.73E10   -0.7208  0.5
                                                UBI   6   SUP
CH(s)    +H2O(s)  =>CH2(s)      +OH(s)              6.49E11   -0.5033  0.5
                                                UBI   6   SUP
CH2(s)   +OH(s)   =>CH(s)       +H2O(s)             1.54E10    0.5033  0.5
                                                UBI   6   SUP
C(s)     +H2O(s)  =>CH(s)       +OH(s)              9.74E11   -0.3882  0.5
                                                UBI   6   SUP
CH(s)    +OH(s)   =>C(s)        +H2O(s)             6.41E10    0.3882  0.5
                                                UBI   6   SUP
CO(s)    +Rh(s)   =>C(s)        +O(s)               1.25E09    0.5712  0.5
                                                UBI   5   SUP
C(s)     +O(s)    =>CO(s)       +Rh(s)              7.22E09   -0.5712  0.5
                                                UBI   5   SUP
```

```
CO(s)    +H(s)    =>CH(s)      +O(s)                9.07E09    0.8176  0.8
                                                UBI   6   SUP
CH(s)    +O(s)    =>CO(s)      +H(s)                1.10E12   -0.8176  0.8
                                                UBI   6   SUP
CO(s)    +H(s)    =>C(s)       +OH(s)               1.18E12    0.2944  0.15
                                                UBI   6   SUP
C(s)     +OH(s)   =>CO(s)      +H(s)                7.60E12   -0.2944  0.15
                                                UBI   6   SUP
CO(s)    +CO(s)   =>C(s)       +CO2(s)              1.11E09    0.2644  0.5
                                                UBI   7   SUP
C(s)     +CO2(s)  =>CO(s)      +CO(s)               8.10E09   -0.2644  0.5
                                                UBI   7   SUP
END
```

# Appendix C – Equations solved in catalyticFOAM

In this section the derivations of conservation equations of mass and energy present in catalyticFOAM solver are provided. The equations have been written considering a batch reactor.

**Total mass conservation**

The expression of the total mass balance for a batch reactor can be written as:

$$\frac{dm_{tot}}{dt} = \sum_{i=1}^{NC} \frac{dm_i}{dt} \tag{C.4}$$

Splitting the source term in the homogeneous and heterogeneous terms:

$$\sum_{i=1}^{NC} \frac{dm_i}{dt} = V_{react} \left( \sum_{i=1}^{NC} \dot{m}_i^{\hom} + \sum_{i=1}^{NC} \sum_{k=1}^{NCF} \dot{m}_{i,k}^{het} \right) \tag{C.5}$$

$$\dot{m}_{i,k}^{het} = A_{cat}^{(k)} \tilde{R}_{i,k}^{het} MW_i \tag{C.6}$$

$$\dot{m}_i^{\hom} = \tilde{R}_i^{\hom} MW_i \tag{C.7}$$

Where NC indicates the number of species , $\tilde{R}_i^{\hom}$ is the consumption/production rate of the i-th specie due to homogeneous reactions in $\left[ \frac{mol}{m_{react}^3 s} \right]$ , $\tilde{R}_{i,k}^{het}$ is the consumption/production rate of the i-th specie due to heterogeneous reactions in k-th catalytic face of the computational cell in $\left[ \frac{mol}{m_{cat}^2 s} \right]$, $V_{react}$ is the reactor volume in $m_{react}^3$ and $A_{cat}^{(k)}$ the total catalytic surface of the k-th catalytic face of the computational cell in $m_{cat}^2$ .

In order to express the area of the k-th catalytic face of the cell in terms of geometric area, the parameter $\alpha_{cat}$ is introduced. This is an intensive property of the catalyst and is defined as:

$$\alpha_{cat} = \frac{A_{cat}}{A_{react}} \tag{C.8}$$

Since the sum of production rates in the gas phase is zero, the equation can be written as:

$$\frac{dm_{tot}}{dt} = \sum_{i=1}^{NC}\sum_{k=1}^{NCF} \dot{m}_{i,k}^{het} = \sum_{i=1}^{NC}\sum_{k=1}^{NCF} \left( \alpha_{cat}^{(k)} A_{face}^{(k)} \tilde{R}_{i,k}^{het} MW_i \right) = \sum_{k=1}^{NCF} \alpha_{cat}^{(k)} A_{face}^{(k)} \sum_{i=1}^{NC} \tilde{R}_{i,k}^{het} MW_i \tag{C.9}$$

**Species mass conservation**

The generic expression for the mass balance of the ith species is defined as the accumulation (derivative of mass over time) equal to the net mass flow (inlet minus outlet mass flows) plus the mass generation due to the reactions ( $R_i$ ). The mathematical formula is:

$$\frac{dm_i}{dt} = \dot{m}_i^{IN} - \dot{m}_i^{OUT} + R_i \tag{C.10}$$

The inlet and outlet mass flows are neglected because we adopt a batch reactor model, i.e. the system is thermodynamically closed. Splitting the reaction term into homogeneous and heterogeneous:

$$\frac{d(m_{tot}\omega_i)}{dt} = \omega_i \frac{dm_{tot}}{dt} + m_{tot}\frac{d\omega_i}{dt} = \tilde{R}_i^{\hom} MW_i V + \sum_{k=1}^{NCF} \left( \alpha_{cat}^{(k)} A_{face}^{(k)} \tilde{R}_{i,k}^{het} MW_i \right) \tag{C.11}$$

Recalling the expression for the total mass balance derived in section C.1:

$$\frac{d\omega_i}{dt} = \frac{\tilde{R}_i^{\hom} MW_i V}{m_{tot}} + \frac{\sum_{k=1}^{NCF} \left( \alpha_{cat}^{(k)} A_{face}^{(k)} \tilde{R}_{i,k}^{het} MW_i \right)}{m_{tot}} - \frac{\omega_i}{m_{tot}} \sum_{k=1}^{NCF} \alpha_{cat}^{(k)} A_{face}^{(k)} \sum_{i=1}^{NC} \tilde{R}_{i,k}^{het} MW_i \tag{C.12}$$

Introducing the density:

$$\frac{d\omega_i}{dt} = \frac{\tilde{R}_i^{\hom} MW_i}{\rho} + \frac{\sum_{k=1}^{NCF} \left( \alpha_{cat}^{(k)} A_{face}^{(k)} \tilde{R}_{i,k}^{het} MW_i \right)}{\rho V_{react}} - \frac{\omega_i}{\rho V_{react}} \sum_{k=1}^{NCF} \alpha_{cat}^{(k)} A_{face}^{(k)} \sum_{i=1}^{NC} \tilde{R}_{i,k}^{het} MW_i \tag{C.13}$$

Grouping the surface terms:

$$\frac{d\omega_i}{dt} = \frac{\tilde{R}_i^{\hom} MW_i}{\rho} + \frac{1}{\rho V_{react}} \left( \sum_{k=1}^{NCF} \left( \alpha_{cat}^{(k)} A_{face}^{(k)} \tilde{R}_{i,k}^{het} MW_i \right) - \omega_i \sum_{k=1}^{NCF} \alpha_{cat}^{(k)} A_{face}^{(k)} \sum_{i=1}^{NC} \tilde{R}_{i,k}^{het} MW_i \right) \tag{C.14}$$

The final expression for the mass conservation of the ith species is:

$$\frac{d\omega_i}{dt} = \frac{\tilde{R}_i^{\hom} MW_i}{\rho} + \frac{1}{\rho V_{react}} \left[ \sum_{k=1}^{NCF} \alpha_{cat}^{(k)} A_{face}^{(k)} \left( \tilde{R}_{i,k}^{het} MW_i - \omega_i \sum_{i=1}^{NC} \tilde{R}_{i,k}^{het} MW_i \right) \right] \tag{C.15}$$

**Energy conservation equation**

The equation for the energy conservation in a batch reactor is written as follows:

$$\frac{dH_{tot}}{dt} = 0 \tag{C.16}$$

The total enthalpy of the system is expanded as follows:

$$H_{tot} = \sum_{i=1}^{NC} m_i \hat{H}_i \tag{C.17}$$

By consequence, for the primary derivation rules:

$$\frac{dH_{tot}}{dt} = \sum_{i=1}^{NC} m_i \frac{d\left(\hat{H}_i\right)}{dt} + \sum_{i=1}^{NC} \hat{H}_i \frac{d(m_i)}{dt} = 0 \tag{C.18}$$

Expressing the enthalpy variation with differential with respect to pressure, temperature and composition, it becomes:

$$\sum_{i=1}^{NC} m_i \frac{d(\hat{H}_i)}{dt} = \sum_{i=1}^{NC} m_i \frac{\partial(\hat{H}_i)}{\partial T} \frac{dT}{dt} + \sum_{i=1}^{NC} m_i \frac{\partial(\hat{H}_i)}{\partial P} \frac{dP}{dt} + \sum_{i=1}^{NC} m_i \frac{\partial(\hat{H}_i)}{\partial \omega_i} \frac{d\omega_i}{dt} \tag{C.19}$$

Since the Joule-Thomson effect is considered neglectable $\left( \frac{\partial(\hat{H}_i)}{\partial P} = 0 \right)$ and the mixture is considered to be ideal $\left( \frac{\partial(\hat{H}_i)}{\partial \omega_i} = 0 \right)$ and being $\frac{\partial(\hat{H}_i)}{\partial T} = \hat{C}p_i$ the expression becomes:

$$\sum_{i=1}^{NC} m_i \hat{C}p_i \frac{dT}{dt} + \sum_{i=1}^{NC} \hat{H}_i \left( m_{tot} \frac{d\omega_i}{dt} + \omega_i \frac{dm_{tot}}{dt} \right) = 0 \tag{C.20}$$

Replacing with the expression of the material balance already derived in Eq. (C.9)-(C.15) is possible to obtain the final expression of the energy balance:

$$\sum_{i=1}^{NC} m_i \hat{C}p_i \frac{dT}{dt} = -\sum_{i=1}^{NC} \hat{H}_i m_{tot} \left\{ \frac{\tilde{R}_i^{\hom} MW_i}{\rho} + \frac{1}{\rho V_{react}} \left[ \sum_{k=1}^{NCF} \alpha_{cat}^{(k)} A_{face}^{(k)} \left( \tilde{R}_{i,k}^{het} MW_i - \omega_i \sum_{i=1}^{NC} \tilde{R}_{i,k}^{het} MW_i \right) \right] \right\} -$$
$$-\sum_{i=1}^{NC} \hat{H}_i \omega_i \left[ \sum_{k=1}^{NCF} \alpha_{cat}^{(k)} A_{face}^{(k)} \sum_{i=1}^{NC} \tilde{R}_{i,k}^{het} MW_i \right]$$

# Appendix D – Equations solved in catalyticFOAM multiregion

In this section the derivations of conservation equations of mass and energy present in catalyticFOAM multiRegion solver are provided. The equations have been written considering a batch reactor.

**Total mass conservation**

The expression of the total mass balance for a batch reactor can be written as:

$$\frac{dm_{tot}}{dt} = \sum_{i=1}^{NC} \frac{dm_i}{dt} \tag{D.21}$$

Splitting the source term in the homogeneous and heterogeneous terms:

$$\sum_{i=1}^{NC} \frac{dm_i}{dt} = V_{react} \tilde{R}_i^{\hom} MW_i + A_{cat} \sum_{i=1}^{NC} \tilde{R}_i^{het} MW_i \tag{D.22}$$

Where NC indicates the number of species, $\tilde{R}_i^{\hom}$ is the consumption/production rate of the i-th specie due to homogeneous reactions in $\left[\frac{mol}{m_{react}^3 s}\right]$, $\tilde{R}_i^{het}$ is the consumption/production rate of the i-th specie due to heterogeneous reactions in $\left[\frac{mol}{m_{cat}^2 s}\right]$, $V_{react}$ is the reactor volume in $m^3$ and $A_{cat}$ is the total catalytic surface in $m_{cat}^2$.

In order to express the area of catalytic surface of each computational cell, the parameter $a_{cat}$ is introduced. This is an intensive property of the catalyst defined as the specific catalytic area per unit of catalyst volume in $\left[m^{-1}\right]$:

$$a_{cat} = \frac{A_{cat}}{V_{cat}} \tag{D.23}$$

Since the sum of production rates in the gas phase is zero, the equation can be written as:

$$\frac{dm_{tot}}{dt} = \sum_{i=1}^{NC}\left(a_{cat}V_{react}\tilde{R}_i^{het}MW_i\right) = a_{cat}V_{react}\sum_{i=1}^{NC}\tilde{R}_i^{het}MW_i \tag{D.24}$$

**Species mass conservation**

The generic expression for the mass balance of the ith species is defined as the accumulation (derivative of mass over time) equal to the net mass flow (inlet minus outlet mass flows) plus the mass generation due to the reactions ( $R_i$ ). The mathematical formula is:

$$\frac{dm_i}{dt} = \dot{m}_i^{IN} - \dot{m}_i^{OUT} + R_i \tag{D.25}$$

The inlet and outlet mass flows are neglected because we adopt a batch reactor model, i.e. the system is thermodynamically closed. Splitting the reaction term into homogeneous and heterogeneous, and considering a generic catalytic cell in which both homogeneous reactions in the gaseous pores and heterogeneous reactions on the catalytic surface occur:

$$\frac{d(m_{tot}\omega_i)}{dt} = \omega_i\frac{dm_{tot}}{dt} + m_{tot}\frac{d\omega_i}{dt} = \tilde{R}_i^{\hom}MW_iV_{react} + a_{cat}V_{react}\tilde{R}_i^{het}MW_i \tag{D.26}$$

Recalling the expression for the total mass balance derived in section D.1:

$$\frac{d\omega_i}{dt} = \frac{\tilde{R}_i^{\hom}MW_iV_{react}}{m_{tot}} + \frac{a_{cat}V_{react}\tilde{R}_i^{het}MW_i}{m_{tot}} - \frac{\omega_i}{m_{tot}}a_{cat}V_{react}\sum_{i=1}^{NC}\tilde{R}_i^{het}MW_i \tag{D.27}$$

Introducing the density:

$$\frac{d\omega_i}{dt} = \frac{\tilde{R}_i^{\hom}MW_i}{\rho_{mix}\varepsilon} + \frac{a_{cat}V_{react}\tilde{R}_i^{het}MW_i}{\rho_{mix}\varepsilon} - \frac{\omega_i}{\rho_{mix}\varepsilon}a_{cat}\sum_{i=1}^{NC}\tilde{R}_i^{het}MW_i \tag{D.28}$$

Grouping the surface terms:

$$\frac{d\omega_i}{dt} = \frac{\tilde{R}_i^{\hom}MW_i}{\rho_{mix}\varepsilon} + \frac{1}{\rho_{mix}\varepsilon}\left(a_{cat}\tilde{R}_i^{het}MW - \omega_i a_{cat}\sum_{i=1}^{NC}\tilde{R}_i^{het}MW_i\right) \tag{D.29}$$

The final expression for the mass conservation of the i-th specie is:

$$\frac{d\omega_i}{dt} = \frac{\tilde{R}_i^{\text{hom}} MW_i}{\rho_{mix}\varepsilon} + \frac{a_{cat}}{\rho_{mix}\varepsilon}\left( \tilde{R}_i^{het} MW - \omega_i \sum_{i=1}^{NC} \tilde{R}_i^{het} MW_i \right) \tag{D.30}$$

**Energy conservation equation**

The equation for the energy conservation in a batch reactor is written as follows:

$$\frac{dH_{tot}}{dt} = 0 \tag{D.31}$$

The total enthalpy of the system is expanded as follows:

$$H_{tot} = \sum_{i=1}^{NC} m_i \hat{H}_i \tag{D.32}$$

By consequence, for the primary derivation rules:

$$\frac{dH_{tot}}{dt} = \sum_{i=1}^{NC} m_i \frac{d\left(\hat{H}_i\right)}{dt} + \sum_{i=1}^{NC} \hat{H}_i \frac{d(m_i)}{dt} = 0 \tag{D.33}$$

Expressing the enthalpy variation with differential with respect to pressure, temperature and composition, it becomes:

$$\sum_{i=1}^{NC} m_i \frac{d(\hat{H}_i)}{dt} = \sum_{i=1}^{NC} m_i \frac{\partial(\hat{H}_i)}{\partial T}\frac{dT}{dt} + \sum_{i=1}^{NC} m_i \frac{\partial(\hat{H}_i)}{\partial P}\frac{dP}{dt} + \sum_{i=1}^{NC} m_i \frac{\partial(\hat{H}_i)}{\partial \omega_i}\frac{d\omega_i}{dt} \tag{D.34}$$

Since the Joule-Thomson effect is considered neglectable $\left(\frac{\partial(\hat{H}_i)}{\partial P} = 0\right)$ and the mixture is considered to be ideal $\left(\frac{\partial(\hat{H}_i)}{\partial \omega_i} = 0\right)$ and being $\frac{\partial(\hat{H}_i)}{\partial T} = \hat{C}p_i$ the expression becomes:

$$\sum_{i=1}^{NC} m_i \hat{C}p_i \frac{dT}{dt} + \sum_{i=1}^{NC} \hat{H}_i \left( m_{tot} \frac{d\omega_i}{dt} + \omega_i \frac{dm_{tot}}{dt} \right) = 0 \tag{D.35}$$

Replacing with the expression of the material balance already derived in Eq. (D.24)-(D.30) is possible to obtain the final expression of the energy balance:

$$\begin{aligned} \sum_{i=1}^{NC} m_i \hat{C}p_i \frac{dT}{dt} = &-\sum_{i=1}^{NC} \hat{H}_i m_{tot} \left[ \frac{\tilde{R}_i^{\text{hom}} MW_i}{\rho_{mix}\varepsilon} + \frac{a_{cat}}{\rho_{mix}\varepsilon}\left( \tilde{R}_i^{het} MW - \omega_i \sum_{i=1}^{NC} \tilde{R}_i^{het} MW_i \right) \right] - \\ &-\sum_{i=1}^{NC} \hat{H}_i \omega_i \left[ a_{cat} V_{react} \sum_{i=1}^{NC} \tilde{R}_i^{het} MW_i \right] \end{aligned} \tag{D.36}$$

# List of figures

# List of tables

# Bibliography


1. Calonaci, M., Furnari, F., *A computational framework for the simulation of gas-solid catalytic reactors based on a multiregion approach.* 2012.
2. Nova, I., M. Colombo, and E. Tronconi. *Development of chemically consistent models of NH3-SCR reactions over Fe-zeolite catalysts for the aftertreatment of Diesel engine exhausts*. 2012.
3. Nova, I. and E. Tronconi. *Kinetic study of the NO/NO2-NH3 SCR reactions over a V2O5-WO3/TiO2 commercial catalyst for the after treatment of Diesel engines exhausts*. 2009.
4. Thiele, H., *Drei Kuckuks-Eier in einem Nest aufgefunden - Mittheilung.* Journal für Ornithologie, 1874. **22**(1): p. 80-81.
5. Thiele, J., *Zur Scheidung und Bestimmung des Antimons.* Zeitschrift für Analytische Chemie, 1891. **30**(1): p. 473-482.
6. Maestri, M. and K. Reuter, *Semiempirical rate constants for complex chemical kinetics: First-principles assessment and rational refinement.* Angewandte Chemie - International Edition, 2011. **50**(5): p. 1194-1197.
7. Salciccioli, M., et al., *A review of multiscale modeling of metal-catalyzed reactions: Mechanism development for complexity and emergent behavior.* Chemical Engineering Science, 2011. **66**(19): p. 4319-4355.
8. Matera, S. and K. Reuter. *From electrons to reactive flow: Coupling first-principles statistical mechanics with continuum level simulations*. 2009.
9. Goisis, S., Osio, A. , *Computational fluid dynamics of gas-solid catalytic reactors based on microkinetic description of surface chemistry*. 2011.
10. Mangani, L., *Development and Validation of an Object Oriented CFD Solver for Heat Transfer and Combustion Modeling in Turbomachinery Applications.* 2008.
11. Fluent, I., *GAMBIT 2.2 - Tutorial Guide.* 2004.
12. OpenFoam, *The Open Source CFD Toolbox - User Guide.* 2011.
13. Ahrens J., G.B.a.L.C., *ParaView: An End-User Tool for Large Data Visualization.* In the Visualization Handbook. Edited by C.D. Hansen and C.R. Johnson. Elsevier., 2005.
14. Quarteroni, A.a.A.V., *Domain decomposition methods for partial differential equations (Numerical mathematics and scientific computation).* Oxford University Press, 1999.
15. Versteeg, H.K.a.W.M., *An introduction to Computational Fluid Dynamics.* Longman Scientific & Technical, 1995.
16. Patankar, S.V.a.D.B.S., *A calculation procedure for heat, mass and momentum transfer in three-dimensional parabolic flows.* 1972.
17. Van Doormaal, J.P.a.G.D.R., *An evaluation of the segregated approach for predicting incompressible fluid flows.* 1985.
18. Buzzi-Ferraris, G., *Metodi numerici e software in C++*. Wiley Longmann Italia, 1998.
19. Jasak, H., *Error analyis and estimation for the finite element method with applications to fluid flows*. 1996, Empirial College: London.
20. M., H.F.H.a.P., *Computational Methods for Fluid Dynamics.* Springer, 1999.
21. Dumesic, J.A., G. W. Huber, et al., *Microkinetics: Rates of Catalytic Reactions.* Handbook of Heterogeneous Catalysis. Ertl, et al., Editors, 2008.
22. Gokhale, A.A., S. Kandoi, et al., *Molecular-level descriptions of surface chemistry in kinetic models using density functional theory.* Chemical Engineering Science 59(22-23): 4679-4691, 2004.
23. Schlögl, R., *Theory in heterogeneous catalysis - An experimentalist's view.* Cattech 5(3): 146-170, 2001.

24. ReactorDesign, *CHEMKIN-PRO® Software - Input Manual* *http://www.cadfamily.com/download/CAE/Chemkin-Tutorial/Input.pdf*. 2008.
25. Shustorovich, E.a.H.S., *The UBI-QEP method: a practical theoretical approach to understanding chemistry on transition metal surfaces.* Surface Science Reports, 1998.
26. Maestri, M., Vlachos, D.G., Beretta, A. Groppi, G., Tronconi, E., *A C1 microkinetic model for CH4 conversion to syngas on Rh/Al2O3.* A.I.Ch.E. Journal, 2009. **55**: p. 993-1008.
27. LAMMPS, *http://lammps.sandia.gov/*. 1995. p. LAMMPS Molecular Dynamics Simulator.
28. Strang , G., *On the construction and comparison of different schemes* SIAM Journal of numerical analysis, 1968. **5**: p. 506.
29. Bird, R.B., W.E. Stewart, and E.N. Ligthfott, eds. *Transport Phenomena*. Second ed. 2002, John Wiley & Sons, Inc.: New York.
30. Maestri, M.B., A., *Two dimensional detailed modelling of fuel-rich H2 combstion over Rh/Al2O3 catalyst.* Chemical engineering science 2008. **63**: p. 2657-2669.
31. Stanjan. *http://navier.engr.colostate.edu/~dandy/code/code-4/*. [Results at equilibrium conditions].
32. Sportisse, B., *An Analysis of Operator Splitting Techniques in the Stiff Case.* Journal of Computational Physics, 2000. **161**(1): p. 140-168.
33. Sportisse, B., G. Bencteux, and P. Plion, *Method of lines versus operator splitting for reaction-diffusiuon systems with fast chemistry.* Environmental Modelling and Software, 2000. **15**(6-7 SPEC. ISS): p. 673-679.
34. Sportisse, B. and R. Djouad, *Reduction of chemical kinetics in air pollution modeling.* Journal of Computational Physics, 2000. **164**(2): p. 354-376.
35. Issa, R.I., *Soolution of the implicitly discretized fluid flow equations by operator-splitting* Journal of computing phisics, 1986. **62**: p. 40-65.
36. Donazzi, A., Beretta, A., Groppi, G., Forzatti, P., *Catalytic partial oxidation of methane over a 4% Rh/α-Al2O3 catalyst. Part I:Kinetic study in annular reactor.* Journal of Catalysis, 2008. **255**: p. 241-258.
37. Penntinen, Y.e.a., *A PimpleFoam tutorial for channel flow, with respect to different LES models.* 2011.
38. M., H.F.H.a.P., *Computational Methods for Fluid Dynamics.* 2nd Edition. Springer, 1999.
39. Campbell, C.a., *MRconjugateHeatFoam: A Dirichelet-Neumann partitioned multi-region conjugate heat transfer solver.* 6th OpenFOAM Workshop, 2011.
40. Clifford, 6th OpenFOAM Workshop 2011.
41. Torrance, J.a., *Computational Heat Transfer.* Taylor & Francis 2003, 2003.
42. Wheeler, A., *Catalysis*. Vol. II. 1955.
43. Wakao. W, S., J.M., Chem. Eng. Sci. 17, 1962.
44. Hayes, R.E., et al., *Evaluating the effective diffusivity of methane in the washcoat of a honeycomb monolith.* Applied Catalysis B: Environmental, 2000. **25**(2-3): p. 93-104.
45. Linic, S. and M.A. Barteau, *Construction of a reaction coordinate and a microkinetic model for ethylene epoxidation on silver from DFT calculations and surface science experiments.* Journal of Catalysis, 2003. **214**(2): p. 200-212.
46. Maestri, M., et al., *Two-dimensional detailed modeling of fuel-rich H2 combustion over Rh / Al2 O3 catalyst.* Chemical Engineering Science, 2008. **63**(10): p. 2657-2669.
47. Zhu, H.P., et al., *Effect of particle properties on particle percolation behaviour in a packed bed.* Minerals Engineering, 2009. **22**(11): p. 961-969.
48. Tokoro , C.O., K Sadaki,J, *Fast Algorithm for the Discrete Element Method by Contact Force Prediction.* Kona, 2005. **23**.
49. SDEC, *http://geo.hmg.inpg.fr/frederic/Research_project_Discrete_Element_Software.html*. p. An open–source software using a discrete element method to simulate granular material.

50. Yade, *https://www.yade-dem.org/doc/*. p. An extensible open-source framework for discrete numerical models, focused on Discrete Element Method.
51. LIGGHTS, *http://cfdem.dcs-computing.com/?q=OpenSourceDEM*. p. Open Source Discrete Element Method Particle Simulation Code.
52. MechSys, *http://mechsys.nongnu.org/index.shtml*. p. Mechanical Systems: Computing library for simulations in continuum and discrete mechanics.
53. Bai, H., et al., *A coupled DEM and CFD simulation of flow field and pressure drop in fixed bed reactor with randomly packed catalyst particles.* Industrial and Engineering Chemistry Research, 2009. **48**(8): p. 4060-4074.
54. Dixon, A.G., *Wall and particle-shape effects on heat transfer in packed beds.* Chem. Eng. Commun, 1988. **71**: p. 217-237.
55. Eisfeld, B. and K. Schnitzlein, *The influence of confining walls on the pressure drop in packed beds.* Chemical Engineering Science, 2001. **56**(14): p. 4321-4329.
56. Handley , D.H., P.J, *Momentum and heat transfer mechanics in regular shaped pakings.* Transactions of the Institution of Chemical Engineers, 1968. **46**: p. T251-T264.
57. Baker, M.J., P.G. Young, and G.R. Tabor, *Image based meshing of packed beds of cylinders at low aspect ratios using 3d MRI coupled with computational fluid dynamics.* Computers and Chemical Engineering, 2011. **35**(10): p. 1969-1977.
58. Ergun, A., *Fluid Flow through Randomly Packed Columns and Fluidized Beds.* Industrial and engineering chemistry, 1949. **41**(6): p. 1179 - 1184.
59. OpenFoam, *www.openfoam.com*. 2001. p. OpenFoam: the open source CFD.